

PREPARATION AND CHARACTERIZATION OF IRON-OXIDE BIOCHAR COMPOSITES AND THEIR APPLICATIONS IN ARSENIC REMOVAL FROM WATER

**Thesis submitted to Jawaharlal Nehru University in partial fulfillment of
the requirement for the award of the degree**

Doctor of Philosophy

By

PRACHI SINGH



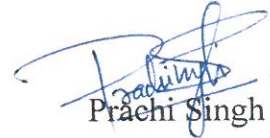
**School of Environmental Sciences
Jawaharlal Nehru University
New Delhi-110067
India, 2019**

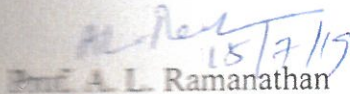


जवाहरलाल नेहरू विश्वविद्यालय
Jawaharlal Nehru University
SCHOOL OF ENVIRONMENTAL SCIENCES
New Delhi - 110067, INDIA

CERTIFICATE

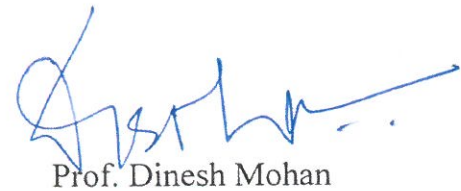
This is to certify that the research work embodied in this thesis entitled "Preparation and Characterization of Iron-Oxide Biochar Composites and their Applications in Arsenic Removal from Water" is submitted to Jawaharlal Nehru University for the award of the degree of **Doctor of Philosophy**. This work is original and has not been submitted in part or in full for any other degree or diploma to any university/institution.


Prachi Singh


Prof. A. L. Ramanathan

(Dean)

प्रो. अ. ल. रामनाथन / Prof. A. L. Ramanathan
विद्यालय / Dean
पर्यावरण विज्ञान संस्थान
School of Environmental Sciences
जवाहरलाल नेहरू विश्वविद्यालय, नई दिल्ली-६७
Jawaharlal Nehru University, New Delhi-67


Prof. Dinesh Mohan

(Supervisor)



Dr. Dinesh Mohan
Professor
School of Environment Sciences
Jawaharlal Nehru University
New Delhi-110067, India

*DEDICATED TO MY
PARENTS*

ACKNOWLEDGEMENTS

The process of writing thesis during last five years 2014-2019 has been the most enriching experiences of my life. The intellectual and technical growth, however, could not have happened without the motivation and support of people from different spheres. The critical inputs and encouragement from all these people have shaped this crucial part of life. I owe my deepest gratitude and thankfulness to all these people.

Foremost, I would like to thank my supervisor Prof. Dinesh Mohan for his excellent support and great confidence he placed in me. Our conversations and his suggestions on conducting experiments, relating output results with the field applicability, writing papers, preparing for conferences/workshops, scientific activity have been a valuable asset to me. His invaluable patience, guidance, perseverance and dedication, have enabled me in preparing my thesis. He had always set high standards and bars for writing papers and giving talks, and the efforts to meet those standards were well worth. I have learnt a lot from him beyond area of academics in art of communicating with the research colleagues, taking care of laboratory, and in developing didactic qualities.

I express my thankfulness to Prof. A L Ramanathan, Dean, School of Environmental Sciences for his enormous motivation. My sincere thanks to the members of my research advisory

committee, Prof. H. L. Bohidar, School of Physical Sciences and Prof. J. K. Tripathi, School of Environmental Sciences who profoundly influenced my thinking and approach about the subject of my thesis. Through presentations of my work at regular intervals, inputs, suggestions and in-depth analyses constantly shaped and improved my doctoral thesis. They have been always here to listen and advice.

My special thanks to Prof. Charles. U. Pittman jr., Department of Chemistry, Mississippi State University, USA for providing great help and expertise in writing mechanism for the removal of arsenic onto developed iron-oxide composite biochars. I extend my love and thanks to Mam Cathy. C. Pittman, Prof. Ashli Brown and Prof. Todd from Mississippi, USA who gave their constant motivation in our friendship.

I also extend my gratitude to my lab collaborators-Dr. Ankur Sarswat, Dr. Rahul Kumar Dhaka, Dr. Shalini Rajput, Dr. Rupa, Hemant, Vineet, Manavendra, Kamal, Abhishek Kumar, Madhu and other young research scholars. I thank my master's batch mates (Sumeet, Arindan, Somak, Kanhaiya, Mayank, Anshul, Anil, Rajkumar, Neha, Anita, Urvashi, Sonali, Monika, Deepika, Priyanka, Harpreet, Madhvi, Prince, Sana) and in particular my roommate Suchita Yadav. They all have filled my journey with joy, fun and cheers in my long tenure and stay at JNU. I also express my immense gratitude to the staff members of my center and JNU academics.

I am extremely thankful to Harshita Asthana and Shailesh Kumar Yadav. They apart from helping me in preparing site map and in collecting and providing field samples from Ballia and Kushinagar, have been a constant motivation and support in all my hard and happy times and bestowed lifelong wonderful friendship upon me.

I also express my sincere thanks to JNUite and DM, Yogendra Singh who motivated me in taking up challenge for treating arsenic and fluoride rich water at grass root levels. I express my sincere gratitude and thanks to my friend Lt. Col. Gaurang Jain who was always there to cheer me up and stood as a source of motivation and made it lighter by bestowing wonderful company and laughter to it. In addition would like to thanks Dr. Ajay Gangwar for his constant guidance and support. Their confidence and trust over me kept my ambition alive.

I owe my deepest gratitude to Prof. Anirban Chakraborty, School of Computational and Integrative Sciences for always being my family. His invaluable guidance, care, protection and motivation both in academics and spiritual part of life have made me reach until here and kept me boosted. I also owe my love and sincere gratitude to my teacher and lecturer of chemistry department, I. T. (PG) college, Lucknow Dr. Archana Talwar. Her motherly care, affection, made me part of her family, and her constant motivation and blessings were foundation to my success. I thanks Dr. Arpita Mitra for becoming invaluable part of my life.

At last I owe my sincere and deepest love and gratitude to my parents and my brother Akshay who were always there for me. The wonderful stay at USA for conference would have not been possible without my brother's support. This journey so far has been possible only without the support and love brother. I do wish to thank them for teaching me great values in life. And in becoming my foundation stone in making me reach so far.

Above all, I thank Swami Vivekananda whose teaching instilled and made me learn to move and escalate in life in strength, struggles and morality and to make the best use of learning in spreading it.

CHAPTER 1
INTRODUCTION AND LITERATURE
REVIEW

Water is one of the nature's gift to all forms of life and substances on earth. It has played an important role in the establishment of civilisations. Our bodies cannot sustain without water. 70% of our body is composed of water (Yasui, 2014). It is used for different purposes including agricultural, industrial and municipal systems, transportation, and for various household applications.

In India, precipitation in the form of rain and snow provides ~4,000 trillion litres of fresh water (Technology Mission Plan Document, you need to give reference). Of the 1,869 trillion litres of water reserves, ~1,122 trillion litres exploited due to topographic constraints and distribution effects (Ministry of Water Resources, you need to give reference). Currently, 581 trillion litres of water (NCIWRD) is needed in the country for irrigation, industrial and domestic purposes. This water demand is going to further increase. At 5th World Water Forum, for 'Clean Water for the World' programme, emphasis was given for clean and safe water access. (M. N. Murty & S. Kumar, 2011). Development of water services with an aim to secure people's access to clean water supply, sanitation, and hygiene is the current area of development (Gimelli, Bos, & Rogers, 2018). India is endowed with water resources. It has several rivers, and glaciers. Fresh water supply in India is comprised of surface and ground waters (Rakhecha, 2018a) . Around 85% of the nation's total supply of surface water met from major river basins (Sharma, Yadav, & Gupta, 2017). Groundwater is an important source of fresh water supply in India. It contributes about 50% of urban and industrial and 80% of domestic rural needs (World Bank, 1998) (Sharma et al., 2017).

Increasing population had contributed to increase in urbanisation, industrialisation that adversely affected the quality of water (Sharma et al., 2017). Fresh water forms only 2.5 % of total water available globally. Out of which 1% is accessible for human and industrial consumption while rest is unusable and trapped in ice caps. (Harikishore Kumar Reddy, 2017). The water scarcity and safe-clean drinking water problems are going to aggravate as the global population is increasing in coming years (Harikishore Kumar Reddy, 2017). Two major challenges associated with water in the developing countries are (a) rapid decline in the per capita water availability and (b) deterioration of water quality i.e. decline to access the safe-clean drinking water (Rakhecha, 2018a). Globally, 2.5 billion people are facing the challenge from scarce water supply and 663 million people do not

have access to safe drinking water (UNICEF/WHO, 2017). Water pollution is a serious problem in India. It has affected 70% of surface water and groundwater reserves by adding toxic biological, organic, and inorganic pollutants (M. Murty & S. Kumar, 2011). Both organic and inorganic contaminants are severely affecting the water quality (Sizmur et al., 2017). Water treatment in India will cost worth 6 million Rs to make it free from water borne diseases (M. Murty & S. Kumar, 2011). According to WHO, 97 million people in India do not have access to safe drinking water. This results into 21% of communicable diseases (Sharma et al., 2017). Industrialisation, urbanisation for economic growth have caused degradation of water quality. Untreated industrial effluents and domestic sewage when discharged into river streams or percolates to groundwater, degrade the water quality and make it unfit for human consumption and for aquatic and other forms of life (Genthe et al., 2013). Such untreated water is an invitation to several diseases for human health and eventually death for human life (Rakhecha, 2018a, 2018b). Thus, water quality assessment, treatment, management, and conservation require real time monitoring to deal with water scarcity, pollution and other water related problems (Rakhecha, 2018a; Sharma et al., 2017).

Groundwater is an important and one of the potential sources for drinking water in India.. About 33% of groundwater resources are polluted or contaminated by various contaminants (Chakraborti, Das, & Murrill, 2011). About 8.56 % of the total annual rainfall of the country recharges groundwater (Gangwar, 2013). Because of it lesser vulnerability to contamination and pollution, it is readily available source of drinking water in India (Kumar and Shah, 2006). (Kumar et al., 2012).

Groundwater resources are polluted due to anthropogenic contaminants (nitrate, pesticides, industrial discharge, heavy metals like chromium, nickel cadmium and mercury, bacteria, and radionuclides) and geogenic contaminants (fluoride, arsenic, iron, salinity) (Chakraborti et al., 2011; M. Murty & S. Kumar, 2011). The inorganic contaminants are of primary concern.

1.1.Arsenic Contamination

Metals and metalloids with density greater than 4 g/cm³ are termed as ‘heavy metals’ including arsenic (As), boron (B), cadmium (Cd), copper (Cu), chromium

(Cr), cobalt (Co), iron (Fe), lead (Pb), mercury (Hg), molybdenum (Mo), nickel (Ni), strontium (Sr), tin (Sn), titanium (Ti), vanadium (V) and zinc (Zn) (Hawkes, 1997). Heavy metal contamination is a serious problem. Heavy metal pollution affects plants and human life. Plants growing in metal contaminated regions have shown reduction in growth, biomass and accumulation of metals in them (Nagajyoti, Lee, & Sreekanth, 2010). Heavy metals are detrimental to human life causing various diseases that includes, cancer, depression, renal and gastrointestinal failures, osteoporosis, hematic and glomerular dysfunction (Vogtmann et al., 2013) (WHO, 2010., European Food Safety Authority, 2012). There are broadly two sources of heavy metal contamination of water: Geogenic and Anthropogenic sources.

Arsenic contamination and its severity drew attention when large-scale deaths and health impacts were reported in 1990s in Bangladesh (WHO, 2018). About 140 million people in 50 countries have found affected with the arsenic present in drinking water above 10 µg/L (WHO, 2018). Its complex nature, occurrence and speciation makes it difficult to predict or come up with a universal solution that can define the natural arsenic contamination in groundwater (Bhowmick et al., 2018).

Arsenic poisoning results into abdominal pain, vomiting, diarrhoea, muscular cramps and death in extreme cases. Long-term exposure observes symptoms including hard patches, skin lesions, and pigmentation on palm soles. International Agency for Research on Cancer (IARC) considered arsenic in drinking water as carcinogenic agent responsible for skin, bladder and lungs cancer (WHO, 2018)(Mazumder & Dasgupta, 2011).

WHO and UNICEF have taken several preventive measures to avoid further exposure to arsenic contaminated water.

1. Replacing drinking water supplies of arsenic contaminated water by treated surface water and rainwater.
2. Tube wells and hand pumps have been marked with different colours to differentiate between arsenic contaminated water and safe water.
3. Installing arsenic removal units at domestic and centralised scales. Thus, it aimed at promoting and using techniques like oxidation, ion exchange, membranes, coagulation-precipitation and absorption.

Thus, keeping in mind the toxic effects of arsenic, we aimed to find solution using low cost, highly efficient adsorbents, which could be produced with least of expertise, is sustainable, utilises waste by products and is easy to implement and operate. This will give a helping hand to the initiatives taken by governmental and different non-governmental agencies to find the remedy for removing arsenic and provide safe drinking water.

1.2. Biochar and Biochar-nanocomposites.

Biomass conversion into chars is an ancient practice (Joseph et al., 2010; Lehmann et al., 2011). Biochar has been an important additive to improve soil fertility (Graber & Elad, 2013). Charcoal together with bones, manures, and pottery shards was added to the infertile soils in pre-Columbian era of Amazon Basin (Sombroek, 1966). These “Terra Preta” soils thus existed some 100s and 1000s of years ago (N. J. H. Smith, 1980). Similar charcoal-containing fertile soils were reported from Peru, Ecuador, Western Africa, Australia, Asia, South Africa in the soil that hastened the process of seed germination, seedling vigour (Allen, 1860).

Biochar is a carbonaceous solid mass produced by pyrolysis of any organic matter (M. Deem & Crow, 2017) or biomass in absence of oxygen (Z. Tan, Lin, Ji, & Rainey, 2017) (IBI, 2012). It is highly stable in the environment (Zimmerman & Gao, 2013). It has recently become a subject of interest for researchers and scientists. Agenda to promote the use of ‘char’ as a soil amendment has shown remarkable development since 2007 (Graber & Elad, 2013). There are four fillers (Graber & Elad, 2013). Renewable energy production: this will act as alternative for fossil fuels with biofuels produced as by-product while synthesizing char; Waste treatment: utilising agricultural wastes etc.; Soil fertility: to replace chemical additives to improve soil fertility; Carbon sequestration: below-ground sequestration of carbon as biochar has been estimated with half-life of tens of thousands of years.

Biochar properties depend on feedstock type (wood-grass, dry-wet, energy crop), types of pyrolysis (fast pyrolysis, slow pyrolysis) and pyrolysis conditions (temperature, residence time, heating rate, pressure) (J. Lee, A. K. Sarmah, & E. E. Kwon, 2019b; Masek et al., 2018; Mohan, Sharma, Singh, Steele, & Pittman, 2012; Z. Tan et al., 2017; Uchimiya, Wartelle, Klasson, Fortier, & Lima, 2011). Fast pyrolysis or flash pyrolysis aimed at producing ‘bio-oil’ as a primary product and

biochar as a secondary product (Z. Tan et al., 2017; K. Weber & Quicker, 2018). Slow pyrolysis concentrates on 'biochar' as primary product (Z. Tan et al., 2017; K. Weber & Quicker, 2018). Those with subsequently higher oxygen and poor hydrogen results in generating less porous biochar rigid versus those with lower oxygen and higher hydrogen resulting in generating more porous material (J. Lee, A. Sarmah, & E. Kwon, 2019a) (Uchimiya et al., 2011). Biomass with higher lignin content usually gives high biochar yield and lower volatile matter as compared to those characterized by higher cellulosic content (Keiluweit, Nico, Johnson, & Kleber, 2010).

During pyrolysis, biomass undergoes several chemical transformations including carbonisation, decomposition, polymerisation, graphitisation, and evaporation etc towards more stable molecular structures results in altering the chemical composition and change in physical properties of biomass (Uchimiya et al., 2011; K. Weber & Quicker, 2018; Zimmerman & Gao, 2013). Biomass is made up of carbohydrates (Cellulose, hemicellulose etc.) and lignin (Uchimiya et al., 2011). Because of different behaviour of cellulose, hemicellulose, pectin and lignin towards heat treatment, the product and yield of biochar is directly influenced (K. Weber & Quicker, 2018). At 250⁰C, dehydration predominates causing majority of biomolecules to get altered to phenols, furan and some aromatic C structures (Knicker, Hilscher, González-Vila, & Almendros, 2008; K. Weber & Quicker, 2018). At higher temperatures 400-500⁰C, sheets of fused aromatic rings are formed due to depolymerisation, loss of functional groups, aromatisation, dehydrogenation reactions and removal of substituents. While at temperatures >600⁰C more condensed structures of crystallitic graphitic forms are observed (Keiluweit et al., 2010). Residence time is another important factor affecting properties of biochar. Average pore size has been found to increase with the increase in residence time in most of the cases (Z. Tan et al., 2017).

Biochars are categorized as (a) Transition chars, with crystalline character of the minerals in chars intact; amorphous chars, with aromatic polycondensates and heat-altered molecules; composite chars, amorphous phases containing graphene stacks embedded; turbostratic chars, with graphitic crystallites (Keiluweit et al., 2010). Pyrolysis process causes the formation of unpaired electrons/radicals that induces complex reactions at the surface of the biochar (Joseph et al., 2010). Formation of defects also takes place between graphene sheets and amorphous

carbon, and between various other carbon structures and minerals formed in biochar (Bourke et al., 2007). Table 1.1. shows different types of biochars and their properties as function of temperature.

There are number of techniques to enhance the efficacy of biochars before application such as chemical activation by acid/alkaline treatment, steam activation, impregnation method, by metal salts. These modifications enhances adsorption efficiency either by providing additional functional groups on the surfaces of biochars, or by increase in hydrophilic nature, or by enhanced porosity (Joseph et al., 2010; Lee et al., 2019a).

1.3 Biochar adsorbent

High porosity, greater availability of active sites, high surface area, rigidity, stability, high cation exchange capacity, easy separation micro-mesoporous nature that offers less resistance to diffusion makes biochar a good adsorbent (Steiner, 2018). Moreover, they also act as a support by providing stable and larger surface area for the development of nanoparticles on their surfaces and act as nanoadsorbents in conjugation with metals/metal oxides (Lata & Samadder, 2016; Salem Attia, Hu, & Yin, 2014).

Several studies have been conducted to identify the mechanism by which biochar coated with iron/manganese/aluminium (hydr)oxides can sorb negatively charged oxyanions like arsenic, mercury etc. from water (Cao & Harris, 2010; Harvey, Herbert, Rhue, & Kuo, 2011; Uchimiya et al., 2011; Zimmerman & Gao, 2013). Arsenic is very toxic at lower concentration and has been reported to get bound to positively charged surfaces of Fe and Mn oxides. Mikutaa and Kretzschmar (2011) have observed formation of ternary complex formation between ferric iron complexes and arsenates (Mikutta & Kretzschmar, 2011). Thus, metallic biochar composites/nano-composites have found to be highly effective in removal of metalloids like arsenic.

1.4 Biochar Nanocomposites:

Magnetic biochars and nanocomposites can be obtained by impregnating pristine biochars with iron-(hydr)oxides. This can be done by soaking (B. Chen & Huang, 2011) or co-precipitation of biomass/biochars with ferrous/ferric salts and

then co-pyrolysing them (B. Chen & Huang, 2011; Mohan, Singh, Sarswat, Steele, & Pittman, 2015; S.-y. Wang et al., 2014). Formation of iron minerals can lead to increase in sorption efficiency that could be used for remediating metal contaminants and metalloids like As, Hg etc. (Mohan, Singh, Sarswat, Steele, & Pittman, 2015; S.-y. Wang et al., 2014). Iron oxides retain metals and metalloids by inner and outer complex formation (G. A. Waychunas, Kim, & Banfield, 2005). Biochar nanocomposites serve as potential adsorbents as they reduce the drawbacks associated with nanoparticles and provides support to iron-oxide nanoparticles on porous biochar surface (Lata & Samadder, 2016; Salem Attia et al., 2014). Nanocomposites thus provide micro-molecular size, large surface area, high catalytic property, small diffusion resistance, and greater active sites that favours arsenic removal (Gehrke, Geiser, & Somborn-Schulz, 2015; Lata & Samadder, 2016). Nanocomposites (P. Xu et al., 2012) are promising solution by taking advantages of both the hosts and the impregnated functional nanoparticles (L. Zhang, T. Zhu, X. Liu, & W. Zhang, 2016). They not only mitigated the release of nanoparticles into the environment, but also improved the compatibility in terms of stability, dispersion and reusability (L. Zhang et al., 2016).

Large scale applications of nanoparticles in water treatment have several drawbacks. It is difficult to separate the fine powder of nanoparticles. (Siddiqui & Chaudhry, 2017). When used in column method due to their less hydraulic conductivity (Siddiqui & Chaudhry, 2017) and chances of fine powder to get leaked into contact water makes it difficult to be used (Lingfan Zhang, Tianyi Zhu, Xin Liu, & Wenqing Zhang, 2016). More on nanoparticles tend to accumulate and enter into the food cycle. Secondly, nanoparticles are not cost effective. Their method of production increases overall cost of the process (Mostafa & Hoinkis, 2012). The material ensures flexibility in terms of easy treatment technique, good As(III) and As(V) adsorption from water, environmental security, sustainability and its cost effectiveness (Lingfan Zhang et al., 2016)

This study aimed at bringing the combination of nanoparticles system that are reported with high adsorption efficiency with a support on highly porous, stable, and economically viable biochars obtained from waste agricultural wastes. The developed nanocomposite is successfully utilized for the arsenic.

1.5 Literature review

Several studies have been conducted to develop metal/metal oxide based nanocomposites for the removal of arsenic from water.

Zeolites, clays, industrial by products have been used through modifications for As(III) and As(V) removal (Asere, Stevens, & Du Laing, 2019). Natural clay was modified using FeCl₃ followed by heating at 500^oC (Te et al., 2017). Resulting modified clay was utilised for As(V) removal from water. Adsorption capacity of 0.75 mg/g was reported (Te, Wichitsathian, & Yossapol, 2017). In another study, modified rice straw biochar by co-pyrollysing rice straw mixed in red mud (RM-BC) and it was used for As(V) removal (Wu et al., 2017). Adsorption capacity of 5.9 mg/g was reported (Wu et al., 2017). Oven dried iron-rich sludge was powdered, sieved and used for As(III) and As(V) adsorption from water. Adsorption capacities of 66.9 mg/g and 21.5 mg/g were reported for As(III) and As(V), respectively (J.-S. Yang, Kim, Park, & Baek, 2014). Pyrite ash and fly ash have also been utilised for As(III) and As(V) removal. Turk et al., 2017 used pyrite ash for As(V) removal of from the water. Adsorption efficiency of 90% was recorded (Turk, 2017).

Iron oxide-graphene oxide nanocomposite having ~80 % wt. of iron content was synthesized Su et al., 2017. The synthesized adsorbent was characterized by 341 m²/g surface area. Anh adsorption capacity (Q_{max}) of 147 mg/g for As(III) and 113 mg/g for As(V) removal was reported (Su, Ye, & Hmidi, 2017). A novel material was obtained by coating activated carbon with zirconium oxide and manganese dioxide (Y. Yin et al., 2019). The developed material was utilized for removing As(III). In the presence of zirconium dioxide As(III) was oxidised to less toxic As(V) and was adsorbed over manganese oxide nanoparticles through inner sphere complexation (Y. Yin et al., 2019). The synthesized material showed adsorption capacity of 132.28 mg/g and 95.6 mg/g for As(III) and As(V), respectively (Y. Yin et al., 2019). Similarly, metal oxide-biochar composites was synthesized through pre-treatment of biomass. It was then used for arsenic treatment in water. Synthesized AlCl₃-blended biochar, Cu(OH)₂-blended biochar, FeSO₄-blended biochar, KCl-blended biochar, MgCl₂-blended biochar composites were synthesized and utilised for As(III) removal reported adsorption capacities of 14.4 mg/g, 3.9 mg/g, 10.9 mg/g, 3.4 mg/g and 9.6 mg/g (Dieguez-Alonso et al., 2019). AlOOH-biochar composites were also prepared by pre-treating biomass with AlCl₃.

Synthesized composite reported adsorption capacity of 17.41 mg/g for As(V) (Zhang & Gao, 2013). The effect of pre-treatment method on biochar composite efficiency for arsenic adsorption were compared. Manganese oxide modified biochar composites were prepared using $MnCl_2$ salt by simple soaking method and co-precipitation method followed by pyrolysis. The biochar composites were denoted as MPB and BPB, respectively. The synthesized composites were applied and compared for the adsorption of As(V). Adsorption efficiency of As(V) on MPB and BPB were found to be 0.59 mg/g and 0.91 mg/g, respectively (S. Wang et al., 2015). Thus, composite synthesized by co-precipitation method were found to be more effective as compared to simple soaking pre-treatment. In another study, iron oxide permeated mesoporous rice-husk biochar (IPMN) were synthesized and utilized for the removal of As(V) from water. High adsorption capacity of 5987 mg/g was reported by IPMN (Nath, Chaliha, & Kalita, 2019). Magnetic gelatin based biochar (MG-CSB) composite was synthesized by co-pyrolysis of gelatin soaked corn stover biomass. The developed MG-CSB was utilized for As(V) removal. It reported adsorption efficiency of 45.8 mg/g for As(V) (Zhou et al., 2017). A ternary oxide loaded biochar composite (HFMB) was synthesized using humic-acid (HA), iron (Fe) and manganese (Mn) by coating them on rice husk (Guo et al., 2019). HFMB showed high adsorption capacity of 35.59 mg/g for As(V). Nath et al., 2019 synthesized iron-oxide permeated mesoporous biochar (IPMN) using rice husk and reported removal efficiency of as high as ~90% was reported for As(V) removal (Nath et al., 2019).

Along with metal oxide-carbon/inorganic frameworks, organic frameworks in conjugation with metal oxides have also been successfully utilised for arsenic removal from water. A nanocomposite was developed in conjugation with zirconium metal oxide and organic frameworks for the adsorption of arsenic. The synthesized material showed removal capacity of 205.0 mg/g and 68.21 mg/g for As(III) and As(V), respectively (X. He et al., 2019). The complex formation between As(V) and As(III) on zirconium oxide-organic frameworks was due to bidentate binuclear and bidentate mononuclear complex formations (X. He et al., 2019). In another study, synthesized starch stabilized ferromanganese binary oxide (starch-FMBO) composite was synthesized and utilized for the removed of As(III) in p range 3.0-11.0. Adsorption capacity of 161.29 mg/g was reported for As(III) on starch-FMBO composite (F. Xu, Chen, Dai, Wu, & Tang, 2019). Fe-Co based

metal organic frameworks (FeCo MOF-74) have been successfully used to remove As(III) and As(V). Synthesized material showed high surface area of 147.82 m²/g (J. Sun, Zhang, Zhang, & Liao, 2019). FeCo MOF-74 was utilized for As(III) and As(V) removal. Adsorption efficiency of 266.52 mg/g and 292.29 mg/g were reported for As(III) and As(V), respectively (J. Sun et al., 2019). In another study chitosan-magnetic-graphene oxide (CMGO) composites was synthesized and was utilized for the removal of As(III) from water (Sherlala, Raman, Bello, & Buthiyappan, 2019). The synthesized composites (CMGO) showed high surface area of 152.38 m²/g and adsorption capacity of 45.0 mg/g for As(III) adsorption (Sherlala et al., 2019). A cost effective metal-organic framework were designed using zirconium oxide and was named as MOF-808 (Z.-Q. Li, Yang, Sui, & Yin, 2015). The developed zirconium oxide-metal organic framework was utilised for removing As(V) from water. Adsorption capacity of 24.83 mg/g was reported for As(V) (Z.-Q. Li et al., 2015). Adsorbents were also synthesized by replacing less easily available metals like zirconium with more common metals like zinc. Metal organic framework was synthesized using zinc oxide and was named as Zn-MOF-74. The synthesized adsorbent was cost effective and showed adsorption capacity of 24.83 mg/g for As(V) (W. Yu et al., 2019). In another study metal organic nanocomposites were synthesized using cellulose impregnated with cerium oxide nanoparticles. The synthesized nanocomposites showed high adsorption capacity for As(V) removal (Santra & Sarkar, 2016).

In the present investigation, biochar composites were synthesized, characterized and used for As(III) and As(V) adsorption. Experiments were conducted at low arsenic concentrations range (µg/L).

1.6 Research Objectives

Present study aimed to develop biochar-nanocomposite using rice husk and wheat husk biomass. The developed material was used to study the efficiency and sustainability to remove arsenic from ground water.

- 1.To develop slow pyrolysis rice husk and wheat husk biochars.
- 2.To synthesize iron oxide-biochar nanocomposite
- 3.To characterize the developed biochars using surface area measurements, X-ray diffraction (XRD), scanning electron microscopy (SEM/EDX), transmission

electron microscopy (TEM), fourier transform infrared (FTIR), X-Ray Diffraction (XRD), EDXRF, physical property measurement system (PPMS) and Vibrating sample Magnetometer (VSM).

4. Sorption and kinetic studies to remediate arsenic from aqueous solution in batch mode. To model the sorption data using Freundlich, Langmuir, Redlich-Peterson, Sips, Koble-Corrigan, Radke and Prausnitz and Toth isotherm equations.
5. To find thermodynamic parameters for arsenic adsorption using sorption data.
6. To investigate the adsorption mechanism of As(III) and As(V) on rice husk iron-oxide (RHIOB) and wheat husk iron-oxide biochar (WHIOB) composites.
7. To carry out column studies to determine dynamic parameters, adsorption efficiency required in fixed-bed reactors to design pilot scale.
8. To study the regeneration and desorption efficiency of exhausted biochars and recovery of arsenic.
9. To study the effect on adsorption of arsenic in multicomponent system.
10. To apply synthesized RHIOB and WHIOB in the treatment of real ground water samples contaminated with arsenic.

1.7 Thesis Outline

The thesis deals with the synthesis of biochar composites, their characterized and utilization in As(III) and As(V) remediation from water. The thesis has been divided into following six chapters.

CHAPTER 1:

This chapter covers the general introduction about arsenic problem in India. The introductory chapter also covers various methods used for arsenic remediation. Brief discussion about biochar and biochar nano-composites is also included in this chapter.

CHAPTER 2: This chapter discusses about the methodology used for the synthesis of rice husks biochar (RHB), wheat husks biochar (WHB), rice husk iron-oxide biochar (RHIOB) and wheat husk iron-oxide biochar (WHIOB) composites. Various equipment, chemicals, and experimental methodologies used in the present studies are discussed.

CHAPTER 3: This chapter describes the characterization of rice husk iron-oxide biochar (RHIOB) and wheat husks iron-oxide biochar (WHIOB) composites.

CHAPTER 4: This chapter presents the optimization of As(III) adsorption on RHIOB and WHIOB composites. Batch sorption and kinetic data were fitted to different models. The chapter also covers the fitting of equilibrium and kinetic data to different models. .

CHAPTER 5: This chapter covers the optimization of As(V) adsorption on RHIOB and WHIOB composites. Batch sorption and kinetic data were fitted to different models similar to As(III) adsorption discussed in Chapter 4. CHAPTER 6: This chapter contains all the possible mechanisms for As(III) and As(V) adsorption on rice husk iron-oxide biochar (RHIOB) and wheat husks iron-oxide biochar (WHIOB) composites.

CHAPTER 7: This chapter is divided into four sections. The first section of this chapter contains discussion about the As(III) and As(V) adsorption studies carried out in column mode. The second section of this chapter incorporates all the experiments carried out for the desorption, recovery and regeneration of RHIOB and WHIOB. The third section of the chapter mainly contains discussion about the multicomponent studies. The last section of the chapter covers the application of developed RHIOB and WHIOB to the real arsenic contaminated samples collected from Ballia and Kushinagar, Uttar Pradesh.

CHAPTER 8: The final chapter consists of summary, conclusions and future recommendations.

Introduction and literature review

Table 1.1 Types of biochars and their properties with the increasing temperatures.

TRANSITION CHARS	AMORPHOUS CHARS	COMPOSITE CHARS	TURBOSTRATIC CHARS
<ul style="list-style-type: none"> Cellulose & hemicellulose tends to depolymerize 	<ul style="list-style-type: none"> Cellulose almost completely depolymerized. Cellulosic crystallinity lost. 	<ul style="list-style-type: none"> Lignin continue to depolymerize. 	<ul style="list-style-type: none"> Successive growth and increase in turbostratic crystallite.
<ul style="list-style-type: none"> H/C & O/C decreases 	<ul style="list-style-type: none"> Sharp rise in aromatic C 	<ul style="list-style-type: none"> High Surface Area 	<ul style="list-style-type: none"> Higher density and nanopores
<ul style="list-style-type: none"> Small volatile by products 	<ul style="list-style-type: none"> Small randomly arranged aromatic rings (lack of 1s-σ^* feature) 	<ul style="list-style-type: none"> Condensation of small and large aromatic C rings into sheets. 	<ul style="list-style-type: none"> Lateral growth of graphene like sheets. Poor crystallinity.
<p>REACTIONS:</p> <ol style="list-style-type: none"> TRANSFORMATION- anhydrosugars, pyrans & furans 2^o REACTION- Phenolic compound + derived intermediates e.g. levoglucosenone DISSOCIATION- <ul style="list-style-type: none"> Ketones, aldehydes 	<p>REACTIONS:</p> <ol style="list-style-type: none"> DISSOCIATION continued 2^o REACTION- Pyranones, quinones, pyrroles, furans. Enrichment of stable aromatic lignin residues due to loss of less heat-resistant material. 	<p>REACTIONS:</p> <ol style="list-style-type: none"> CONDENSATION-very high degree. Non condensed volatile component retained. Trapping of these re-condensed volatile components in pores. 	<p>REACTIONS:</p> <ol style="list-style-type: none"> CONDENSATION LATERAL GROWTH OF SHEETS REPLACEMENT: aliphatic and aromatic amorphous C by denser GRAPHITIC CRYSTALLITES.
<p>CRYSTALLINE (cellulosic crystallinity) STRUCTURE IS STILL INTACT (due to incomplete decomposition of cellulose)+ CENTERS WITH VOLATILE DISSOCIATION PRODUCTS.</p>	<p>AMORPHOUS MIXTURE containing SMALL AROMATIC RINGS+ heat resistive ALIPHATIC AND AROMATIC ELEMENTS.</p>	<p>TURBOSTRATIC CRYSTALLITES embedded in LOW DENSITY (trapping of re-condensed volatile matter) AMORPHOUS PHASE.</p>	<p>TURBOSTRATIC CRYSTALLITES with NANOPOROUS and DENSER phase .</p>

CHAPTER 2

MATERIALS AND METHODS

2.0. Reagents and equipment

All the reagents used were either AR or GR grade. $\text{FeCl}_3 \bullet 6\text{H}_2\text{O}$ (>97.0%) was obtained from CDH. An As(III) stock solution (1000 mg/L) was prepared using NaAsO_2 (>90.0 %, Sigma Aldrich) in double distilled water. An As(V) stock solution (1000 mg/L) was prepared using sodium arsenate dibasic heptahydrate ($\text{HAsNa}_2\text{O}_4 \cdot 7\text{H}_2\text{O}$; >98.0 %, Sigma Aldrich) in double distilled water. KI (>99.0 %), NaBH_4 (>95.0 %) and ascorbic acid $\text{C}_6\text{H}_8\text{O}_6$ (>99.0 %) were obtained from Merck, India. Solution pHs were maintained using HNO_3 (0.1 N) and NaOH (0.1 N) and measured on a multiparameter ion meter (model Orion 5 star, Thermo Scientific). Adsorbent-adsorbate sample agitation was conducted with water bath shakers (model MSW-275, Macro Scientific India and RC51000, Scientech India) at 10, 25 and 40°C. As(III) concentrations were analyzed using an atomic absorption spectrometer (model Analyst 400, Perkin Elmer) equipped with a mercury hydride system (MHS) and an arsenic electrodeless discharge lamp (EDL) at 193.7 nm. Iron oxide-biochar composites were formed in a controlled atmosphere muffle furnace (model Thermolyne, Thermo Scientific). All sample filtrations were performed using a Whatman No. 1 filter paper. Magnetic collection of the adsorbent was also used in adsorption studies.

2.1. Characterization of rice husk iron-oxide (RHIOB) and wheat husk iron-oxide biochar (WHIOB) composites

With the expansion of biochar research into water science, mining, environmental and agricultural practices, routine and advanced characterization of biochar has become important for researchers and industries (Singh, Camps-Arbestain, & Lehmann, 2017). Because biochar is, a pyrolysed product of organic mass, chances for the formation of crystalline compounds, and other compounds is not ruled out (Singh et al., 2017). Thus, it is important to identify these compounds and minerals formed during biochar formation.

The iron oxidation states in iron oxide-biochar composites were determined using XPS (model Versa Probe II, PSI, FEI Inc.). The mineralogy, phase analyses and crystallinity was identified on a powder X-ray diffractometer (model X'Pert PRO, PANalytical). Functional groups in the surface regions were identified using FTIR (model 7000, Varian). Surface morphology was studied by SEM (electron microscope, model EVO 40, Zeiss). XPS analyses were carried

out using a monochromatic Al-X-ray source ($h\nu = 187.85$ eV; power = 24.6 W; and beam spot size = 100 μm). Elemental distribution in the surface/near surface region in the biochar composites was determined by SEM-EDX (model Epsilon 5, PANalytical). Qualitative analysis was done using ICP-MS (ELAN-DRC-e). Crystallinity and diffraction patterns were obtained using a TEM (model JEM 2100F, JEOL) microscope. Surface areas were analyzed by the BET method using a Quantachrome Autosorb 1 Automated Gas Sorption System (outgas temperature: 150 $^{\circ}\text{C}$, outgas time: 5.0 h). CHNS combustion analysis was performed using a vario MICRO CHNS instrument. Magnetic moments were calculated using a model T-415 Cryogenic USA system at 5 and 300 K from -5 to +5T magnetic field strengths.

2.1.1. X-ray photoelectron spectroscopy (XPS):

XPS is relatively simple and yet very useful instrument as far the depth of information it provides for a sample or material is concerned. Its basis lies upon the principle of photo electronic effect where number of emitted electrons directly relates to the number of photo emitting atoms. In XPS technique, soft X-ray beam of ~1.5 keV energy irradiates the sample. When near surface atoms of the examined sample undergoes irradiation, they absorb energy $h\nu$ (h , Planck's constant, ν , frequency) from an incident X-ray beam. The excited atoms while coming to ground state releases energy in the form of photoelectrons emission, from an energy level of the binding energy E_B of an atom (G. C. Smith, 1994). The emitted photoelectrons once oncoming the work function ϕ comes out with a kinetic energy E_K and gives energy spectrum reflecting the structure of energy levels of atoms (fig. 2.1. a). Thus, it allows the identification of the atomic species near surface region (G. C. Smith, 1994) (eqn. 1).

$$E_K = h\nu - E_B - \Phi \quad [\text{eqn. 1}]$$

Once the photoelectrons are released, atom relaxes either by filling the holes from higher levels, known as auger process or by generating X-ray through fluorescence (fig. 2.1. b). Energy lines obtained from the spectrum are very informative as they also tells about the local electronic environment of the emitted

atoms of that specimen/sample. This makes XPS technique informative to element-specific chemical state for the material (G. C. Smith, 1994).

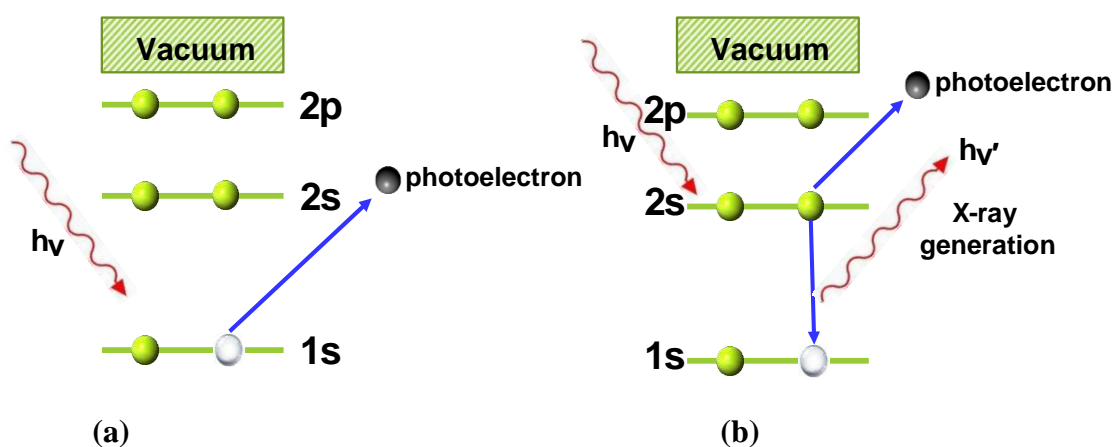


Figure 2.1: (a) Photoelectron ejection: X-ray photon of energy $h\nu$ causing excitation and release of photoelectron from core 1s level of atom. (b) Auger process and X-ray generation: relaxation of atom by filling hole in 1s level by electron from higher 2s level, with simultaneous release of photoelectrons from 2s level or energy released in form of X-ray generation of $h\nu'$ energy.

XPS operates in very high vacuum ranging from $1-5 \times 10^{-7}$ Pa, in order to avoid contamination, oxidation of X-ray anodes. Generation of X-rays occur by electrons impact on

Al or Mg coated copper anode. They result in generating strong $K\alpha$ X-ray emission lines. Generated array of photoelectrons are collected and directed to electron energy analyser (Singh et al., 2017; G. C. Smith, 1994). Biochar being porous and inhomogeneous in nature are crushed and made homogenous by quadrant mixing.

XPS patterns of RHIOB, WHIOB before and after As(III) and As(V) adsorption, and their precursor biochars RHB and WHB were obtained. Analyses was carried out using a monochromatic Al-X-ray source ($h\nu = 187.85$ eV; power = 24.6 W; and beam spot size = 100 μm). De-convolution of peaks done using Origin 2018b. Figure 2.2 shows the XPS used in analyses of the samples during studies.



Figure 2.2 X-ray photoelectron spectrometer.

2.1.2. X-ray diffraction spectroscopy (XRD):

Mineralogical identification of biochar on one hand will give an information about any crystalline compounds or amorphous compounds formed during biochar formation. On the other hand, it will also help in identification of any mineral impurity formed due to contamination from either feedstock or during process of synthesis. In addition, the mineralogical information will help in predicting availability, solubility of elements present in biochar in context to soil amendments (Fujimoto, 2003)(Singh and Raven, 2017).

X-ray diffraction (XRD) is a non-destructive technique for studying the crystalline property of materials (Singh and Raven, 2017). It is a unique identification for that particular crystal (Fujimoto, 2003). XRD patterns generates because of constructive and destructive interferences between primary and secondary waves produced when electron of an orderly/periodic crystal oscillates (Singh and Raven, 2017). Spacings between planes of atoms reflects XRD patterns, which is measured by applying Bragg's Law (eqn. 2).

$$n\lambda = 2d_{hkl} \sin \theta \quad [\text{eqn.2}]$$

Where, n is the order of diffracted beam, λ is the wavelength of the incident X-rays, d is the distance between the (hkl) diffracting planes and θ is the angle between the incident beam and diffracting planes (Singh et al., 2017) (fig. 2.3).

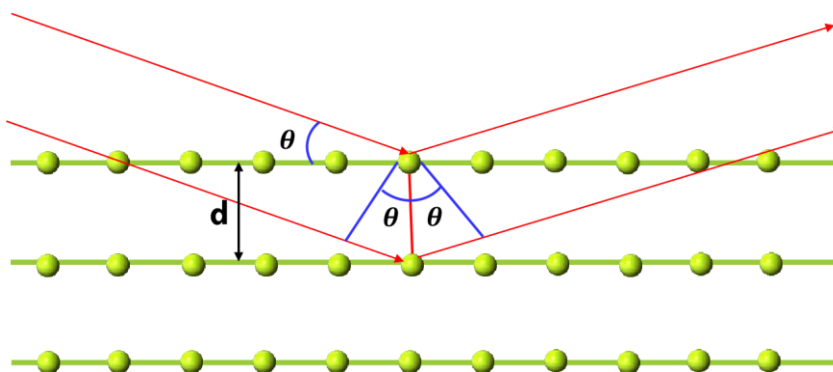


Figure 2.3: Interaction of X-ray beams from crystal planes according to Bragg's law.

Monochromatic X-ray beam is generated by bombarding anode (target metal Cu/Co) with highvelocity electrons produced from cathode (tungsten filament) by passing electric current through it. A crystalline material on being irradiated with these X-ray beams causes scattering that generates diffraction pattern. The sample rotates and is at θ degree with the incident beam.

The diffracted X-rays are collected by detector at 2θ degree (Singh et al., 2017).

XRD patterns of RHIOB, WHIOB after and before As(III) and As(V) adsorption as well their precursor biochars RHB and WHB were obtained using XRD model X'Pert PRO, PANalytical. Analyses was carried out using a monochromatic Cu-X-ray source ($\lambda = 0.15$ nm; Voltage= 45 KV; Current= 40 mA). Samples scanned in the range 5° to 90° at rate of $2^{\circ}/\text{min}$. Fig. 2.4 shows the XRD instrument used for the studies.



Figure 2.4. X-ray diffraction spectrometer

2.1.3. Fourier transform infra-red spectroscopy (FT IR):

Biochar is largely composed of pyrogenic carbon. The proportion of aliphatic to aromatic carbon decreases with the increasing pyrolysis temperature (Gaskin, Steiner, Harris, Das, & Bibens, 2008; Keiluweit et al., 2010).

Fourier transform infra-red spectroscopy (FT IR) has helped in providing lots of information about structure and reactivity of organic and inorganic components in biochar, char, graphite, ash etc. in conjugation with other spectroscopic studies (Lin, Johnston, Grant, & Heber, 2018; Nguyen, Lehmann, Hockaday, Joseph, & Masiello, 2010). All organic and inorganic components in material comprising of vibrational bands thus exhibiting vibrational spectrum forms basis for getting information from FT IR spectroscopy (Nguyen et al., 2010; Singh, Fang, & Johnston, 2016). In general, FT IR of biochar comprises of hydroxyl groups (OH) and CH groups due to sorbed water ranging from 4000-2700 cm^{-1} (K. Sharma et al., 2004; Keiluweit et al., 2010; Kloss et al., 2012). Region from 1800-1000 cm^{-1} is attributed to aliphatic and aromatic carbon constituents, carboxylate, carbonates, Si-O spectral bands of biochar. Whereas, region $< 1000 \text{ cm}^{-1}$ is due to out of plane C-H deformations (K. Sharma et al., 2004; Keiluweit et al., 2010; Kloss et al., 2012). Moreover, region $< 1000 \text{ cm}^{-1}$ is of great significance in cases where biochars are impregnated with metal-oxides (e.g. iron-oxides etc.) (Kloss et al., 2012).

FT IR spectra obtained when a sample is irradiated with IR radiation. Part of IR incident radiation is absorbed by the sample while the remaining part of radiation is re-emitted from the sample and passed on to the detector (Singh et al., 2016). In order to reduce specular reflectance KBr is used to prepare pellets with the samples (Singh et al., 2016).

FT IR patterns of RHIOB, WHIOB after and before As(III) and As(V) adsorption, and their precursor biochars RHB and WHB were obtained using FT IR model 7000, Varian. Spectrum obtained in wavelength range 4000-500 cm^{-1} ; samples prepared by DR-FT IR method where they were mixed and grounded with KBr, and pellets were made by using hydraulic press (model CAP15T,

Spectrachron instruments, India) of 10 tons for 25 s. Fig. 2.5 shows the FT IR instrument used for the studies.



Figure 2.5. Fourier transform infra-red spectrometer.

2.1.4. Scanning electron microscope (SEM) and Scanning electron microscope-Energy dispersive X-ray spectroscopy (SEM-EDX):

Scanning electron microscopy (SEM) is a surface analysis technique that provides details of surface morphology of samples (Ratner, 2013). SEM is based on irradiating samples in vacuum with primary electron beam of relatively higher energy (5-100 keV). This causes emission of backscattered low energy secondary electron beam (1-20 eV) from sample surface (Amidon, Meyer, & Mudie, 2017; de Ven, Mack, Dunner, Ferrari, & Serda, 2012; Ratner, 2013). Intensity of the secondary electrons is function of atomic composition of the sample (Amidon et al., 2017; Ratner, 2013). This results in generating images with higher resolution and magnification (Amidon et al., 2017; de Ven et al., 2012). These images thus have high depth of field that gives information about surface morphology and topography of samples (de Ven et al., 2012). Moreover, high resolution makes it easier to understand about the shape, size, and structure of any material.

For rapid and stable analysis of composition of biochar, SEM-EDX is one of the simple method (Xing-zhu et al., 2016). In SEM-EDX primary electron beam stimulates the emission of X-rays, that penetrates deep inside the bulk of sample. This helps in identification of elements in the specimen (Ratner, 2013). Moreover, on scanning the results one can also analyse the structural properties of

biochar prepared at different temperatures (Xing-zhu et al., 2016). Figure 2.6 shows the schematic principle of SEM/SEM-EDX working.

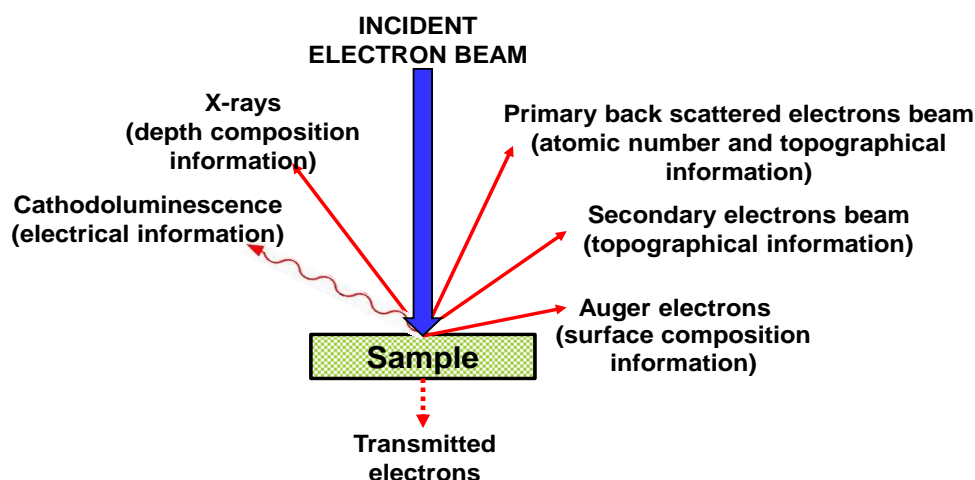


Figure 2.6. Scheme of SEM and SEM-EDX showing different signals on being irradiated by high-energy electron beam.

Surface morphology and topography of RHIOB and WHIOB obtained using SEM technique model EVO 40, Zeiss (accelerating voltage, 10,000 V; working distance, 8500-1100 μm ; emission current, 13,300 nA). Elemental composition obtained for RHIOB and WHIOB using SEM-EDX (model Bruker EDX system). Sample powder is sprinkled on to the surface of two-sided carbon tape fixed to sample stub. 20-50 nm coating of gold applied to the sample surface to make them conductive. Prepared sample is analysed inside highly vacuum generated SEM chamber for SEM imaging and SEM-EDX. Fig. 2.7 shows the SEM instrument used for the studies.



Figure 2.7. Scanning electron microscope.

2.1.5. Transmission electron microscopy (TEM):

Transmission electron microscopy is a powerful tool in analysing some of the very fine structures of dimensions less than 100 nm (Tang & Yang, 2017). Because of its excellent resolution, it can measure the lattice thickness and interplanar spacings of crystals; thus making it a unique technique for finding out the electronic and chemical structures, dislocations and grain boundaries of material/nanocrystals (Bhattacharya, 2016; Tang & Yang, 2017). TEM imaging and electron diffraction techniques have played significant role in defining the crystallographic properties of carbon (Bonnamy & Oberlin, 2016). This has led to precise description of graphitised, amorphous, turbostratic, partially graphitised and disordered forms of carbon (Bonnamy & Oberlin, 2016). Moreover, TEM has been utilised in finding out the morphology, crystalline structures of nanoparticles incorporated with membrane/carbons (Bonnamy & Oberlin, 2016; Ebnesajjad, 2014).

TEM is similar in principle to SEM except beam passes through deeper layers of specimen/sample/material. Solid sample of thickness ranging from 100-200 nm is irradiated with a very high voltage (80-200 keV) of electron beam (Ebnesajjad, 2014). On encountering, the crystalline phase of material, electrons causes scattering or diffraction from lattice planes that results in producing diffraction images (Ebnesajjad, 2014). Irradiating samples with such high voltage electron beam V , produces high-resolution images for even shorter wavelengths, λ (Tang & Yang, 2017) (eqn 3). Fig 2.8 shows the schematic principle of TEM working.

$$\lambda \sim \frac{1.23}{\sqrt{V}} \text{ (nm)} \quad \text{[eqn 3.]}$$

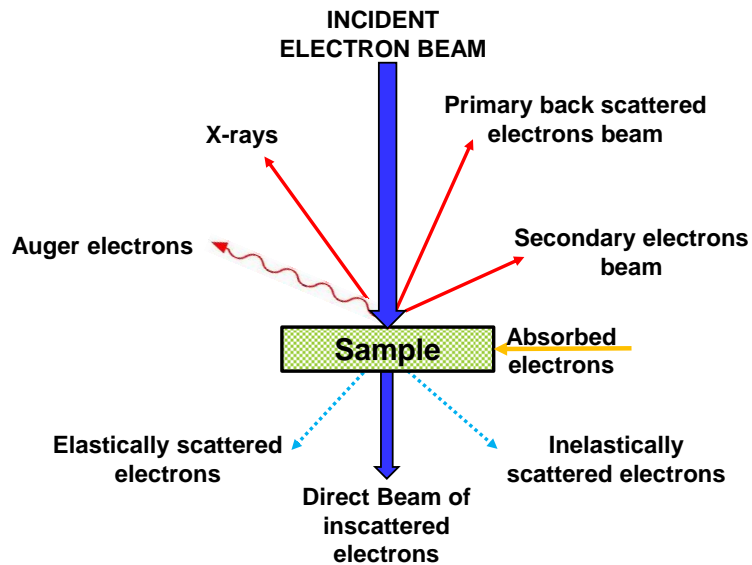


Figure 2.8. Scheme of TEM showing different signals on being irradiated by high-energy electron beam.

Keeping in view the importance of information that it provides, RHIOB and WHIOB were characterised for their structural morphology; in finding out the formation/impregnation, lattice thickness, interplanar spacing of crystals of iron-oxide nanoparticles using TEM, JEOL, JEM 2100F; voltage, 200 keV. Diffraction graphs obtained for RHIOB and WHIOB using selected area (electron) diffraction (SAED) technique (JEOL, JEM 2100F). Powdered samples were dispersed in ethanol, ultrasonicated and placed on copper grids. Samples were analysed by placing them in sample compartment. Fig 2.9 shows the TEM instrument used for the studies.



Figure 2.9. Transmission electron microscope.

2.1.6. Surface area and porosity analysis:

Surface area and pore structure of any solid sample are important parameters as they provide information about mass exchange of that sample molecules between the mobile and stationary phase by forming thin film of liquid (Rotzsche, 1991). Similarly, adsorption/desorption phenomenon and efficiency of sample is defined by pore size and its distribution (Rotzsche, 1991). There is no one specific method to find surface area of sample because of the complexities of micro/meso porous (Thommes, Cychoz, & Neimark, 2012). Still Brunauer-Emmett-Teller (BET) is most widely and accepted methods to estimate surface area of pores (Thommes et al., 2012). BET theory is based on an assumption considering monolayer adsorption on uniform surface (Brunauer, Macko, H. E. Emmett, Teller, & Edward, 1938; Rouquerol, Llewellyn, & Rouquerol, 2007; Thommes et al., 2012). From the adsorption isotherm monolayer, capacity and surface area is calculated (Brunauer et al., 1938; Rouquerol et al., 2007; Thommes et al., 2012).

RHIOB, WHIOB and their respective precursor biochars RHB, WHB were characterized using Quantachrome surface area analyser (model Autosorb-I). Samples outgassed at 150^o for 5h at <10⁻³ torr pressure. Specific surface area (S_{BET}), micropore volume (V_{mi}) and mesopore volume (V_{me}) for materials obtained by applying BET adsorption isotherm. Average area occupied by N₂ molecule taken as 16.2 Å² in relative pressure (p/p^o) ranging from 0.05-0.35 (Brunauer et al., 1938).

2.1.7. Magnetic moment measurements:

Magnetic properties and hysteresis measurements of RHIOB, WHIOB and their respective precursor biochars RHB and WHB were done to study the magnetic property. Because rice husk and wheat husk biochars impregnated with iron-oxide particles it was necessary to study and analyse magnetisation, the type of magnetism if any occurred in RHIOB and WHIOB. Magnetic strength, coercivity and remanence were determined from the hysteresis graphs. Magnetic moment measurements done using PPMS system, model T-415, Cryogenic, at 10 K and 300 K from -10 to +10T. ~0.025g of samples taken in capsules sealed with

Teflon and Kabton tape for measurements. Fig 2.10 shows the PPMS instrument used for the studies.



Figure 2.10. Physical properties measurement system.

2.1.8. Zero point charge (pHzpc) measurements:

pHzpc is an important parameter that interprets adsorption process and dissolution rate for any solid in solution (Lindblad & Duroux, 2017; Sverjensky, 1994). It is a pH at which positive and negative charge on the surface are equal, i.e. net charge is zero (Fiol & Villaescusa, 2009). Thus, it demonstrates the charge distribution on the surface of material/specimen, which helps in explaining electrostatic attraction and the pH resulting in adsorption between adsorbent-adsorbate system (Lindblad & Duroux, 2017; Shen, 2016). Thus, pHzpc for synthesised biochars/materials were done in order to explain the mechanism of adsorption. Adsorption by electrostatic attraction takes place in the pH interval between pHzpc of material/specimen and the opposite electric charges exhibited by the ions in the solution (Lindblad & Duroux, 2017; Shen, 2016).

The point of zero charge (pHzpc) were calculated for RHIOB and WHIOB. 0.025g of RHIOB and WHIOB were added in 0.01 M of NaCl solution prepared at pH 2.0, 4.0, 6.0, 8.0, and 10.0 for 24h, 25° C. pH was adjusted using 0.1 N NaOH and 0.1 N HCl solutions. An XY plot of initial pH versus change in pH of solution was plotted. Point of zero intersection were reported as pHzpc for RHIOB and WHIOB.

2.1.9. Ultimate and Quantitative analysis:

Biochars have high carbon contents that determine the property of that biochar. Moreover, it contains several major and trace elements that get modified, released during pyrolysis. Thus, it becomes important to have an accurate measurement of different elemental compositions. This defines biochar properties and changes taking place during pyrolysis. Accurately weighed amount of samples are combusted and quantified by comparing it with standards of known composition. The results are presented as mass percent of the original mass of sample (Singh et al., 2017). Ultimate analysis thus determines the composition of biomass/biochars in terms of wt% carbon, hydrogen, nitrogen, and oxygen is calculated by difference (Mohan & Pittman, 2007b).

Elemental analysis of RHIOB, WHIOB and their respective precursor biochars RHB, WHB was done by dry combustion and ashing (750°C; 6 h) of 1g samples in muffle furnace. It was followed by acid digestion (3:1 v/v % HNO₃: HF). Atomic absorption spectrometer, AAS (Perkin Elmer 400 AAnalyst) and Inductively coupled plasma-atomic emission spectrometer, ICP-AES (Agilent ICP-AES 5100) were used for analysis. Both AAS and ICP-AES work upon the principle of Beer Lambert's law, where absorbance is related to the measurement of concentration of elements in solution.

For CHNS elemental analysis, sample of known amount is combusted (~1000°C temperature) in furnace under inert gas atmosphere maintained by introducing helium. This is followed by flash combustion (~1800°C temperature) of samples in tin capsule by introducing pulse of oxygen with stream of inert gas (Bird, Keitel, & Meredith, 2017; Singh et al., 2017). This ensures complete oxidation of samples to CO₂, SO₂, and H₂O. Nitrogen obtained as N₂ as the gas is reduced in presence of copper (Bird et al., 2017; Singh et al., 2017). CHNS analysis of RHIOB, WHIOB and their respective precursor biochars RHB and WHB was done using CHNS analyser with helium as carrier gas (flow rate= 80mL/min) and oxygen as fuel gas (flow rate= 20mL/min) operated at ~1000°C.

Acetanilide standards were used for calibrating the instrument.

2.2 Equilibrium and Kinetic experiments

All sorption experiments were conducted in the batch mode. Adsorption experiments at pH values from 2.0 to 10.0 were performed with an initial As(III) solution at 25 °C for 24 h (adsorbent dose = 2.0 g/L; RHIOB and 1.0 g/L, WHIOB; initial As(III) concentration = 100 µg/L; agitation speed 100 rpm). Similarly, adsorption experiments were conducted for As(V) solution at 25 °C for 24 h at pH values from 2.0 to 10.0 (adsorbent dose = 2.0 g/L, RHIOB and 1.0 g/L, WHIOB; initial As(V) concentration = 100 µg/L; agitation speed 100 rpm). Kinetic experiments were conducted at various iron oxide-biochar hybrid composite dosages (0.5, 1.0, and 2.0 g/L) and contact times (0.5, 1.0, 2.0, 4.0, 6.0, 8.0, 10.0, 24.0, and 48.0 h) at 25 °C. Sorption equilibrium studies were conducted at 10, 25 and 40 °C for 24 h. As(III) and As(V) concentrations ranged from 50 to 1000 µg/L, and adsorbent dosages were 2.0 and 1.0 g/L for RHIOB and WHIOB, respectively. All the As(III) equilibrium and kinetic studies were carried out in the optimum pH range of 7.0-7.5 for RHIOB and 6-6.5 for WHIOB. For As(V) equilibrium and kinetic studies were carried out in the optimum pH range of 5.0-5.5 for RHIOB and for WHIOB.

The percent As(III) and As(V) removal for a particular adsorbent-adsorbate suspension was calculated using equation 4 and 5,

$$\text{Removal Efficiency, \%} = [(C_0 - C_e)/C_0]100 \quad [\text{eqn. 4}]$$

Here, C_0 and C_e are initial and equilibrium arsenic concentrations in µg/L.

The adsorption capacities, (q_e) of RHIOB and WHIOB were calculated using eqn. 5.

$$q_e = [(C_0 - C_e)/M] * V \quad [\text{eqn. 5}]$$

Here, V is the adsorbate volume in litres, M is the adsorbent amount in grams, C_0 and C_e are initial and equilibrium adsorbate concentrations (µg/L).

2.2.1 Sorption kinetic models

High adsorption capacities and quick adsorption kinetics are important factors for excellent adsorbents. Former is determined using pseudo first order and pseudo second order kinetic models (R. Viegas, M. Campinas, H. Costa, & M. Rosa, 2014). The latter is determined using mass transfer modelling that tells about how fast the adsorption is taking place (R. Viegas et al., 2014). To interpret

material design and system selection it is important to study the rate determination step during adsorption by fitting data obtained from kinetic experiments into various kinetic models. These parameters help in providing information to design fixed-bed reactor.

(a) Pseudo-first order

In 1898, Lagergren (Lagergren, 1898) devised a model for systems with nearing equilibrium with long adsorption times. Hence, the rate mechanism is controlled by adsorption time and experimental conditions like concentrations and dosages (Mussa et al., 2017; K. L. Tan & Hameed, 2017). It thus assumes physisorption adsorption where adsorbate is attached to the adsorbent surface by weak van der waal's forces of attraction and is favoured by multi-layer adsorption (K. L. Tan & Hameed, 2017). The linear and non-linear forms of equations are given in table 2.1(a).

(b) Pseudo-second-order

In pseudo-second-order process the rate mechanism is controlled by both the concentrations of adsorbate and the concentration of adsorbent as well (Ho & McKay, 1999b). Thus, number of active sites present on adsorbent surface greatly influence the rate of reaction. The rate-limiting step is chemisorption (Ho & McKay, 1999b). It defines adsorption taking place between adsorbate and adsorbent by strong chemical bond formation, favoured by monolayer adsorption at higher temperatures. The linear and non-linear forms of equations are given in table 2.1(b).

(c) Boyd's model/Diffusion model

Rate of adsorption depends on external or internal or both types of diffusion. Adsorption generally occurs by three processes namely film diffusion, particle diffusion and exterior surface diffusion (Boyd, Adamson, & Myers, 1947; Nethaji, Sivasamy, & Mandal, 2013; R. Viegas et al., 2014). The diffusion occurs in three steps (figure 2.11 (1-4)):

1. Transfer of solute from bulk solution (bulk diffusion) (figure 2.11.(1)) to the external surface of the particle (film surrounding particle) (figure 2.11.(2))

2. Transfer of solute within particle i.e. intraparticle diffusion. This can be surface diffusion, where particle hops from one pore site to another pore site (figure 2.11.3(a)), or pore diffusion due to fluid filled pores (figure 2.11. 3(b)), or combination of both.
3. Adsorption of solute particle on pore surface site (figure 2.11.(4)).

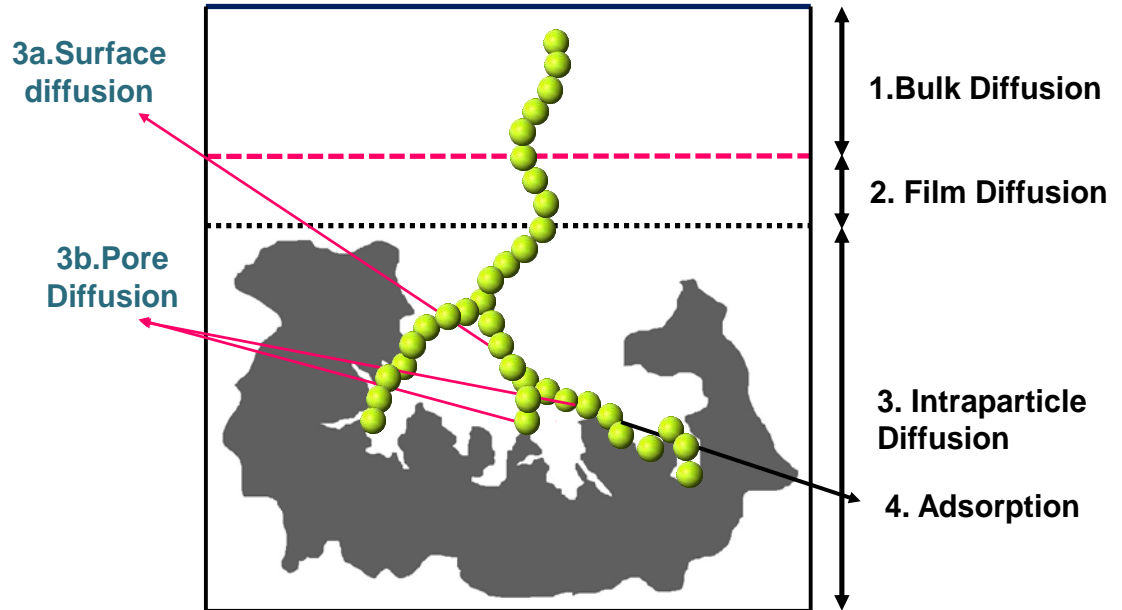


Figure 2.11. Diffusion mechanisms involved in the adsorption process.

Step 1 and step 2 are the rate limiting steps, as step 3 is very rapid. Pseudo-first order and pseudo-second-order kinetic models takes only step 3 into consideration. Hence, it is necessary to fit kinetic data using diffusion model. This helps in completely explaining the mechanism of adsorbate-adsorbent system.

Boyd’s model is the most accepted model to explain diffusion kinetics of adsorbate-adsorbent system as it not only determines the rate of diffusion, rate-limiting steps but also establishes coefficient of intraparticle diffusion (D_i) (R. Viegas et al., 2014). Equations 5, 6, 7 and table 2.2.(c) used to identify different parameters explaining diffusion mechanism.

$$F = 1 - \frac{6}{\pi^2} \sum_{n=1}^{\infty} \frac{1}{n^2} \exp \left[\frac{-D_i t \pi^2 n^2}{r_0^2} \right] \quad [\text{eqn 5}]$$

$$F = \frac{Q_t}{Q_0} = \frac{\text{adsorbate uptake time } t}{\text{adsorbate uptake at equilibrium}} \quad [\text{eqn 6}]$$

$$B = \frac{\pi^2 D_i}{r_0^2} \quad [\text{eqn 7}]$$

F is fractional attainment of equilibrium time 't', B, is the Boyd number, D_i is the effective coefficient within the adsorbent phase, r_0 radius of the adsorbent particle, n integer of infinite series.

Boyd's diffusion model was applied on the kinetic data of RHIOB and WHIOB on As(III) and As(V) adsorption to identify different parameters to determine that rate and mechanism of diffusion. Boyd's effective intraparticle diffusion coefficients (D_i), Boyd's criteria to establish the controlling adsorption steps were identified for RHIOB and WHIOB by applying Boyd and Reichenberg equations (Table 2.1.). Linear graph plots passing through origin implies film diffusion as the rate limiting step, whereas linear plots not passing through origin implies particle diffusion as the rate limiting step. However, if the plots are non-linear it signifies step 3 i.e. adsorption of solute particle at pore surface site, as the rate limiting step.

(d) Adsorption thermodynamic studies

Thermodynamic parameters were obtained at three different temperature (10°C, 25°C and 45°C) on RHIOB and WHIOB from isotherm experiments. Different parameters such as equilibrium constant (K_0), standard free energy changes (ΔG^0), standard enthalpy change (ΔH^0) and standard entropy change (ΔS^0), were obtained that defines the rate of reaction to be exothermic or endothermic were calculated using equations shown in table 2.1. (d).

Table 2.1. List of kinetic models applied for studies:

S. No	Equilibrium models	Nonlinear form	Linear form	Plot	Parameters	References
1.	Pseudo first order	$q_t = q_e(1 - e^{-k_1 t})$	$\log(q_e - q_t) = \log(q_e) - \frac{k_1}{2.303}t$	$\ln(q_e - q_t) vs t$	k_1 -first order rate constant (min^{-1}), q_e -adsorbate adsorbed per gram of adsorbent, q_t -adsorbate adsorbed at time 't'	(Lagergren, 1898)
2.	Pseudo second order	$\frac{dq_t}{dt} = k_2(q_e - q_t)^2$	$\frac{t}{q_t} = \frac{1}{k_2 q_e^2} + \frac{t}{q_e}$	$\frac{t}{q_t} vs t$	k_2 -second order rate constant (g/mg/min), q_e -adsorbate adsorbed per gram of adsorbent, q_t -adsorbate adsorbed at time 't'	(Ho & McKay, 1999b)
3.	Boyd's Diffusion model	-	$B_t = -\ln \frac{\pi^2}{6} - \ln(1 - F(t))$ for $F(t) > 0.85$ $B_t = \left(\sqrt{\pi} - \sqrt{\pi - \frac{\pi^2 F(t)}{a}} \right)^2$ for $F(t) < 0.85$	$B_t vs t$	F is mathematical function of B_t . F(t) is fourier transform, given by Reichenberg, 1953. For given value of F, dF/dt and dq/dt are proportional to B, Boyd's constant.	(Boyd, Adamson, & Myers, 1947; Reichenberg, 1953a)
4.	Thermodynamic Equilibrium	-	$\ln K_c = \frac{\Delta S}{2.303 R} - \frac{\Delta H}{2.303 RT}$	$\ln K_c vs 1/T$	K_c is equilibrium constant, R is the gas constant (J/mole), T is temperature in Kelvin, ΔH is enthalpy change, ΔS entropy change	(Von Helmholtz, 1882 and Gibbs, 1888)

2.2.3 Sorption isotherm experiments:

Adsorption is physico-chemical process that occurs when adsorbate is transported from bulk solution to the interior surfaces of adsorbent where they are adsorbed (Proctor & Toro-Vazquez, 2009). However, at thermodynamic equilibrium no further adsorption occurs. This equilibrium can be optimised for different pH, temperature conditions that defines adsorbate-adsorbent interactions (Proctor & Toro-Vazquez, 2009). It is important to find and predict how much solute an adsorbent can adsorb. This is done by performing adsorption isotherm experiments at different temperatures, which gives an information about the maximum adsorption capacity of an adsorbent. Thus, how the solutes are distributed between the solid and liquid phase can be predicted at different equilibrium concentrations through isotherm experiments (Proctor & Toro-Vazquez, 2009; Shaarani & Hameed, 2010). The parameters derived from isotherm studies gives quantitative information about the adsorbents. Adsorption isotherm is thus a graphical representation of per unit weight of adsorbent with respect to the remaining amount of adsorbate in solution at equilibrium (Desta, 2013). Data of isotherm adsorption can be analysed using different models. This helps in providing information for designing purpose (Desta, 2013; Shaarani & Hameed, 2010). There are four types of isotherm curves namely S, L, H and C type curves, which describes the adsorptive mechanisms (Sparks, 2003). In S-shaped isotherm curves slope first increases and then gradually decreases with the rising adsorbate concentration in solution. This concludes that with increasing concentration affinity of adsorbate molecules tends to increase towards adsorbent surface. L-shaped (Langmuir) isotherm curves where slope gradually decreases with the rising adsorbate concentration in solution. It concludes towards greater/higher affinity of adsorbate molecules towards adsorbent surface at lower concentrations. H-shaped (high-affinity) curves concludes inner-sphere complex formation resulting in strong adsorbate-adsorbent interactions. C-shaped indicates partitioned distribution of adsorbate molecules that are distributed in bulk and interfacial phase without any specific bond formation between adsorbent-adsorbate system (Sparks, 2003).

Adsorption isotherm experiments were carried out by equilibrating As(III) and As(V) solutions ranging from 50 µg/L-1000 µg/L (50, 100, 200, 400, 600, 700, 800, 1000 µg/L) concentrations at 10 °C, 25 °C, 45°C temperatures for 48 h. Adsorbent amount of 2.0 g/L and 1.0 g/L dosage of RHIOB and WHIOB respectively were added to 50 mL of arsenic solutions.

2.2.3.1. Sorption equilibrium models:

(a) Freundlich isotherm model:

Freundlich (1906) described adsorption of single adsorbate as reversible equilibrium, where equilibrium was attained in short time at fixed temperature. Thus, at low-solute concentrations as the concentration increases adsorption of adsorbate increases. However, at high-solute concentrations the amount of adsorbate approached a constant value (Freundlich, 1906). Freundlich found that at constant temperature amount of adsorbate adsorbed per unit weight of adsorbent is function of amount of residual concentration of solute in solution at equilibrium. Thus, it describes adsorption of solute occurring heterogeneously, in multilayers. Because there is no finite limit to describe the adsorption capacity, Freundlich isotherm model is limited.

The non-linear and linear form of equations are given in table 2.2. (a).

(b) Langmuir isotherm model

Irving Langmuir developed an isotherm model to describe gas-solid-phase adsorption on porous carbon materials (Langmuir, 1918). Since then the model is modified and has successfully used to find adsorption capacity of liquid-solid-phase systems on various bio sorbents. It is based on an assumption that adsorption is taking place on adsorbent surface homogeneously. Moreover, monolayer adsorption of adsorbate occurring on the sites of the adsorbents are finite, identical, equivalent and localized. In addition it assumes, there will be no lateral exchange or steric hindrance between adsorbed molecules on the adjacent sites of adsorbent, and that each site will occupy one adsorbate molecule at a time. At lower temperatures, this isotherm model is consistent as it changes to Henry's law.

The non-linear and linear form of equations are given in table 2.2. (b).

(c) Sips or Langmuir-Freundlich model

Sips isotherm is derived by combining both Langmuir and Freundlich isotherm (Sips, 1948). It overcomes the limitation associated with Freundlich isotherm model as the adsorbate concentration rises. This model like Freundlich isotherm model predicts adsorption on heterogeneous systems. At higher adsorbate concentrations, it predicts monolayer adsorption capacity, the characteristic of Langmuir isotherm model. While at lower adsorbate concentrations, it gets reduced to Freundlich isotherm.

The non-linear and linear form of equations are given in table 2.2. (c).

(d) Temkin isotherm model

Temkin and Pyzhev developed an isotherm model to describe the adsorption of hydrogen on platinum electrodes in acidic solutions. Its derivation is based on the assumption that during adsorption uniform distribution of the bonding energies takes place (Temkin and

Pyzhev, 1940). Model ignores adsorption occurring at very high and very low concentrations of solutions, where heat of adsorption decreases linearly rather logarithmic as function of temperature. Temkin isotherm model works best for gas-solid-phase systems.

The non-linear and linear form of equations are given in table 2.2. (d).

(e) Redlich-Peterson isotherm model

Redlich-Peterson isotherm model is a versatile model operating for both heterogeneous and homogeneous systems (O. Redlich & D. L. Peterson, 1959). This is done by introducing three parameters in equation that includes both Langmuir and Freundlich isotherms. Where in numerator model shows linear dependency on concentrations, in denominator adsorption varies with concentrations as exponential function. The third parameter β , is an exponent that varies between 0 and 1. For β

$\beta=0$, it gets reduced to Henry's law, while $\beta=1$, it assumes Langmuir isotherm model. The non-linear and linear form of equations are given in table 2.2. (e).

(f) Radke-Prausnitz isotherm model

The Radke and Prausnitz isotherm usually works well with high chi-square values.

Hence, it is applicable for wide range of concentrations (Radke & Prausnitz, 1972a).

The non-linear form of equation is given in table 2.2. (f).

(g) Toth isotherm model

Toth developed an isotherm model to improve the fittings from Langmuir isotherm. Thus, it satisfies both high and low-end boundaries of the concentrations, and applies to heterogeneous adsorptions (Toth, 1962). Toth isotherm model explains adsorption by asymmetrical quasi-gaussian energy distribution (Toth, 1962). It assumes most of the adsorption sites have energy lower than the mean value, which is the maximum adsorption energy.

The non-linear and linear form of equations are given in table 2.2. (g).

Table 2.2. List of isotherm models applied for studies.

S.No	Equilibrium models	Nonlinear form	Linear form	Plot	Parameters	References
1.	Freundlich	$q_e = K_F C_e^{1/n}$	$\log q_e = \log K_f + \frac{1}{n} \log C_e$	$\log q_e$ vs $\log C_e$	q_e , adsorption capacity defined as solute adsorbed per unit weight (mg/g); K_f , adsorption capacity constant of adsorbent (mg/g); C_e , equilibrium constant of solute concentration (mg/L); $1/n$, constant of the intensity of adsorption.	(HMFZ Freundlich, 1906)
2.	Langmuir	$q_e = \frac{Q^{\circ} b C_e}{1 + b C_e}$	$\frac{1}{q_e} = \frac{1}{b C_e} + \frac{1}{Q^{\circ} b}$	$\frac{1}{q_e}$ vs $\frac{1}{C_e}$	q_e , adsorption capacity defined as solute adsorbed per unit weight (mg/g); b net enthalpy constant of adsorption ($b \propto e^{-\Delta H/RT}$); C_e , equilibrium constant of solute concentration (mg/L)	(Langmuir, 1918)
3.	Sips or Langmuir-Freundlich	$q_e = \frac{K_{LF} C_e^{n_{LF}}}{1 + (a_{LF} C_e)^{n_{LF}}}$	$n_{LF} \ln C_e = -\ln\left(\frac{K_{LF}}{q_e}\right) + \ln(a_{LF})$	$\ln\left(\frac{K_{LF}}{q_e}\right)$ vs $\ln(C_e)$	q_e , adsorption capacity defined as solute adsorbed per unit weight (mg/g), C_e , equilibrium constant of solute concentration (mg/L), K_{LF} , a_{LF} and n_{LF} are the Sips constant.	(Sips, 1948)
4.	Temkin	$q_e = \frac{RT}{b_{T_e}} \ln(A_{T_e} C_e)$	$q_e = \frac{RT}{b_{T_e}} \ln A_{T_e} + \left(\frac{RT}{b_{T_e}}\right) \ln C_e$	q_e vs $\ln C_e$	b_{T_e} , is heat of sorption constant; a_{T_e} , Temkin isotherm constant; C_e , equilibrium constant of solute concentration (mg/L); R is gas constant; T ,	(M. Temkin & V. Pyzhev, 1940)

Development and characterization of rice husk and wheat husk iron-oxide biochar

					absolute temperature; A_{T_e} is Temkin constant.	
5.	Redlich Peterson	$q_e = \frac{K_{RP} C_e}{(1 + a_{RP} C_e^{\beta_{RP}})}$	$\ln\left(K_{RP} \frac{C_e}{q_e} - 1\right) = \beta_{RP} \ln C_e + \ln(a_{RP})$	$\ln\left(K_{RP} \frac{C_e}{q_e} - 1\right) \text{ vs } \ln C_e$	q_e , adsorption capacity defined as solute adsorbed per unit weight (mg/g), C_e , equilibrium constant of solute concentration (mg/L); K_{RP} , is Redlich Peterson constant (L/g); a_{RP} , is constant (L/mg) $^\beta$; β , exponent 0 and 1.	(O. Redlich & D. L. Peterson, 1959)
6.	Radke and Prausnitz	$q_e = \frac{abC_e^\beta}{a + bC_e^\beta - 1}$	-	-	q_e , adsorption capacity defined as solute adsorbed per unit weight (mg/g); C_e , equilibrium constant of solute concentration (mg/L); a, b, and β are constants.	(Radke & Prausnitz, 1972a)
7.	Toth	$q_e = \frac{K_T C_e}{(1 + \beta_T C_e^{\beta_T})^{\frac{1}{\beta_T}}}$	$\ln\left(\frac{q_e}{K_T}\right) = \ln(C_e) - \frac{1}{\beta_T} \ln\left(1 + \beta_T C_e^{\beta_T}\right)$	$\ln\left(\frac{q_e}{K_T}\right) \text{ vs } \ln(C_e)$	q_e , adsorption capacity defined as solute adsorbed per unit weight (mg/g); C_e , equilibrium constant of solute concentration (mg/L); a, b, and β_T , K_T are Toth constants.	(Toth, 1971)
8.	Koble-Corrigan	$q_e = \frac{aC_e^\beta}{1 + bC_e^\beta}$	-	-	When $\beta = 1$, Koble Corrigan reduces to Langmuir. If bC_e^β is less than 1, equation reduces to Freundlich model.	(Robert A Koble & Thomas E Corrigan, 1952)

2.3 Effect of co-existing ions on the adsorption of arsenic on RHIOB and WHIOB:

In order to study the effect of other multiple/co-existing ions and their competitiveness with arsenic oxyanions (arsenites and arsenates) on adsorptive sites (T. Sun et al., 2017a), studies conducted on RHIOB and WHIOB. Separate solutions of As(III) and As(V) were prepared. 100 mg/L and 200 mg/L solutions were prepared using five anions chloride, nitrate, sulphate, bicarbonate, phosphate, and their corresponding salts of sodium, potassium and calcium. Concentration of 100 µg/L of arsenic solution prepared. Test solutions prepared at pH 7.5. Adsorption studies conducted at 25° C by adding 1.0 g/L of adsorbent to 50 mL of 100 mg/L and 200mg/L test solutions. Studies were conducted for 24 h, followed by filtration, washing and measurements on atomic adsorption spectrometer.

2.4 Fixed-bed column studies for As(III) and As(V) removal on RHIOB and WHIOB: To check the practical applicability and the performance of adsorption on synthesised material in continuous operation, column studies were conducted. This will help in providing the information for column operation applicable for large-scale water volumes (Westerhoff, De Haan, Martindale, & Badruzzaman, 2006). Column studies were conducted on RHIOB and WHIOB. Information about various parameters including flow rate, bed-height, column width, breakthrough time were evaluated. Arsenic solutions of 100 µg/L was constantly added through columns containing RHIOB and WHIOB for two bed heights 5cm and 10cm.

2.5 Reusability of RHIOB, WHIOB and recovery of As(III) and As(V) through adsorption/regeneration studies:

For the practical applicability of the synthesised material, it is important that material can reused repeatedly for the removal (T. Sun et al., 2017a; J. Zhu et al., 2015). Thus, adsorbent regeneration studies performed to identify the sustainability of the synthesised material. This is significant in further improvement in the sustainability and onall cost treatment (J. Zhu et al., 2015). Three consecutive adsorption cycles were performed with 50 mL of 100 µg/L of As(III) and As(V) solutions. Whereas, regeneration cycles were performed in aliquots of 10 mL of

regenerant solution, for 24 h. Alkaline solution was preferred for removal keeping in mind the participation of hydroxyl exchange on iron-oxide surface (T. Sun et al., 2017b). 0.01 M NaOH (in 0.01 M NaCl) solution was used as regenerant solution. The desorbed material was thoroughly washed, dried and used for next adsorption cycle. Results measured on atomic adsorption spectrometer (Perkin Elmer AAnalyst 400) using mercury hydride system (MHS).

2.6. Application of RHIOB and WHIOB on actual ground water samples:

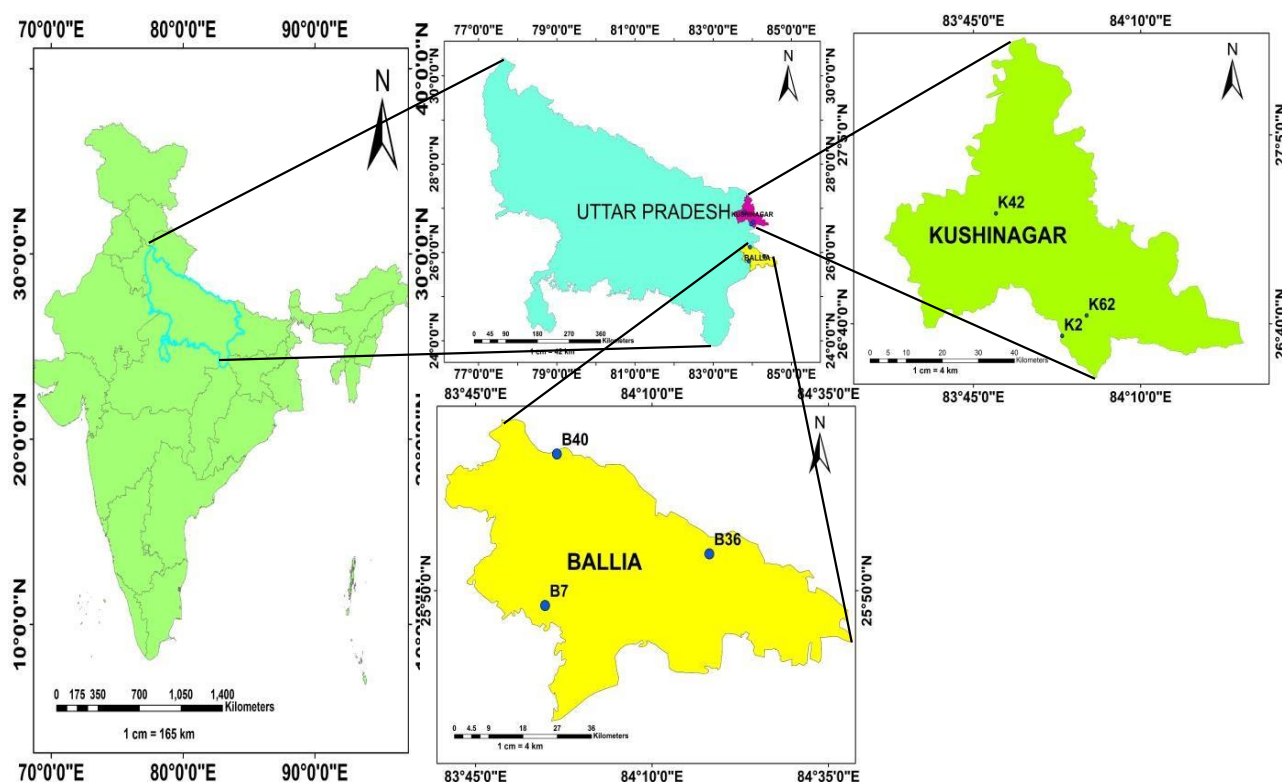


Figure 2.12. Groundwater sample collection sites. Ballia district (B7, B36, B40), Uttar Pradesh and Kushinagar district (K2, K42, K62), Uttar Pradesh, India.

Batch and column studies conducted in solution prepared in situ under laboratory conditions. In order to find the applicability of developed material in real, adsorption studies were conducted on actual ground water samples. Because actual water samples contains multiple ions, they may affect the chemistry of adsorption through competitiveness and interference during remediation. Experiments conducted on six groundwater samples collected from Ballia and Kushinagar

Development and characterization of rice husk and wheat husk iron-oxide biochar

districts of Uttar Pradesh, India. Because these regions reported to have ground water with high arsenic contents, the samples of interest were collected from the same.

The geographical location of the sampling area was between 26°12'-25°91' N (latitude) and

83°94'-84°30' E (longitude) for Ballia district and 26°64'-26°69' N (latitude) and 83°97'-84°03'

E (longitude) for Kushinagar district. Water parameters pH, conductivity, total dissolved solid (TDS), concentrations of fluoride, Na, K, Mg, Ca and other trace elements are measured. Adsorption studies conducted with 2.0 g/L and 1.0 g/L of RHIOB and WHIOB in 50 mL of samples for 24 h. Before and after concentrations of arsenic measured and reported in terms of percent removal.

CHAPTER 3

**DEVELOPMENT AND
CHARACTERIZATION OF RICE HUSK
IRON-OXIDE (RHIOB) AND WHEAT
HUSK IRON-OXIDE BIOCHAR (WHIOB)
COMPOSITES**

3.1. Synthesis of rice husk iron-oxide (RHIOB) and wheat husk iron-oxide biochar (WHIOB) composites:

Iron-oxide composite biochars were prepared by modified co-pyrolysis method using rice husk and wheat husk precursor biomass (filed in Indian Patent Application No. 20181010032). Scheme for preparation of RHIOB and WHIOB shown in figure 3.1. Rice husk biomass and wheat husk biomass were collected from Maszid moth village, south extension II, New Delhi. The biomass were thoroughly dried. Approximately 70 g rice husk and 130 g wheat husk were soaked separately in iron salt solution. The solution was prepared by dissolving ferric chloride hexahydrate salt ($\text{FeCl}_3 \cdot 6\text{H}_2\text{O}$) in distilled water to obtain 2.8 M concentration solution. The biomass soaked in the iron solution for 24 h. The iron soaked biomass(s) were oven dried at 80°C for 2 h. The biochar(s) development was initiated by slow pyrolysis of the soaked biomass(s). Pyrolysis was carried out using muffle furnace in N_2 supply (flow rate = $0.1 \text{ m}^3/\text{h}$) to prevent combustion of the fed biomass. The temperature of the muffle furnace raised to 600°C at rate of $10^\circ\text{C}/\text{min}$ and held for 1 h residence time. After overnight cooling of muffle furnace, pyrolysed composites washed repeatedly with double distilled water to ensure removal of excess iron, water-soluble salts and organic compounds. Washing stopped as soon the pH of water obtained after washing became constant (~ 7.5 for RHIOB and WHIOB). The pyrolysed biomass(s) were oven dried at 95°C overnight, sieved into 30-50, 50-100, 100-200 B.S.S. mesh size and kept in airtight containers. 50-100 mesh sized composite biochars used for studies and experimentations. Biochar obtained by soaking rice husk biomass and wheat husk biochar separately in ferric chloride solution followed by pyrolysis coded as rice husk iron-oxide biochar (RHIOB) and wheat husk iron-oxide biochar (WHIOB) composites.

3.2. Characterization of RHIOB and WHIOB:

3.2.1 Ultimate and Quantitative analysis:

Ultimate analysis was performed to find carbon, hydrogen, sulphur and nitrogen (Mohan et al., 2007). Percent oxygen was calculated by difference (Table 3.1). RHIOB has a higher percent carbon (39.2 wt%) than WHIOB (37.8 wt%).

Both biochars have large ash contents (RHIOB: 48.5 wt% and WHIOB: 46.7 wt%) which include Fe (RHIOB: 16.02 wt% and WHIOB: 19.03 wt%) and Si (RHIOB: 64.37 wt% and WHIOB: 60.96 wt%) as the most abundant components. Qualitative analysis was carried out by inductively coupled plasma mass spectrometry (ICP-MS) (Table 3.1). The composites were ashed (6h at 650⁰C) to find the percent iron loading and other inorganic constituents. Ash was then dissolved in the mixture of HNO₃ and HF (3:1 v/v %). Conc. HCl was added to stabilize Fe and Al in solution. Digested samples were then analysed by ICP-MS. RHIOB and WHIOB hybrid composites contained 16.02 and 19.03 wt% Fe loadings, respectively (Table 1). In contrast, pristine biochars from rice and wheat husk pyrolysis alone, (RHB and WHB) and their respective precursor husk biomasses (RH and WH) contain very little iron content (Table 3.1). Other elements were also present in minor quantities. This was also confirmed from their respective intense peaks in SEM-EDX graphs [Figure.3.2 (a-f)].

In RHIOB and WHIOB after As(III) and As(V) adsorption there is decrease in the percentage of silicon. This may be attributed to the displacement of silica with arsenic oxyanions during adsorption. This is also in justified by the SEM-EDX results as described in the later sections. Trace elements are present in negligible percentage. Small percentage of Ca (RHIOB: ~5 wt.%; WHIOB: ~7 wt.%), Na (RHIOB: ~7 wt.%; WHIOB: ~5 wt.%), K (RHIOB: ~0.4 wt.%; WHIOB: ~1 wt.%) and Mg (RHIOB: ~1 wt.%; WHIOB: ~2 wt.%) is attributed to the characteristic feature of lignocellulosic biomass from which the biochars are obtained [table 3.1].

3.2.2. Surface area analysis:

Table 3.1. shows surface area measurements before and after arsenic adsorbed RHIOB and WHIOB. Both composite biochars have very high BET surface area (S_{BET}) with greater surface area for WHIOB (~339 m²/g) as compared to RHIOB (~300 m²/g). Reduction in S_{BET} is observed for RHIOB and WHIOB after arsenic loading. This could be attributed to clogging of pores due to arsenite/arsenate ions. S_{BET} of RHIOB and WHIOB after-As(V) loading is lower as compared to RHIOB and WHIOB loaded with As(III) [table 3.1.] due to greater occupancy and adsorption of arsenates as compared to arsenites. This is supported

by greater adsorption capacity (reported in chapter 5) of RHIOB and WHIOB towards As(V) as compared to As(III). RHIOB and WHIOB reported external surface areas ~ 13.0 and ~ 15.0 m²/g, respectively, and micropore volume ~ 18.0 and ~ 19.0 cm³/g, respectively [table 3.1].

3.2.3. SEM-Energy dispersive X-ray analysis (SEM-EDX):

SEM-EDX analyses of RHIOB and WHIOB before and after arsenic adsorption were carried out [Figure 3.2 (a-f)]. C, O, Si, Cl, and Fe were the major elements observed in SEM-EDX spectra of RHIOB and WHIOB before As(III) and As(V) adsorption [Figure 3.2 (a-b) and Table 3.1]. Na, K, Mg, Ca, Al, Mn, Cu, Rb, Mo, W, and Pb were also observed before As(III) and As(V) adsorption. Silicon content was higher in RHIOB than in WHIOB (Figure 3.2). Traces of arsenic were also observed in both RHIOB and WHIOB samples only after arsenic adsorption had occurred, corresponding to the arsenic observed in capacity measurements [Figure 3.1 (c-f)].

Adsorbent ash contents were determined by dry combustion for 6h at 750⁰ C. The higher WHIOB ash content versus RHIOB (Table 3.1) is attributed to higher WHIOB silica content than that in RHIOB (Al-Wabel, Al-Omran, El-Naggar, Nadeem, & Usman, 2013). The H/C ratio is the degree of carbonization based on the original biomass's hydrogen content (Ahmed, Zhou, Ngo, & Guo, 2016). Both RHB and WHB have similar H/C ratios (Table 3.1) indicating comparable extents of carbonization. The biochar O/C ratio reflects oxygen from biomass functional groups that have not yet been lost during carbonization (Ahmed et al., 2016; Al-Wabel et al., 2013).

3.2.4. Scanning electron microscopy (SEM):

SEM micrographs of the RHIOB and WHIOB morphologies before and after-As(III) adsorption samples are provided in Figures 3.3 and 3.4, respectively. SEM micrographs of the RHIOB and WHIOB morphologies before and after-As(V) adsorption samples are provided in Figures 3.5 and 3.6, respectively. RHIOB samples at 200 X and 500 X magnification exhibit conical arrays of raised surface features lined up in rows which are characteristic of original rice husk morphology [Figure 3.3 (a, c)]. These protrusions are epidermal hairs where most of the silica is

concentrated (Ahiduzzaman & Islam, 2016). This is in general the characteristic morphology of rice husk biochar and is in agreement with the results reported elsewhere (Ahiduzzaman & Islam, 2016; Prakongkep, Gilkes, Wiriyakitnateekul, Duangchan, & Darunsontaya, 2013). Pores at the edges of RHIOB were visible at 2KX magnifications [Figure 3.3 (b, d)] which also reflect their original morphological features. RHIOB exhibited smooth surfaces before As(III) adsorption [Figure 3.3 (a, b)], which have roughened after adsorption. Some partially clogged pores are seen after As(III) adsorption [Figure 3.3 (c, d)]. Similarly, WHIOB surfaces appear to have adjacent parallel canals leftover from the wheat husk morphology [Figure 3.4 a]. Honeycomb-like pores with an average diameter of 22 μm were observed at 2 KX magnifications [Figure 3.4 b]. At 1 KX and 3 KX magnifications after As(III) adsorption [Figure 3.4 (c, d)], this surface morphology roughened due to surface deposits formed during adsorption [Figure 3.4 (c, d)]. SEM micrograph of RHIOB at 500 KX magnification before As(V) loading [figure 3.5. (a)] shows several pores present in the cross section of epidermis. At 2 KX magnification the enlarged picture of pores can be seen [figure 3.5. (b)]. Average pore diameter of 18-8 μm can be seen at 5 KX magnification [figure 3.5. (c)]. In RHIOB, stomata cells with slightly roughened canals are visible at 10 KX magnification [figure 3.5. (d)]. Significant difference are not observed in the images obtained for RHIOB and WHIOB before and after As(V) loading. Several porous honeycomb structures are seen for the WHIOB at 1, 3 and 5 KX before and after As(V) loaded SEM micrographs [figure 3.6. (a, c)]. Pores showed an average size of 2-1 μm [figure 3.6. (b)]. SEM micrograph of WHIOB after As(V) adsorption at 10 KX magnification shows array of honeycomb shaped pores with slightly roughened surfaces, due to clogging by arsenates deposits [figure. 3.6 (d)].

3.2.5. Transmission electron spectroscopy (TEM):

TEM micrographs of RHIOB and WHIOB after As(III) adsorption are shown in Figure 3.7 (a-f). TEM elemental mapping for RHIOB and WHIOB before and after arsenic loading are shown in figure 3.10-3.13. Magnetite (Fe_3O_4) nanoparticles are clearly observed for RHIOB [Figure 3.7 (a)] and WHIOB [Figure 3.7 (d)]. Magnetite primary particle diameters range from 2 to 20 nm. Some primary Fe_3O_4

particles appear spherical while others are hexagonal on both RHIOB and WHIOB and form loose sheet-like or clustered networks (Figure 3.7 a and d). Lattice fringes of 0.291 Å width were captured for Fe₃O₄ on RHIOB [Figure 3.7 b] that correspond to the 220 plane of Fe₃O₄ (Boruah, Sharma, Karbhal, Shelke, & Das, 2017). The SAED pattern of the Fe₃O₄ on RHIOB [Figure 3.7 c] showed fringe widths of 1.52, 2.08, 2.56, and 2.98 Å confirming Fe₃O₄ crystallinity (Rajput, Singh, Pittman, Jr., & Mohan, 2017). A lattice fringe of 0.268 Å was found for Fe₃O₄ on WHIOB [Figure 3.7 e]. The Fe₃O₄ particles on WHIOB gave a SAED diffraction pattern which showed fringes (1.52, 2.08, 2.56 and 2.98 Å) confirming a crystalline structure [Figure 3.7 f].

Similarly, TEM micrographs of RHIOB and WHIOB after As(V) adsorption are shown in Figure 3.8 (a-d) and Figure 3.9 (a-d), respectively. Magnetite (Fe₃O₄) nanoparticles clusters are clearly observed for RHIOB [Figure 3.8 (a, b)] and WHIOB [Figure 3.9 (a, b)] after As(V) adsorption. Lattice fringes of 0.291 Å width were captured for Fe₃O₄ on RHIOB [Figure 3.8 c] and 0.324 nm on WHIOB [Figure 3.9 c]. The Fe₃O₄ particles on RHIOB after As(V) adsorption gave a SAED diffraction pattern which showed fringes (3.09, 2.54, 2.09 and 1.6 nm) confirming a crystalline structure [Figure 3.8 d]. Similarly, for WHIOB, SAED diffraction pattern showed fringes (3.08, 2.52, 2.09 and 1.59 nm) that confirms crystalline structure. [Figure 3.9 d]. 0.291 nm and 0.324 nm lattice fringe width corresponds to plane of Fe₃O₄ (Boruah et al., 2017; W. Lei et al., 2017), (Moeck & Bjørge, 2007).

Figure 3.10-3.13 shows two-dimensional elemental mapping for C, O, Fe and Si before and after arsenic loading on RHIOB and WHIOB. However, RHIOB and WHIOB showed less intense regions for Fe, O and Si, before arsenic loading which can be attributed to sites occupied by arsenite/arsenate ions. This confirms the adsorption of arsenic in conjugation with the pockets where iron-oxide is present.

3.2.6. X-ray photoelectron spectroscopy (XPS):

XPS is a surface sensitive technique identifying elements, their oxidation states, and approximate surface region abundances. It analyzes ejected electrons while probing to about 100 Å below the surface, with increasing sensitivity the

closer these elements are to the surface (Shao, Guan, Tian, Guan, & Wu, 2016). XPS analyses were carried out using X-ray monochromators in combination with Al K-alpha radiation ($h\nu = 187.85$ eV; power = 24.6 W, and beam spot size = 100 μm). Comparative wide scan spectra of pristine rice husk and wheat husk biochars and their respective iron-oxide loaded RHIOB and WHIOB after As(III) and As(V) adsorption is shown in Figure 3.14 a and 3.14 b respectively. Pristine rice husk and pristine wheat husk biochars show the absence of any peak in Fe 2p, As 3s and As 3d regions. Whereas RHIOB and WHIOB displayed peaks the presence of peaks in these regions. This depicts successful loading of iron-(oxides) and adsorption of As in RHIOB and WHIOB which otherwise is not present in their respective pristine biochars. High-resolution de-convoluted XPS spectra for Fe, C, O and As are shown for RHIOB [Figure 3.15, 3.16, 3.17, 3.18 (a,c)] and WHIOB [Figure 3.15, 3.16, 3.17, 3.18 (b,d)]. De-convolution was done using Gaussian-Lorentzian sum function in OriginLab 2018(b) software. For a detailed study, high-resolution de-convoluted scans for Fe, O, C and As were obtained for RHIOB and WHIOB after As(III) and after As(V) adsorption.

In general, peak at ~ 706.7 eV assigns to Fe 2p₃ metal peak. Both RHIOB and WHIOB displayed peaks at (710.17 and 710.15 eV) due to deposited iron oxide (Boruah et al., 2017). Fe 2p spectra of RHIOB and WHIOB were deconvoluted to three components, differentiating peaks at 710.15 eV and 723.71 eV which corresponds to Fe 2p_{3/2} and Fe 2p_{1/2}, respectively. These two peaks correspond to Fe(III) and Fe(II) iron atoms occurring in Fe₃O₄ (Boruah et al., 2017; Hu, Ding, Zimmerman, Wang, & Gao, 2015; Liang et al., 2013) and/or FeOOH (Hu et al., 2015; X. Yang et al., 2017b) [Figures 3.15]. The small satellite peak at 715.5 eV that is due to charge transfer between Fe(II) and Fe(III), depicts the formation of mixed oxides as in Fe₂O₃ [RHIOB (Figure 3.15 a and c and WHIOB (Figure 3.15 b and d)] (M. Wang et al., 2017).

High-resolution XPS spectra for O 1s for RHIOB and WHIOB after As(III) and As(V) loaded is depicted in figure 3.16 (a-d). O 1s XPS peak deconvoluted to three distinct components. The first peak region at ~ 533.7 -532.98 eV for RHIOB and WHIOB after As(III) and As(V) loading is associated with OH bonded to C as

C-O-H [figure. 3.16.]. This can also be associated to carbonyl oxygen or C=O peak region (Hao et al., 2014). Second peak ranging from ~531.1-530.90 eV corresponds to -OH group in hydroxyl [figure. 3.16.]. This attributes to -OH group in phenolic hydroxyls and H₂O of the biochar and surface Fe-OH groups of Fe₃O₄ (J. Yang, Chai, Yue, & Li, 2015; Z. Yang et al., 2015). Third peak from ~529.75-528.73 eV attributes to O²⁻ species [figure. 3.16.]. The binding energies of O²⁻ species for RHIOB and WHIOB after As(III) and As(V) adsorption corresponds to iron bound oxygen species present in Fe-O (FeOx, Fe₃O₄, FeOOH) (Hwang, Choi, Park, Kim, & Jeon, 2015; Ramos Guivar et al., 2016). Binding energies corresponding to carbonyl oxygen (C=O) and phenolic hydroxyl oxygens (-OH) are attributed to incomplete biomass carbonization (Z. Yang et al., 2015; Zhuang, Huang, Wang, & Chen, 2015). It is hard to distinguish between the oxygen associated with phenolic hydroxyl groups and those found in small amount of water adsorbed (Yahui Li, Zhang, Wu, & Guo, 2017; Z. Yang et al., 2015; Zhuang et al., 2015). The iron oxide oxygen peak area in WHIOB after As (III/V) adsorption is greater than RHIOB after As (III/V) adsorption supporting greater metal-oxide (Fe-O) loading in WHIOB as determined in elemental analysis.

The C 1s spectra were deconvoluted to three components, differentiating into peaks at 284.3 eV, 285.15 eV and a very broadband from ~286 – 289 eV in both RHIOB [Figure. 3.17] and WHIOB after As(III) and As(V) adsorption [Figure. 3.17]. The peak at 284.3 eV depicts C-H and C-C stretching vibration due to sp² carbon (Ermolieff et al., 2001). The peak at 285.15 eV depicts C-H and C-C stretching vibration in sp³ carbon (Ermolieff et al., 2001). It is adjacent to sp² carbon peak and is shifted slightly towards higher binding energy as compared to sp² peak (Boukhvalov et al., 2018; Y. Li et al., 2017). Presence of both sp² and sp³ contributions suggest the formation of graphene-like structures (Boukhvalov et al., 2018). This is in agreement with the formation of turbostratic biochars produced at higher temperatures due to the formation of graphene-like growths at the expense of aromatic carbon and hence exhibiting both aromatic and aliphatic carbon (Keiluweit et al., 2010). Broad flat peak ranging from 286-289 eV includes -C-O and -C=O and represents to the phenolic carbon groups and aryl ether groups

respectively. Broad flat peak suggests that very small amount of oxygen bounds to carbon in both the materials.

Deconvoluted spectra of As 3d is shown for RHIOB and WHIOB after As(III) and after As(V) adsorption in figure 3.18 (a-d). Arsenic is known to appear as AsO_4^{3-} (44.9 eV), HAsO_4^{2-} (45.5 eV), and H_2AsO_4^- (46.7 eV) (Liang et al., 2013) in XPS spectra. Appearance of As 3d peak in RHIOB and WHIOB loaded with As(III) at 44.1 eV and for As(V) at 45.5 eV confirms adsorption of arsenite and arsenate onto RHIOB and WHIOB conducted in separate studies (Hu et al., 2015; Liang et al., 2013; T. Liu, Yang, Wang, & Sun, 2016; Sasaki, Nakano, Wilopo, Miura, & Hirajima, 2009). The peak for As(III) oxidation state appears at lower binding energy as compared to As(V) oxidation state that is known to occur at higher binding energies. Absence of other deconvoluted components of arsenic confirms adsorption of arsenic in its original form. In other words no oxidation state of arsenic has shown no changes from (III) to (V) and vice versa occurred while being adsorbed onto RHIOB and WHIOB (Hao et al., 2014). As(V) show higher intensity peak formation as compared to As(III) adsorbed RHIOB and WHIOB. This indicates higher capacity of RHIOB and WHIOB for arsenates adsorption as compared to arsenite adsorption. This is further justified with the adsorption capacities calculated for both the cases.

Not much difference in the peaks were observed after As(III) and As(V) on RHIOB and WHIOB. Lowering in the intensities of Fe 2p_{3/2} peaks, metal oxide peak (~529 eV) and metal hydroxyl peak (~578 eV) of O 1s on RHIOB and WHIOB loaded with As(V) as compared to As(III) indicates the formation of metal oxide (Fe-O) and replacement of singly coordinated hydroxyl (Fe-OH) by As(III) and As(V) (Hao et al., 2014). This justifies the greater adsorption capacity of arsenates over arsenites on RHIOB and WHIOB.

3.2.7. X-ray powder diffraction (XRD):

XRD pattern for RHIOB and WHIOB before and after As(III) loaded [Figure 3.19 (c, d)] and before and after As(V) loaded [Figure 3.19 (e, f)] and As(V) loaded [Figure 3.19 (g) and (h)] obtained [Table 3.2.]. Changes due to iron-impregnation and 600^oC pyrolysis are observed by comparing the XRD patterns for

the precursor rice husk (RHB) and wheat husk (WHB) biochars with RHIOB and WHIOB [Figure.3.19 (a) and (b); Table 3.2.]. RHIOB and WHIOB XRD patterns were also compared to those of Fe_2O_3 and Fe_3O_4 . RHB and WHB had a broad peak from 2θ from 19-29 degrees. RHIOB and WHIOB also contained this same broad diffraction where the peak maximum was shifted to somewhat higher 2θ values. These represent an amorphous range of inter-aromatic plane distances of the partially graphitized biochars. The wide diffraction peaks at 26.5° and 44.7° correspond to the (002) and (100) planes of graphite (JCPDS card no. 41-1487). (Huang et al., 2009; Jin, Ge, Xu, Peterson, & Zhu, 2017; Zhong, Wang, Yu, Xia, & Wen, 2017) These peaks correspond to a combination of carbon in sp^2 (26.5° ; d spacing 3.35 \AA) and sp^3 (44.7° ; d spacing 2.06 \AA) hybridization states. (Huang et al., 2009; Jin, Ge, Xu, Peterson, & Zhu, 2017) The C(002) plane represents parallel and azimuthal orientation of the aromatic lamellae, while C(100) is indicative of the aromatic lamina size. Greater peak sharpness indicates a more aromatic lamellae formation and progressive aromatic ring condensation. (T. Chen, R. Liu, & N. R. Scott, 2016b; Huang et al., 2009) Other XRD peaks common to RHB, WHB, RHIOB and WHIOB belonged to the mineral oxides present (T. Chen et al., 2016b) (SiO_2 , CaCO_3 , CaO , and MnO_2), often found in biochars. These peaks occurred at 26.7° , 38.4° , 50.2° , 64.9° , 68.1° , 76.6° and 83.2° and are assigned specifically to SiO_2 (quartz), CaO (lime), CaCO_3 (calcite) and MnO_2 in Table 2 (Jin, Ge, Xu, Peterson, & Zhu, 2017; X. Li, Zhang, Hou, Ye, & Li, 2017; Xiaoming Ma et al., 2013; Madrid & Lanzón, 2017b).

The sharp peaks in RHIOB and WHIOB, but absent from RHB and WHB, belonged to iron-oxide crystalline phases formed from FeCl_3 during pyrolysis, cooling and exposure to air. The observed peaks clearly demonstrated two iron-oxide species formed. Diffraction peaks centered at 35.7° (311), 41.7° (400), 53.4° (422), 57.1° (511), 62.5° (440), 70.9° (620) and 78.9° (444) all correspond to Fe_3O_4 (magnetite) peaks (JCPDS card no. 19-0629) (Baig et al., 2014b). Peaks at 24.2° (012), 25.5° (110), 33.1° (104), 54.4° (116), 64.0° (300) and 72.3° (119) are attributed to Fe_2O_3 (maghemite) (JCPDS card no.84-0310) (G. Cheng, Xu, Xiong, & Yi Wei, 2017; Lei, Ni, Chen, Zhang, & Li, 2017; Zhong et al., 2017). Two extra

peaks observed at 31.8° (210) and 37.1° (21-2) could possibly belong to small amounts FeOOH (goethite) (JCPDS card no. 34-1266) (X. Qiu et al., 2008; Y. X. Yang, Liu, Zhu, Chen, & Jia, 2008).

3.2.8. Fourier transform infra-red spectroscopy (FT IR):

FTIR spectra before and after As(III) loading, were obtained for both RHIOB and WHIOB [Figure 3.20] and after As(V) adsorption [Figure 3.21]. Several sharp peaks observed from 3935 to 3510 cm^{-1} correspond to O-H stretching vibrations of absorbed water molecules (Boruah et al., 2017; Rajput, Pittman, Jr., & Mohan, 2016) [Figure 3.20-3.21]. The broad peak ranging from 3500 - 3000 cm^{-1} is due to O-H stretching vibration in hydrogen bond due to stretching vibrations of absorbed water molecules (Boruah et al., 2017; Keiluweit et al., 2010; Kloss et al., 2012). Another broad peak at 3430 - 3460 cm^{-1} peak in RHIOB and WHIOB spectra, before and after As(III) adsorption [Figure 3.20] and before and after As(V) adsorption [Figure 3.21], corresponds to O-H stretching modes of surface Fe-OH stretching groups on the magnetite and maghemite particles (Cai & Wan, 2007; W. Lei et al., 2017) on the surface of rice and wheat husk biochars. Small peak at 3010 cm^{-1} and 2787.2 cm^{-1} relates to C-H stretching in aromatic and heat resistive aliphatic structures [Figure. 3.20 and 3.21]. The peak at 2360 cm^{-1} is due to O=C=O vibration in CO₂ (Rajput et al., 2016). The broad peak region from 1750 - 1650 cm^{-1} in figures 3.20 and 3.21 is due to various saturated and unsaturated carbonyl functional groups in biochars (Mohan, Singh, Sarswat, Steele, Pitmann, et al., 2015). Very small sharp peak at 1270 cm^{-1} indicates to C-O stretching vibration associated with undecomposed lignin and cellulosic part (pyranone rings and guaiacyl monomers) (Keiluweit et al., 2010). Distinct peaks at 1115 - 1057 cm^{-1} depict both sp³- and sp²-hybridized C-O vibrations in C-O-C and C-O-H functions (Baig et al., 2014b; Cai & Wan, 2007; W. Lei et al., 2017). The sharp peak at 667 cm^{-1} is due to C-C-C angle bending (Mohan, Singh, Sarswat, Steele, Pitmann, et al., 2015). The two sharp peaks at 584 and 456 cm^{-1} are Fe-O stretching vibrations of iron atoms occupying octahedral and tetrahedral sites, respectively in Fe₃O₄ (W. Lei et al., 2017) in good agreement with reported values (Sarswat & Mohan, 2016). One key absorbance at 835 cm^{-1} appeared only after As(III) adsorption [depicted in (red)

Figure 8a and 8c) in both RHIOB and WHIOB. This is due to the As-O stretching vibration of As-O-Fe (G. Qiu, Gao, Hong, & Zheng, 2017).

Enlarged region from 1000-500 cm^{-1} for RHIOB and WHIOB after As(V) adsorption showed peaks [Figure. 3.21]. Small broad peak at 803-755 cm^{-1} corresponds to vibration out of plane due to the deformation of aromatic C-H. Sharp intense peak at 667 cm^{-1} is due to C-C-C angle bending (Mohan, Singh, Sarswat, Steele, & Pittman, 2015). An intense peak is observed at 456 and 584 cm^{-1} on RHIOB and WHIOB before and after As(III) adsorption [Figure 3.20] and at 601 cm^{-1} on RHIOB and WHIOB before and after As(V) adsorption [Figure 3.21] (W. Lei et al., 2017; P. Gallios et al., 2017). This attributes to Fe-O stretching vibration in octahedral and tetrahedral sites (W. Lei et al., 2017; P. Gallios et al., 2017; J. Yang et al., 2015). Thus, it confirm the presence/formation of iron oxides in RHIOB and WHIOB.

A key absorbance peak observed in spectra obtained after As(III) adsorption in RHIOB and WHIOB [Figure 3.20, circled red]. This is due to As(III)-O stretching vibration of As-O-Fe (Jia, Xu, Wang, & Demopoulos, 2007; J. Yang et al., 2015). Similarly, a new band is visible in the spectra obtained after As(V) adsorption in RHIOB and WHIOB at 830 cm^{-1} (Jia et al., 2007; J. Yang et al., 2015). This indicates the adsorption of As(III) and As(V) by RHIOB and WHIOB through Fe-O linkages.

3.2.8. Saturation Magnetisation:

Magnetic measurements were done at 10 K and 300 K for RHIOB, WHIOB, and their precursor biochars RHB and WHB [Figure 3.22-3.23]. Saturation magnetization (M) reached a maxima of ~ 7.0 emu/g (10 K) and ~ 3.0 emu/g (300 K) for RHIOB and ~ 14 emu/g (10 K) and ~ 8.5 emu/g (300 K) for WHIOB. In both the cases, their precursor biochars RHB and WHB showed almost negligible saturation magnetization values at 10 K and 300 K. Since magnetic Fe_3O_4 phases were confirmed on both adsorbents, saturation magnetization curves were measured. Closer inspection in inset figure 3.22. (a). and figure 3.23. (b) showed the formation of small hysteresis loop for RHIOB and WHIOB at 10 K and 300 K, respectively. Remanence (M_r) and coercivity (H_c) were found to be ~ 1.2 emu/g (10

K) and 0.02 Oe (10 K), respectively for RHIOB [figure 3.22.], and 2.8 emu/g (10 K) and 0.03 Oe (10 K), respectively for WHIOB [figure 3.23.]. Such small value of remanence and coercivity corresponded to super-paramagnetic behaviour of the composites, that indicates the absence of magnetism when external field is not applied (Köferstein, Walther, Hesse, & Ebbinghaus, 2013; X. Yu et al., 2013). The values are given in table 3.4.

3.2.9. Point of zero charge, pH_{zpc}:

In order to interpret the adsorption process and dissolution rate for the solids in the solution, pH_{zpc} provides information for the same (Lindblad & Duroux, 2017). pH_{zpc} is the pH at which the positive and the negative charges over the adsorbent surface becomes equal, or the net charge on the surface becomes zero (Fiol & Villaescusa, 2009). The pH_{zpc} were determined for RHIOB, WHIOB and their precursors biochars RHB and WHB [Figure 3.24]. The graph was plotted between ΔpH vs $\text{pH}_{\text{initial}}$ with the point of zero intersection taken as pH_{zpc}. The pH_{zpc} values for RHIOB ~5.5 and WHIOB ~7.0 were found to be lower than RHB, ~6.8 and WHB~8.3, respectively [figure 3.24]. The pH_{zpc} values are given in table.3.5. Role of pH_{zpc} in explaining the mechanism of adsorption of arsenite and arsenate onto RHIOB and WHIOB has been dealt in detail in chapter 6.

Development and characterization of rice husk and wheat husk iron-oxide biochar

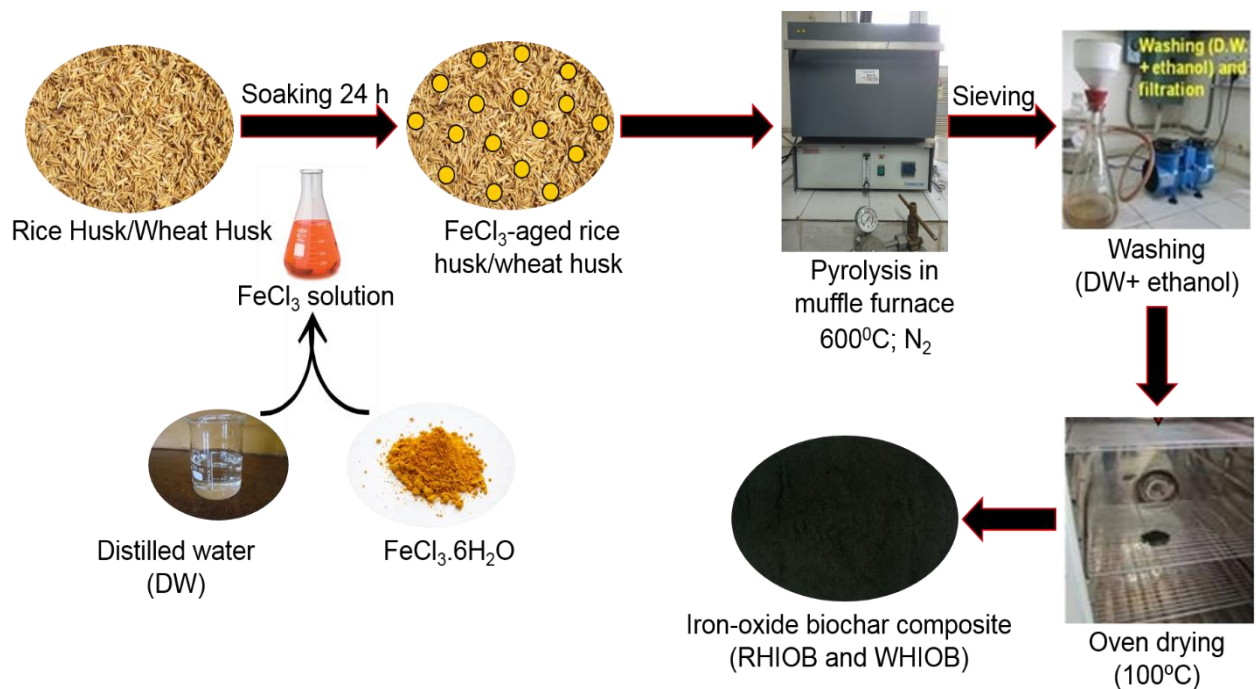


Figure 3.1 Scheme for the development of rice husk (RHIOB) and wheat husk iron-oxide biochar (WHIOB) composites.

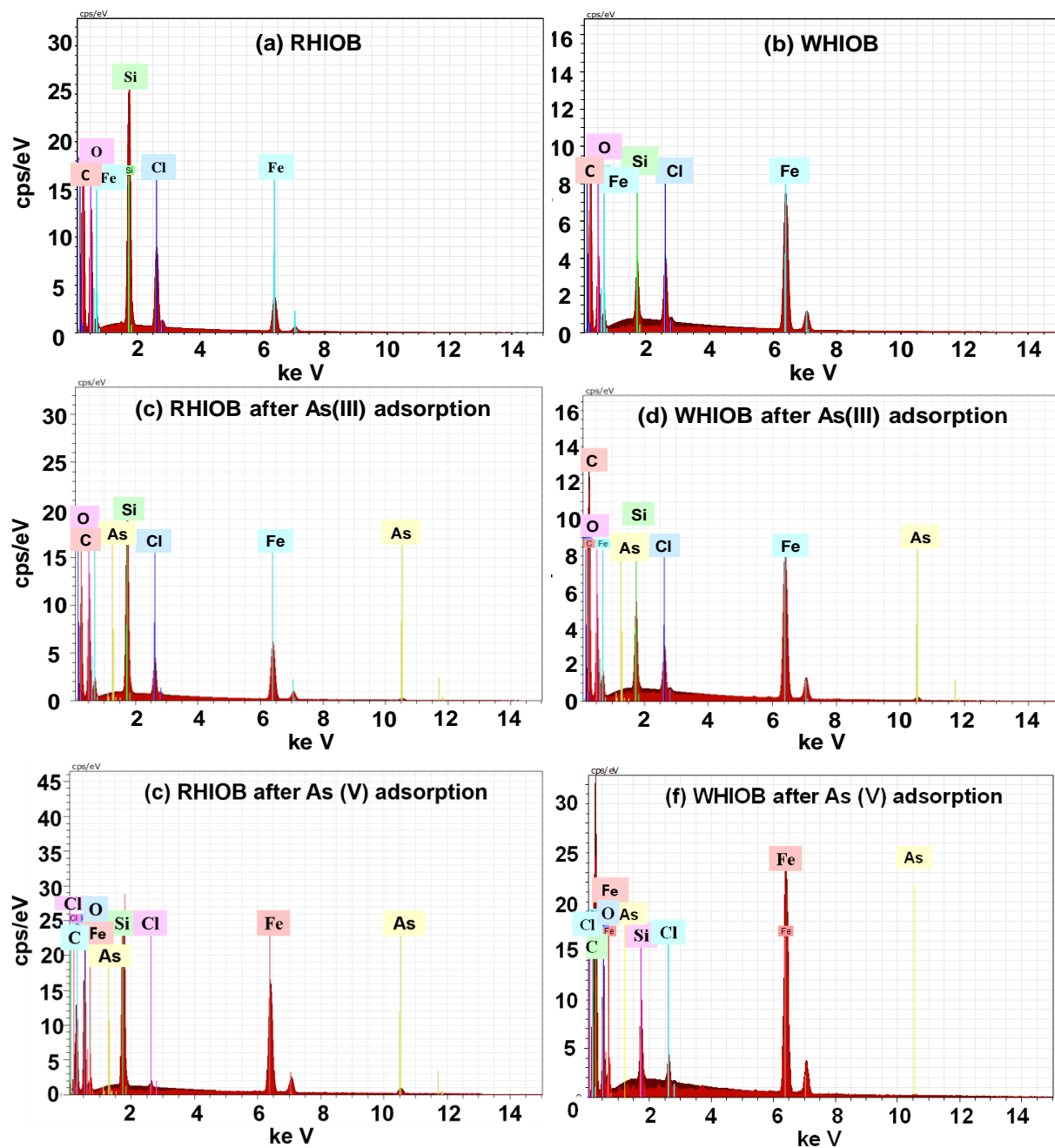


Figure 3.2 SEM-EDX spectra of the iron-oxide biochar composites (a) unloaded RHIOB, (b) unloaded WHIOB, (c) As(III)-loaded RHIOB, (d) As(III)-loaded WHIOB, (e) As(V)-loaded RHIOB and (f) As(V)-loaded WHIOB.

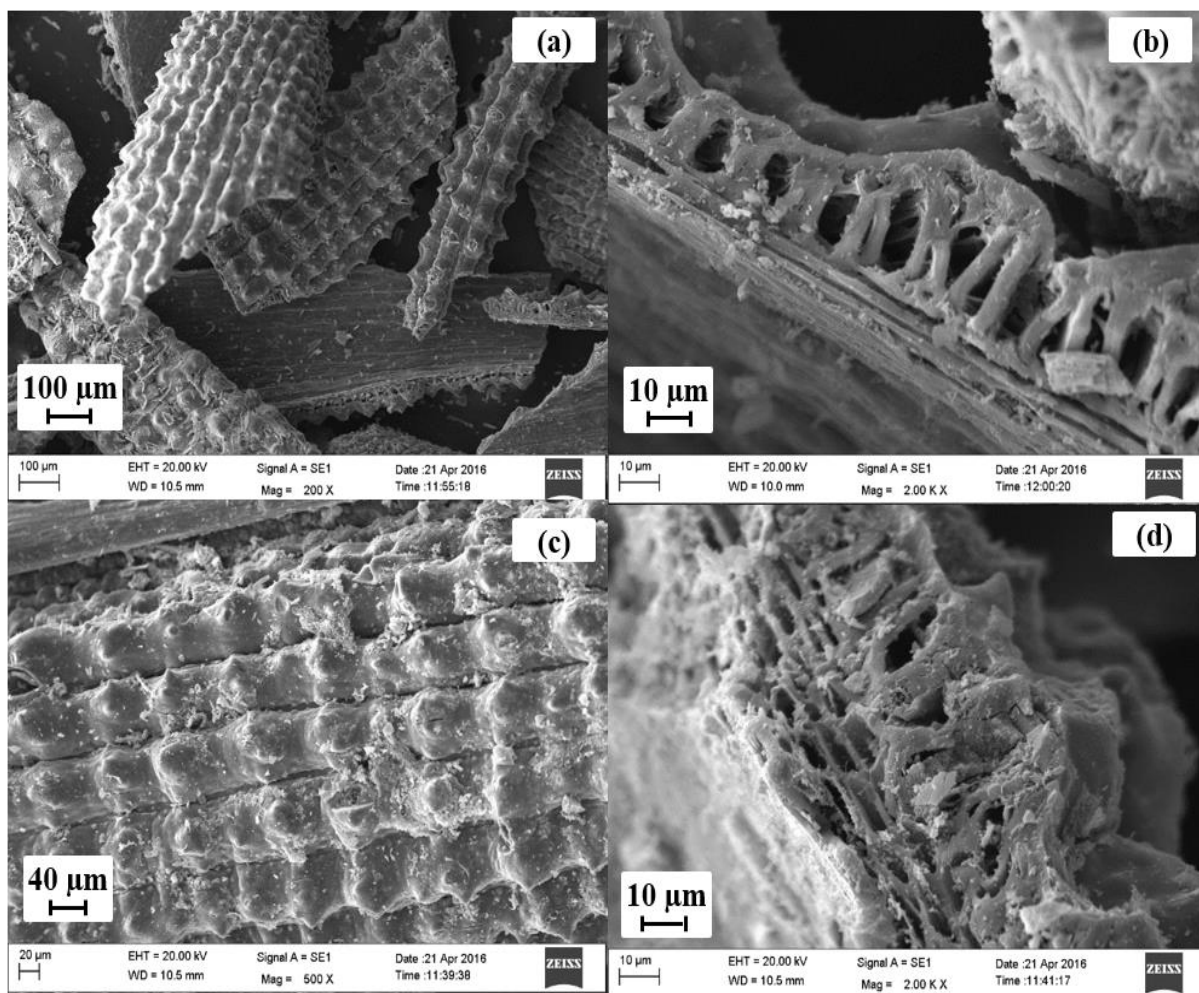


Figure 3.3. SEM micrographs of RHIOB at different magnifications. (a) 200 X without As(III) loaded, (b) 2 KX without As(III) loaded, (c) 500 X As(III) loaded, and (d) 2 KX As(III) loaded.

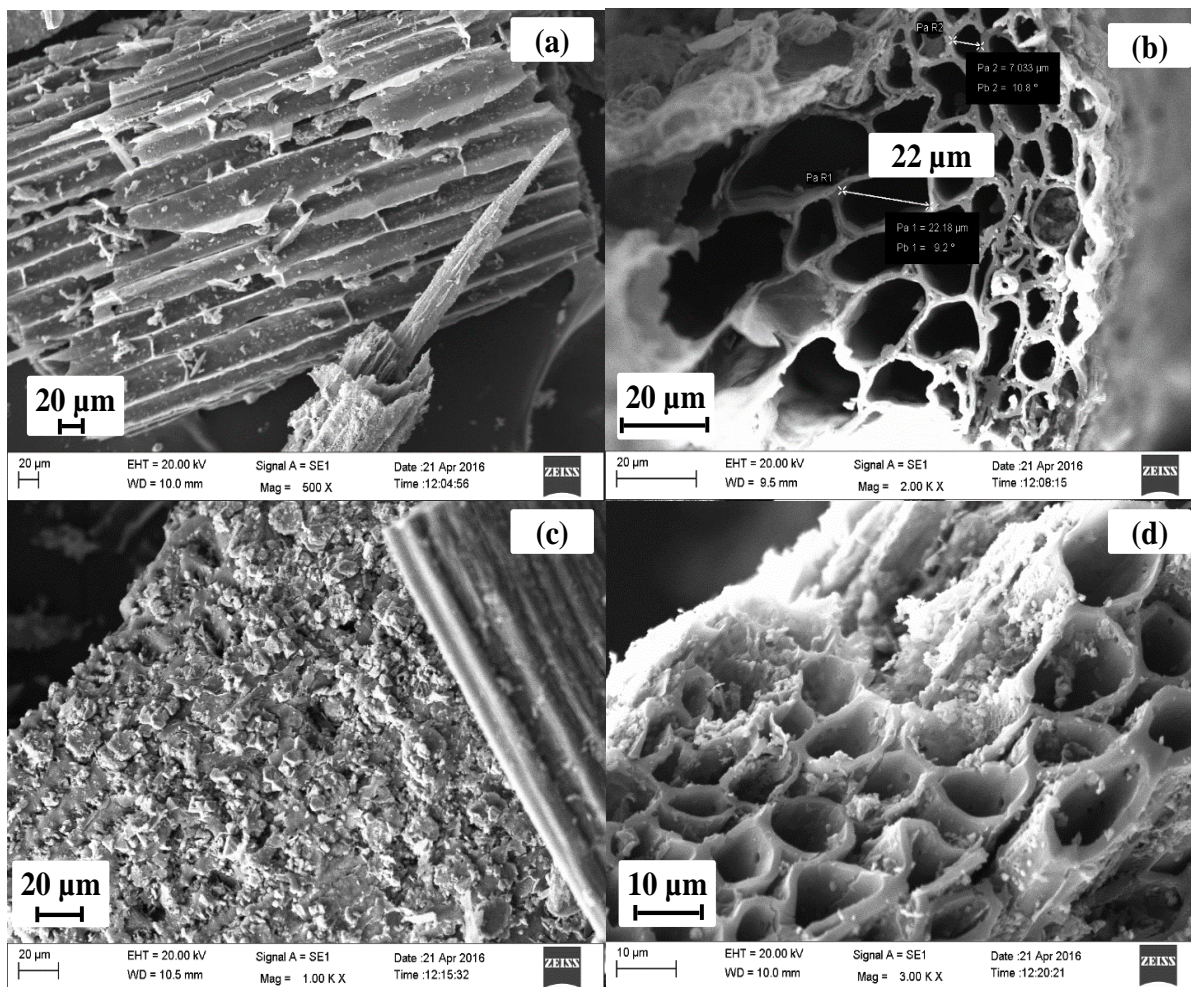


Figure 3.4. SEM micrographs of WHIOB at different magnifications. (a) 500 X without As(III) loaded, (b) 2 KX without As(III) loaded, (c) 1 KX As(III) loaded, and (d) 3 KX As(III) loaded.

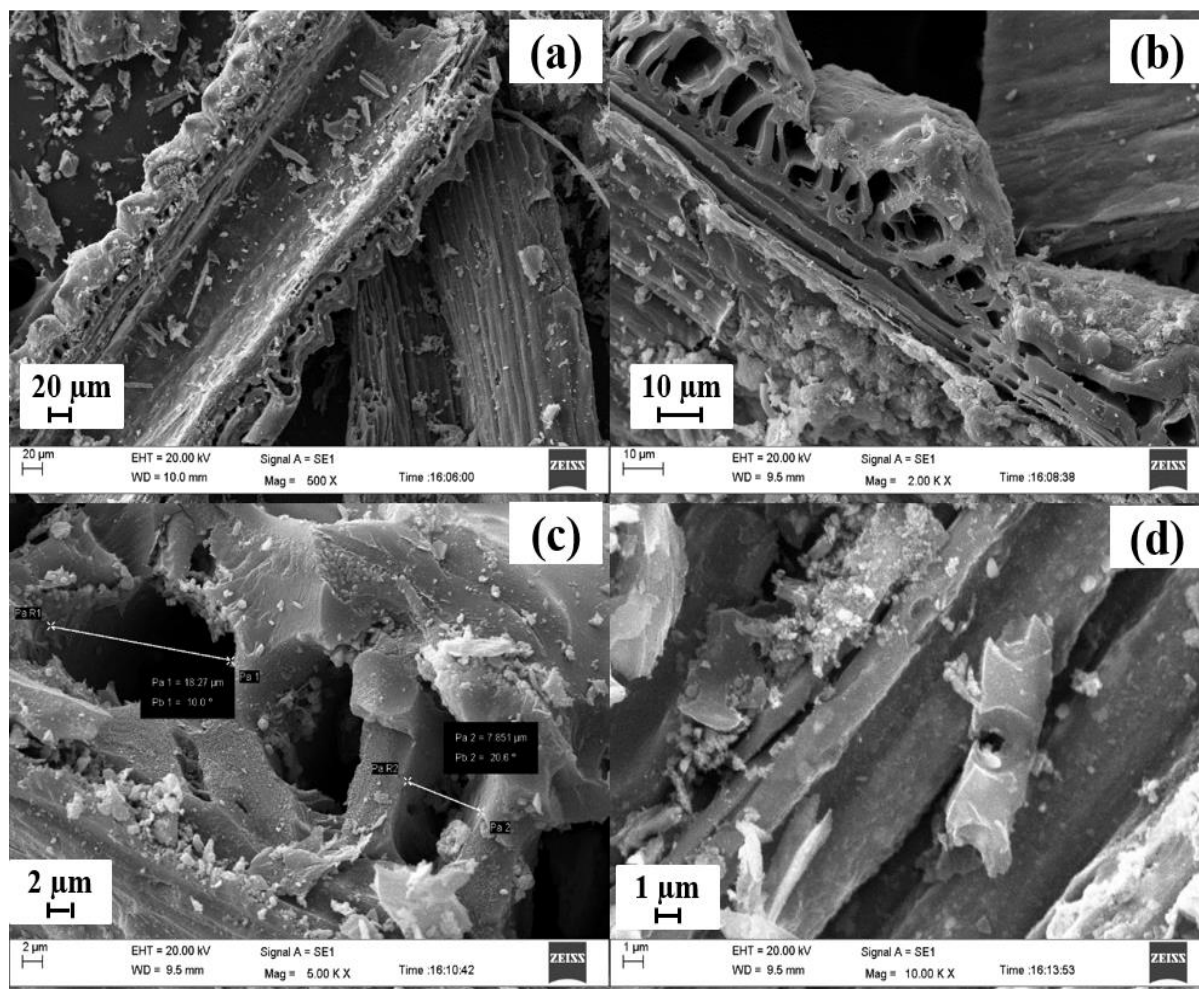


Figure 3.5. SEM micrographs of RHIOB at different magnifications. (a) 500 KX without As(V) loaded, (b) 2 KX without As(V) loaded, (c) 5 KX As(V) loaded, and (d) 10 KX As(V) loaded.

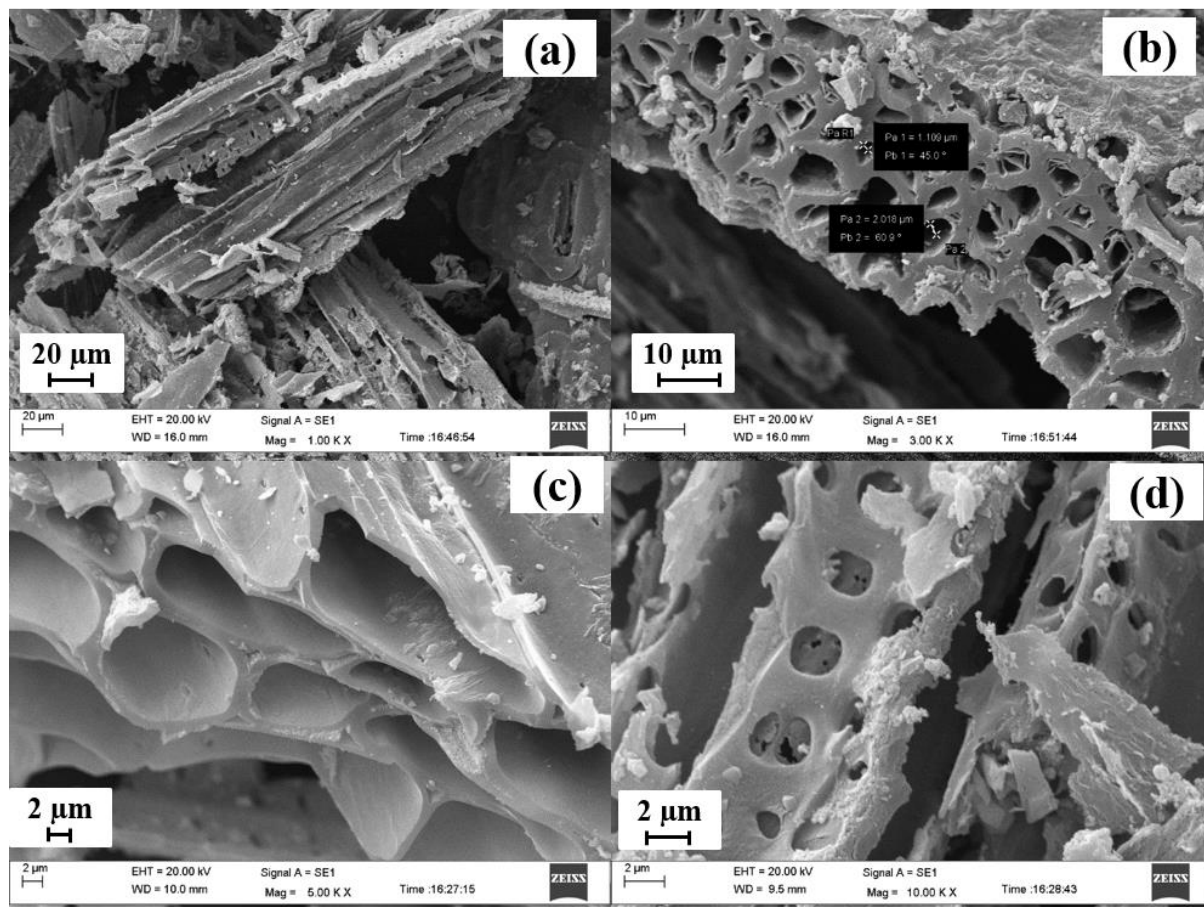


Figure 3.6. SEM micrographs of WHIOB at different magnifications. (a) 1 KX without As(V) loaded, (b) 3 KX without As(V) loaded, (c) 5 KX As(V) loaded, and (d) 10 KX As(V) loaded.

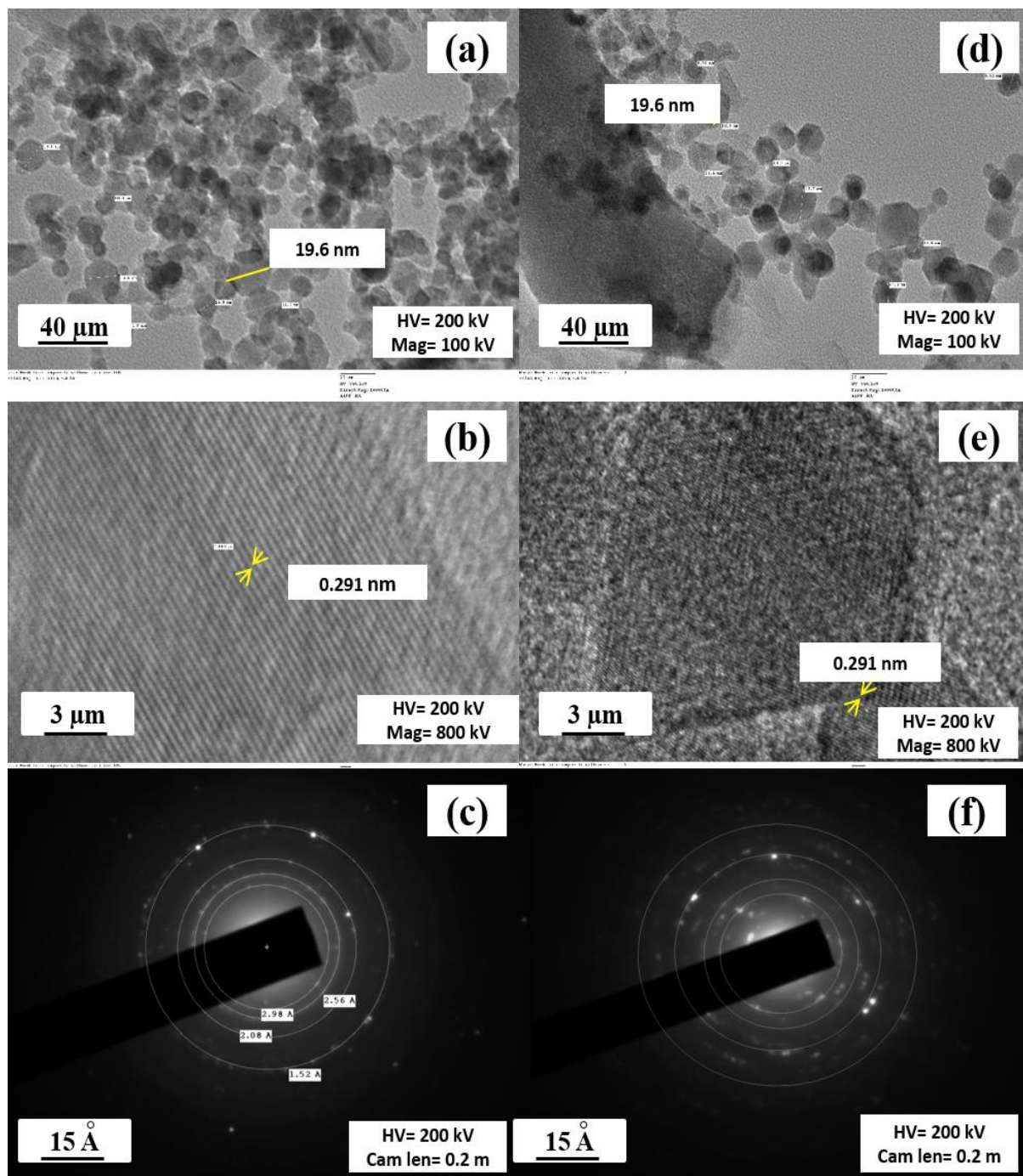


Figure 3.7. TEM micrographs of RHIOB after As(III) adsorption at different magnification (a) 100 KX (clusters hexagonal-pentagonal structures), (b) crystal lattice (formation of iron-oxide crystals) (c) SAED pattern, 220 plane (corresponds to magnetite particles). TEM micrographs of WHIOB after As(III) adsorption at different magnification (d) 100 KX (clusters hexagonal-pentagonal structures), (e) crystal lattice (formation of iron-oxide crystals) (f) SAED patter, 220 plane (corresponds to magnetite particles)

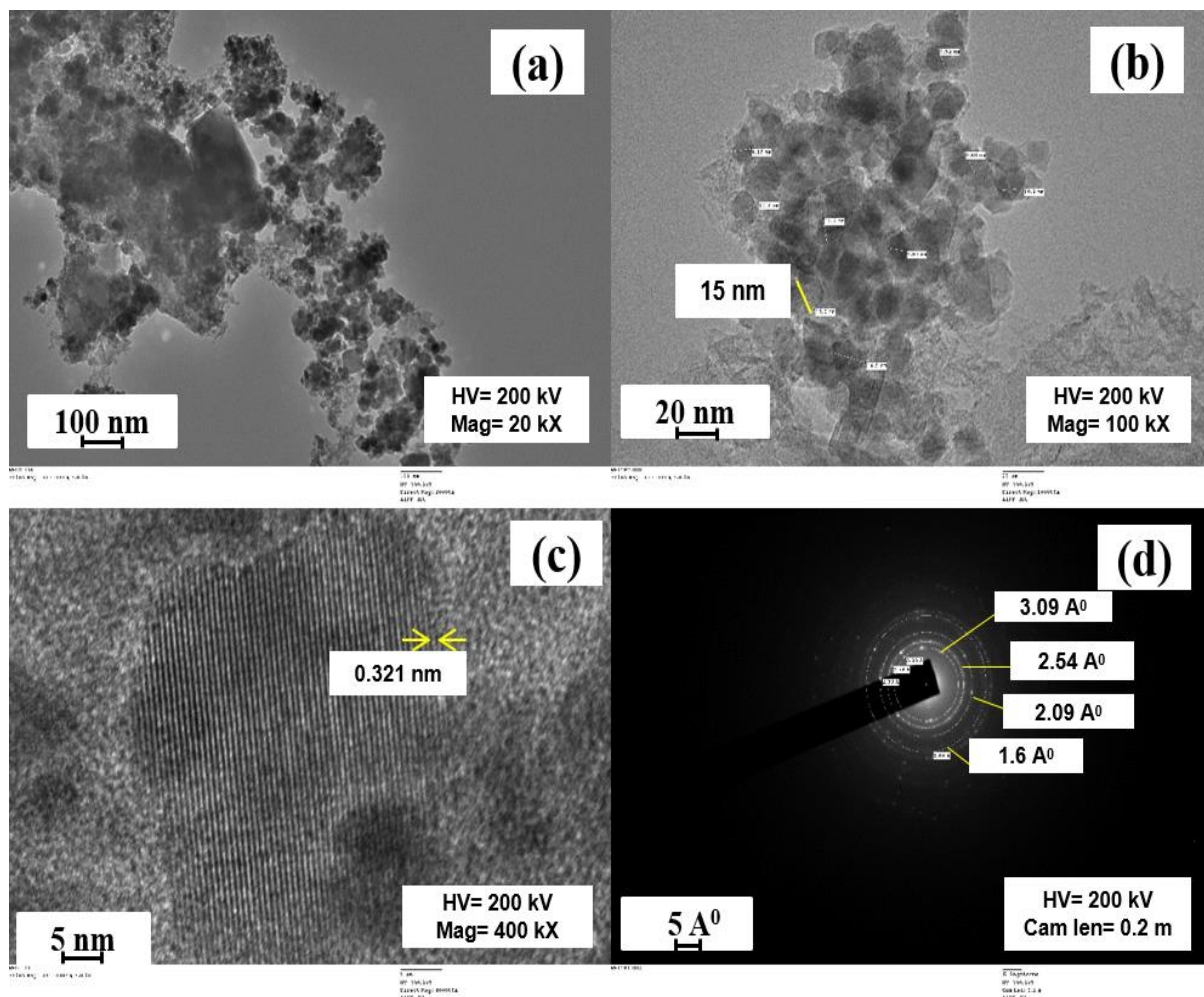


Figure 3.8. TEM micrograph of RHIOB after As(V) adsorption at different magnifications (a) 10 KX (clusters hexagonal-pentagonal structures) and (b) 50 KX (clusters hexagonal-pentagonal structures magnified), (c) crystal lattice (formation of iron-oxide crystals) (d) SAED pattern, (110) plane (corresponds to magnetite particles).

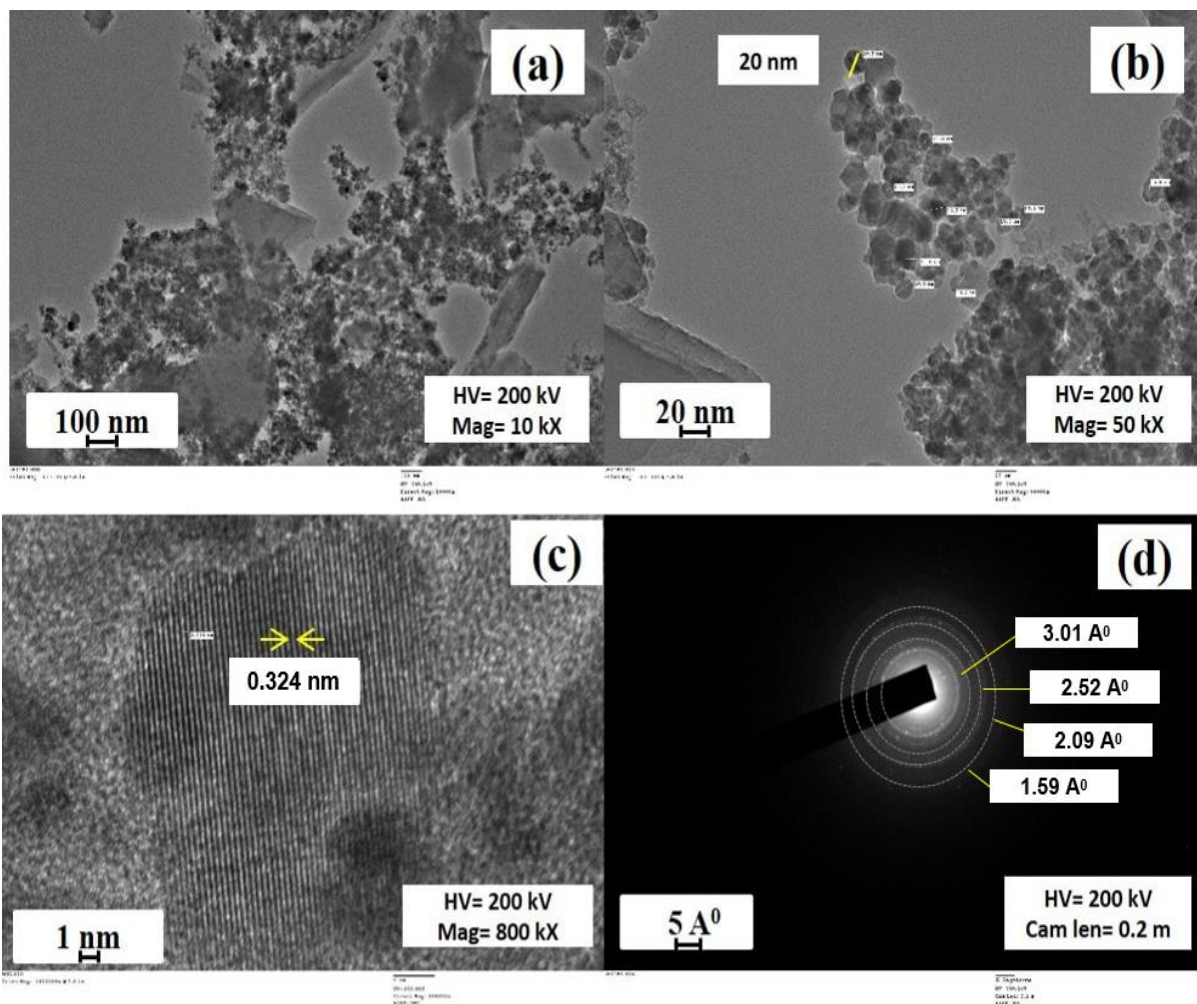


Figure 3.9. TEM micrograph of WHIOB after As(V) adsorption at different magnifications (a) 10 KX (clusters hexagonal-pentagonal structures) and (b) 50 KX (clusters hexagonal-pentagonal structures magnified), (c) crystal lattice (formation of iron-oxide crystals) (d) SAED pattern, (110) plane (corresponds to magnetite particles).

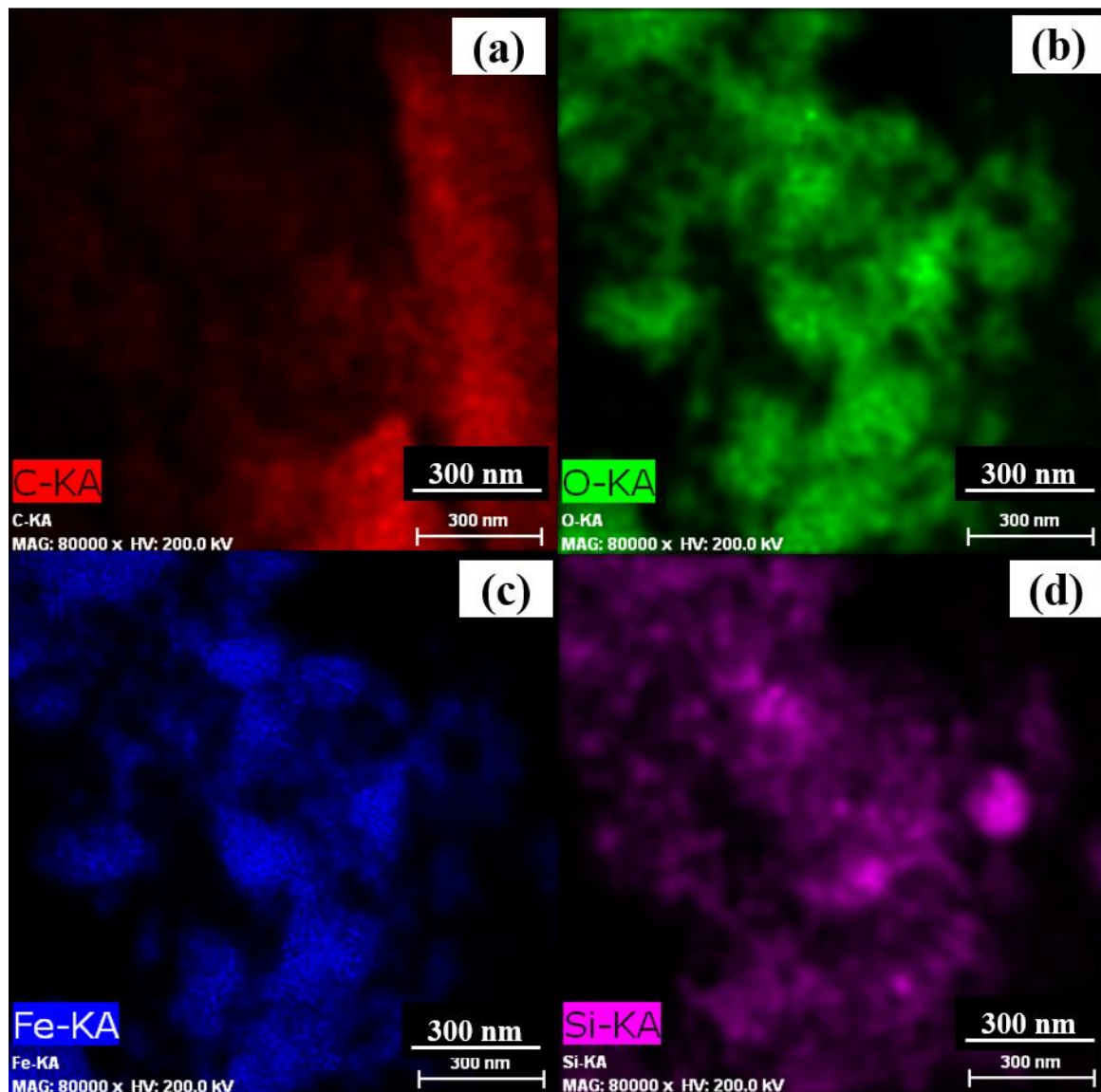


Figure 3.10. TEM elemental mapping of unloaded RHIOB. (a) C-deposits (red), (b) O-deposits (green), (c) Fe-deposits (blue) and (d) Si-deposits (violet).

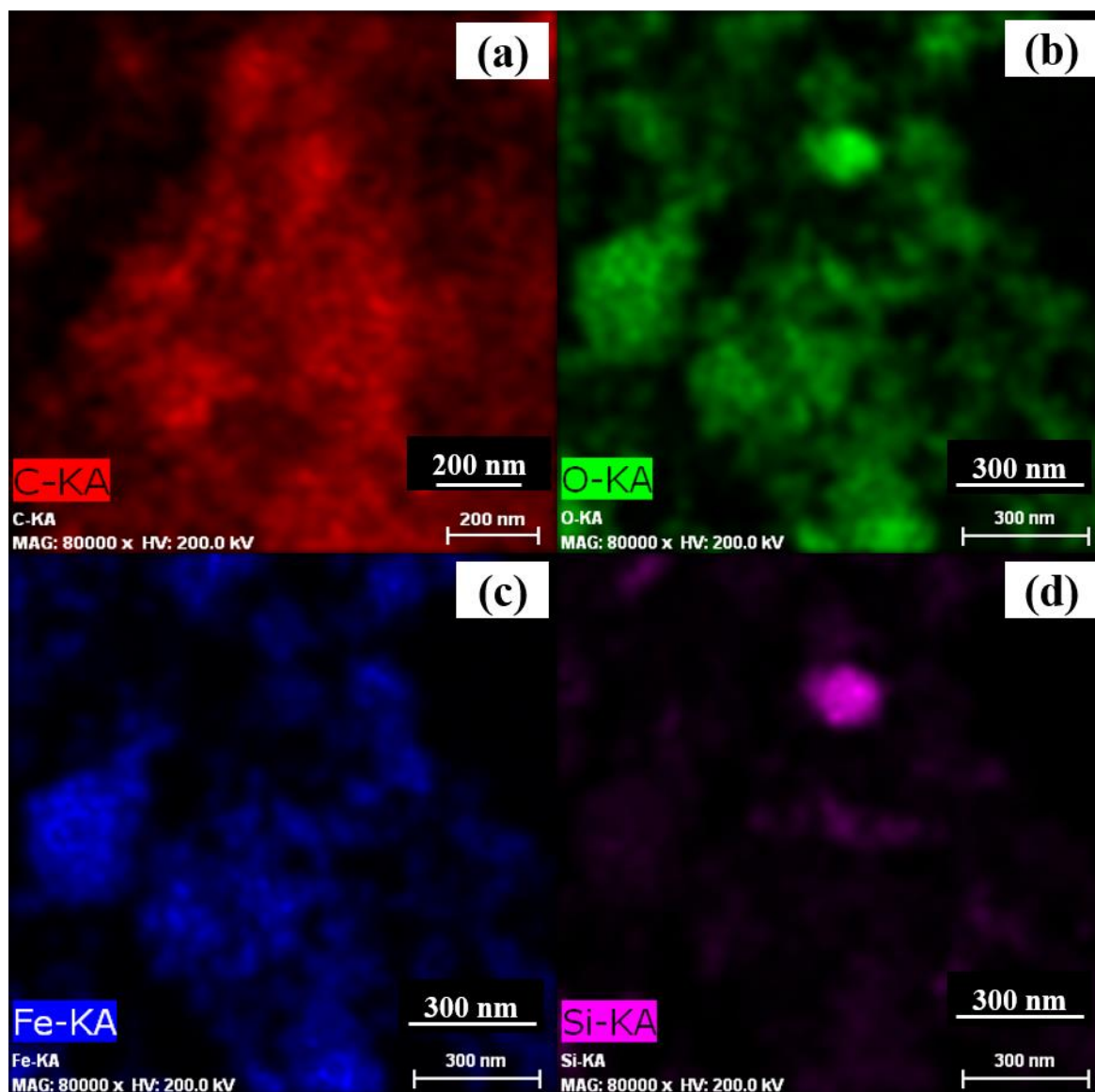


Figure 3.11. TEM elemental mapping of unloaded WHIOB. (a) C-deposits (red), (b) O-deposits (green), (c) Fe-deposits (blue) and (d) Si-deposits (violet).

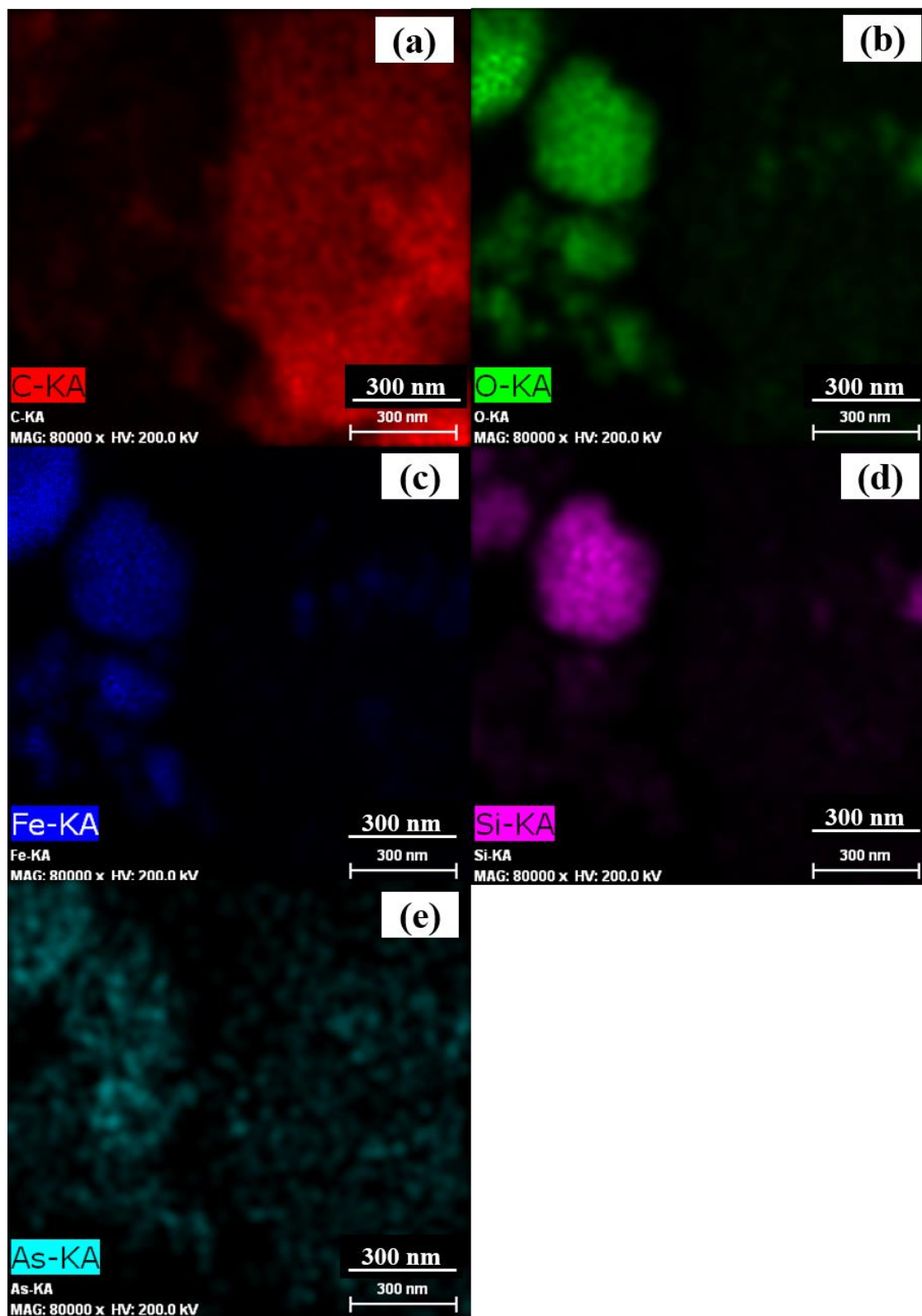


Figure 3.12. TEM elemental mapping of RHIOB after As adsorption. (a) C-deposits (red), (b) O-deposits (green), (c) Fe-deposits (blue), (d) Si-deposits (violet) and (e) As-deposits (light blue).

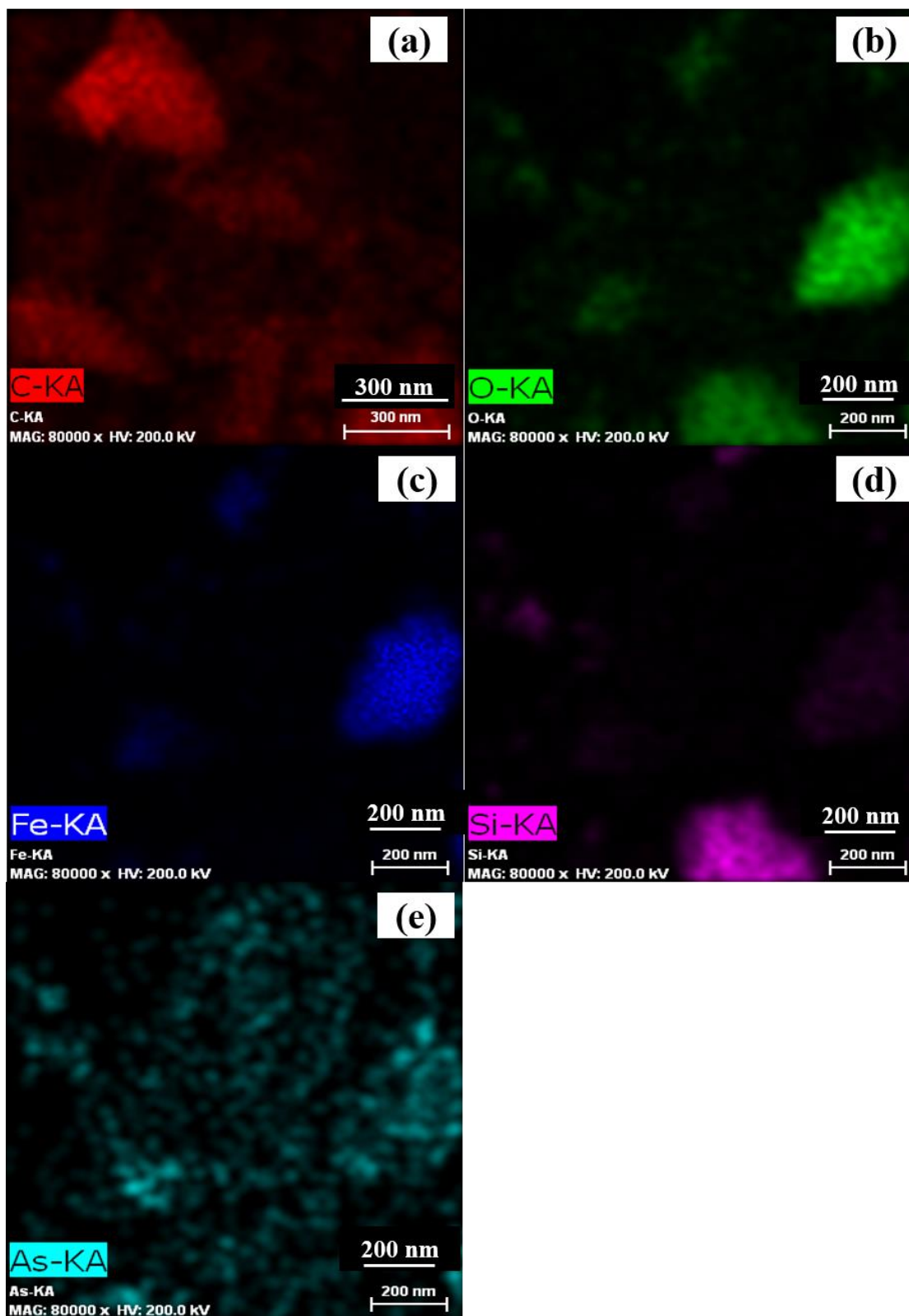


Figure 3.13. TEM elemental mapping of WHIOB after As adsorption. (a) C-deposits (red), (b) O-deposits (green), (c) Fe-deposits (blue), (d) Si-deposits (violet) and (e) As-deposits (light blue).

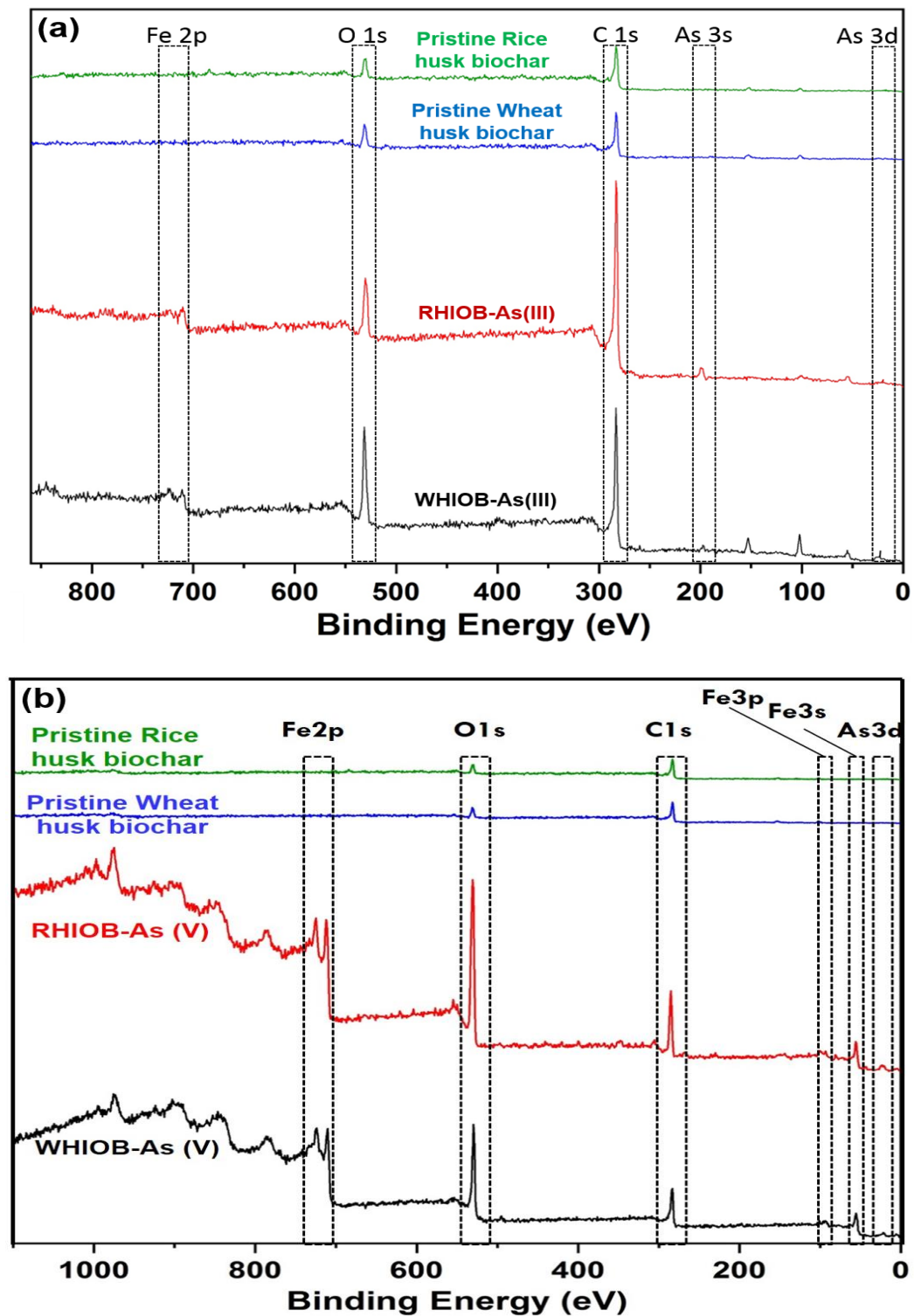


Figure 3.14. Comparative XPS wide scan spectrum of RHIOB and WHIOB (a) after As(III) and (b) As(V) loading in comparison to their respective pristine rice husk and wheat husk biochars.

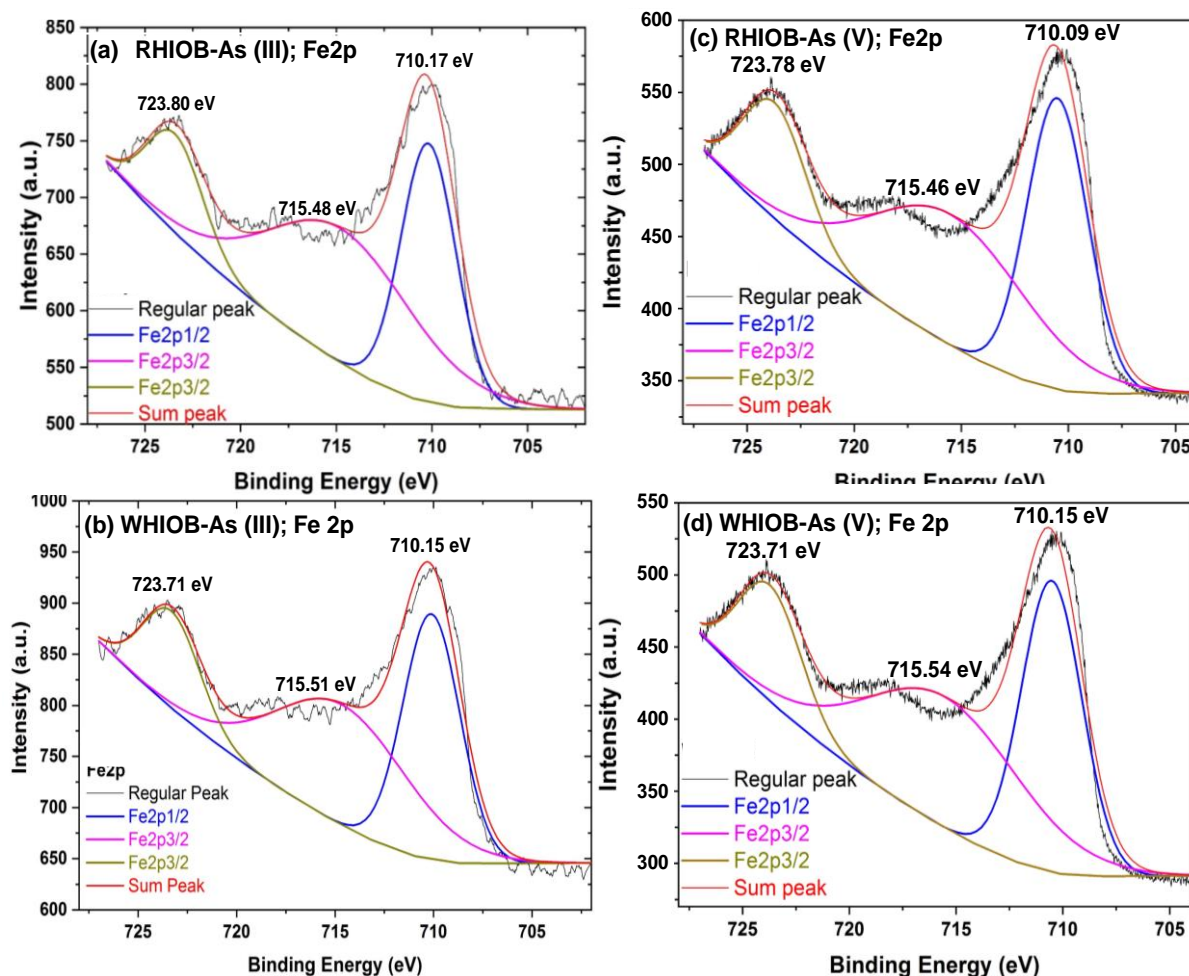


Figure 3.15. Comparative deconvoluted XPS spectra of Fe 2p_{3/2} (a) As(III) loaded RHIOB, (b) As(III) loaded WHIOB, (c) As(V) loaded RHIOB and (d) As(V) loaded WHIOB. (As loaded RHIOB = 2.0 g/L; As loaded WHIOB = 1.0 g/L, As (III/V) concentration = 100 µg/L, pH = 7.5 (As(III)), 5.5 (As(V)), equilibrium time = 24 h).

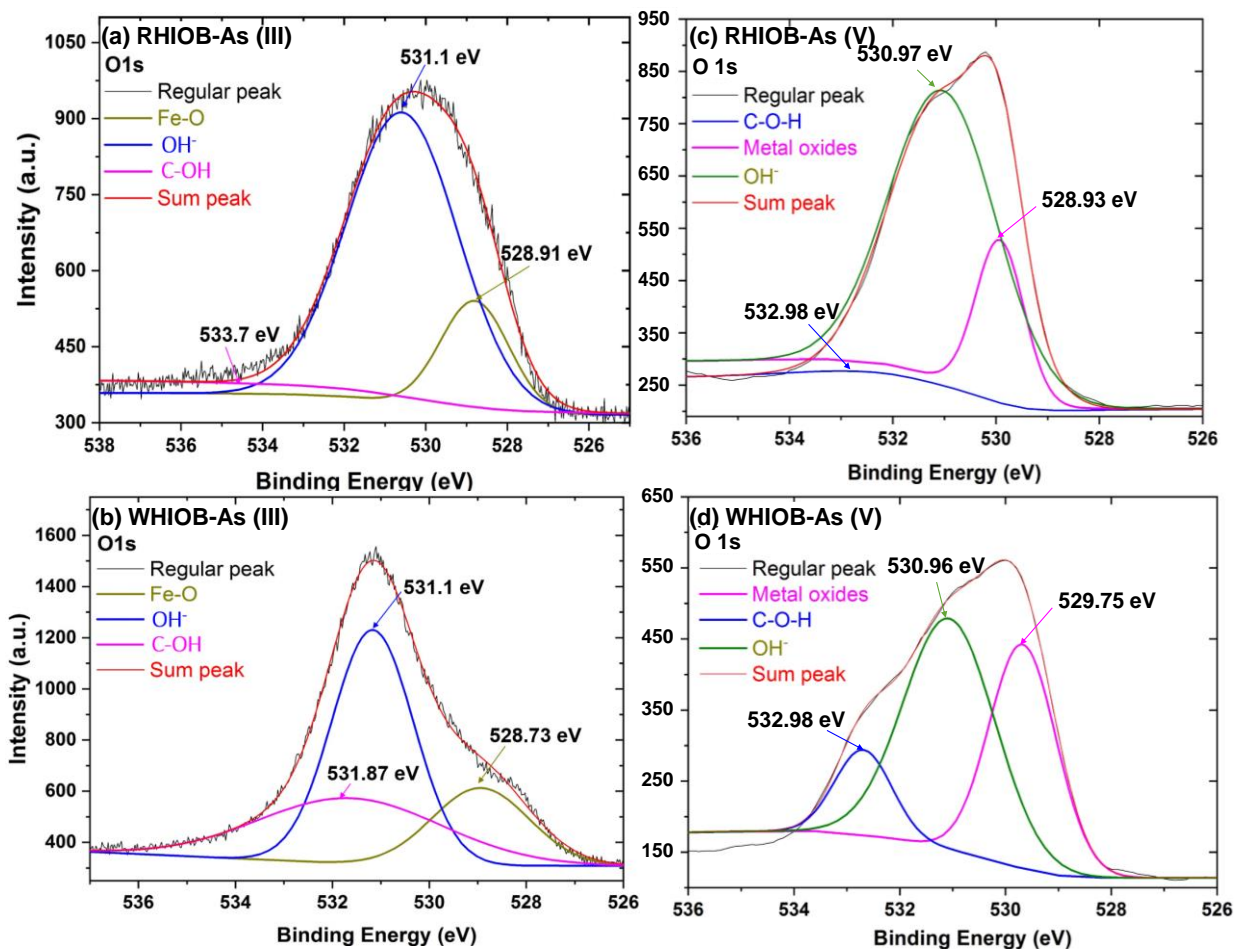


Figure 3.16. Comparative deconvoluted XPS spectra of O 1s (a) As(III) loaded RHIOB, (b) As(III) loaded WHIOB, (c) As(V) loaded RHIOB and (d) As(V) loaded WHIOB. (As loaded RHIOB = 2.0 g/L; As loaded WHIOB = 1.0 g/L, As (III/V) concentration = 100 μ g/L, pH = 7.5 (As(III)), 5.5 (As(V)), equilibrium time = 24 h).

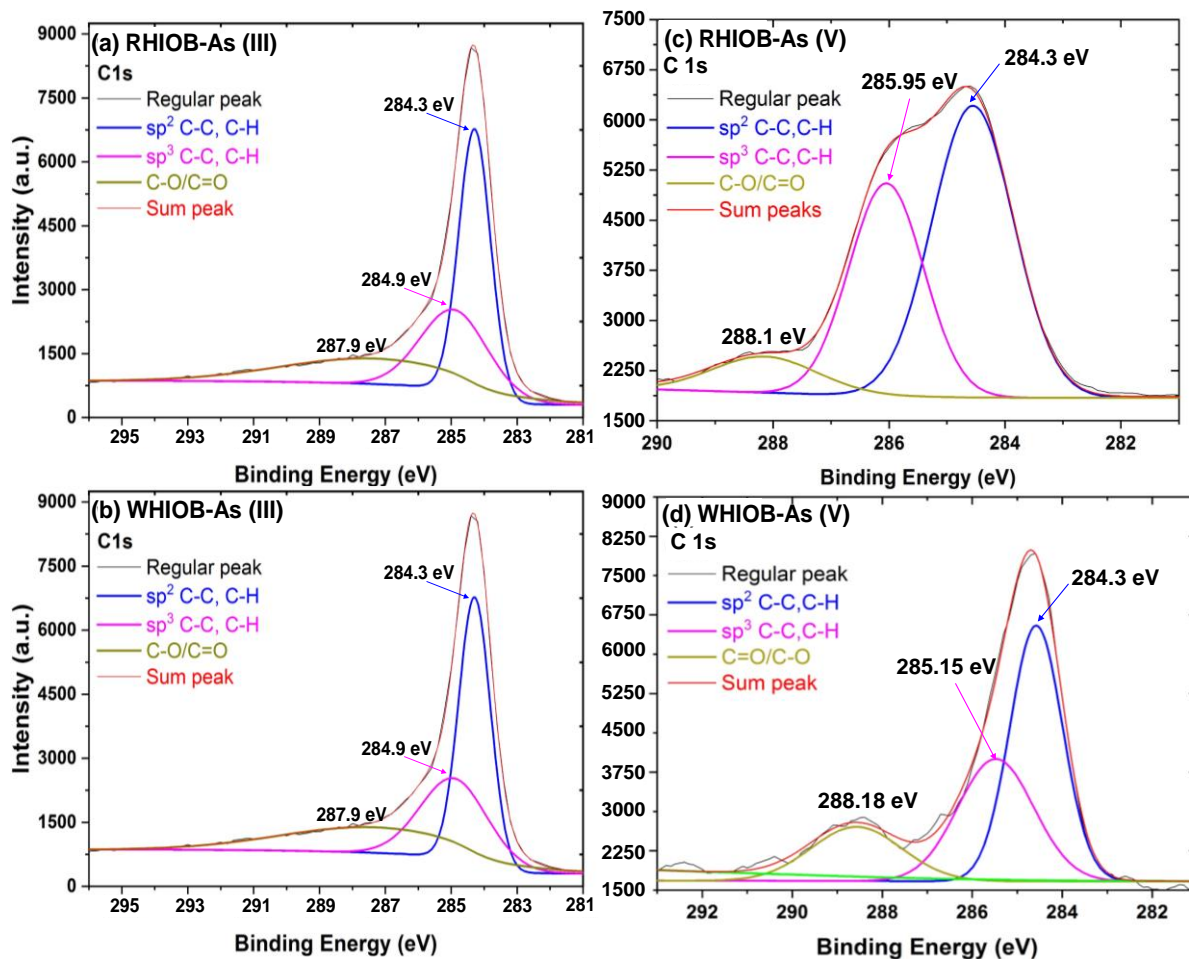


Figure 3.17. Comparative deconvoluted XPS spectra of C 1s (a) As(III) loaded RHIIOB, (b) As(III) loaded WHIIOB, (c) As(V) loaded RHIIOB and (d) As(V) loaded WHIIOB. (As loaded RHIIOB = 2.0 g/L; As loaded WHIIOB = 1.0 g/L, As (III/V) concentration = 100 μ g/L, pH = 7.5 (As(III)), 5.5 (As(V)), equilibrium time = 24 h).

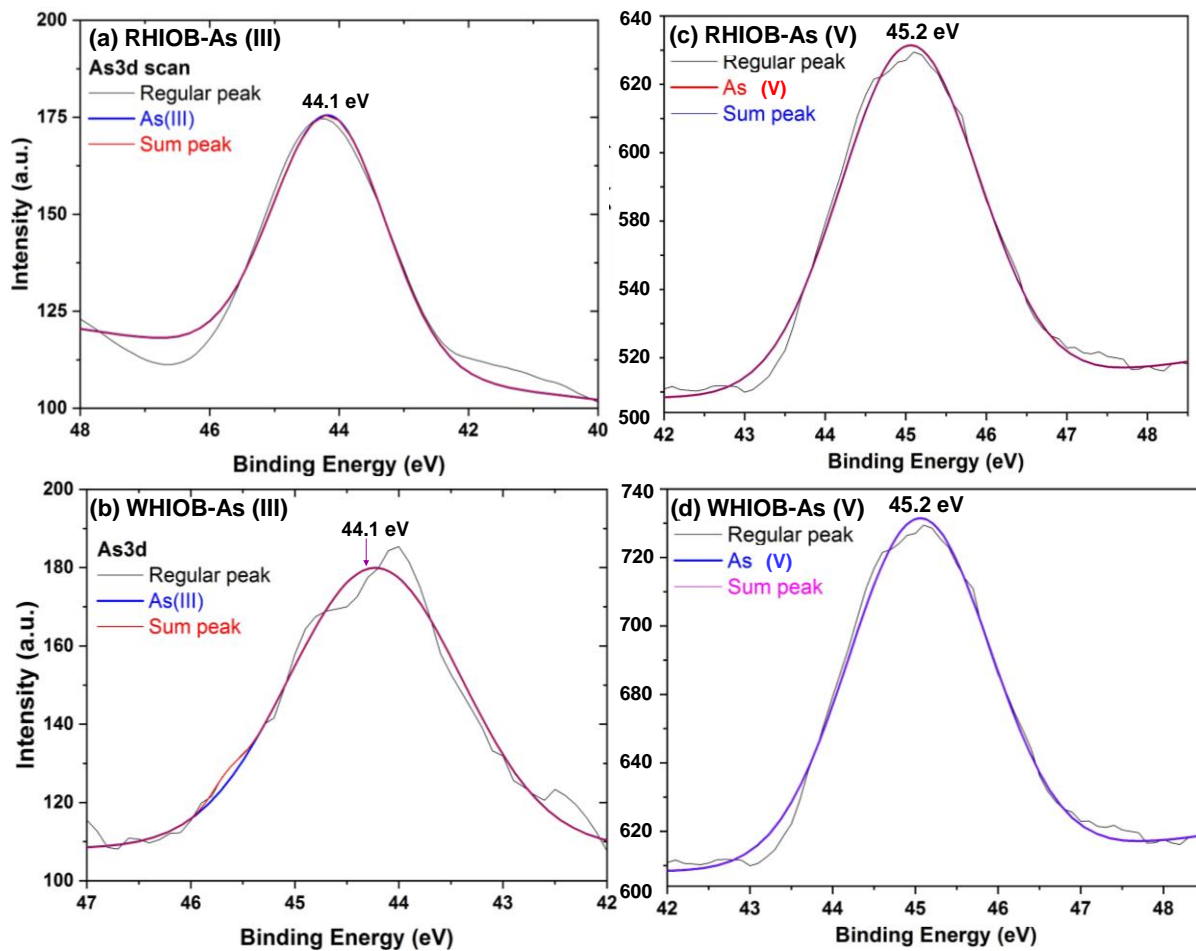


Figure 3.18. Comparative deconvoluted XPS spectra of As 3d (a) As(III) loaded RHI OB, (b) As(III) loaded WHI OB, (c) As(V) loaded RHI OB and (d) As(V) loaded WHI OB. (As loaded RHI OB = 2.0 g/L; As loaded WHI OB = 1.0 g/L, As (III/V) concentration = 100 μ g/L, pH = 7.5 (As(III)), 5.5 (As(V)), equilibrium time = 24 h).

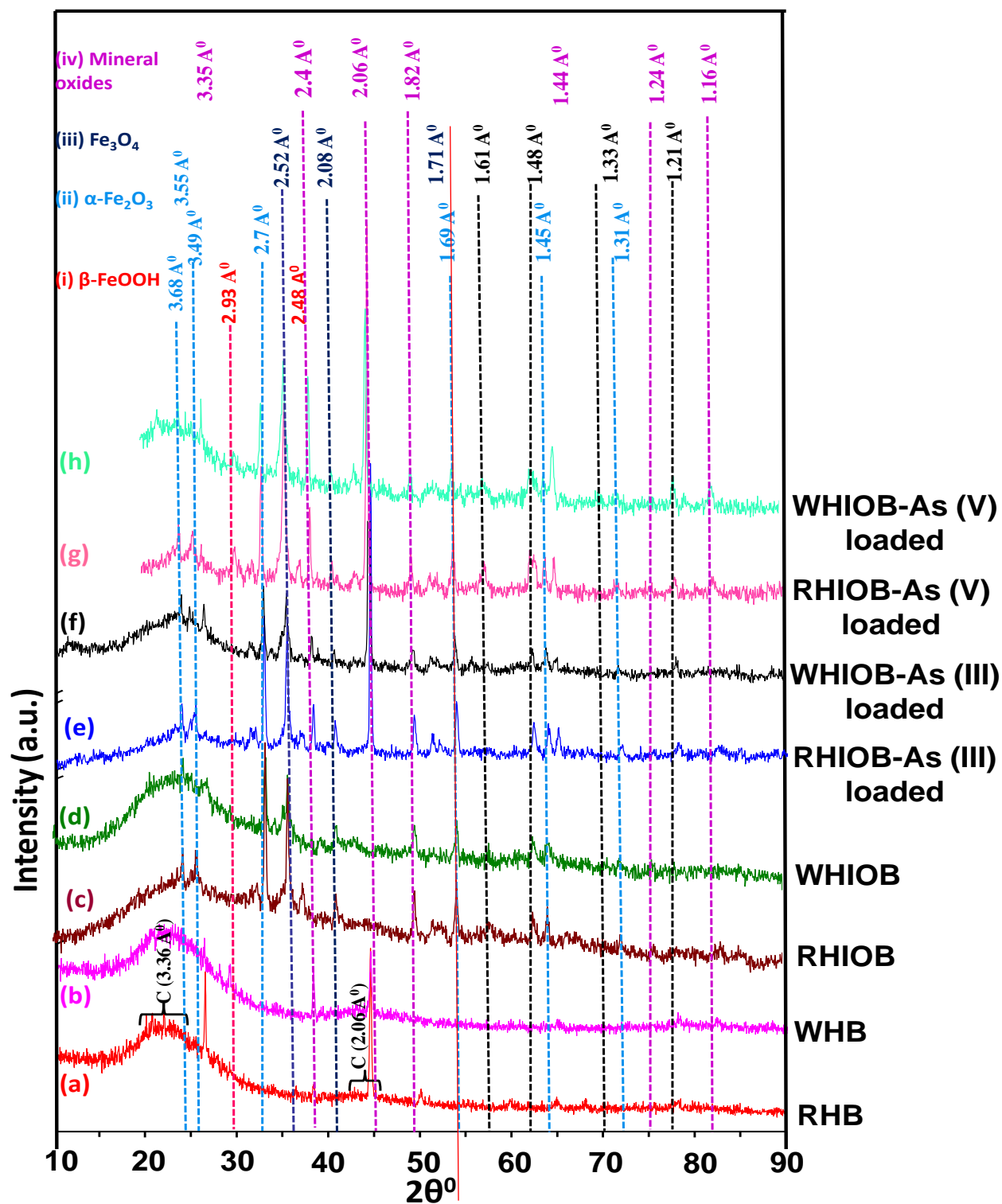


Figure 3.19. XRD spectra of (a) precursor RHB (rice husk biochar), (b) precursor WHB (wheat husk biochar), (c) RHI OB (rice husk iron-oxide biochar composite), (d) WHIOB (wheat husk iron-oxide biochar composite), (e) RHI OB-As(III) loaded, (f) WHIOB-As(III) loaded, (g) RHI OB-As(V) loaded and (h) WHIOB-As(V) loaded.

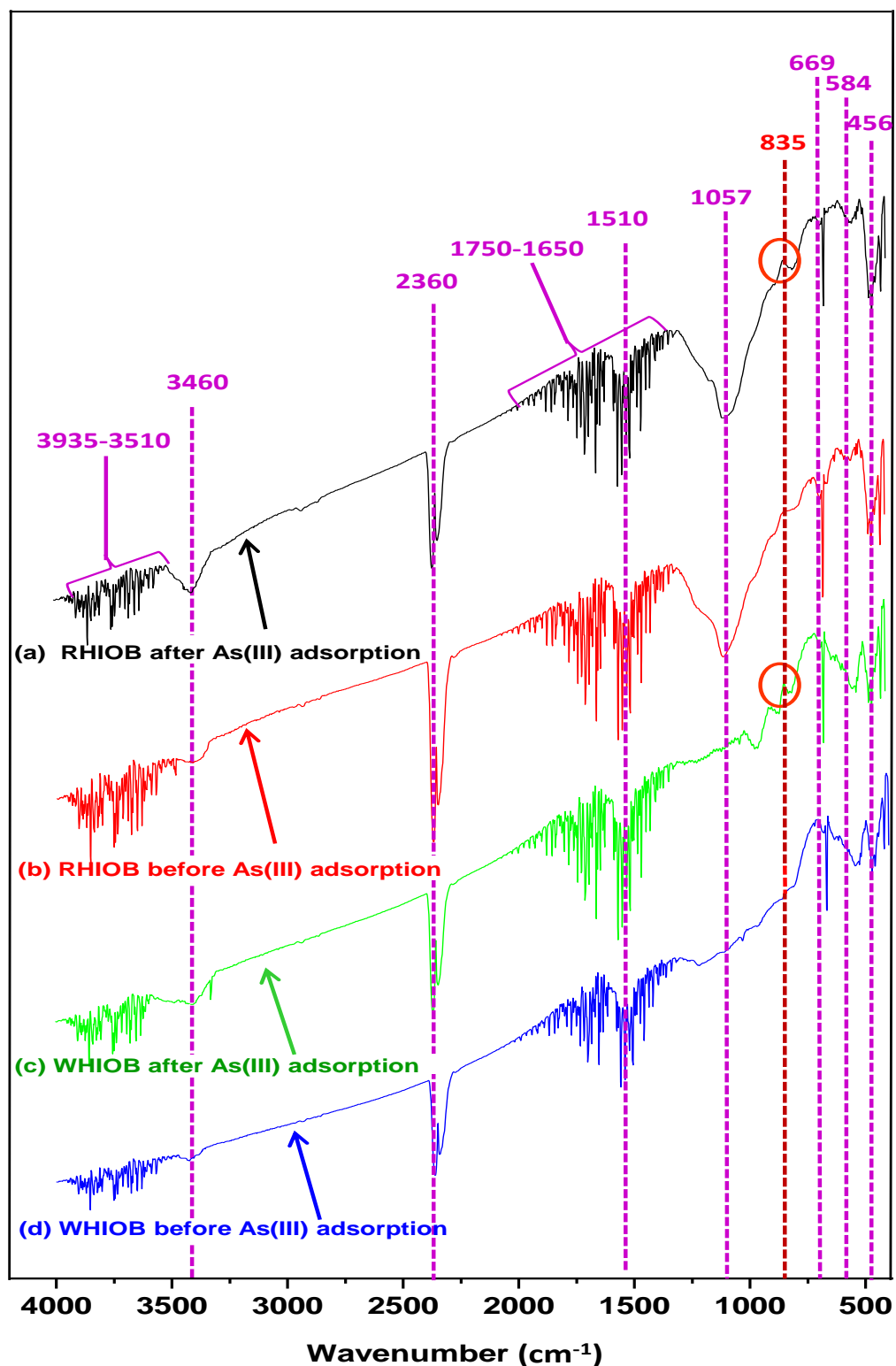


Figure 3.20. FT IR spectra of (a) RHIOB-As(III) loaded, (b) RHIOB, (c) WHIOB-As(III) loaded and (d) WHIOB. Red circle highlights the peak obtained in As(III) loaded RHIOB and WHIOB due to As-O bonding.

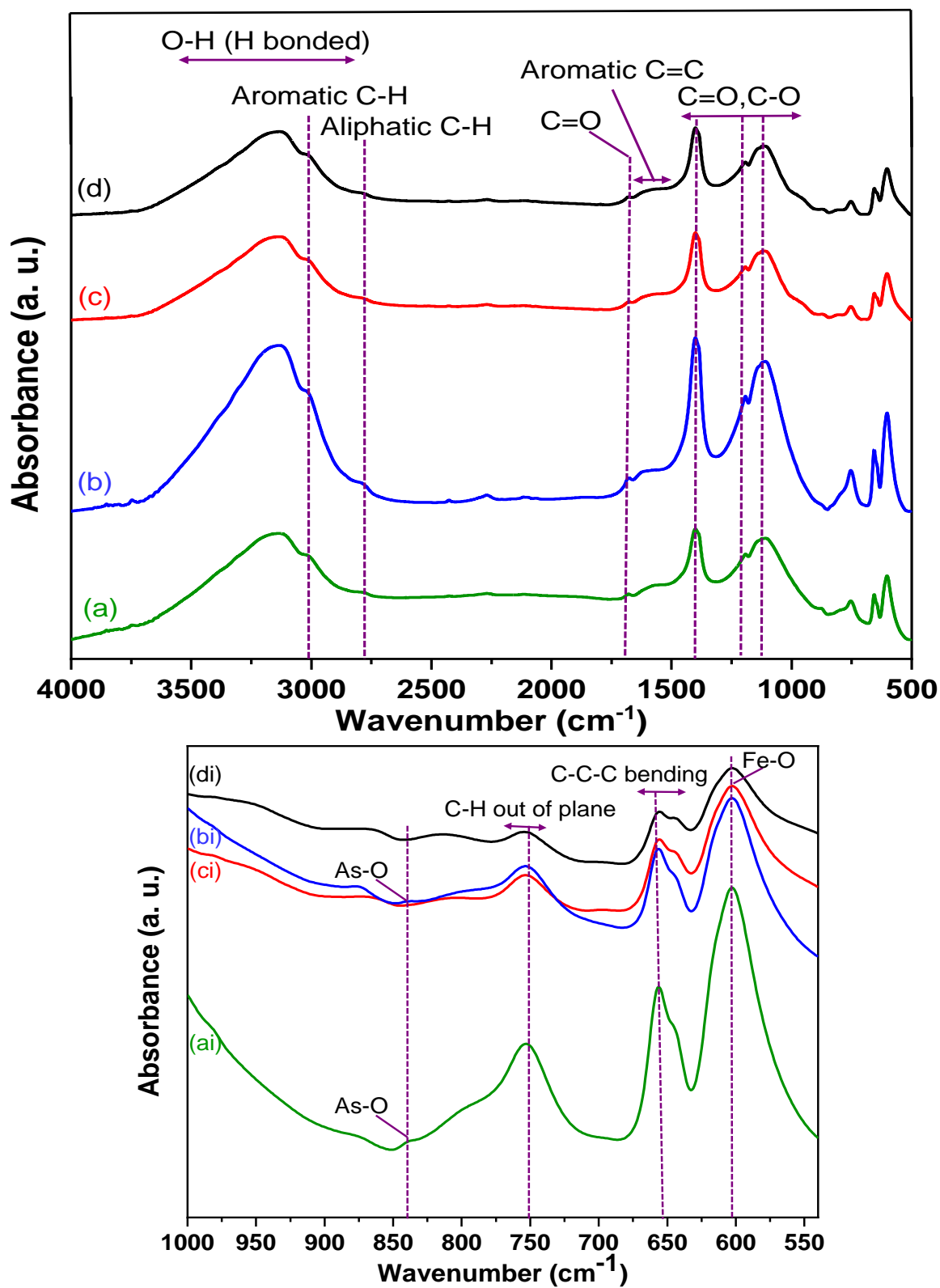


Figure 3.21. FT IR spectra of (a) RHIOB-As(V) loaded, (b) WHIOB-As(V) loaded, (c) RHIOB and (d) WHIOB. Inset shows the magnified region from 1000-550 cm^{-1} .

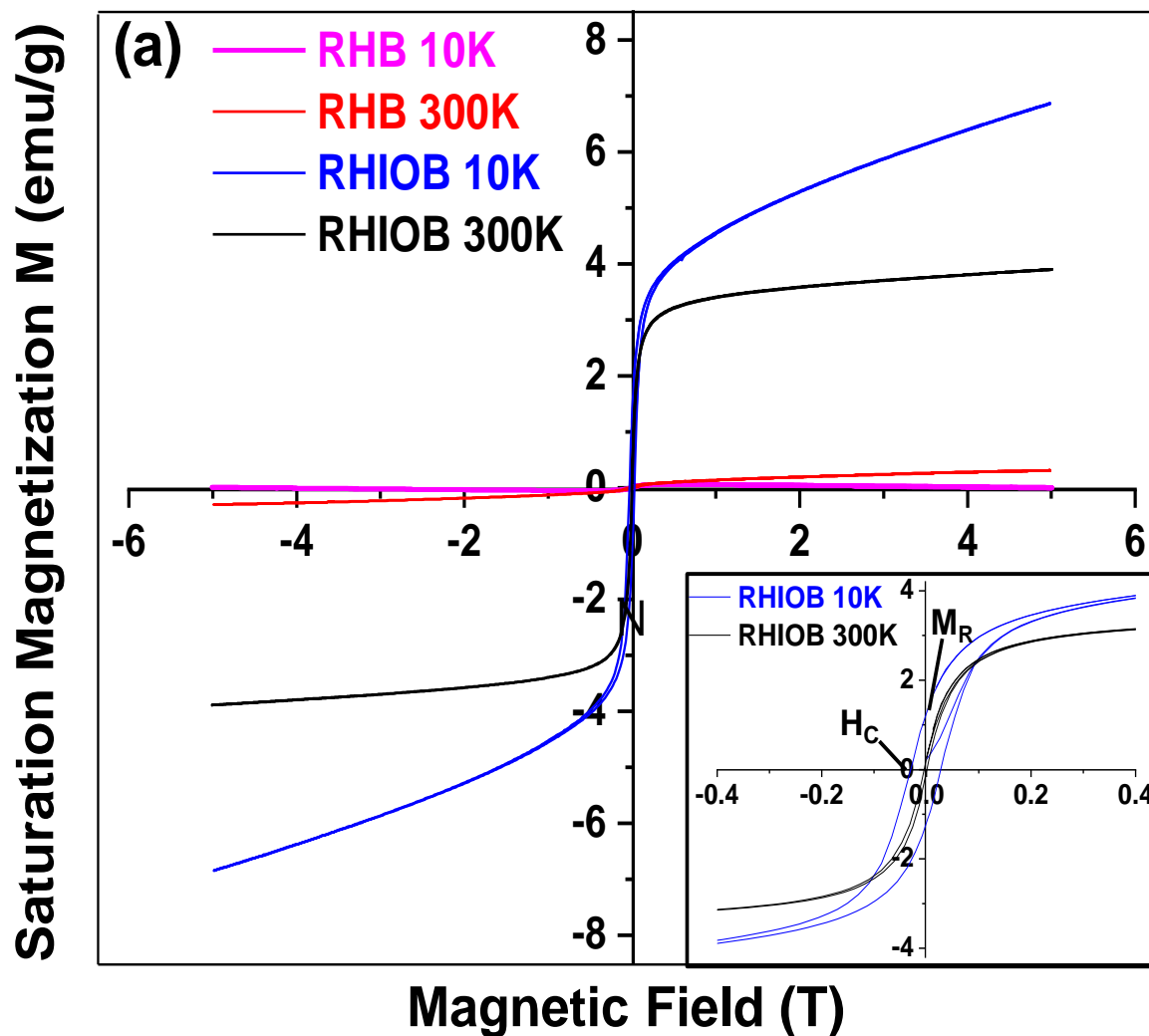


Figure 3.22. Saturation magnetization curves for (a) RHIOB and its precursor rice husk biochar RHB at 10 and 300 K. Inset shows magnified hysteresis loop for RHIOB and corresponding values of remanence, M_R and coercivity, H_c .

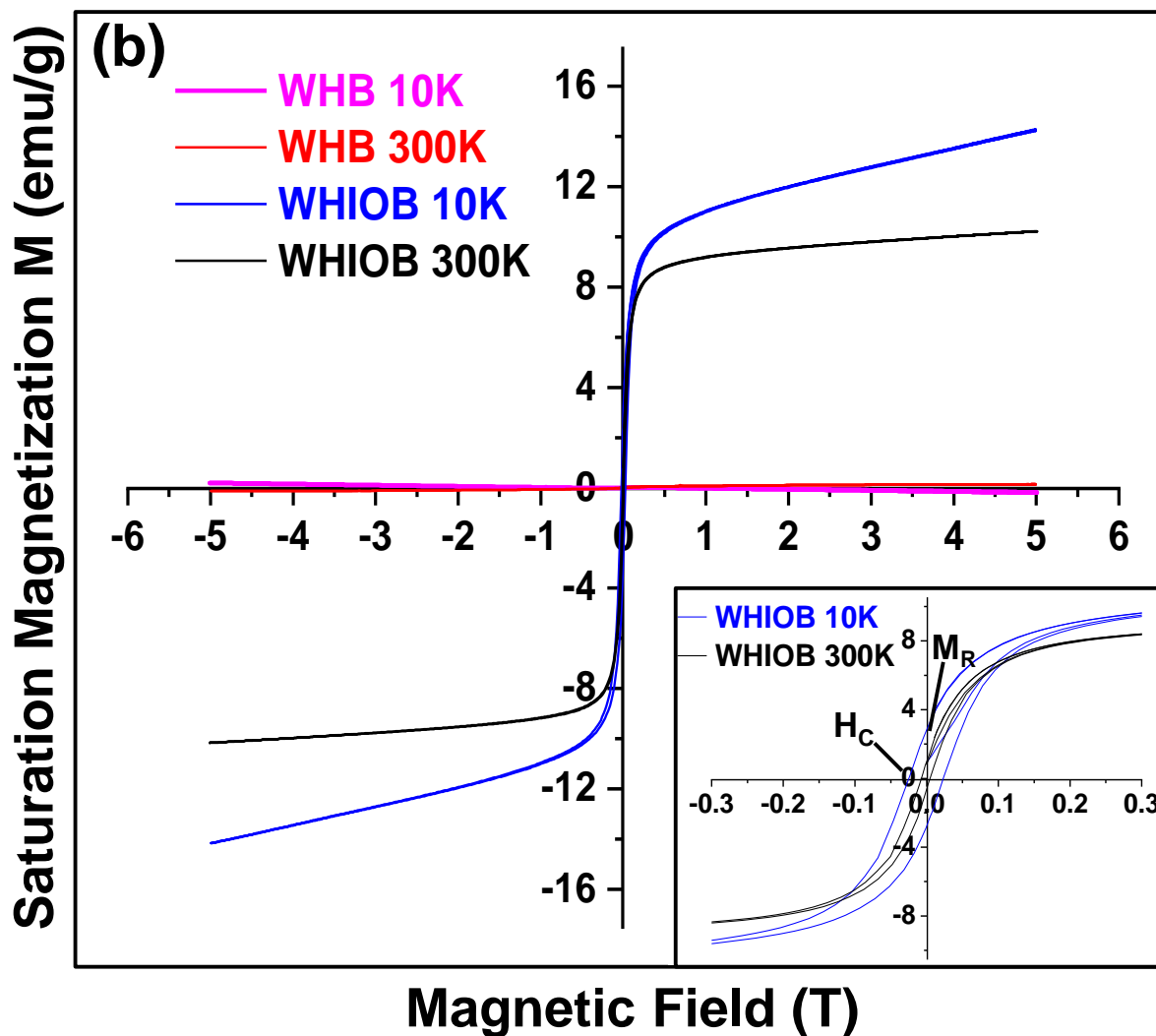


Figure 3.23. Saturation magnetization curves for (b) WHIOB and its precursor wheat husk biochar WHB at 10 and 300 K. Inset shows magnified hysteresis loop for WHIOB and corresponding values of remanence, M_R and coercivity, H_C .

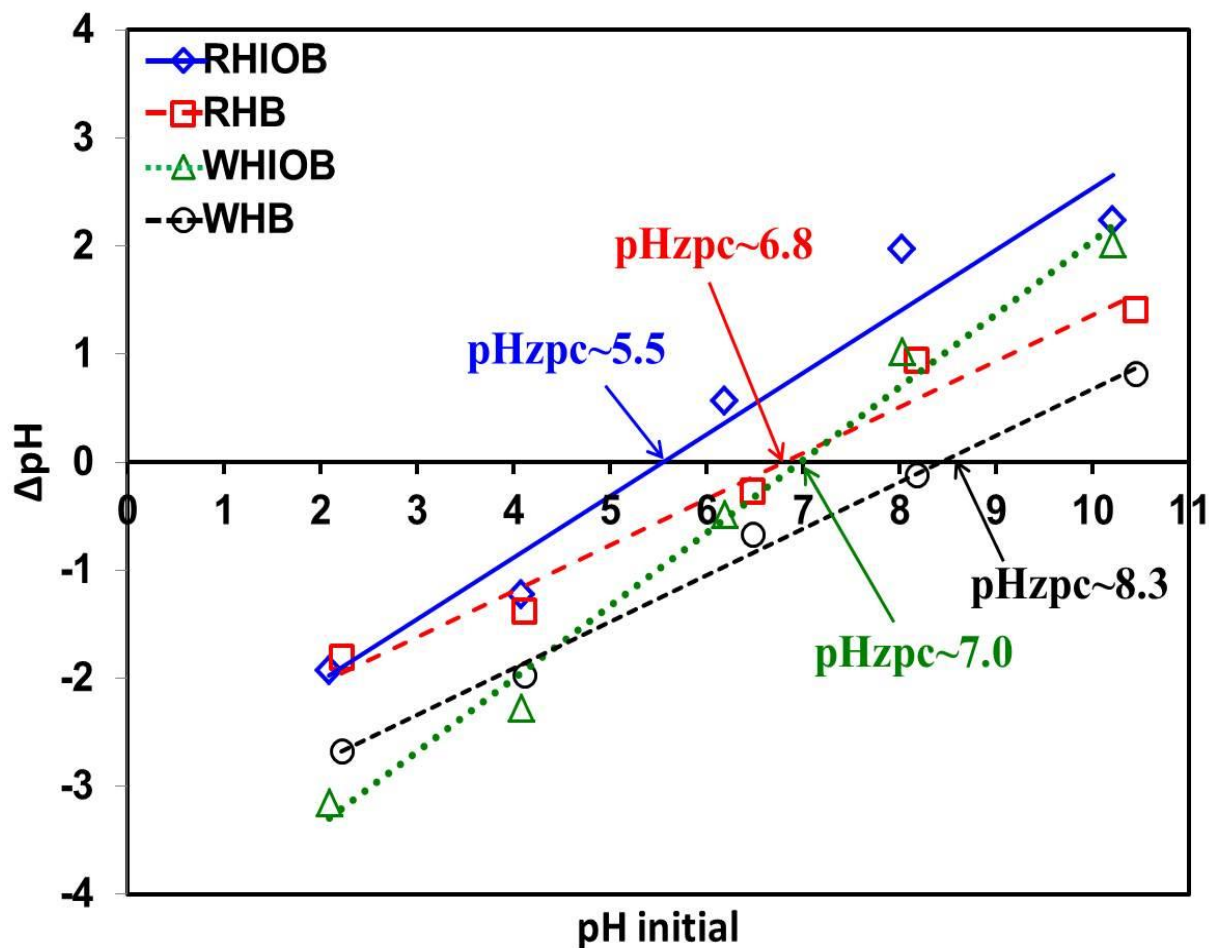


Figure 3.24. pHzpc (point of zero charge) for RHIOB and WHIOB and their respective RHB and WHB (0.025 g material in 0.01 M NaCl solution; pH= 2.0, 4.0, 6.0, 8.0, and 10.0; 25°C).

Table 3.1. Properties of slow pyrolysis rice husk iron -oxide (RHIOB) and wheat husk iron-oxide composite (WHIOB) biochars before and after As(III) and As(V) adsorption.

Properties	RHIOB before As adsorption	WHIOB before As adsorption	RHIOB As(III)- loaded	WHIOB As(III)- loaded	RHIOB As(V)- loaded	WHIOB As(V)- loaded
Ultimate						
C (%)	39.2	37.8	38.4	36.8	43.5	42.2
H (%)	1.23	1.2	1.21	1.19	1.3	1.16
N (%)	0.00	0.00	0.01	0.03	0.00	0.00
S (%)	0.23	0.54	0.22	0.14	0.69	0.26
O (%)*	10.79	13.72	6.68	11.33	7.1	10.93
Ash (%)	48.55	46.74	53.49	50.51	47.41	45.45
H/C ratio	0.37	0.38	0.32	0.39	0.36	0.33
O/C ratio	0.21	0.27	0.13	0.23	0.12	0.19
Quantitative analysis (%)						
Al	1.52	2.16	1.51	0.76	0.33	0.36
As	BDL	BDL	0.01	0.2	0.63	0.74
Ca	4.97	7.14	0.56	0.46	1.65	2.89
Cd	BDL	BDL	BDL	BDL	BDL	BDL
Co	BDL	BDL	BDL	BDL	BDL	BDL
Cr	0.01	0.04	0.04	0.16	0.03	0.04
Cu	0.03	0.03	0.01	0.02	0.05	0.03
Fe	16.02	19.03	15.92	19.23	17.06	20.07
K	0.42	1.25	0.15	0.05	0.5	0.36
Mg	1.14	1.78	0.1	0.18	0.36	0.47
Mn	0.33	0.41	0.16	0.13	0.08	0.1
Na	7.38	4.6	0.06	0.13	0.62	0.42
Ni	BDL	BDL	0.01	BDL	BDL	BDL
Pb	BDL	BDL	BDL	BDL	BDL	BDL
Si	64.37	60.96	61.27	58.34	59.04	57.65
Zn	0.08	0.12	0.03	0.02	0.08	0.01
Surface area characterization						
S _{BET} (m ² g ⁻¹)	300.0	339.0	295.0	330.0	290.0	301.0
External Surface Area (m ² g ⁻¹)	12.71	15.03	12.65	15.02	10.65	14.03
Dubinin-Radushkevich micropore volume, W ₀ (cm ³ g ⁻¹)	18.07	18.72	17.12	17.45	17.1	17.39
Average Pore Diameter (Å ⁰)	0.14	0.12	0.13	0.14	0.14	0.11

Table 3.2. XRD peaks and corresponding planes identified in RHIOB and WHIOB before As loading, after As(III) and As(V) loading.

2θ (°)		2θ (°)		Plane (h k l)	Spacing (Å)	JCPDS Card no.	Fe oxide(s)	Others	References
RHB	WHB	RHIOB/ RHIOB- As(III)/RH IOB-As(V)	WHIOB/ WHIOB- As(III)/WHI OB-As(V)						
		24.2		0 1 2	3.68	84-0310	α-Fe ₂ O ₃		(Zhong et al., 2017)
		25.5		1 1 0	3.49	84-0310	α-Fe ₂ O ₃		(W. Lei et al., 2017); (W. Cheng, Tang, Qi, Sheng, & Liu, 2010)
26.5		26.5		0 0 2	3.36	41-1487		graphitic-C	(Jin, Ge, Xu, Peterson, Jian, et al., 2017), (T. Chen, R. Liu, & N. Scott, 2016a)
26.7		26.7		1 0 0	3.35	46-1045		SiO ₂	(Y. Li et al., 2017)
		31.8		2 1 0	2.93	34-1266	β-FeOOH		(J. Yang et al., 2015), (G. Qiu, Gao, Hong, Tan, et al., 2017)
		33.1		1 0 4	2.70	84-0310	α-Fe ₂ O ₃		(Zhong et al., 2017)
		35.7		3 1 1	2.52	19-0629	Fe ₃ O ₄		(Baig et al., 2014a)
		37.1		2 1 -2	2.48	34-1266	β-FeOOH		(J. Yang et al., 2015), (G. Qiu, Gao, Hong, Tan, et al., 2017)
37.4		37.4		1 0 0	2.40	011-1160		CaO	(Madrid & Lanzón, 2017a)
		41.7		4 0 0	2.08	19-0629	Fe ₃ O ₄		(Baig et al., 2014a)
44.7		44.7		1 0 0	2.06	41-1487		graphitic-C	(Jin, Ge, Xu, Peterson, Jian, et al., 2017), (T. Chen et al., 2016a)
50.2		50.2		1 1 2	1.82	46-1045		SiO ₂	(Y. Li et al., 2017)
		53.4		4 2 2	1.71	19-0629	Fe ₃ O ₄		(Baig et al., 2014a)
		54.4		1 1 6	1.69	84-0310	α-Fe ₂ O ₃		(Zhong et al., 2017)
		57.1		5 1 1	1.61	19-0629	Fe ₃ O ₄		(Baig et al., 2014a)
		62.5		4 4 0	1.48	19-0629	Fe ₃ O ₄		(Baig et al., 2014a)

Development and characterization of rice husk and wheat husk iron-oxide biochar

	64.0	3 0 0	1.45	84-0310	α -Fe ₂ O ₃		(Zhong et al., 2017)
64.9	64.9	0 0 2	1.44	44-0141		α -MnO ₂	(Jin, Ge, Xu, Peterson, Jian, et al., 2017)
68.1		2 0 3	1.37	46-1045		SiO ₂	(Y. Li et al., 2017)
	70.9	6 2 0	1.33	19-0629	Fe ₃ O ₄		(Baig et al., 2014a)
	72.3	1 1 9	1.31	84-0310	α -Fe ₂ O ₃		(Zhong et al., 2017)
76.6	76.6	4 2 0	1.24	05-0586		CaCO ₃	(Xingzhu Ma et al., 2016)
	78.9	4 4 4	1.21	19-0629	Fe ₃ O ₄		(Baig et al., 2014a)
83.2		2 1 2	1.16	44-0141		α -MnO ₂	(Jin, Ge, Xu, Peterson, Jian, et al., 2017)

Table 3.3. FT IR adsorption bands observed in RHIOB, WHIOB and As(III) and As(V)-loaded RHIOB and WHIOB.

S. No	Peak (cm ⁻¹)	Functional group		References
1.	3200-3500	O-H	Stretching vibration due to hydrogen bond	(K. Sharma et al., 2004; Keiluweit et al., 2010; Kloss et al., 2012)
2.	3010	C-H	Stretching vibration due to aromatic C-H	(K. Sharma et al., 2004; Keiluweit et al., 2010; Kloss et al., 2012)
3.	2787	C-H	Stretching vibration due to heat resistive aliphatic C-H	(K. Sharma et al., 2004; Keiluweit et al., 2010; Kloss et al., 2012)
4.	1680	C=O	Stretching vibration due to ketones, anhydrides, esters and carboxylic C	(K. Sharma et al., 2004; Keiluweit et al., 2010; Kloss et al., 2012)
5.	1578	C=C	Stretching due to aromatic C	(K. Sharma et al., 2004; Keiluweit et al., 2010; Kloss et al., 2012)
6.	1440	C=O	Stretching vibration from ketones in ligneous products	(K. Sharma et al., 2004; Keiluweit et al., 2010; Kloss et al., 2012)
7.	1270	C-O	Stretching vibration due to undecomposed lignin and cellulosic part (pyranone rings and guaiacyl monomers)	(K. Sharma et al., 2004; Keiluweit et al., 2010; Kloss et al., 2012)
8.	1114	C-OH	Bending vibration in phenols/metal hydroxyl species	(K. Sharma et al., 2004; Keiluweit et al., 2010; Kloss et al., 2012)
9.	830-825	As-O	As-O bonded to Fe (metal)	(P. Gallios et al., 2017)
10.	803-755	C-H	Vibration out of plane due to deformation of aromatic C-H	(Keiluweit et al., 2010)
11.	667	C-C-C	Angle bending vibration	(Keiluweit et al., 2010)
12.	601	Fe-O	Stretching vibrations of Fe-O bond in tetrahedral site	(W. Lei et al., 2017; P. Gallios et al., 2017)
13.	456	Fe-O	Stretching vibrations of Fe-O bond in octahedral site	(W. Lei et al., 2017; P. Gallios et al., 2017)

Table 3.4. Saturation magnetization of RHIOB, WHIOB and their precursor rice husk (RHB) and wheat husk biochars (WHB). From hysteresis, values of remanence and coercivity reported for RHIOB and WHIOB.

S. No	Adsorbent	RHB		WHB		RHIOB		WHIOB	
		10K	300K	10K	300K	10K	300K	10K	300K
1.	Saturation magnetization (emu/g)	0.00	-	0.00	-	6.5	5.5	13.5	8.0
2.	Remanence, M_R	-	-	-	-	± 1.5	-	± 3.0	-
3.	Coercivity, H_c	-	-	-	-	± 0.03	-	± 0.025	-

Table 3.5. pH_{zpc} (zero point charge) of RHIOB, WHIOB and their precursor their precursor rice husk (RHB) and wheat husk biochars (WHB).

S.No.	Adsorbent	pH_{zpc}
1.	RHB	6.8
2.	WHB	8.3
3.	RHIOB	5.5
4.	WHIOB	7.0

CHAPTER 4

ARSENITE [As(III)] ADSORPTION ON RICE HUSK IRON-OXIDE (RHIOB) AND WHEAT HUSK IRON-OXIDE BIOCHAR (WHIOB) COMPOSITES

Sorption studies were conducted at various initial pHs, adsorbent-adsorbate doses, concentrations, temperatures and time intervals to optimize the As(III) sorption process. Mechanism of adsorption of As(III) over RHIOB and WHIOB was optimized and established through batch sorption studies discussed in chapter 6.

4.1. Effect of initial pH

The As(III) speciation [Figure 6.2, (a)] and surface charge experienced by the adsorbate species are greatly affected by solution pH. (Rajput et al., 2016; X. Song, Li, Geng, Zhou, & Ji, 2017) H_3AsO_3 greatly predominates until pH 8.0 and constitutes above half of the As(III) in solution at pH 9.2 with H_2AsO_3^- the other half. HAsO_3^{2-} appears as pH exceeds 11 and reaches a maximum at pH ~12.8. The effect of pH from 2.0 to 10.0 was investigated for As(III) adsorption on RHIOB, WHIOB, RHB and WHB at an initial As(III) concentration of 100 $\mu\text{g/L}$ and adsorbent dose of 2.0 g/L [Figure 4.1]. Over this pH range, only H_3AsO_3 needs to be considered up to somewhat above pH 7.0 and beyond that both H_3AsO_3 and H_2AsO_3^- could adsorb. High As(III) removal occurred over this entire pH range with WHIOB (~97%) and RHIOB (~85%) [Figure 4.1] versus modest removal with WHB (~20%) and RHB (~12%) at their highest points [Figure 4.1]. Thus, iron oxide surfaces adsorb most of the As(III) in WHIOB and RHIOB whereas RHB and WHB only can uptake As(III) on the biochar and its surface mineral ash contents. WHIOB removed more As(III) than RHIOB over the entire pH range [Figure 4.1], most likely because of its higher Fe_3O_4 loading (23.8 wt% in WHIOB versus 18.2 wt% in RHIOB). The higher WHIOB Fe_3O_4 loading provides more surface area for adsorption. As(III) adsorption efficiency increased as pH rose from 2.0 to 7.0 and then dropped somewhat. However, substantial adsorption occurred over the entire pH range. Equilibrium pH values were also recorded [shown in Figure 4.1] and rose for WHIOB, RHIOB, WHB and RHB in the pH range from 3.0 to 4.0 [Figure 4.1]. A very small equilibrium pH rise occurred for WHIOB and RHIOB in the pH range of 4.0-8.0. At high pH (>8.0), the equilibrium pH values using RHIOB and WHIOB increased to ~5.0 [Figure 4.1]. Further kinetic and equilibrium experiments were conducted in pH range 6.5-7.5.

4.1.1. Adsorption mechanism: pH and pH_{zpc}

Figure 4.2 shows percent removal of As(III) over RHB, WHB, RHIOB and WHIOB with respect to initial pH, pH_{zpc} and fractional composition of As(III) speciation. The pH_{zpc} of RHB, WHB, RHIOB and WHIOB are ~6.8, ~8.3, ~5.5 and ~7.0 respectively [Figure 4.2]. High pH of RHB and WHB without any iron-oxide deposition is attributed to the oxides/hydroxides due to Ca, Mg, Na and K etc. (Zimmerman & Gao, 2013). pH_{zpc} of natural magnetite is 6.5 (Milonjic, M. Kopečni, & E. Ilić, 1983) to 7.4 (Rajput et al., 2016). Fall in pH_{zpc} in RHIOB and WHIOB is due to the formation of the magnetite surfaces. At $pH < pH_{zpc}$ for magnetite, iron-oxide gets protonated to $-FeOH_2^+$, $Fe-OH^+-Fe$ (Cornell & Schwertmann, 2003). The neutral species of As(III) (H_3AsO_3) close to this pH (~6.5-7.5) gets adsorbed over protonated surface of magnetite (iron-oxide) at $pH < pH_{zpc}$, causing removal. Detailed mechanism of the adsorption of As(III) on RHIOB and WHIOB is discussed in chapter 6.

4.2. As(III) adsorption kinetics and modelling

As(III) adsorption studies were conducted at 0.5, 1.0 and 2.0 g/L RHIOB and WHIOB doses [Figure 4.3] and 50, 100 and 200 μ g/L As(III) solution concentrations [Figure 4.4].

4.2.1 Effect of adsorbent dose on As(III) percent removal:

Sorption was enhanced by increasing adsorbent dosages. As the adsorbent dosage were increased from 0.5 g/L to 1.0 g/L percent removal of As(III) increased from ~40% to ~60% on RHIOB (figure 4.3 (A)). Percent removal further increased from ~60% to ~80% as the dosage increased from 1.0 g/L to 2.0 g/L (figure 4.3 (A)). This is due to the increase in the availability of the sites that increased the As(III) adsorption. Similarly, with the increase in adsorbent dosage for WHIOB from 0.5 g/L to 1.0 g/L percent removal of As(III) increased from ~60% to ~85% (figure 4.3 (B)). However, unlike RHIOB percent removal of As(III) on WHIOB did not increased as the dosage increased from 1.0 g/L to 2.0 g/L. Thus, increase in adsorbent dosage increased the sites for adsorption of As(III). 2.0 g/L dose of RHIOB and 1.0 g/L of dose of WHIOB were taken to conduct the studies.

Maximum percent removal of As(III) was achieved in 12h. After this, significant removal of As(III) on RHIOB and WHIOB was not observed.

4.2.2 Effect of As(III) initial concentration on its adsorption capacity:

Results of the effect of initial concentration of As(III) on its removal capacity on RHIOB and WHIOB are shown in figure 4.4 (A) and (B). There was significant increase in the adsorption capacity from $\sim 20 \mu\text{g/g}$, $\sim 39 \mu\text{g/g}$ to $\sim 53 \mu\text{g/g}$ [Figure 4.4 (A)] as the initial concentration of As(III) increased from $50 \mu\text{g/L}$, $100 \mu\text{g/L}$ to $200 \mu\text{g/L}$ on RHIOB. Similarly, adsorption capacity of As(III) increased from $\sim 30 \mu\text{g/g}$, $\sim 53 \mu\text{g/g}$ to $\sim 57.5 \mu\text{g/g}$ [Figure 4.4 (B)] as the concentration rose from $50 \mu\text{g/L}$, $100 \mu\text{g/L}$ to $200 \mu\text{g/L}$ on WHIOB. Increase in the removal capacities with increasing initial concentrations is attributed to the availability of greater As(III) molecules per gram of adsorbent (Padmavathy, Madhu, & Haseena, 2016). Moreover, a gradient of chemical potential gets developed between adsorbent sites and As(III) molecules that created a driving force for the movement of molecules towards adsorbent sites. This driving force gets increased as the concentration of As(III) solution increased, unless reaching a point of saturation where all the sites are occupied over adsorbent surface and no further adsorption takes place (Padmavathy et al., 2016; Rahmi & Lelifajri, 2017).

4.2.3 Kinetic modelling:

Sorption kinetics data were fitted to both pseudo-first-order [Table 2.1, 1] and pseudo-second-order [Table 2.1, 1] rate equations (Ho & McKay, 1999a). The first order linear fitting plots over different adsorbent dosage and As(III) initial concentrations are shown in Figure 4.5-and Figure 4.6, respectively. Parameters for first order linear plots are given in Table 4.1. Similarly, the second order linear and non-linear fitting plots over different adsorbent dosage and As(III) initial concentrations are shown in Figures 4.7-4.8 and Figures 4.10-4.11, respectively. Parameters are calculated and summarised in Table 4.2. The pseudo-second-order linear equation best described As(III) sorption on RHIOB and WHIOB [Figures 4.7-4.8; Table 4.2]. The experimental linear pseudo-second order q_e values also agreed with the calculated q_e values, and the linear pseudo-second order R^2 values were excellent [Table 4.2]. Second order kinetics is consistent with rate-

determining As(III) chemisorption over magnetite surface sites. (Rajput et al., 2016) As(III) uptake at different adsorbent dosages was higher on WHIOB than RHIOB (Table 4.2) due to WHIOB's higher iron loading (Table 3.1). As As(III) concentrations rise, the time-dependent adsorption efficiencies for RHIOB and WHIOB also rose.

Adsorption half-life, $t_{1/2}$, is the time when the reactant concentration decreases by half i.e. 50% of total adsorption. (Mohan, Singh, Sarswat, Steele, Pitmann, et al., 2015) The $t_{1/2}$ values for As(III) adsorption on RHIOB and WHIOB at different initial adsorbent dosages and concentrations are listed in Table 4.2. The As(III) adsorption half-life values obtained for RHIOB and WHIOB dropped as adsorbent dosages rose (from 0.5 g/L to 2.0 g/L). Half-life, $t_{1/2}$ values increased with a rise in As(III) concentrations (50-200 $\mu\text{g/L}$) for RHIOB and WHIOB [Table 4.2].

Rate-determining step identification during adsorption is crucial for interpreting sorption/ion exchange kinetics, (Mohan, Singh, Sinha, & Gosh, 2004) aiding material selection and system design (R. M. C. Viegas, M. Campinas, H. Costa, & M. J. Rosa, 2014) Rate depends on external or internal or both types of diffusion. Adsorption generally occurs in three steps including film diffusion, particle diffusion and exterior surface diffusion (Mohan et al., 2004). Adsorption on the exterior surface is very rapid and cannot be considered as a rate determining step. (Mohan & Singh, 2002) Therefore, either film or particle diffusion is rate controlling. Kinetic data were analysed according to Boyd (Boyd, Adamson, Myers, & Jr., 1947) and Reichenberg (Reichenberg, 1953b) to differentiate between the particle and film diffusion using the equations 5-7 and table 2.1 mentioned in chapter 2.

Bt values were obtained for each F value from Reichenberg's table (Reichenberg, 1953b) at different concentrations. Bt versus time plots for RHIOB and WHIOB at different As(III) concentrations were constructed [Figure SM7(a, b)]. RHIOB and WHIOB gave linear plots at all the concentrations. However, at lower As(III) concentration (50 $\mu\text{g/L}$) the linear Bt versus time plot does not pass through origin. Thus, particle diffusion is the rate limiting step. However, at higher

concentrations (100 and 200 $\mu\text{g/L}$) the Bt versus. time lines pass through origin. Therefore, film diffusion is the rate limiting step at these As(III) concentrations. Effective diffusion coefficients were calculated from Bt versus time plots using equations given summarised in Table 2.1, (3). D_i values of RHIOB and WHIOB rose as As(III) concentration increased from 50 $\mu\text{g/L}$ to 100 $\mu\text{g/L}$ and then fell with a further concentration rise from 100 to 200 $\mu\text{g/L}$. This drop in D_i may result from a mobility decrease of As(III) ions due to the increase in retarding force acting on diffusing ions.

4.3 Thermodynamic studies

Thermodynamic parameters were determined by from isotherm studies at three different temperatures 283 K, 298 K and 318 K. The distribution coefficient K_d for the adsorption, was obtained from equations given in chapter 2, table 2.1. Graph was plotted between, $\ln K_d$ versus $1/T$ (Vant Hoff equation). From graph values of enthalpy ΔH^0 and entropy ΔS^0 were obtained using equation given in chapter 2, table 2.1. Gibbs free energy change ΔG^0 was obtained from equation mentioned in chapter 2, table 2.1. The results are tabulated in table 4.4.

The positive value of ΔH^0 (56.552 KJ/mol; 59.209 KJ/mol) indicates that the adsorption process is endothermic in nature (figure 4.12). This is also indicated with the increasing value of K_d (1.13 (283 K), 3.05 (298 K), 15.85 (318 K) RHIOB; 1.36 (283 K), 4.20 (298 K), 21.81 (318 K) WHIOB) with increasing temperature. Positive value of entropy ΔS^0 (0.21 KJ/mol K; 0.25 KJ/mol K) after As(III) adsorption suggests that system has moved towards greater randomness or disorderness, and is irreversible. This is in agreement with the negative value of Gibbs free energy ΔG^0 suggesting that As(III) adsorption may be spontaneous in nature (Alam et al., 2018; S. Liu et al., 2017). This suggests strong electrostatic attraction developed between negatively charged arsenite oxyanions species (H_2AsO_3^-) and positively charged surface of iron oxide (FeOH^+).

4.4 As(III) adsorption equilibrium studies

Sorption isotherm experiments were conducted at 10, 25 and 40 $^\circ\text{C}$ between pH 6.5 and 7.5 and initial As(III) concentrations varying from 50 $\mu\text{g/L}$ to 1000 $\mu\text{g/L}$

Arsenite adsorption on rice husk and wheat husk iron-oxide biochar composites

[Figure 4.13-4.20]. This concentration range was selected based on arsenic concentrations reported worldwide in ground and surface waters. Equilibrium As(III) adsorption amounts on RHIOB and WHIOB increased going from 10 °C to 45 °C [Table 4.5]. Thus, adsorption is endothermic. With rising temperature, adsorptive capacity rose with increasing adsorbent mobility (Baig et al., 2014b). WHIOB's adsorption capacity was higher than RHIOB's, in accord with WHIOB's modestly higher surface area and significantly higher iron content [Table 4.5].

Freundlich, (Herbert Freundlich, 1907) Langmuir, (Langmuir, 1916) Temkin, (M. I. Temkin & V. Pyzhev, 1940) Sips or Langmuir-Freundlich, (Sips, 1948) Redlich-Peterson, (OJDL Redlich & D L Peterson, 1959) Radke and Prausnitz, (Radke & Prausnitz, 1972b) and Toth (Toth, 1971) isotherms (table 2.2, respectively) were used to fit the sorption equilibrium data and to determine the adsorption behaviour, capacity, and parameters used in fixed-bed reactor design. The Freundlich isotherm (Herbert Freundlich, 1907) describes (table 2.2, 1) the adsorption equilibrium on heterogeneous surfaces. The Langmuir isotherm (table 2.2, 2) assumes a uniform sorbent surface sites with identical energies, (Langmuir, 1916) where adsorption occurs as a single surface adsorbate layer. The Sips isotherm (Sips, 1948) is a combination of the Langmuir and Freundlich isotherms (table 2.2, 3). The Temkin model is described by table 2.2, 4. The Redlich-Peterson model (table 2.2, 5) (OJDL Redlich & D L Peterson, 1959) is a three parameter model, describing equilibrium on heterogeneous surfaces and contains a heterogeneity factor. The three parameter Radke and Prausnitz isotherm, (Radke & Prausnitz, 1972b) derived from thermodynamic considerations (table 2.2, 6), is capable of describing data over a wide concentration range. The Toth isotherm, (Toth, 1971) an empirical model, assumes an asymmetric quasi-Gaussian distribution of site energies (table 2.2, 7). This model describes an improved fit versus Langmuir isotherm model and is often used to describe heterogeneous systems. The Koble-Corrigan isotherm (Robert A. Koble & Thomas E. Corrigan, 1952) is also a three parameters model (table 2.2, 8).

Langmuir fittings of arsenic(III) sorption equilibrium data for WHIOB and RHIOB are given [Figure 4.13] with the fittings for the other isotherm models

[Figures 4.14-4.20]. Parameters and regression coefficient from all eight of these non-linear isotherm fittings are summarized in Table 4.5. The fits at 25, 35 and 45⁰C for all RHIOB and WHIOB adsorption data were ranked based on their R² values. At 45⁰C, the Redlich-Peterson (R² = 0.9909) equation fit the RHIOB equilibrium data best, while the Sips and Koble-Corrigan gave equal best fits to WHIOB data. The Redlich-Peterson isotherm constant β values for RHIOB at 45⁰C are very close to 1 [Table 4.5], reducing As(III) adsorption to the Langmuir isotherm (Azmi, Yusup, & Sabil, 2017; Kumar et al., 2010), and suggesting RHIOB has a homogenous adsorption surface. This agrees with predominant adsorption on the iron oxide surfaces of the hybrid adsorbent. WHIOB data give best fits by the Sips and the Koble Corrigan isotherms, which combines both Langmuir and Freundlich. Hence, at lower As(III) concentrations diffusion dominates while at higher As(III) concentrations monomolecular adsorption dominates (Mohan, Rajput, et al., 2011; Mohan, Sarswat, et al., 2011).

Monolayer adsorption capacities (Q⁰) are reported from the Langmuir adsorption isotherm [Figure 4.13; Table 4.5]. These maximum adsorption capacities were 13.14 $\mu\text{g/g}$ (10⁰C); 94.34 $\mu\text{g/g}$ (25⁰C) and 96.14 $\mu\text{g/g}$ (45⁰C) for RHIOB and 70.35 $\mu\text{g/g}$ (10⁰C); 108.0 $\mu\text{g/g}$ (35⁰C) and 110.73 $\mu\text{g/g}$ (45⁰C) for WHIOB [Figure 4.13; Table 4.5]. These values are very close to the experimental capacities of 11.63 $\mu\text{g/g}$, 91.91 $\mu\text{g/g}$ and 94.34 $\mu\text{g/g}$ for RHIOB and 72.46 $\mu\text{g/g}$, 97.09 $\mu\text{g/g}$ and 103.09 $\mu\text{g/g}$ for WHIOB, respectively [Table 4.5]. Adsorption capacities go up with an increase in temperature for both RHIOB and WHIOB, agreeing with endothermic As(III) adsorption. This As(III) adsorption increase when temperature rises may be due to both endothermic chemical adsorption and an increase in adsorbent ion mobility. Both would raise adsorption efficiencies as temperature rises. (Baig et al., 2014b) Langmuir monolayer adsorption capacities of RHIOB and WHIOB are comparable to many adsorbents (Table 4.5). High sorption capacities of many adsorbents are due to the high As(III) concentrations taken in performing the batch experiments. Some adsorbents capable of remediating arsenic at high concentrations have failed to work in low concentration range. Our present studies were purposely conducted at low As(III) concentrations (50-1000

Arsenite adsorption on rice husk and wheat husk iron-oxide biochar composites

µg/L) where less data exists and because many environmental sites have concentrations in this range. Therefore, these studies may result into low adsorption capacities. RHIOB and WHIOB successfully remediated As(III) at concentrations usually present in the actual water bodies (Table 4.5).

Arsenite adsorption on rice husk and wheat husk iron-oxide biochar composites

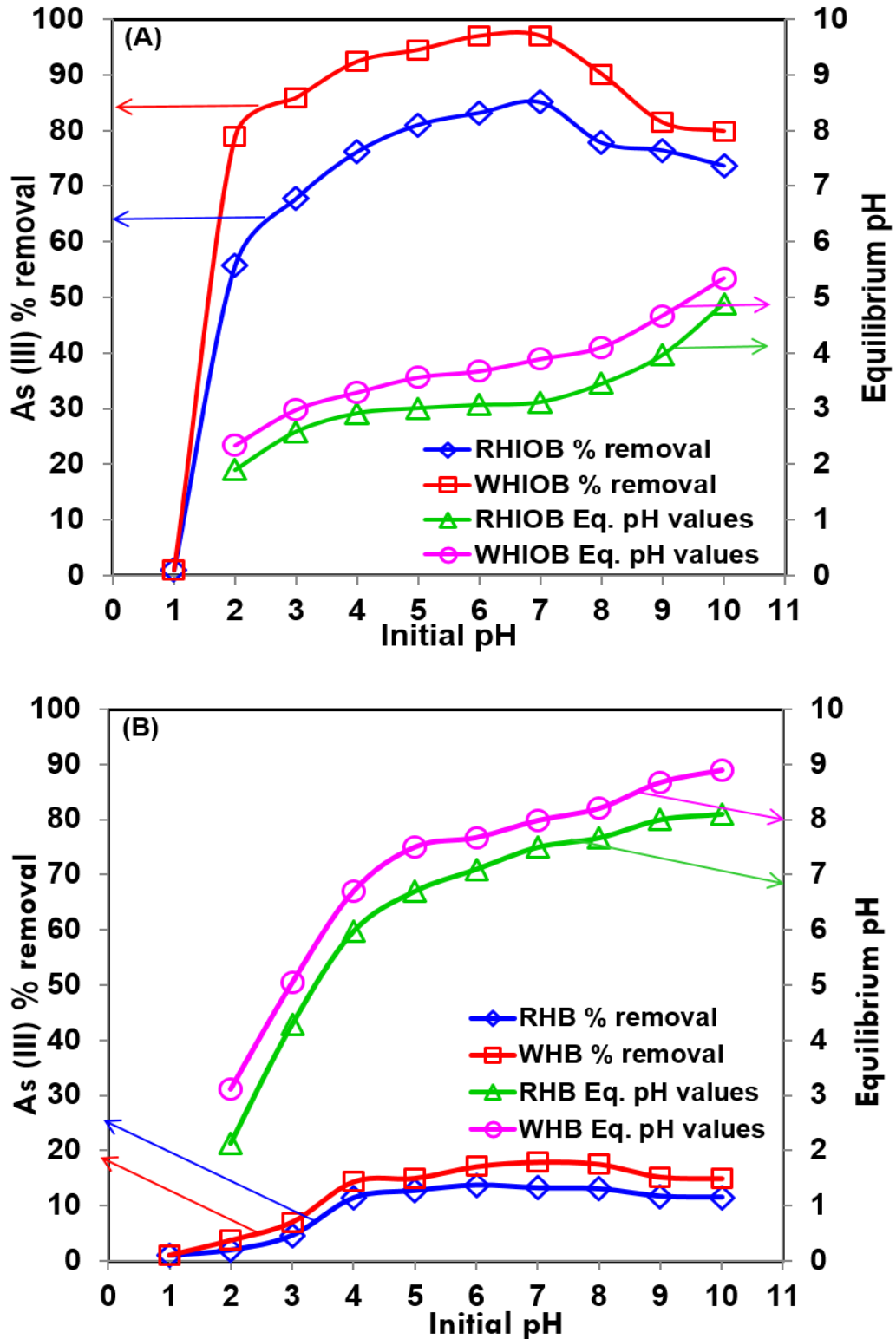


Figure 4.1. Effect of initial pH and equilibrium pH on As(III) removal by (A) RHIOB and WHIOB and (B) their precursor biochars RHB and WHB (adsorbent dose= 2.0 g/L, RHIOB and 1.0 g/L WHIOB; initial As(III) concentration= 100 µg/L; agitation speed= 100 rpm, temperature= 25 °C, contact time= 24 h).

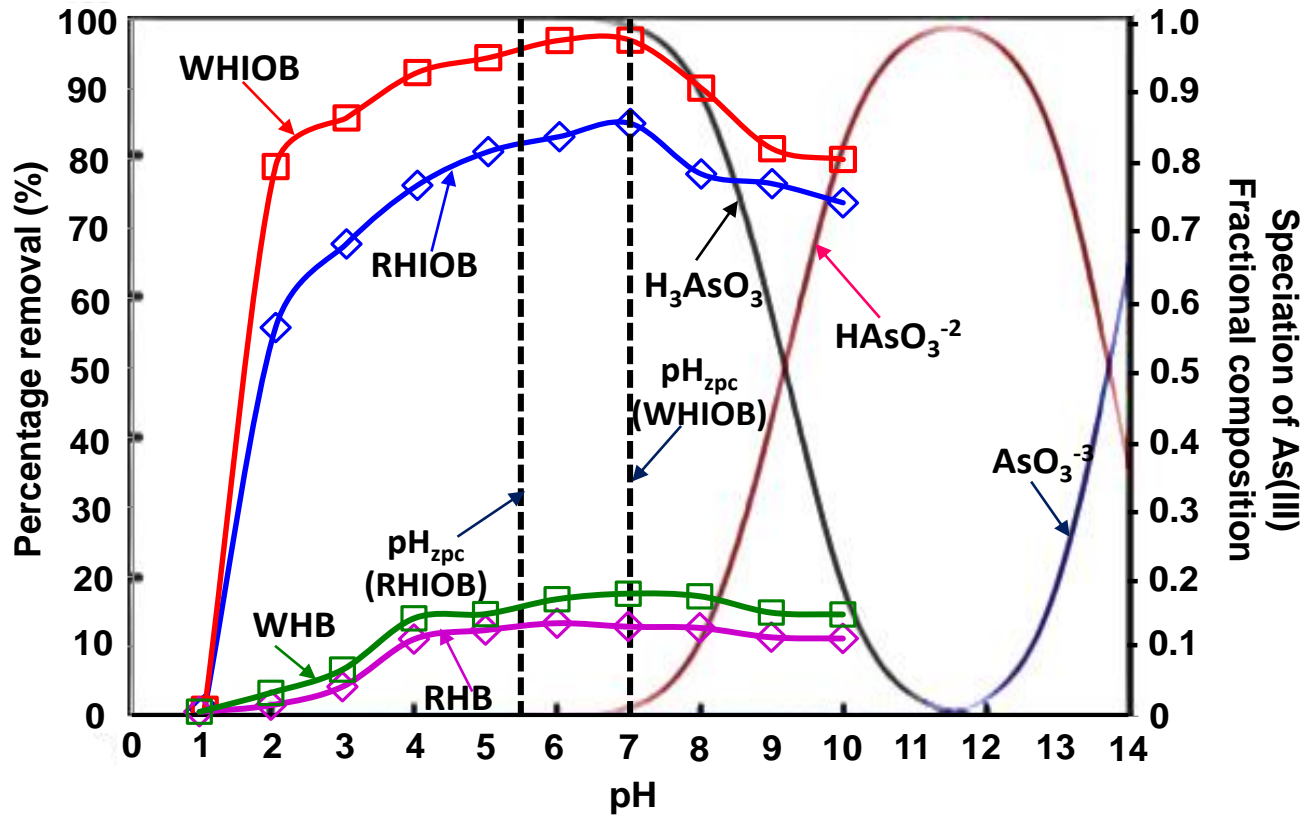


Figure 4.2. Effect of initial pH with respect to pH_{zpc} and fractional composition speciation on percent As(III) removal by RHIOB, WHIOB and their precursor biochars RHB and WHB (adsorbent dose= 2.0 g/L; initial As(III) concentration= 100 $\mu\text{g/L}$; agitation speed= 100 rpm, temperature= 25 $^{\circ}\text{C}$, contact time= 24 h).

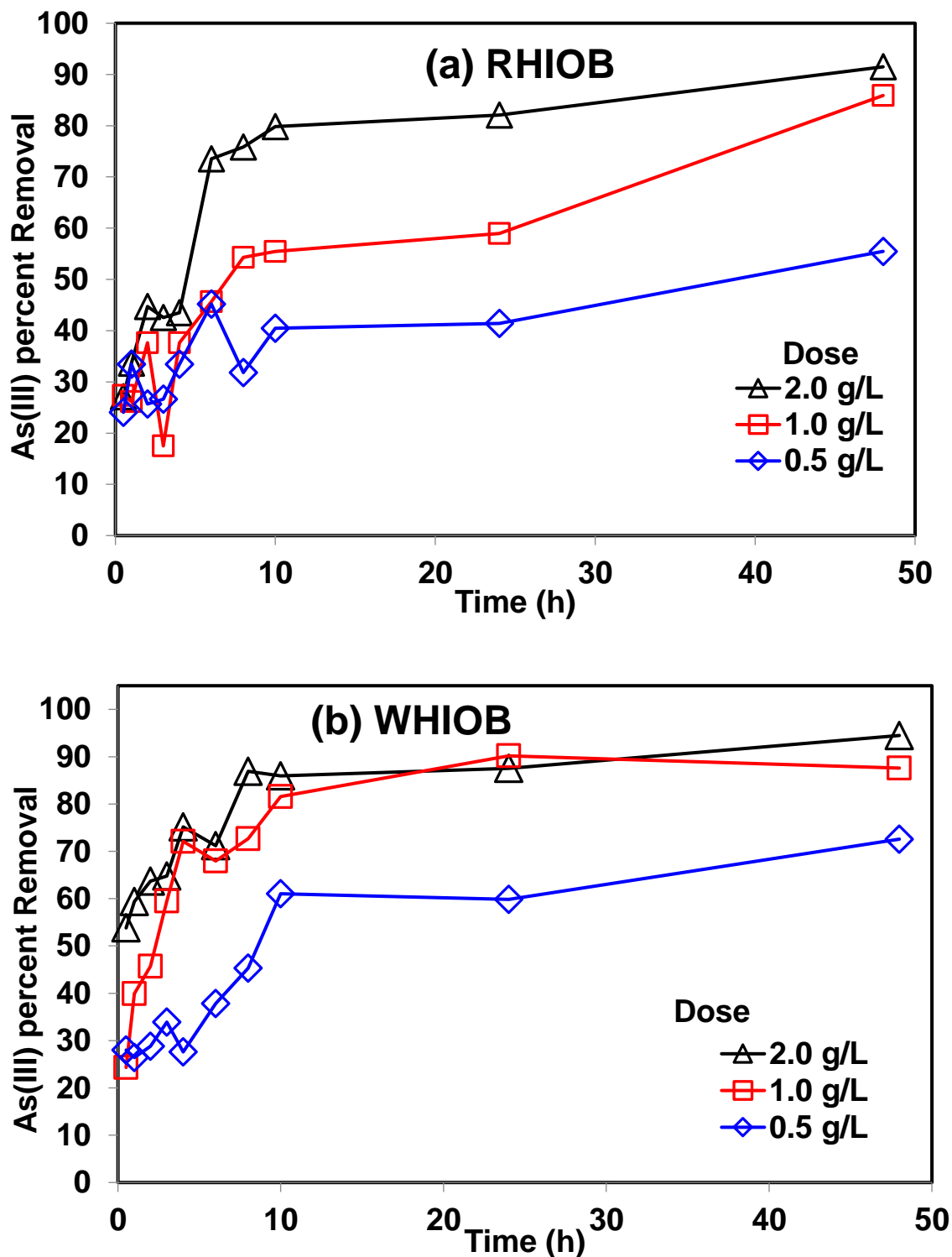


Figure 4.3. Effect of adsorbent dose on percent As(III) removal by (A) RHIOB and (B) WHIOB (pH= 7.5; As(III) concentration=100 μ g/L; temp= 25 $^{\circ}$ C; agitation= 100 rpm; particle size= 30-50 B.S.S. mesh).

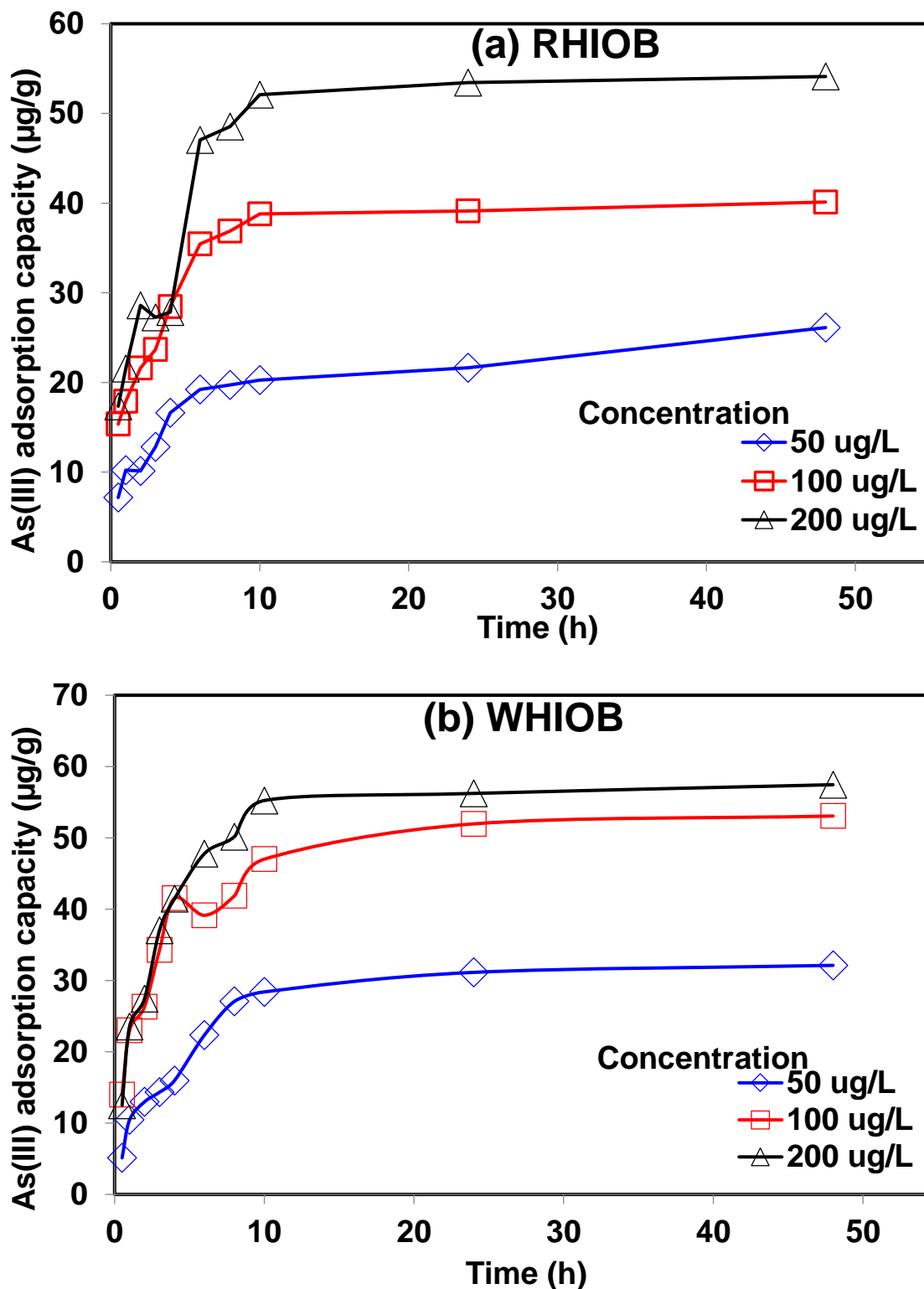


Figure 4.4. Effect of adsorbent concentration on adsorption capacity As(III) ($\mu\text{g/g}$) removal by (A) RHIOB and (B) WHIOB (pH= 7.5; As(III) concentration=100 $\mu\text{g/L}$; temp= 25 $^{\circ}\text{C}$; agitation= 100 rpm; particle size= 30-50 B.S.S. mesh).

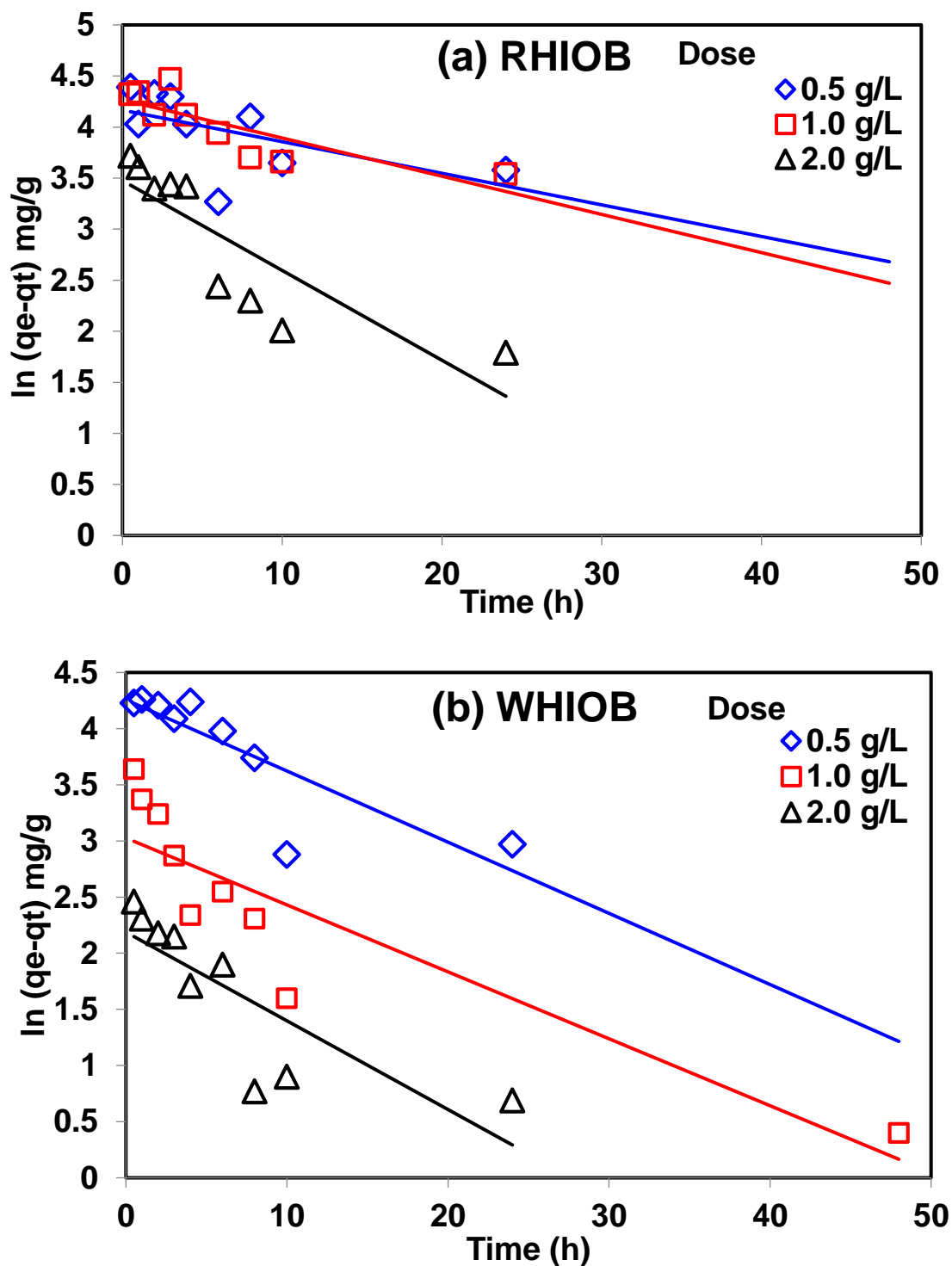


Figure 4.5. Pseudo-first-order linear kinetic plots of As(III) adsorption at different doses (a) RHIOB and (b) WHIOB (pH= 7.5; As(III) concentration=100 μ g/L; temp= 25 $^{\circ}$ C; agitation= 100 rpm; particle size= 30-50 B.S.S. mesh).

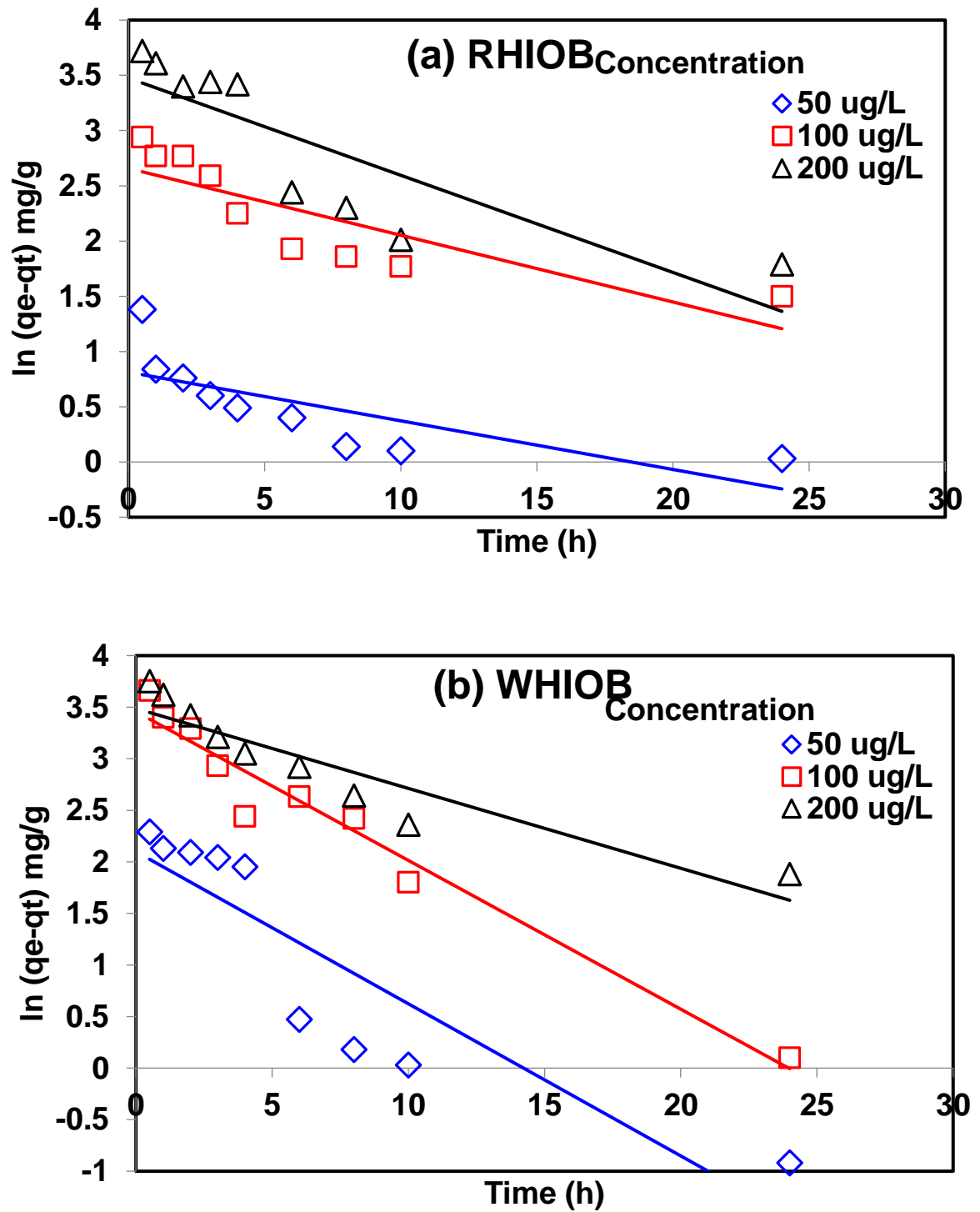


Figure 4.6. Pseudo-first-order linear kinetic plots of As(III) adsorption at different concentrations (a) RHIOB and (b) WHIOB (pH= 7.5; As(III) concentration=100 μ g/L; temp= 25⁰C; agitation= 100 rpm; particle size= 30-50 B.S.S. mesh).

Arsenite adsorption on rice husk and wheat husk iron-oxide biochar composites

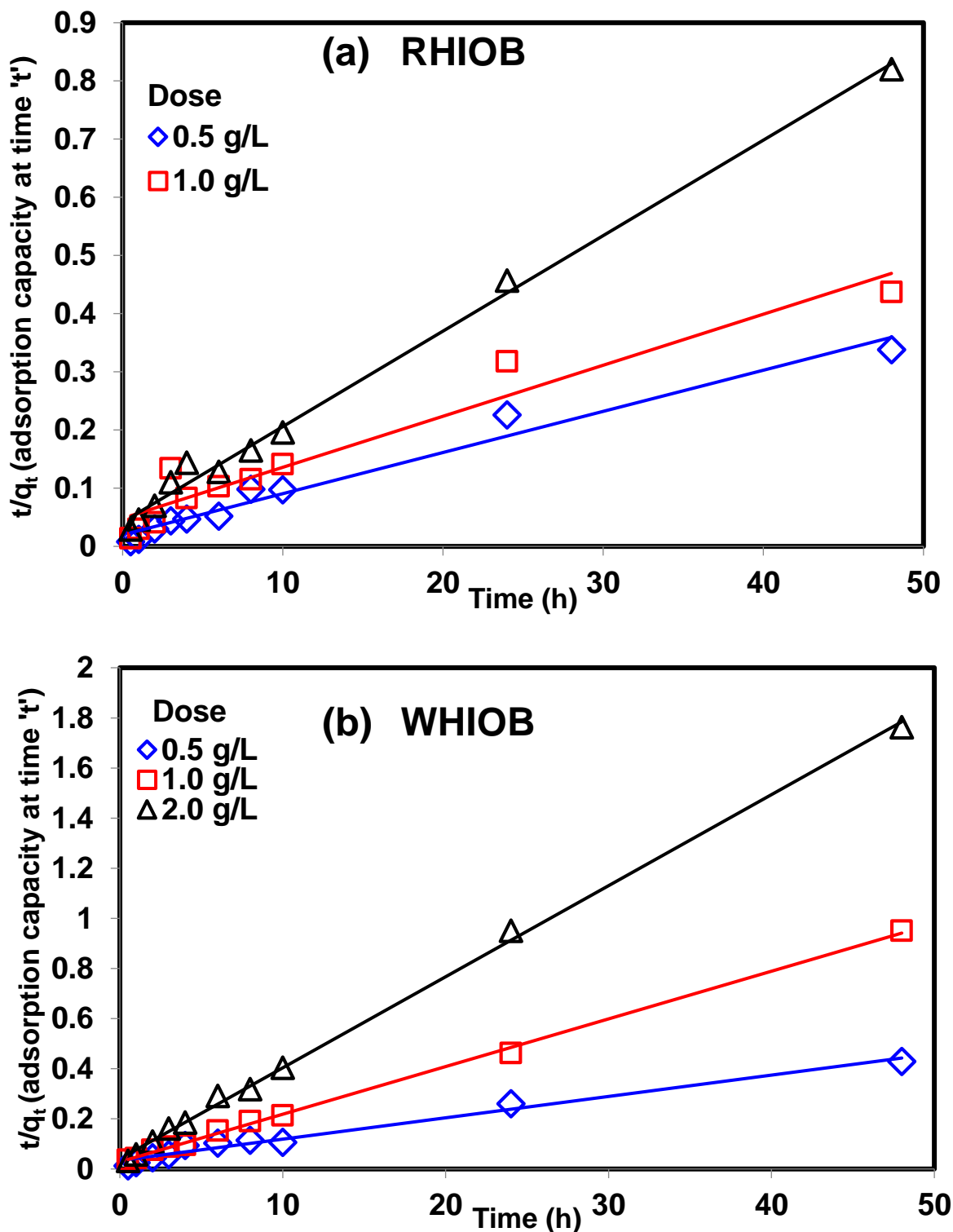


Figure 4.7. Pseudo-second-order linear kinetic plots of As(III) adsorption at different doses (a) RHIOB and (b) WHIOB (pH= 7.5; As(III) concentration=100 μ g/L; temp= 25 $^{\circ}$ C; agitation= 100 rpm; particle size= 30-50 B.S.S. mesh).

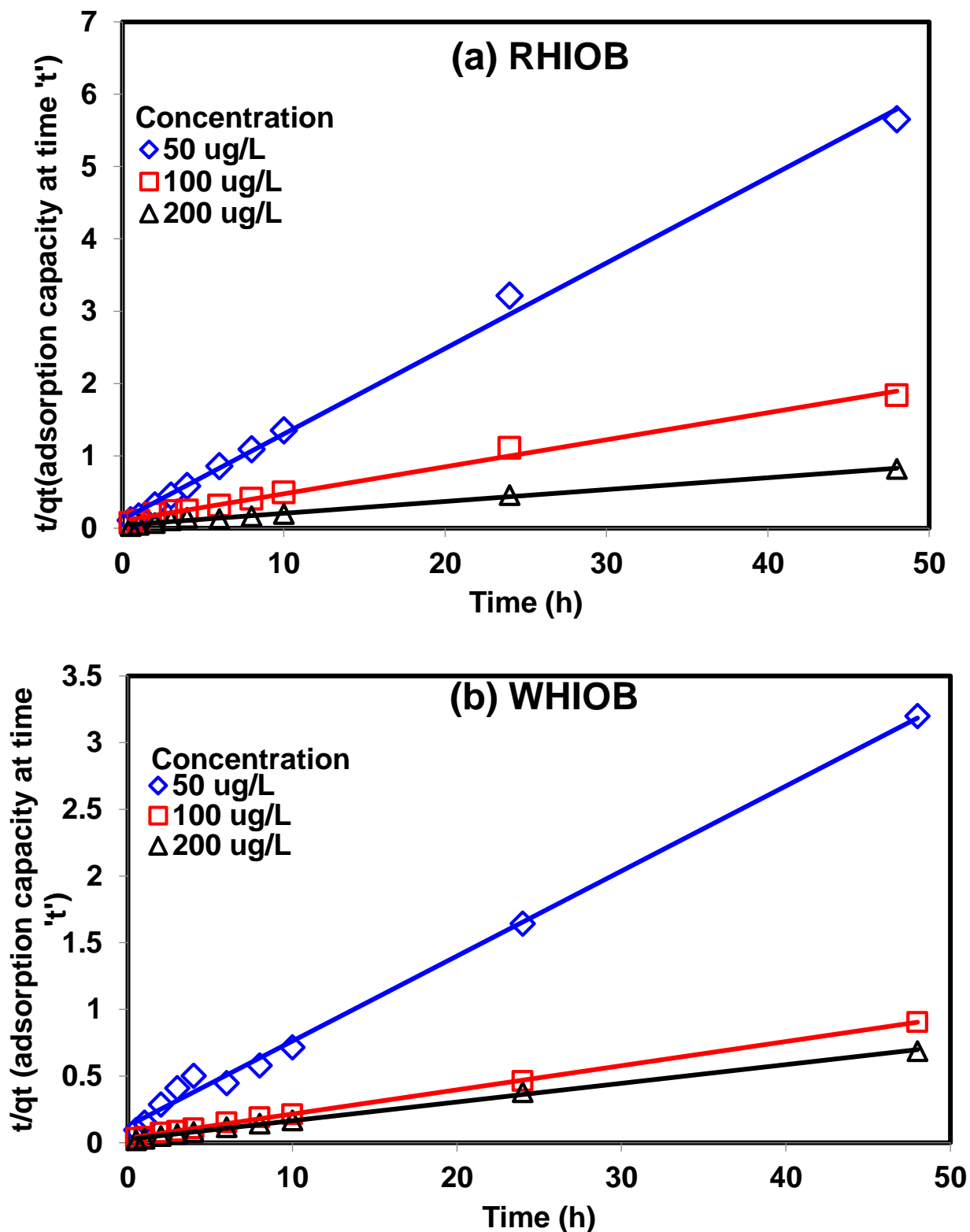


Figure 4.8. Pseudo-second-order linear kinetic plots for As(III) adsorption at different concentrations for (a) RHIOB and (b) WHIOB (pH=7.5 ; dose= 2.0 g/L and 1.0 g/L respectively; temp= 25 °C ; agitation= 100 rpm; particle size= 30- 50 B.S.S. mesh).

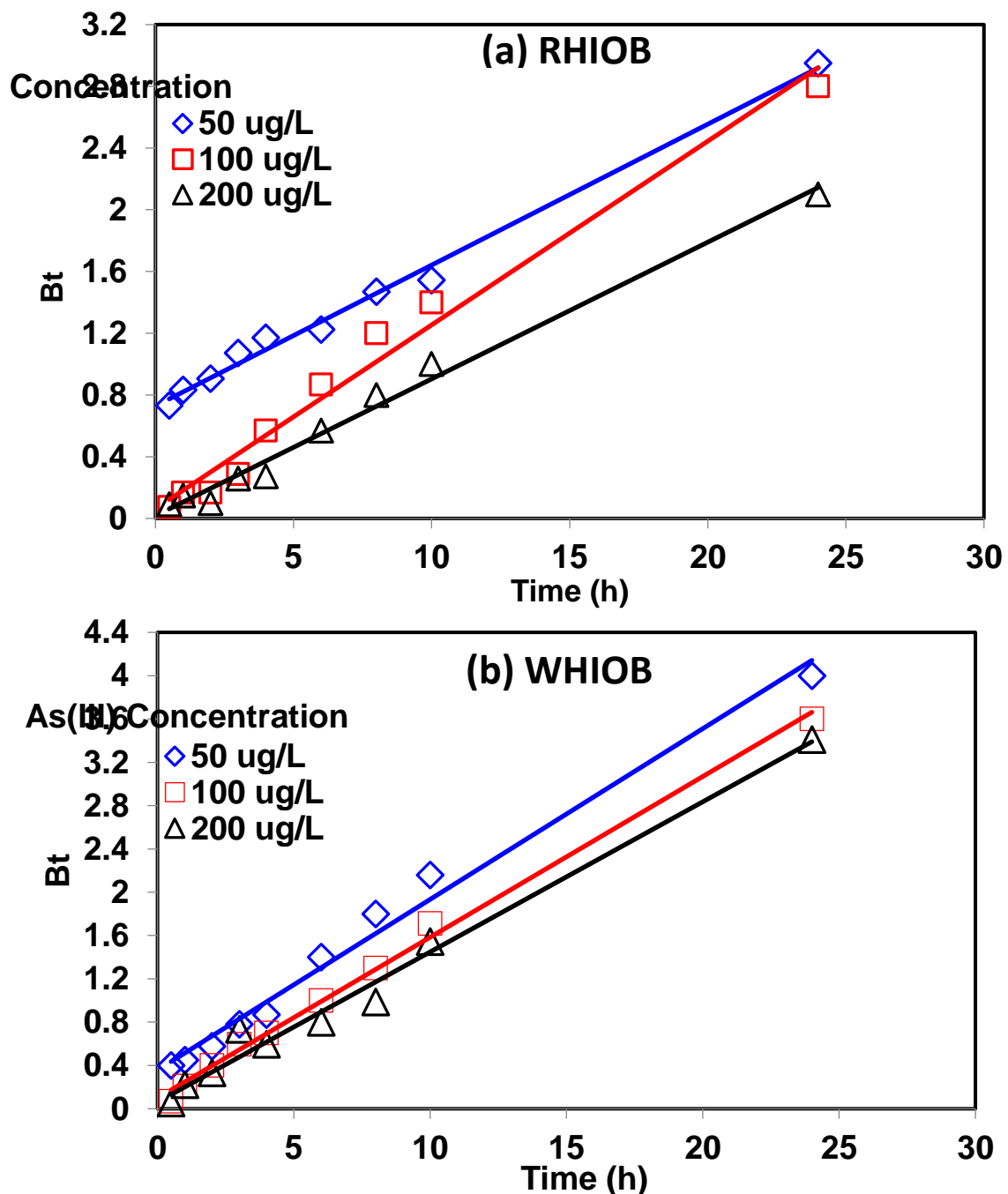


Figure 4.9. Boyd's model plots for As(III) adsorption at different concentrations for (a) RHIOB and (b) WHIOB (pH=7.5 ; dose= 2.0 g/L and 1.0 g/L respectively; temp= 25 °C ; agitation= 100 rpm; particle size= 30- 50 B.S.S. mesh).

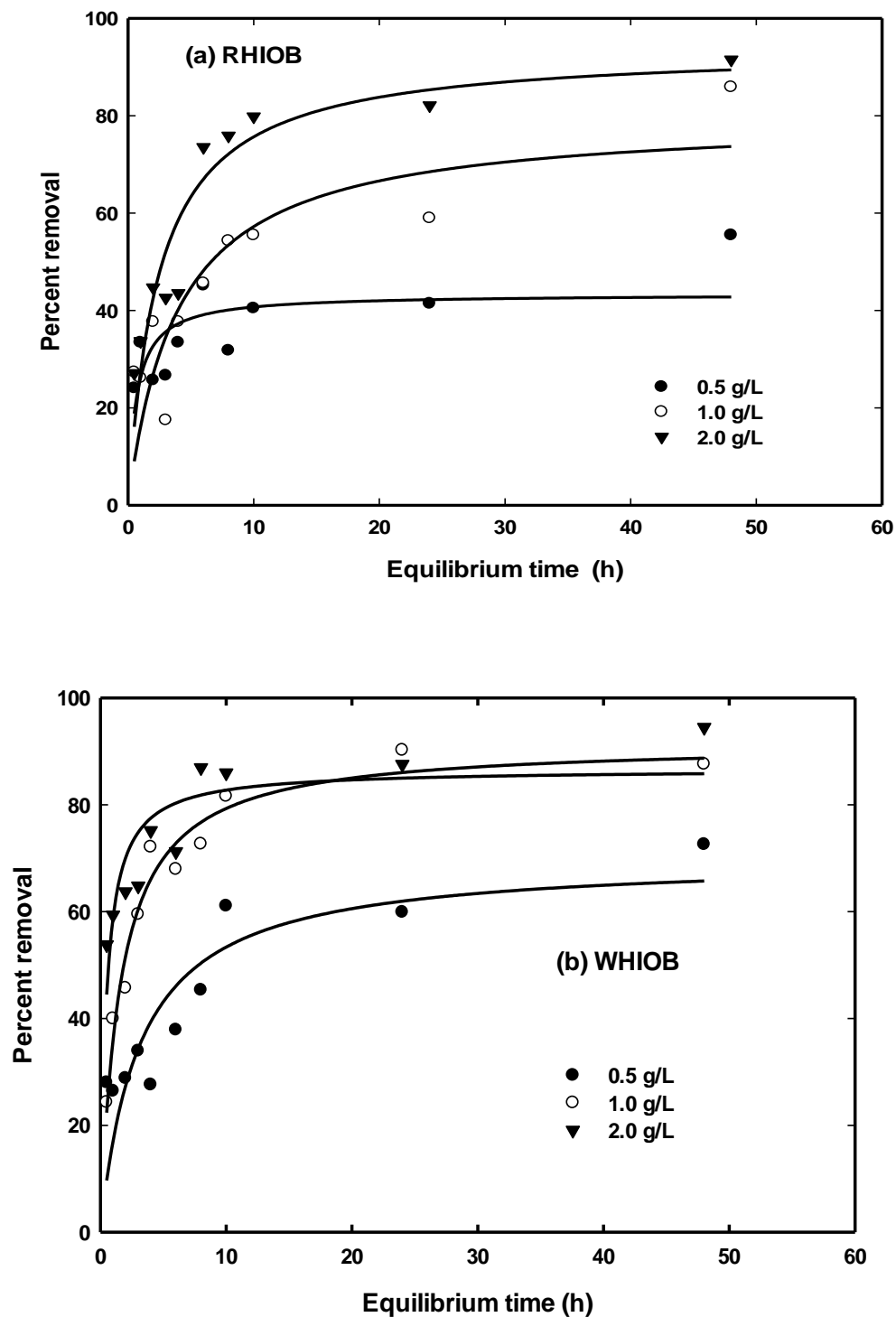


Figure 4.10. Pseudo-second-order non-linear kinetic plots of As(III) adsorption at different doses (a) RHIOB and (b) WHIOB (pH= 7.5; As(III) concentration=100 μ g/L; temp= 25⁰C; agitation= 100 rpm; particle size= 30-50 B.S.S. mesh).

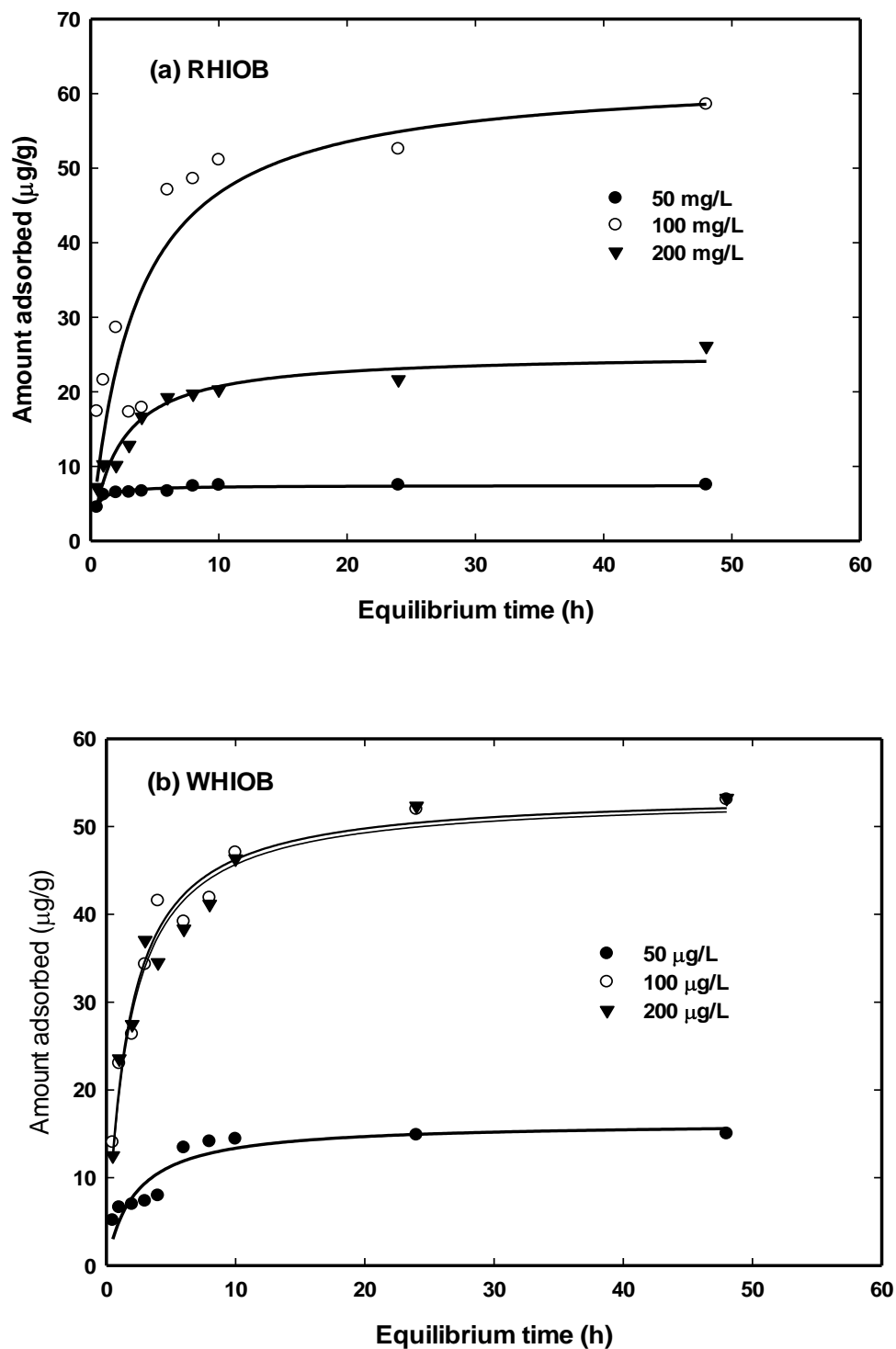


Figure 4.11. Pseudo-second-order non-linear kinetic plots of As(III) adsorption at different concentrations (a) RHIOB and (b) WHIOB (pH= 7.5; As(III) concentration=100 $\mu\text{g/L}$; temp= 25 $^{\circ}\text{C}$; agitation= 100 rpm; particle size= 30-50 B.S.S. mesh).

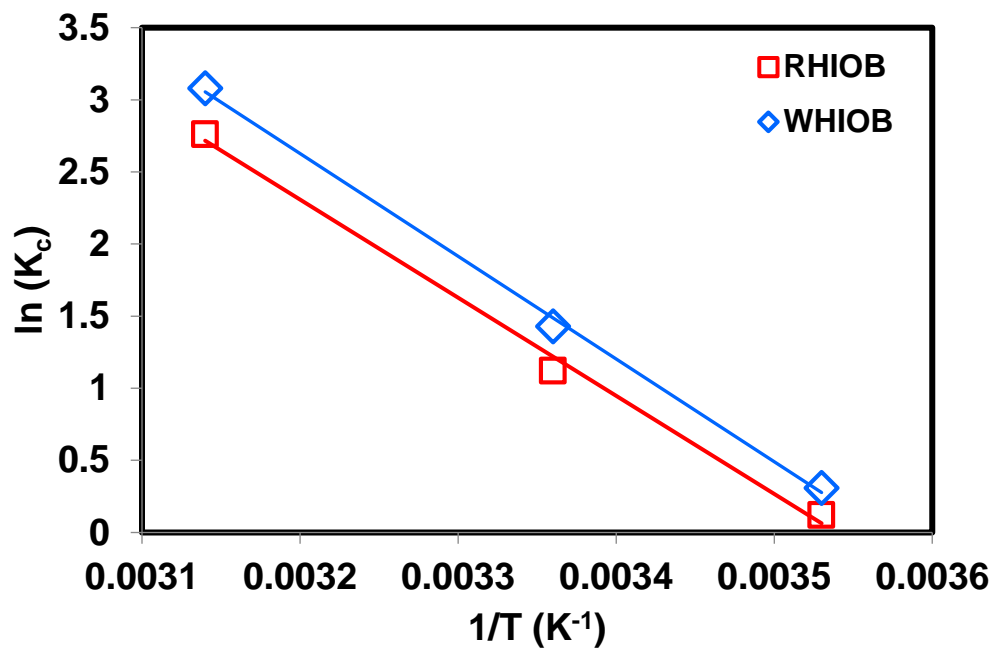


Figure 4.12. Linear plot of ln K versus 1/T for the calculation of thermodynamic parameters to evaluate As(III) adsorption onto RHIOB and WHIOB.

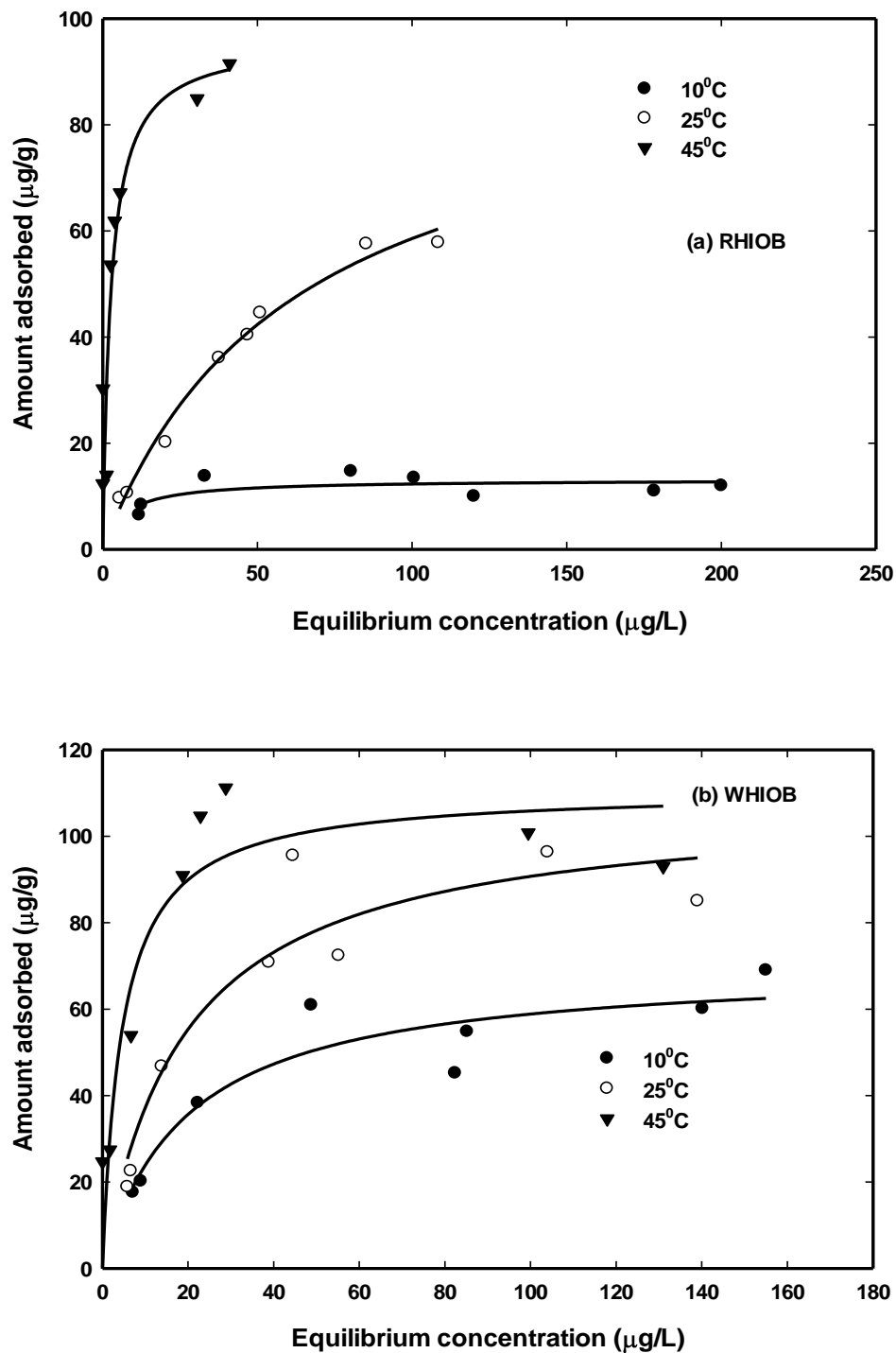


Figure 4.13. Langmuir non-linear adsorption isotherms of As(III) adsorption by (a) RHIOB and (b) WHIOB at different temperatures (pH= 7.5 ; concentration= 100 $\mu\text{g/L}$; temp= 25 $^{\circ}\text{C}$; agitation= 100 rpm; particle size= 30- 50 B.S.S. mesh).

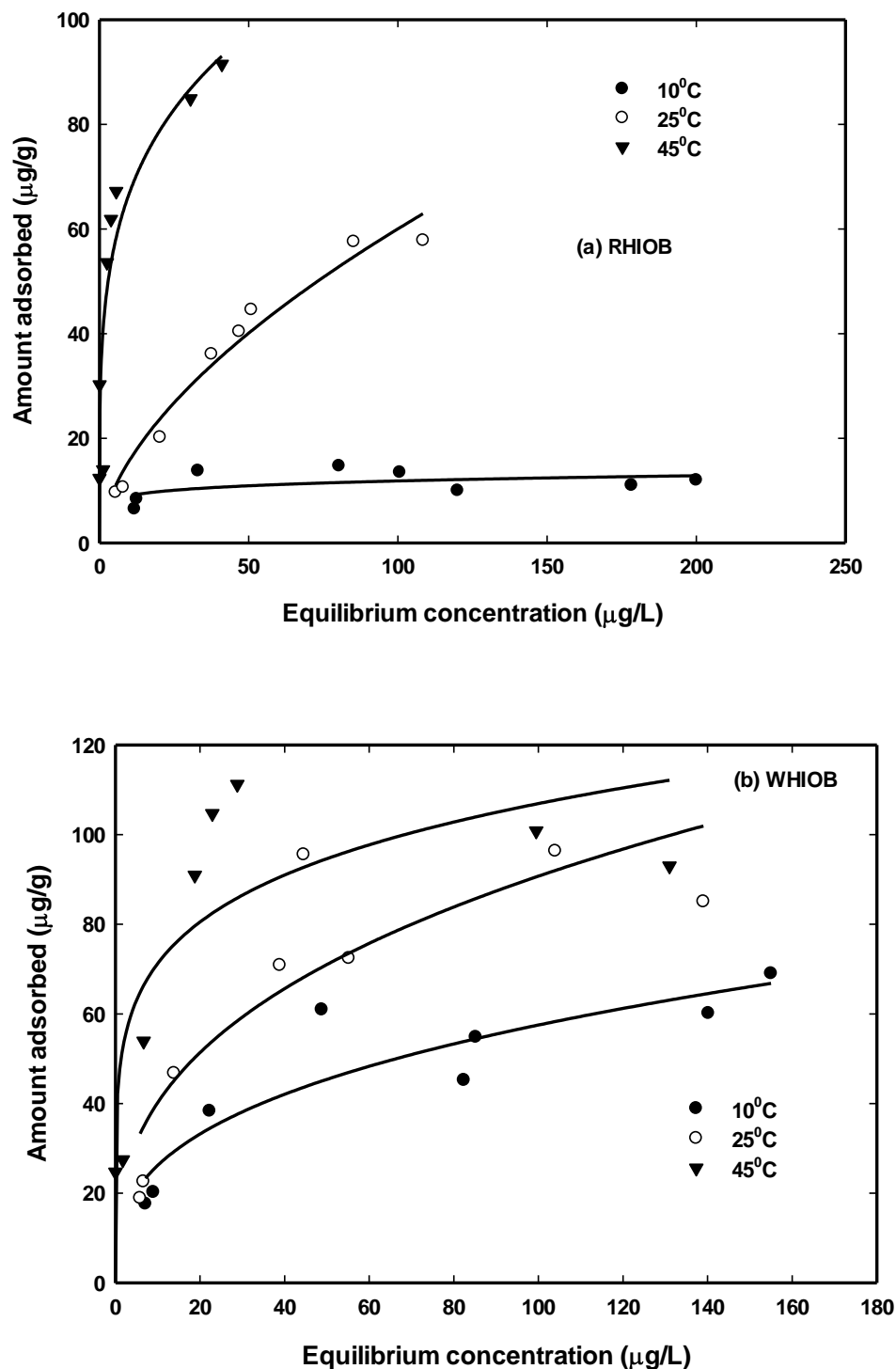


Figure 4.14. Freundlich non-linear adsorption isotherms of As(III) adsorption by (a) RHIOB and (b) WHIOB at different temperatures (pH= 7.5 ; concentration= 100 $\mu\text{g/L}$; temp= 25 $^{\circ}\text{C}$; agitation= 100 rpm; particle size= 30- 50 B.S.S. mesh).

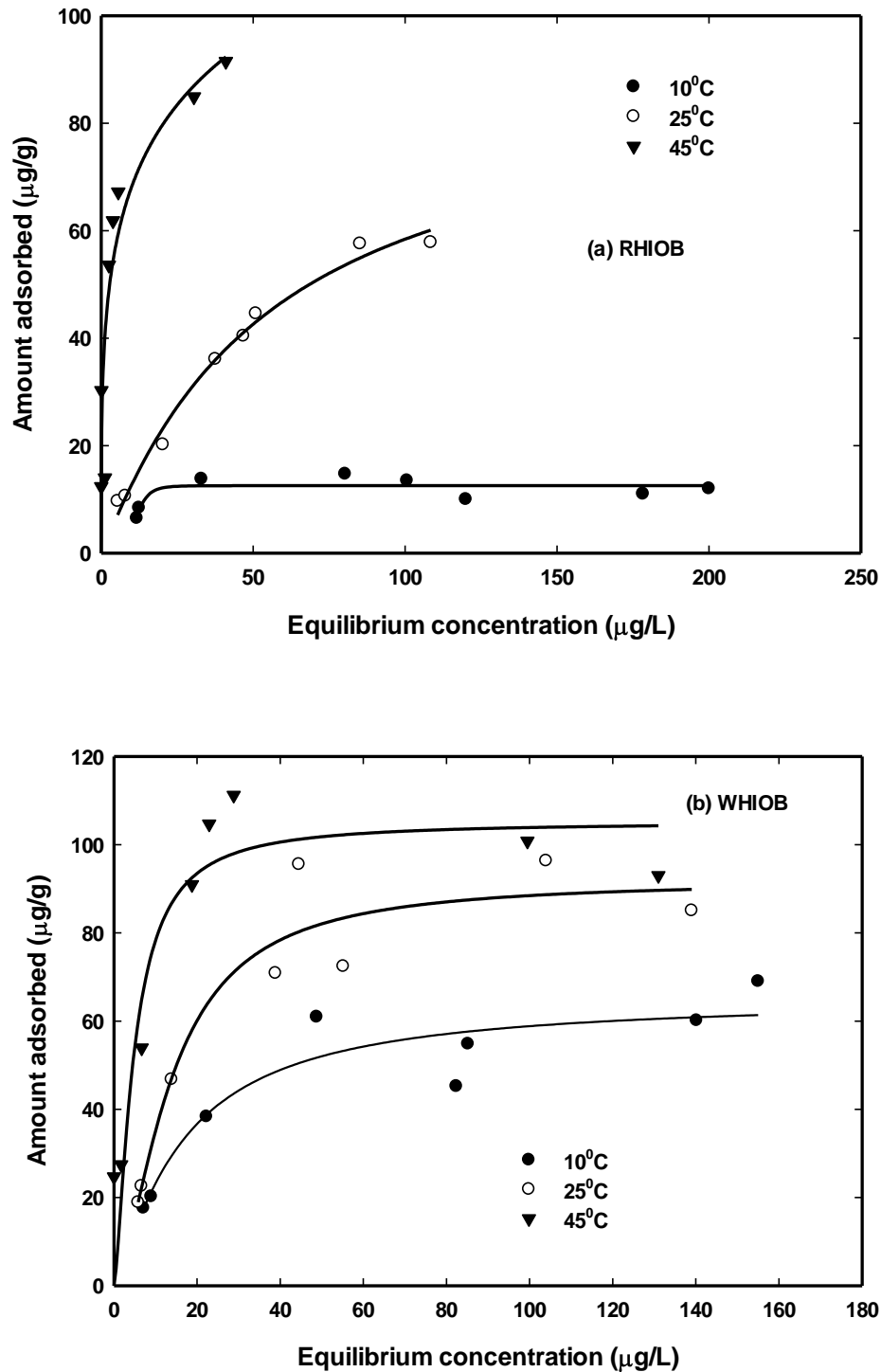


Figure 4.15. Sips non-linear adsorption isotherms of As(III) adsorption by (a) RHIOB and (b) WHIOB at different temperatures (pH= 7.5 ; concentration= 100 ug/L; temp= 25 °C ; agitation= 100 rpm; particle size= 30- 50 B.S.S. mesh).

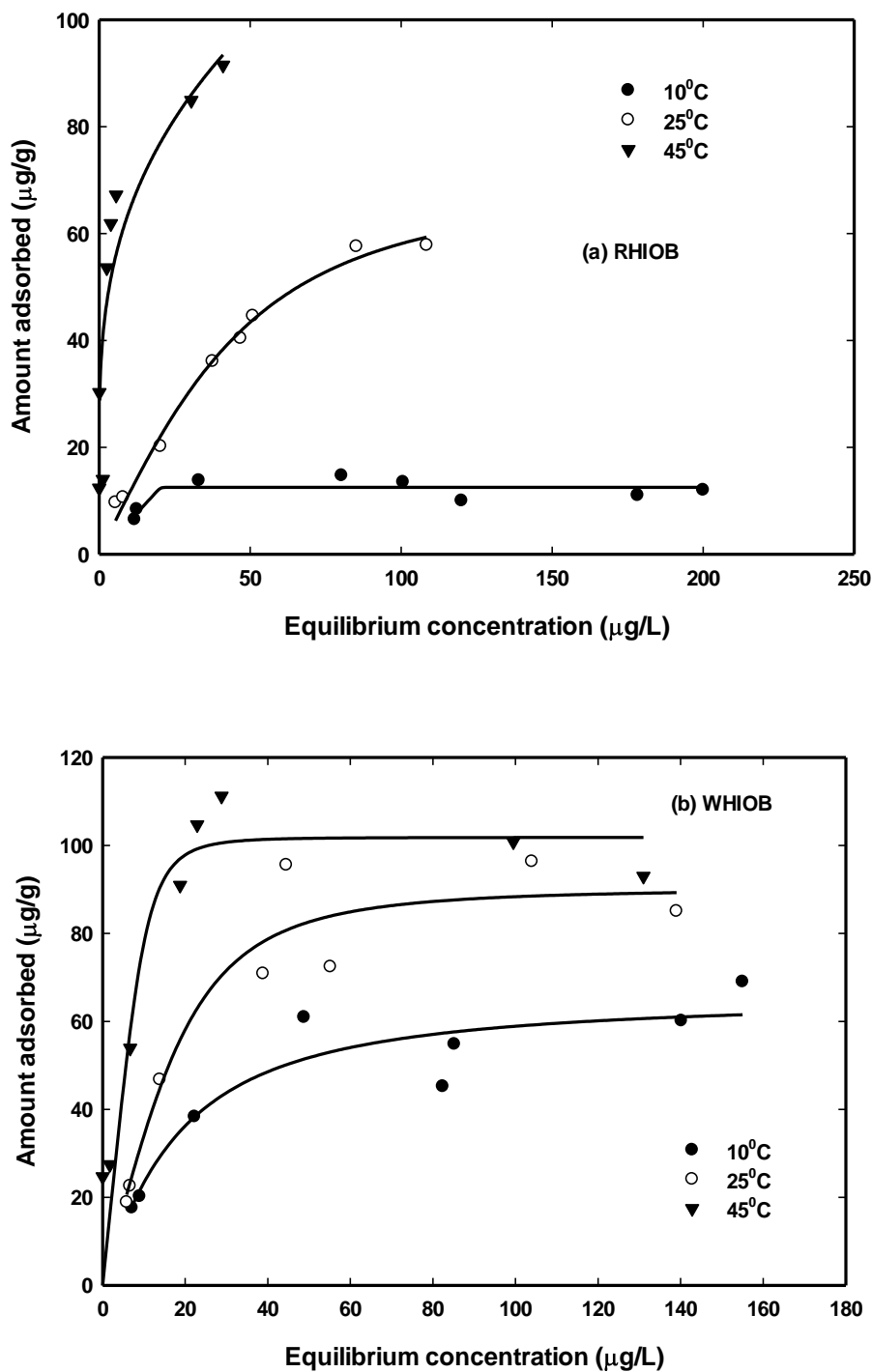


Figure 4.16. Toth non-linear adsorption isotherms of As(III) adsorption by (a) RHIOB and (b) WHIOB at different temperatures (pH= 7.5 ; concentration= 100 ug/L; temp= 25 °C ; agitation= 100 rpm; particle size= 30- 50 B.S.S. mesh).

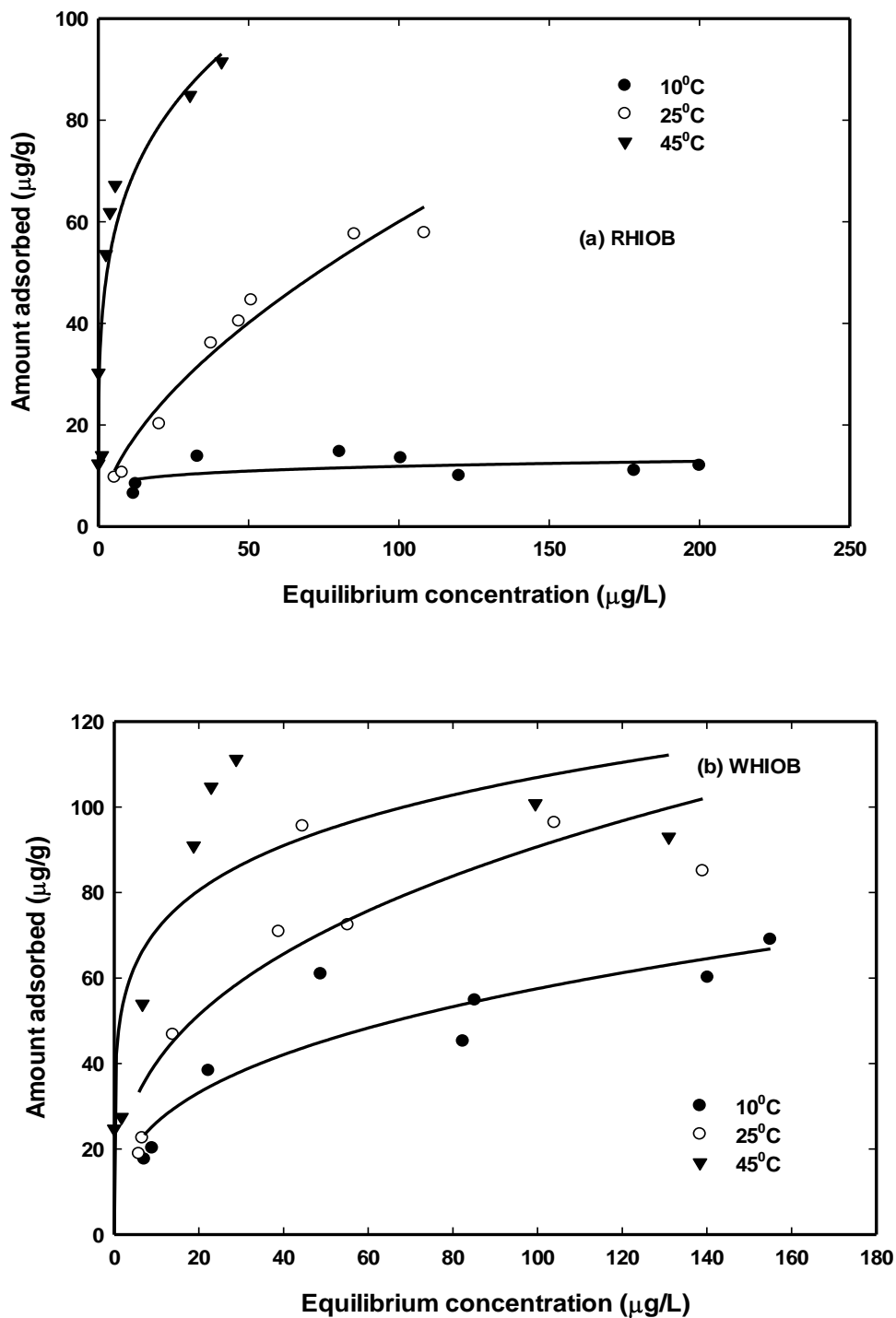


Figure 4.17. Radke- Prausnitz non-linear adsorption isotherms of As(III) adsorption by (a) RHIOB and (b) WHIOB at different temperatures (pH= 7.5 ; concentration= 100 $\mu\text{g/L}$; temp= 25 $^{\circ}\text{C}$; agitation= 100 rpm; particle size= 30-50 B.S.S. mesh).

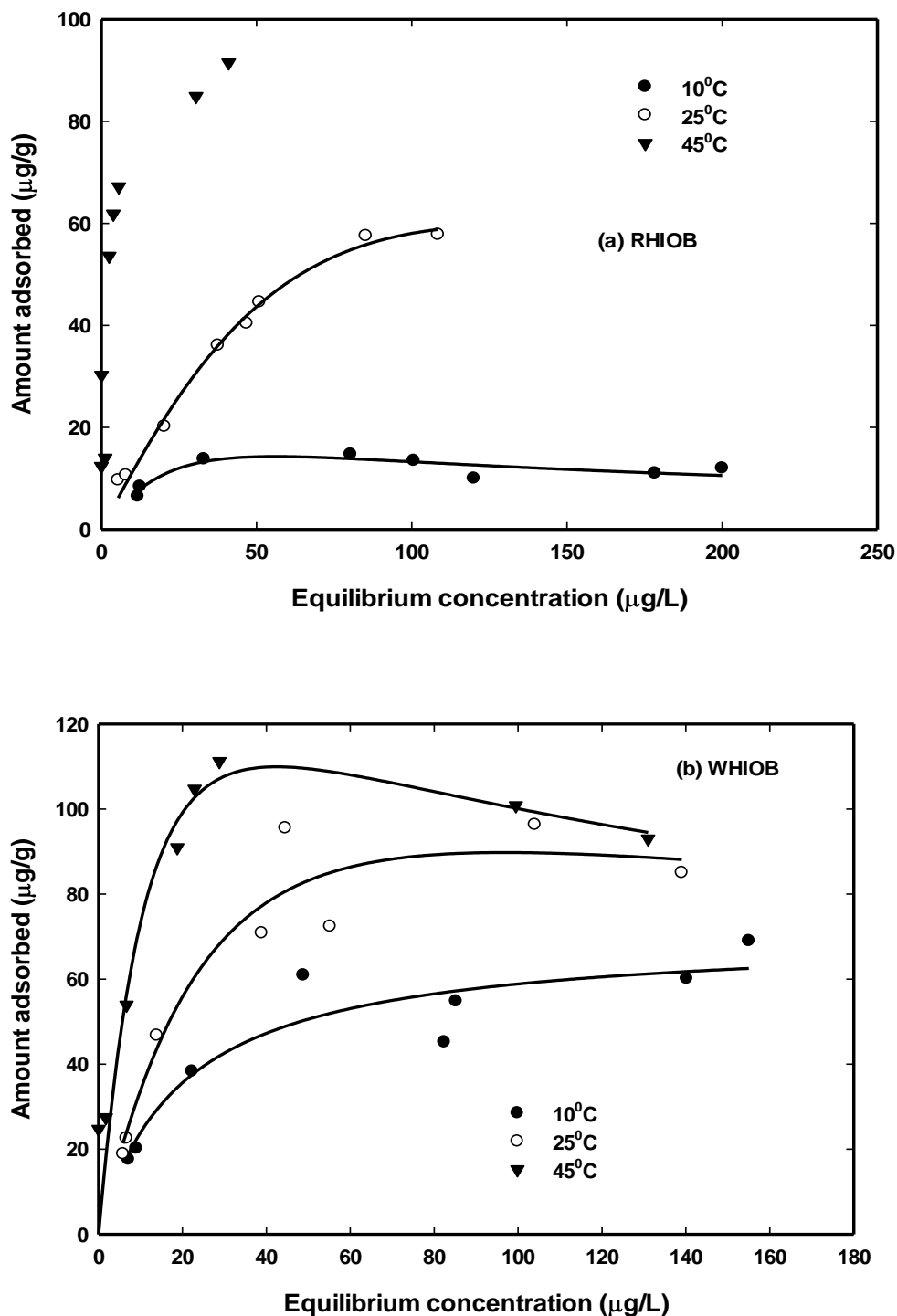


Figure 4.18. Redlich Peterson non-linear adsorption isotherms of As(III) adsorption by (a) RHIOB and (b) WHIOB at different temperatures (pH= 7.5 ; concentration= 100 $\mu\text{g/L}$; temp= 25 $^{\circ}\text{C}$; agitation= 100 rpm; particle size= 30-50 B.S.S. mesh).

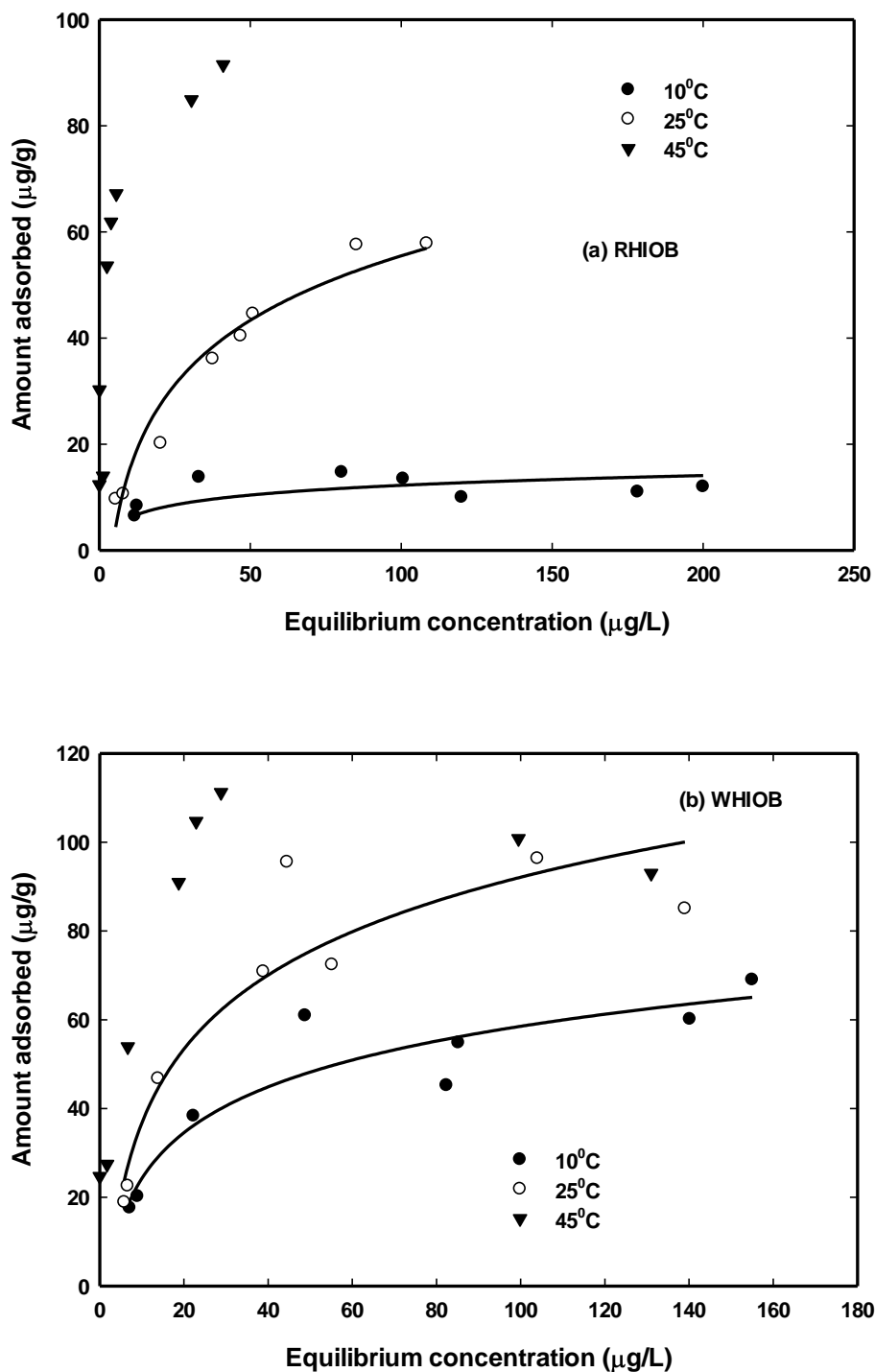


Figure 4.19. Temkin non-linear adsorption isotherms of As(III) adsorption by (a) RHIOB and (b) WHIOB at different temperatures (pH= 7.5 ; concentration= 100 ug/L; temp= 25 °C ; agitation= 100 rpm; particle size= 30- 50 B.S.S. mesh).

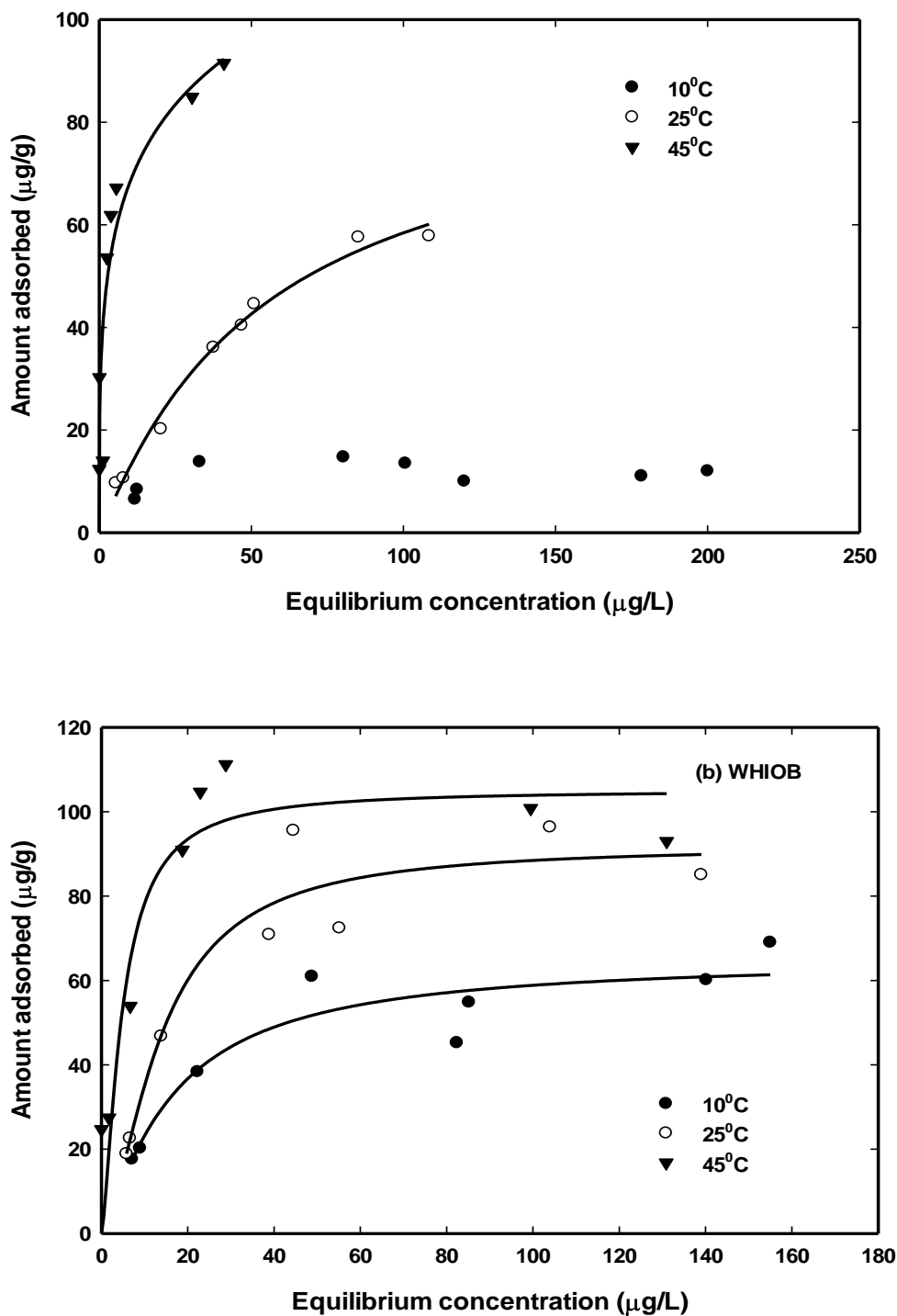


Figure 4.20. Koble-Corrigan non-linear adsorption isotherms of As(III) adsorption by (a) RHI OB and (b) WHIOB at different temperatures (pH= 7.5 ; concentration= 100 $\mu\text{g/L}$; temp= 25 $^{\circ}\text{C}$; agitation= 100 rpm; particle size= 30- 50 B.S.S. mesh).

Table 4.1 Pseudo-first-order rate constant obtained from linear equations and comparison of experimental q_e values with their corresponding q_e calculated values at different dosage and concentrations.

Parameters Values	Linear Plot		q_e , Adsorption capacity at equilibrium <small>(amount of adsorbate adsorbed in μg)</small> <small>(amount of adsorbent used for adsorption in g)</small>	
	Pseudo-first-order rate constant k_1 (h^{-1})	R^2	q_e , ($\mu\text{g/g}$) as obtained experimentally	q_e , ($\mu\text{g/g}$) as calculated using pseudo-first-order linear equation
RHI OB				
At different adsorbent doses (g/L)				
0.5	0.071	0.344	142.0	64.43
1.0	0.086	0.675	109.9	71.27
2.0	0.203	0.719	58.6	32.3
WHI OB				
0.5	0.146	0.714	111.8	70.54
1.0	0.137	0.787	50.5	20.62
2.0	0.182	0.674	27.2	8.91
At different As(III) concentrations ($\mu\text{g/L}$)				
RHI OB				
50	0.101	0.556	8.49	2.25
100	0.139	0.715	26.1	14.26
200	0.203	0.719	58.55	32.3
WHI OB				
50	0.340	0.805	15.0	8.16
100	0.332	0.958	53.1	31.71
200	0.178	0.861	69.9	32.69

Arsenite adsorption over rice husk and wheat husk iron oxide biochar composites

Table 4.2. Pseudo-second-order rate constants obtained from linear and non-linear equations and comparison of experimental q_e values with their corresponding q_e calculated values obtained using second order rate equations at different adsorbent dosage and concentrations.

Parameters Values	Linear Plot		Non Linear Plot		q_e , Adsorption capacity at equilibrium <small>(amount of adsorbate adsorbed in μg)</small> <small>(amount of adsorbent used for adsorption in g)</small>			Half-life time t_{50} (h)
	Second order rate constant k_2 (g/ $\mu\text{g h}$)	R^2	Second order rate constant k_2 (g/ $\mu\text{g h}$)	R^2	q_e , ($\mu\text{g/g}$) as obtained experimentally	q_e , ($\mu\text{g/g}$) as calculated using second order linear equation	q_e , ($\mu\text{g/g}$) as calculated using second order non-linear equation	
RHI OB								
At different adsorbent doses (g/L)								
0.5	0.003	0.919	0.0354	0.442	142.0	142.9	43.35	14.5
1.0	0.001	0.992	0.0032	0.694	109.9	125.0	79.67	7.5
2.0	0.006	0.994	0.004	0.884	58.6	62.5	93.90	5.5
WHI OB								
0.5	0.002	0.979	0.0046	0.696	111.8	125.0	70.00	8.5
1.0	0.013	0.998	0.007	0.963	50.5	52.6	91.57	2.5
2.0	0.032	0.998	0.024	0.749	27.2	27.8	86.65	0.5
At different As(III) concentrations ($\mu\text{g/L}$)								
RHI OB								
50	0.035	0.996	0.451	0.912	8.49	8.3	7.43	0.25
100	0.014	0.992	0.02	0.924	26.1	27.0	25.16	3.5
200	0.006	0.994	0.0046	0.741	58.55	62.5	62.79	4.5
WHI OB								
50	0.035	0.993	0.28	0.842	15.0	15.9	16.31	0.5
100	0.010	0.999	0.01	0.964	53.1	54.6	53.9	2.5
200	0.009	0.998	0.01	0.958	69.9	70.5	53.51	3.0

Table 4.3: Kinetic parameter for Boyd’s model for the adsorption of As(III) onto RHIOB and WHIOB.

Adsorbents→	RHIOB			WHIOB		
Parameters↓	50 µg/L	100 µg/L	200 µg/L	50 µg/L	100 µg/L	200 µg/L
R²	0.9926	0.9809	0.9884	0.9953	0.9866	0.9848
Radius of the adsorbent particle, r₀ (nm)	7.675	7.675	7.675	6.95	6.95	6.95
Effective diffusion coefficient, Di (m²s⁻¹)	54.5 X 10 ¹⁶⁻	71.1 X 10 ¹⁶⁻	52.9 X 10 ¹⁶⁻	88.7 X 10 ¹⁶⁻	94.2 X 10 ¹⁶⁻	82.9 X 10 ¹⁶⁻
Time constant, B (s⁻¹)	0.0913	0.1191	0.0886	0.1485	0.1577	0.1387

Table 4.4: Different thermodynamic parameters for removal of As(III) onto RHIOB and WHIOB.

Adsorbent	$\Delta H^0 (KJ mol^{-1})$	$\Delta S^0 (KJ mol^{-1} K^{-1})$	$\Delta G^0 (KJ mol^{-1})$		
			283 (K)	298 (K)	318 (K)
RHIOB	56.552	0.21	-0.28	-2.77	-7.3
WHIOB	59.209	0.25	-0.73	-3.51	-8.09

Arsenite adsorption over rice husk and wheat husk iron oxide biochar composites

Table 4.5. Freundlich, Langmuir, Redlich-Peterson, Toth, Sips, Radke and Prausnitz and Koble–Corrigan isotherm parameters for As(III) removal on RHIOB and WHIOB at different temperatures.

Isotherm parameters ^a	RHIOB			WHIOB		
	10 ⁰ C	25 ⁰ C	45 ⁰ C	10 ⁰ C	25 ⁰ C	45 ⁰ C
Q⁰ (µg/g) experimental	11.63	91.91	94.34	72.46	97.09	103.09
Freundlich						
K_F (µg/g)	6.90	4.10	38.92	11.93	17.81	47.46
1/n	0.11	0.58	0.23	0.34	0.35	0.18
R²	0.2863	0.9679	0.8270	0.8341	0.7820	0.6477
Langmuir						
Q⁰ (µg/g)	13.14	94.95	96.14	70.35	108.0	110.73
b	0.15	0.02	0.38	0.051	0.052	0.216
R²	0.4856	0.9878	0.8085	0.8801	0.9010	0.8406
Redlich-Peterson						
K_{RP} (l/g)	0.76	1.14	-	3.63	3.95	10.76
arp(l/mg)^β_{RP}	0.0048	0.0005	-	0.05	0.008	0.02
β_{RP}	1.50	1.65	-	1.00	1.30	1.32
R²	0.7971	0.9909	-	0.8801	0.9258	0.9111
Sips						
K_{LF} (l/g)	7.52 x 10 ⁻⁶	1.28	45.19	2.17	1.37	11.00
a_{LF}(l/mg)^a_{LF}	6.0x10 ⁻⁷	0.01	0.18	0.33	0.01	0.10
n_{LF}	5.89	1.06	0.32	1.22	1.62	1.47
R²	0.7048	0.9881	0.8283	0.8826	0.9271	0.8618
Koble-Corrigan						
a	-	1.28	45.26	2.16	1.37	10.47
b	-	0.01	0.18	0.03	0.02	0.10
β	-	1.06	0.32	1.22	1.62	1.47
R²	-	0.9881	0.8283	0.8826	0.9271	0.8618
Radke and Prausnitz						
a	3.78x10 ⁶	2.23x10 ⁶	9.68 x10 ⁶	2.94x10 ⁶	4.26x10 ⁶	10.78x10 ⁷

Arsenite adsorption over rice husk and wheat husk iron oxide biochar composites

r	6.90	4.11	38.93	11.93	17.82	47.44
b	0.11	0.58	0.24	0.34	0.35	0.18
R²	0.2863	0.9679	0.8270	0.8341	0.7820	0.6477
Toth						
K_T	12.50	68.98	9.4	65.43	90.13	101.81
B_T	0.05	0.02	4.50E-0005	0.05	0.04	0.09
β_T	0.02	0.54	-6.8405	0.78	0.45	0.30
R²	0.6939	0.9897	0.7952	0.8815	0.9261	0.8824
Temkin						
B	2.66	17.53	-	14.90	24.06	-
a	1.00	0.24	-	0.51	0.46	-
R²	0.0593	0.9554	-	0.8743	0.8737	-

CHAPTER 5

ARSENATE [As(V)] ADSORPTION ON RICE HUSK IRON-OXIDE (RHIOB) AND WHEAT HUSK IRON-OXIDE BIOCHAR (WHIOB) COMPOSITES

Sorption studies were conducted at various initial pHs, adsorbent-adsorbate doses, concentrations, temperatures and time intervals to optimize the As(V) sorption process. Mechanism of adsorption of As(V) over RHIOB and WHIOB was optimized and established through batch sorption studies discussed in chapter 6.

5.1. Effect of initial pH

The speciation of As(V) [Figure 6.2, (a)], surface charge experienced by the adsorbate species and its removal is greatly affected by the redox and eH-pH values (Issa, Rajaković-Ognjanović, Marinković, & Rajaković, 2011; Smedley & Kinniburgh, 2002). H_3AsO_4 predominates until pH 2.0. As(V) exists predominately as negatively charged species. At $\text{pH} > 2.3$ As(V) solution is dominated by H_2AsO_3^- and at $\text{pH} > 6.9$ with HAsO_4^- . AsO_4^{3-} appears as pH exceeds 11 (chapter 6, eqn 4-6). The effect of pH from 2.0 to 10.0 was investigated for As(V) adsorption on RHIOB, WHIOB, RHB and WHB at an initial As(V) concentration of 100 $\mu\text{g/L}$ and adsorbent dose of 2.0 g/L [Figure 5.1 (A-B)]. Over this pH range, H_2AsO_3^- needs to be considered up to somewhat above pH 2.3 up to 7.0. Beyond that, both HAsO_4^- and AsO_4^{3-} could adsorb. High As(V) removal occurred over this entire pH range with WHIOB (~99%) and RHIOB (~90%) [Figure 5.1] versus modest removal with WHB (~30%) and RHB (~20%) at their highest points [Figure 5.1]. Thus, iron oxide surfaces adsorb most of the As(V) in WHIOB and RHIOB whereas RHB and WHB only can uptake As(V) on the biochar and its surface mineral ash contents. WHIOB removed more As(V) than RHIOB over the entire pH range [Figure 5.1], most likely because of its higher Fe_3O_4 loading (23.8 wt% in WHIOB versus 18.2 wt% in RHIOB). The higher WHIOB Fe_3O_4 loading provides more surface area for adsorption. As(V) adsorption efficiency increased as pH rose from 2.0 to 6.0 and then dropped somewhat. However, substantial adsorption occurred over the entire pH range. Equilibrium pH values were also recorded [shown in Figure 5.1] for RHIOB, WHIOB, RHB and WHB in the pH range from 3.0 to 4.0 [Figure 4.1]. A very small equilibrium pH rise occurred for WHIOB and RHIOB in the pH range of 4.0-7.0. At high pH (>7.0), the equilibrium pH values using RHIOB and WHIOB increased to ~5.0 [Figure 5.1]. Further kinetic and equilibrium experiments were conducted in pH range 5.0-5.5.

Comparing removal of As(III) and As(V) on RHIOB and WHIOB, As(V) had shown greater percent removal (~90% for RHIOB and ~99% for WHIOB) [Figure 5.1 (A)] as compared to As(III) (~85% for RHIOB and ~97% for WHIOB) under similar experimental conditions [Figure 5.1 (A)].

5.1.1. Adsorption mechanism: pH and pH_{zpc}

Figure 5.2 shows percent removal of As(V) over RHB, WHB, RHIOB and WHIOB with respect to initial pH, pH_{zpc} and fractional composition of As(V) speciation. The pH_{zpc} of RHB, WHB, RHIOB and WHIOB are ~6.8, ~8.3, ~5.5 and ~7.0 respectively [Figure 5.2]. High pH of RHB and WHB without any iron-oxide deposition is attributed to the oxides/hydroxides due to Ca, Mg, Na and K etc. (Zimmerman & Gao, 2013). pH_{zpc} of natural magnetite is 6.5 (Milonjic et al., 1983) to 7.4 (Rajput et al., 2016). Fall in pH_{zpc} in RHIOB and WHIOB is due to the formation of the magnetite surfaces. At $pH < pH_{zpc}$ for magnetite, iron-oxide gets protonated to $-FeOH_2^+$, $Fe-OH^+-Fe$ (Cornell & Schwertmann, 2003). Hence, the surface of magnetite (iron-oxide) gets protonated at $pH < pH_{zpc}$ for RHIOB and WHIOB. Unlike As(III), As(V) exists as negatively charged species at $pH > 2.3$ ($H_2AsO_4^-$). At pH above 2.3 (~5.0-5.5), the negatively charged As(V) is adsorbed over protonated surface of magnetite (iron-oxide) by electrostatic attraction. As the pH rises above pH_{zpc} of RHIOB and WHIOB, electrostatic repulsion between negatively charged magnetite (iron-oxide) surface and negatively charged As(V) species causes decline in percent removal. Detailed description of mechanism of arsenic removal is given in Chapter 6.

5.2. As(V) adsorption kinetics and modelling

As(V) adsorption studies were conducted at 0.5, 1.0 and 2.0 g/L RHIOB and WHIOB doses (Figure 5.3) and 50, 100 and 200 μ g/L As(V) solution concentrations (Figure 5.4).

5.2.1 Effect of adsorbent dose on As(V) percent removal:

Sorption was enhanced by increasing adsorbent dosages. As the adsorbent dosage were increased from 0.5 g/L to 1.0 g/L percent removal of As(V) increased from ~60% to ~85% on RHIOB (figure 5.3 (A)). Percent removal further increased from to ~90% as the dosage increased from 1.0 g/L to 2.0 g/L (figure 5.3 (A)). This

is due to the increase in the availability of the sites that increased the As(V) adsorption. Similarly, with the increase in adsorbent dosage for WHIOB from 0.5 g/L to 1.0 g/L percent removal of As(III) increased from ~80% to ~97% (figure 4.3 (B)). However, unlike RHIOB percent removal of As(V) on WHIOB did not increase as the dosage increased from 1.0 g/L to 2.0 g/L. Thus, increase in adsorbent dosage increased the sites for adsorption of As(V). 2.0 g/L dose of RHIOB and 1.0 g/L of dose of WHIOB were taken to conduct the studies. Maximum percent removal of As(V) was achieved in 12h. After this, significant removal of As(V) on RHIOB and WHIOB was not observed.

5.2.2 Effect of As(V) initial concentration on its adsorption capacity:

Results of the effect of initial concentration of As(V) on its removal capacity on RHIOB and WHIOB are shown in figure 5.4 (A) and (B). There was significant increase in the adsorption capacity from ~25 µg/g, ~45 µg/g to ~82 µg/g [Figure 5.4 (A)] as the initial concentration of As(V) increased from 50 µg/L, 100 µg/L to 200 µg/L on RHIOB. Similarly, adsorption capacity of As(V) increased from ~45 µg/g, ~100 µg/g to ~157.5 µg/g [Figure 5.4 (B)] as the concentration rose from 50 µg/L, 100 µg/L to 200 µg/L on WHIOB. Increase in the removal capacities with increasing initial concentrations is attributed to the availability of greater As(V) molecules per gram of adsorbent (Padmavathy et al., 2016). Moreover, a gradient of chemical potential gets developed between adsorbent sites and As(V) molecules that created a driving force for the movement of molecules towards adsorbent sites. This driving force gets increased as the concentration of As(V) solution increased, unless reaching a point of saturation where all the sites are occupied over adsorbent surface and no further adsorption takes place (Padmavathy et al., 2016; Rahmi & Lelifajri, 2017).

5.2.3. As(V) kinetic modelling

Sorption kinetics data were fitted to both pseudo-first-order [Table 2.1, 1] and pseudo-second-order [Table 2.1, 1] rate equations (Ho & McKay, 1999a). The first order linear fitting plots over different adsorbent dosage and As(V) initial concentrations are shown in Figure 5.5-and Figure 5.6, respectively. Parameters for the first order linear plots are given in Table 5.1. Similarly, the second order linear

and non-linear fitting plots over different adsorbent dosage and As(V) initial concentrations are shown in Figures 5.7-5.8 and Figures 5.10-5.11, respectively. Parameters are calculated and summarised in Table 5.2. The pseudo-second-order linear equation best described As(V) adsorption on RHIOB and WHIOB [Figures 5.7-5.8; Table 5.2]. The experimental linear pseudo-second order q_e values also agreed with the calculated q_e values, and the linear pseudo-second order R^2 values were excellent [Table 5.2]. Second order kinetics is consistent with rate-determining As(V) chemisorption over magnetite surface sites. (Rajput et al., 2016) As(V) uptake at different adsorbent dosages was higher on WHIOB than RHIOB (Table 5.2) due to WHIOB's higher iron loading (Table 3.1). As As(V) concentrations rise, the time-dependent adsorption efficiencies for RHIOB and WHIOB also rose.

Adsorption half-life, $t_{1/2}$, is the time when the reactant concentration decreases by half i.e. 50% of total adsorption. (Mohan, Singh, Sarswat, Steele, Pitmann, et al., 2015) The $t_{1/2}$ values for As(V) adsorption on RHIOB and WHIOB at different initial adsorbent dosages and concentrations are listed in Table 5.2. The As(V) adsorption half-life values obtained for RHIOB and WHIOB dropped as adsorbent dosages rose (from 0.5 g/L to 2.0 g/L). Half-life, $t_{1/2}$ values increased with a rise in As(V) concentrations (50-200 $\mu\text{g/L}$) for RHIOB and WHIOB [Table 5.2].

Kinetic data were analysed according to Boyd (Boyd, Adamson, Myers, et al., 1947) and Reichenberg (Reichenberg, 1953b) to differentiate between the particle and film diffusion using the equations 5-7 and Table 2.1 mentioned in chapter 2. Bt values were obtained for each F value from Reichenberg's Table (Reichenberg, 1953b) at different concentrations. Bt versus time plots for RHIOB and WHIOB at different As(V) concentrations were constructed [Figure 5.9 (a, b)]. RHIOB and WHIOB gave linear plots at all the concentrations. However, at all As(V) concentration (50 – 200 $\mu\text{g/L}$) the linear Bt versus time plot does not pass through origin [Figure 5.9 (a, b)]. Thus, particle diffusion is the rate limiting step for As(V) at all concentrations. Effective diffusion coefficients were calculated from Bt versus time plots using equations given summarised in Table 2.1, (3). D_i values of RHIOB and WHIOB increased as As(V) concentration increased from 50

$\mu\text{g/L}$ to $100 \mu\text{g/L}$ and then fell with a further concentration rise from 100 to $200 \mu\text{g/L}$ [Figure 5.9]. This drop in D_i may result from a mobility decrease of As(V) ions due to the increase in retarding force acting on diffusing ions. The parameters are summarised in Table 5.3.

5.3 Thermodynamic studies

Thermodynamic parameters were determined by carrying out adsorption experiments at three different temperatures 283 K , 298 K and 318 K . The distribution coefficient K_d for the adsorption, was obtained from equations given in chapter 2, Table 2.1. For this study graph was plotted, $\ln K_d$ vs $1/T$ (Vant Hoff equation) [Figure 5.12]. From graph values of enthalpy ΔH^0 and entropy ΔS^0 were obtained using equation given in chapter 2, Table 2.1. Gibbs free energy change ΔG^0 was obtained from equation mentioned in chapter 2, Table 2.1. The results are tabulated in Table 5.4.

The positive value of ΔH^0 (28.76 KJ/mol ; 24.34 KJ/mol) indicates that the adsorption process is endothermic in nature [Figure 5.12]. This is also indicated with the increasing value of K_d [Table 5.4]. Positive value of entropy ΔS^0 (0.11 KJ/mol K ; 0.09 KJ/mol K) after As(V) adsorption suggests that system has moved towards greater randomness or disorderness, and is irreversible. This is in agreement with the negative value of Gibbs free energy ΔG^0 suggesting that As(V) adsorption is spontaneous in nature (Alam et al., 2018; S. Liu et al., 2017). This suggests strong electrostatic attraction developed between negatively charged arsenate oxyanions species (H_2AsO_3^-) and positively charged surface of iron oxide (FeOH^+).

5.4 As(V) adsorption isotherm

Sorption isotherm experiments were conducted at 10 , 25 and $40 \text{ }^\circ\text{C}$ between pH 5.0 and 5.5 and initial As(V) concentrations varying from $50 \mu\text{g/L}$ to $1000 \mu\text{g/L}$ [Figure 5.13-5.20]. This concentration range was selected based on arsenic concentrations reported worldwide in ground and surface waters. Equilibrium As(V) adsorption amounts on RHIOB and WHIOB increased going from $10 \text{ }^\circ\text{C}$ to $45 \text{ }^\circ\text{C}$ [Table 5.5]. Thus, adsorption is endothermic. With rising temperature,

adsorptive capacity increased with increasing adsorbent mobility (Baig et al., 2014b). WHIOB's adsorption capacity was higher than RHIOB's, in accord with WHIOB's modestly higher surface area and significantly higher iron content [Table 5.5].

Freundlich, (Herbert Freundlich, 1907) Langmuir, (Langmuir, 1916) Temkin, (M. I. Temkin & V. Pyzhev, 1940) Sips or Langmuir-Freundlich, (Sips, 1948) Redlich-Peterson, (OJDL Redlich & D L Peterson, 1959) Radke and Prausnitz, (Radke & Prausnitz, 1972b) and Toth (Toth, 1971) isotherms (Table 2.2, respectively) were used to fit the sorption equilibrium data and to determine the adsorption behaviour, capacity, and parameters used in fixed-bed reactor design. The Freundlich isotherm (Herbert Freundlich, 1907) describes (Table 2.2, 1) the adsorption equilibrium on heterogeneous surfaces. The Langmuir isotherm (Table 2.2, 2) assumes a uniform sorbent surface sites with identical energies, (Langmuir, 1916) where adsorption occurs as a single surface adsorbate layer. The Sips isotherm (Sips, 1948) is a combination of the Langmuir and Freundlich isotherms (Table 2.2, 3). The Temkin model is described by Table 2.2, 4. The Redlich-Peterson model (Table 2.2, 5) (OJDL Redlich & D L Peterson, 1959) is a three parameter model, describing equilibrium on heterogeneous surfaces and contains a heterogeneity factor. The three parameter Radke and Prausnitz isotherm, (Radke & Prausnitz, 1972b) derived from thermodynamic considerations (Table 2.2, 6), is capable of describing data over a wide concentration range. The Toth isotherm, (Toth, 1971) an empirical model, assumes an asymmetric quasi-Gaussian distribution of site energies (Table 2.2, 7). This model describes an improved fit versus Langmuir isotherm model and is often used to describe heterogeneous systems. The Koble-Corrigan isotherm (Robert A. Koble & Thomas E. Corrigan, 1952) is also a three parameters model (Table 2.2, 8).

Langmuir fittings of As(V) sorption equilibrium data for WHIOB and RHIOB are given [Figure 5.13] with the fittings for the other isotherm models [Figures 5.14-5.20]. Parameters and regression coefficient from all eight of these non-linear isotherm fittings are summarized in Table 5.5. The fits at 25, 35 and 45⁰C for all RHIOB and WHIOB adsorption data were ranked based on their R² values.

Arsenate adsorption over rice husk and wheat husk iron oxide biochar composites

At 45⁰C, the Toth ($R^2 = 0.988$) equation fit the RHIOB as well as WHIOB ($R^2 = 0.998$) equilibrium data best. The isotherm constant β_T values for RHIOB at 45⁰C are given in Table 5.5 and suggests As(V) adsorption to the Langmuir isotherm (Azmi et al., 2017; Kumar et al., 2010). Thus, RHIOB and WHIOB has a homogenous adsorption surface that agrees with the predominant adsorption on the iron oxide surfaces of the hybrid adsorbent (Mohan, Rajput, et al., 2011; Mohan, Sarswat, et al., 2011).

Monolayer adsorption capacities (Q^0) are reported from the Langmuir adsorption isotherm [Figure 5.13; Table 5.5]. The maximum adsorption capacities were 228.96 $\mu\text{g/g}$ (10⁰C); 285.71 $\mu\text{g/g}$ (25⁰C) and 386.88 $\mu\text{g/g}$ (45⁰C) for RHIOB and 346.84 $\mu\text{g/g}$ (10⁰C), 399.12 $\mu\text{g/g}$ (25⁰C) and 421.45 $\mu\text{g/g}$ (45⁰C) for WHIOB [Table 5.5, figure 5.13]. These values are very close to the experimental capacities of 220.85 $\mu\text{g/g}$, 276.3 $\mu\text{g/g}$ and 380.2 $\mu\text{g/g}$ for RHIOB and 286.3 $\mu\text{g/g}$, 365.2 $\mu\text{g/g}$ and 410.3 $\mu\text{g/g}$ for WHIOB [Table 5.5]. Adsorption capacities go up with an increase in temperature for both RHIOB and WHIOB, agreeing with endothermic As(V) adsorption. This As(V) adsorption increase when temperature rises may be due to both endothermic chemical adsorption and an increase in adsorbent ion mobility. Both would raise adsorption efficiencies as temperature rises. (Baig et al., 2014b) Langmuir monolayer adsorption capacities of RHIOB and WHIOB are comparable to many adsorbents (Table 5.5). High sorption capacities of many adsorbents are due to the high As(V) concentrations taken in performing the batch experiments. Some adsorbents capable of remediating arsenic at high concentrations have failed to work in low concentration range. Our present studies were purposely conducted at low As(V) concentrations (50-1000 $\mu\text{g/L}$) where less data exists and because many environmental sites have concentrations in this range. Therefore, these studies may result into low adsorption capacities. RHIOB and WHIOB successfully remediated As(V) at concentrations usually present in the actual water bodies (Table 5.5).

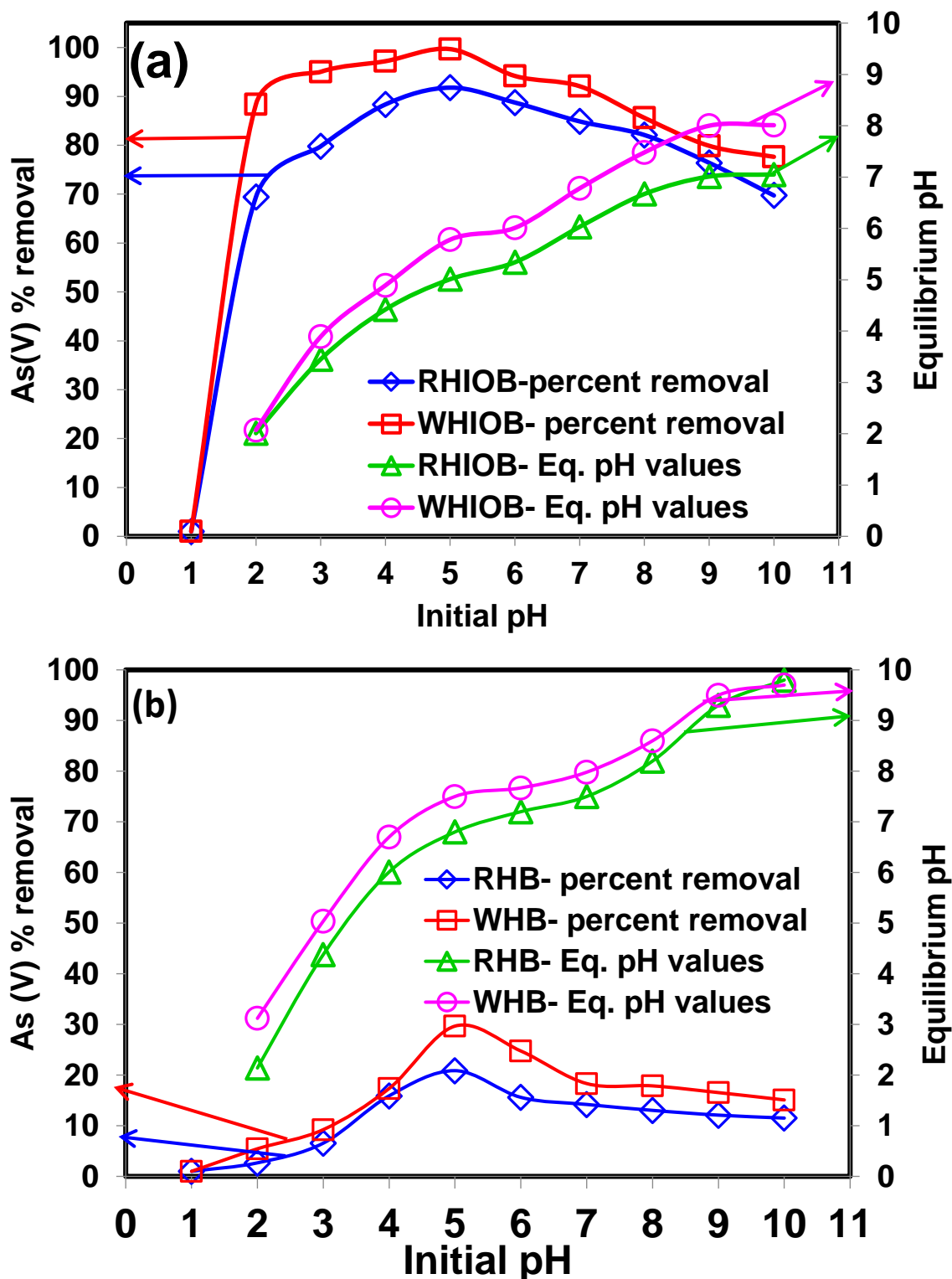


Figure 5.1. Effect of initial pH and equilibrium pH on As(V) removal by (a) RHIOB and WHIOB and (b) their precursor biochars RHB and WHB (adsorbent dose= 2.0 g/L, RHIOB and 1.0 g/L WHIOB; initial As(V) concentration= 100 µg/L; agitation speed= 100 rpm, temperature= 25 °C, contact time= 24 h)

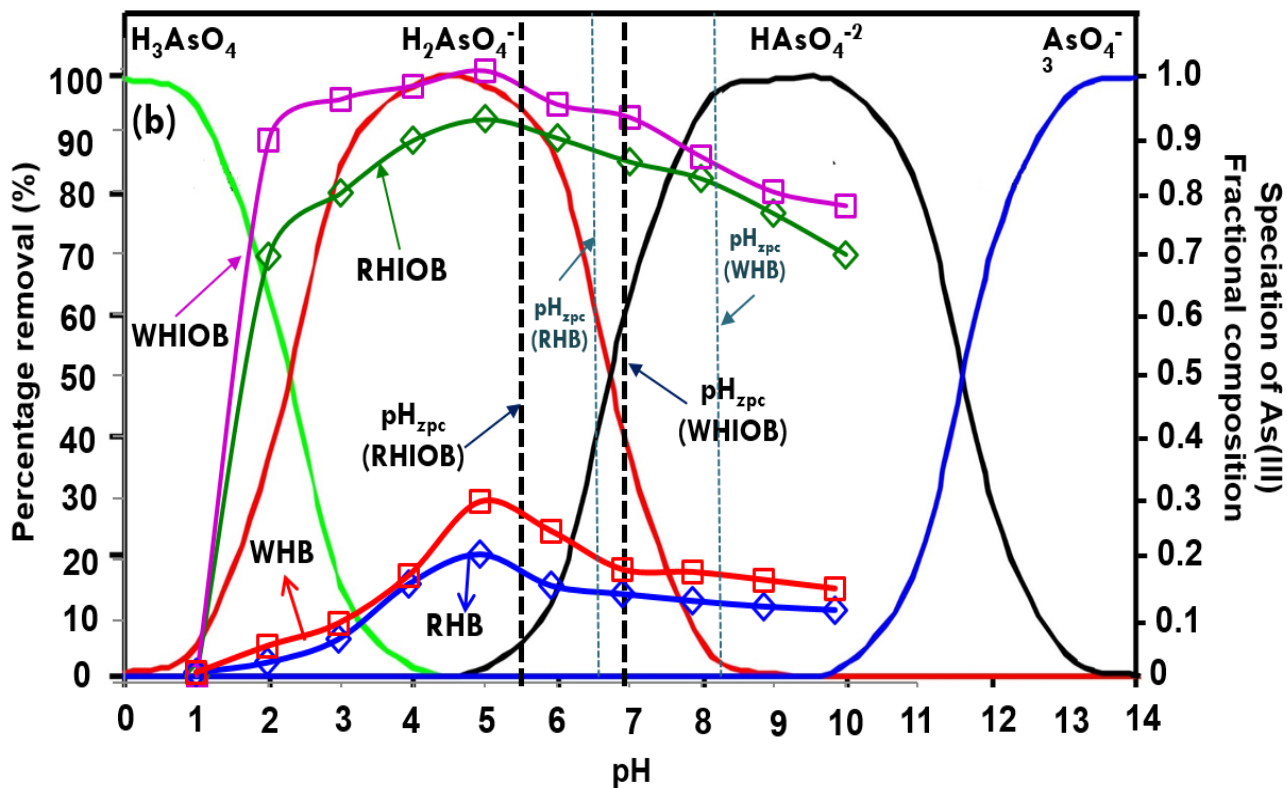


Figure 5.2. Effect of initial pH with respect to pH_{zpc} and fractional composition speciation on percent As(V) removal by RHIOB, WHIOB and their precursor biochars RHB and WHB (adsorbent dose= 2.0 g/L, 1.0 g/L; initial As(V) concentration= 100 $\mu\text{g/L}$; agitation speed= 100 rpm, temperature= 25 $^{\circ}\text{C}$, contact time= 24 h)

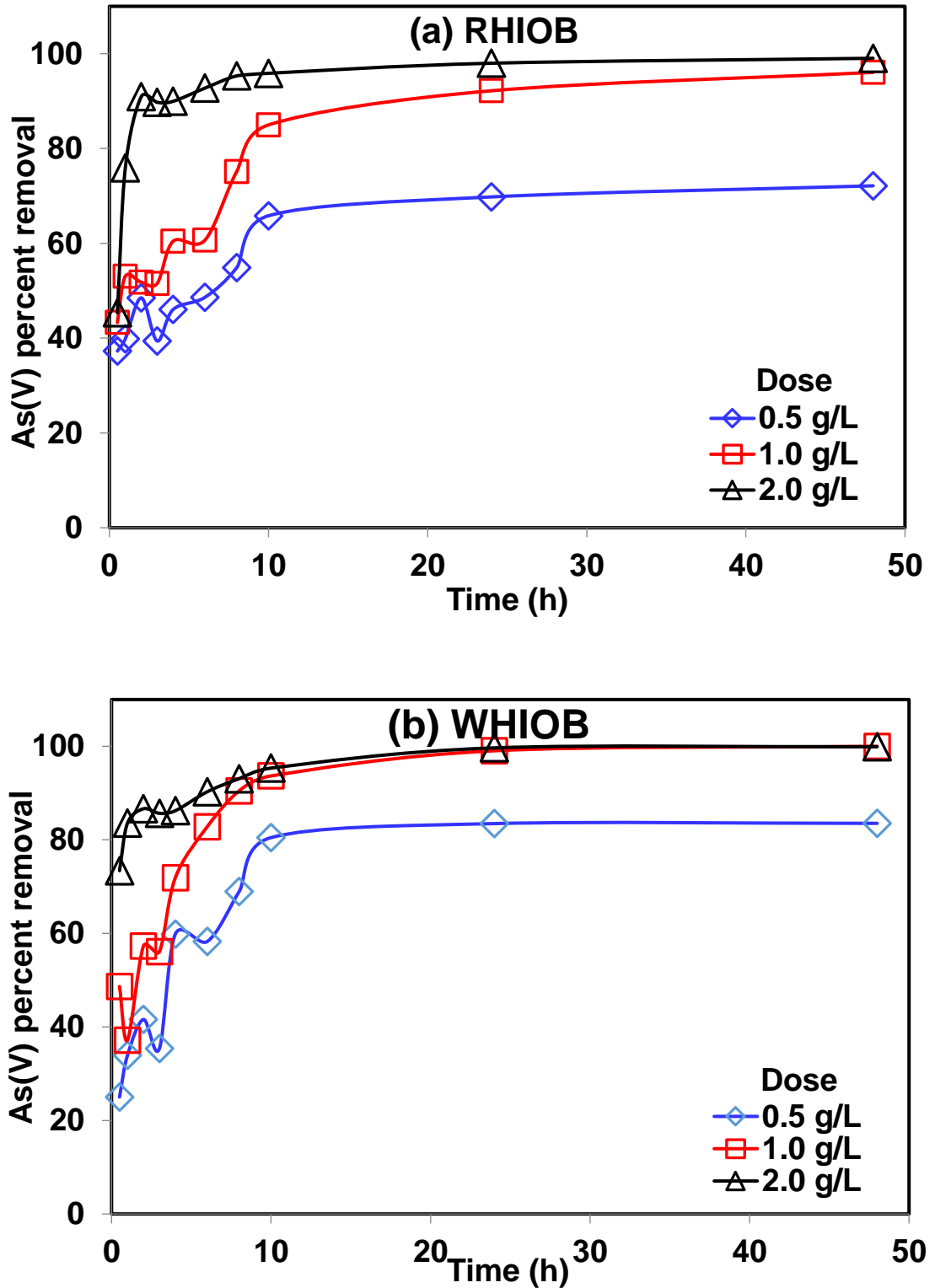


Figure 5.3. Effect of adsorbent dose on percent As(V) removal by (a) RHIOB and (b) WHIOB (pH= 5.0; As(V) concentration=100 μ g/L; temp= 25 $^{\circ}$ C; agitation= 100 rpm; particle size= 30-50 B.S.S. mesh).

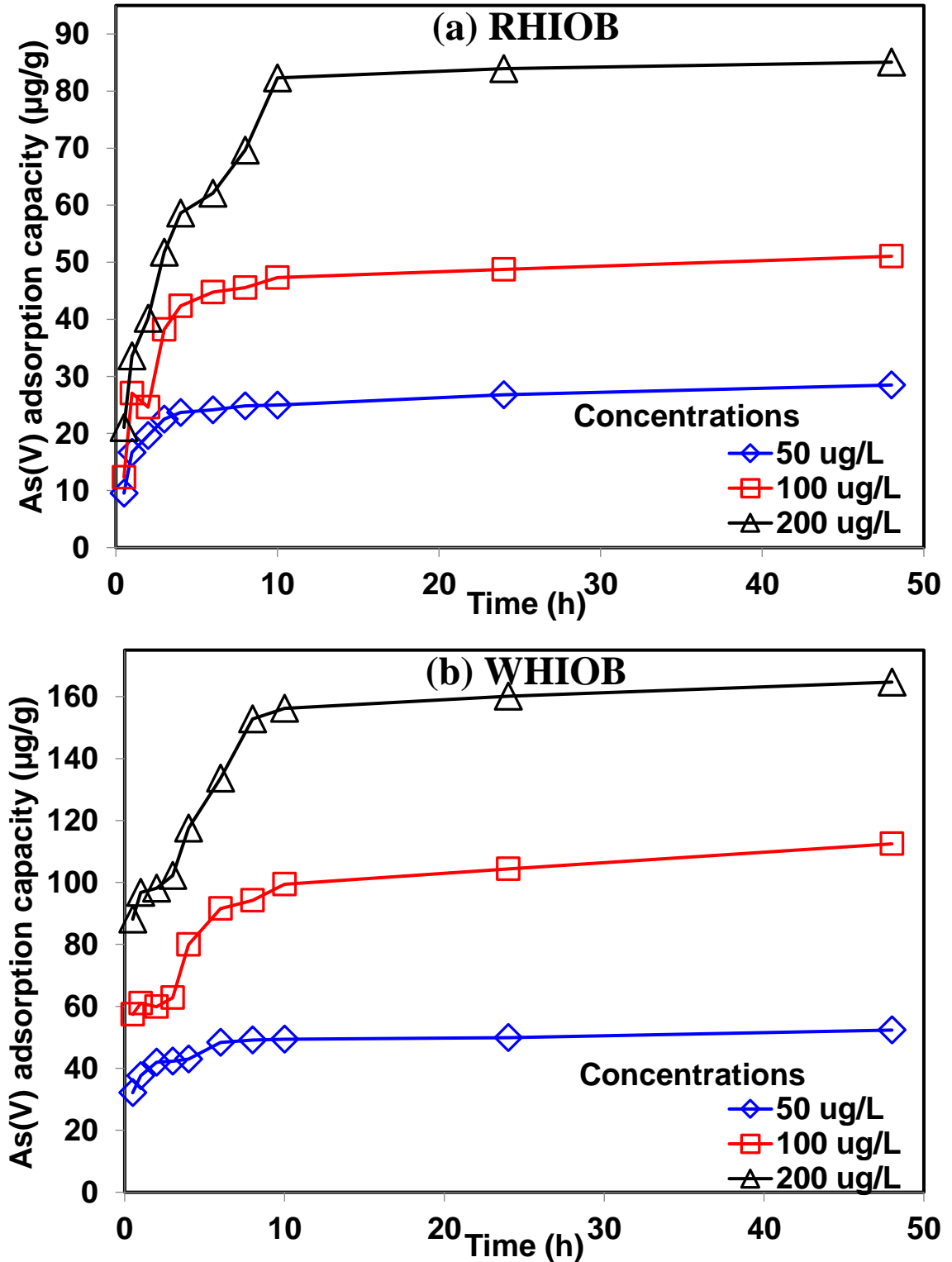


Figure 5.4. Effect of adsorbent concentration on adsorption capacity As(V) ($\mu\text{g/g}$) removal by (a) RHIOB and (b) WHIOB (pH= 5.0; As(V) concentration= $100\mu\text{g/L}$; temp= 25°C ; agitation= 100 rpm; particle size= 30-50 B.S.S. mesh).

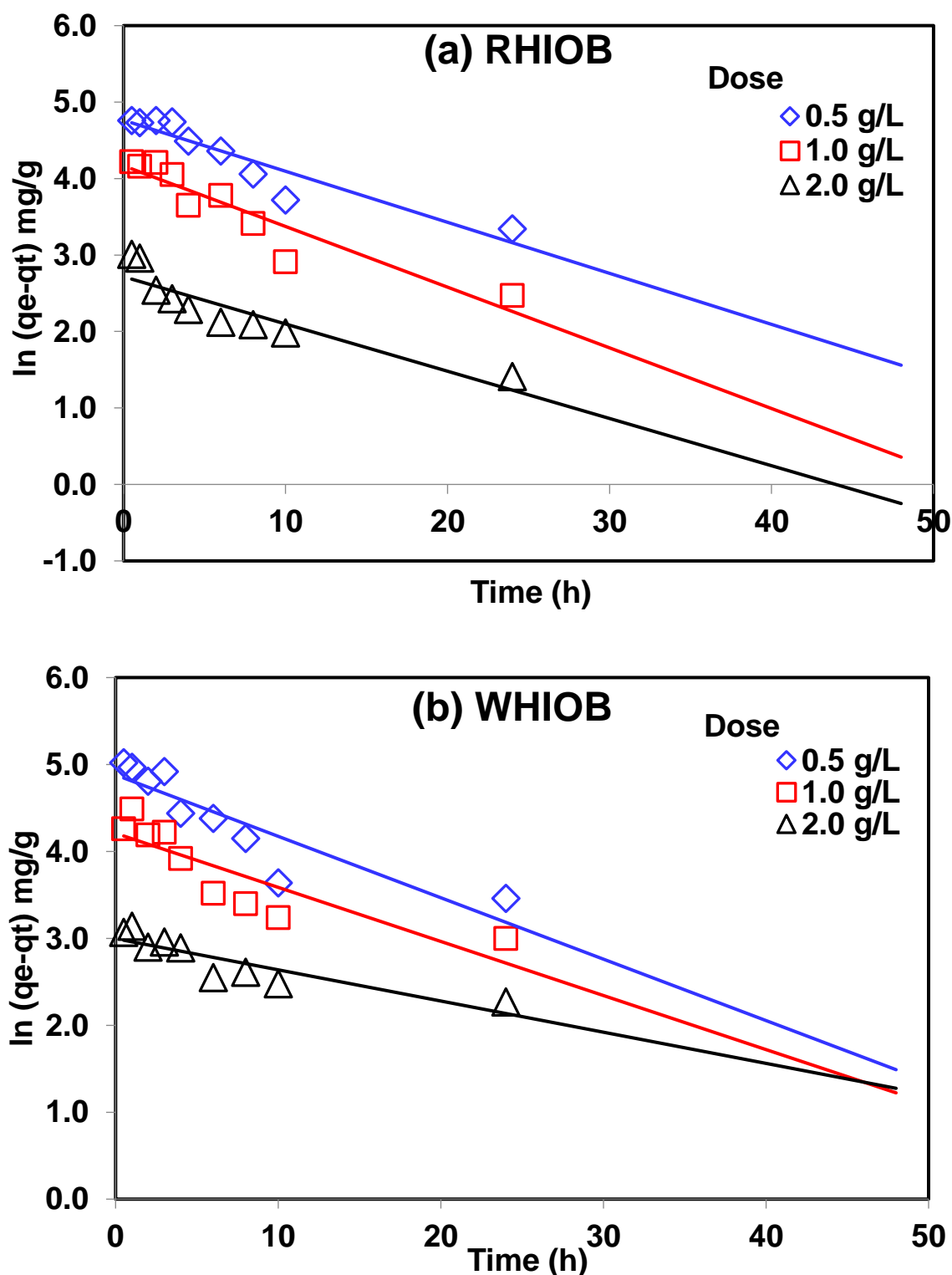


Figure 5.5. Pseudo-first-order linear kinetic plots of As(V) adsorption at different doses (a) RHIOB and (b) WHIOB (pH= 5.0; As(V) concentration=100 μ g/L; temp= 25 $^{\circ}$ C; agitation= 100 rpm; particle size= 30-50 B.S.S. mesh).

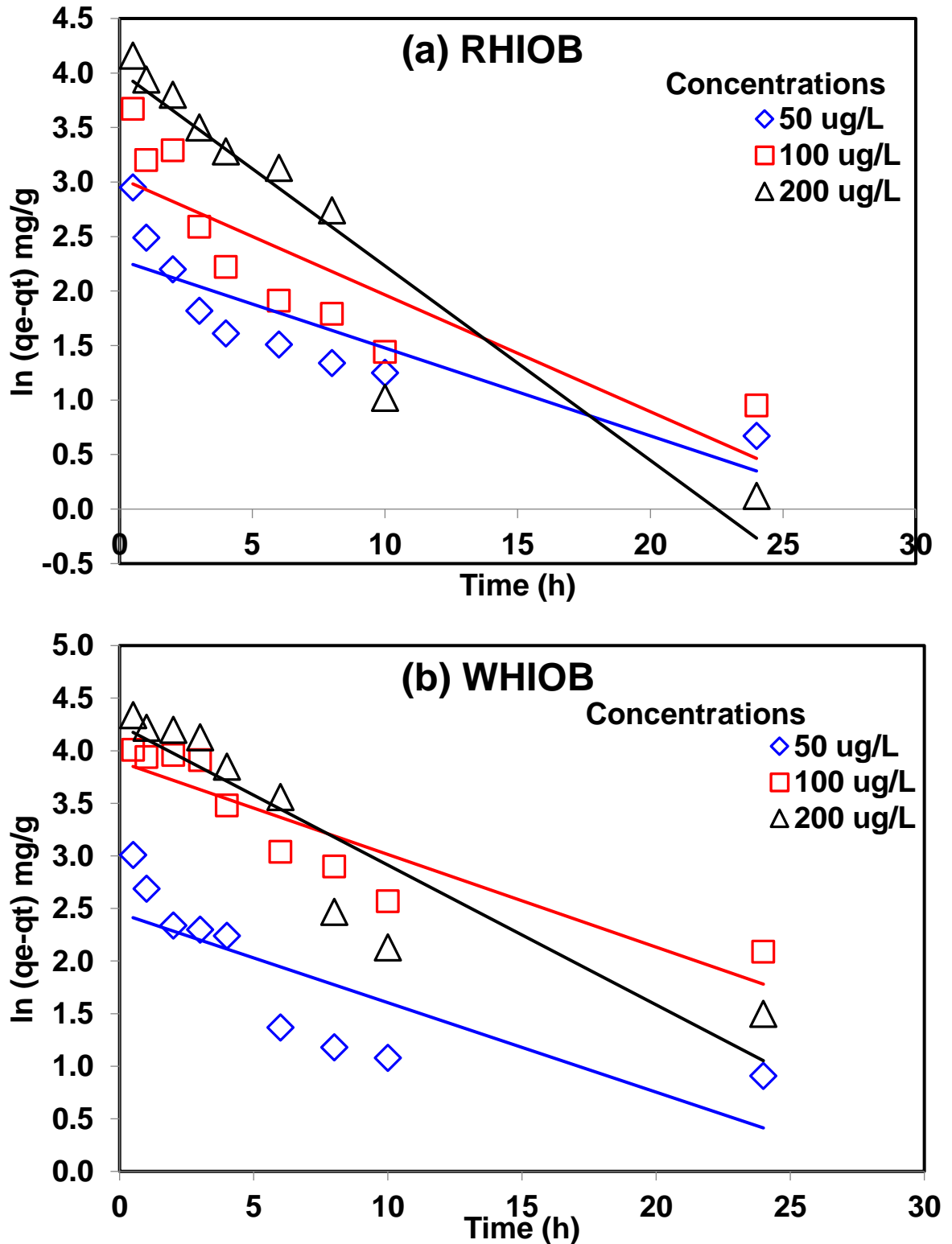


Figure 5.6. Pseudo-first-order linear kinetic plots of As(V) adsorption at different concentrations (a) RHIOB and (b) WHIOB (pH= 5.0; As(V) concentration=100µg/L; temp= 25°C; agitation= 100 rpm; particle size= 30-50 B.S.S. mesh).

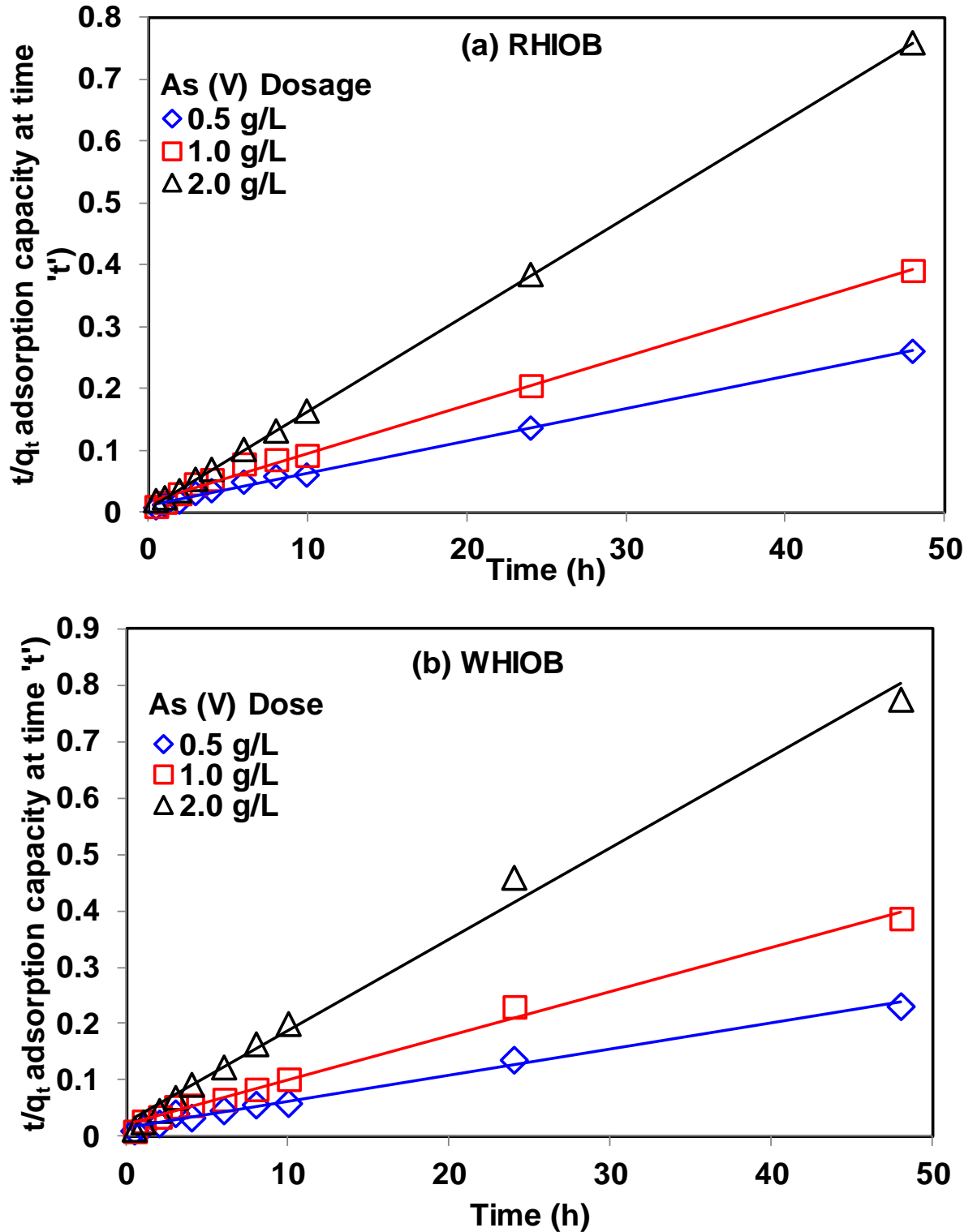


Figure 5.7. Pseudo-second-order linear kinetic plots of As(V) adsorption at different dose (a) RHIOB and (b) WHIOB (pH= 5.0; As(V) concentration=100µg/L; temp= 25°C; agitation= 100 rpm; particle size= 30-50 B.S.S. mesh).

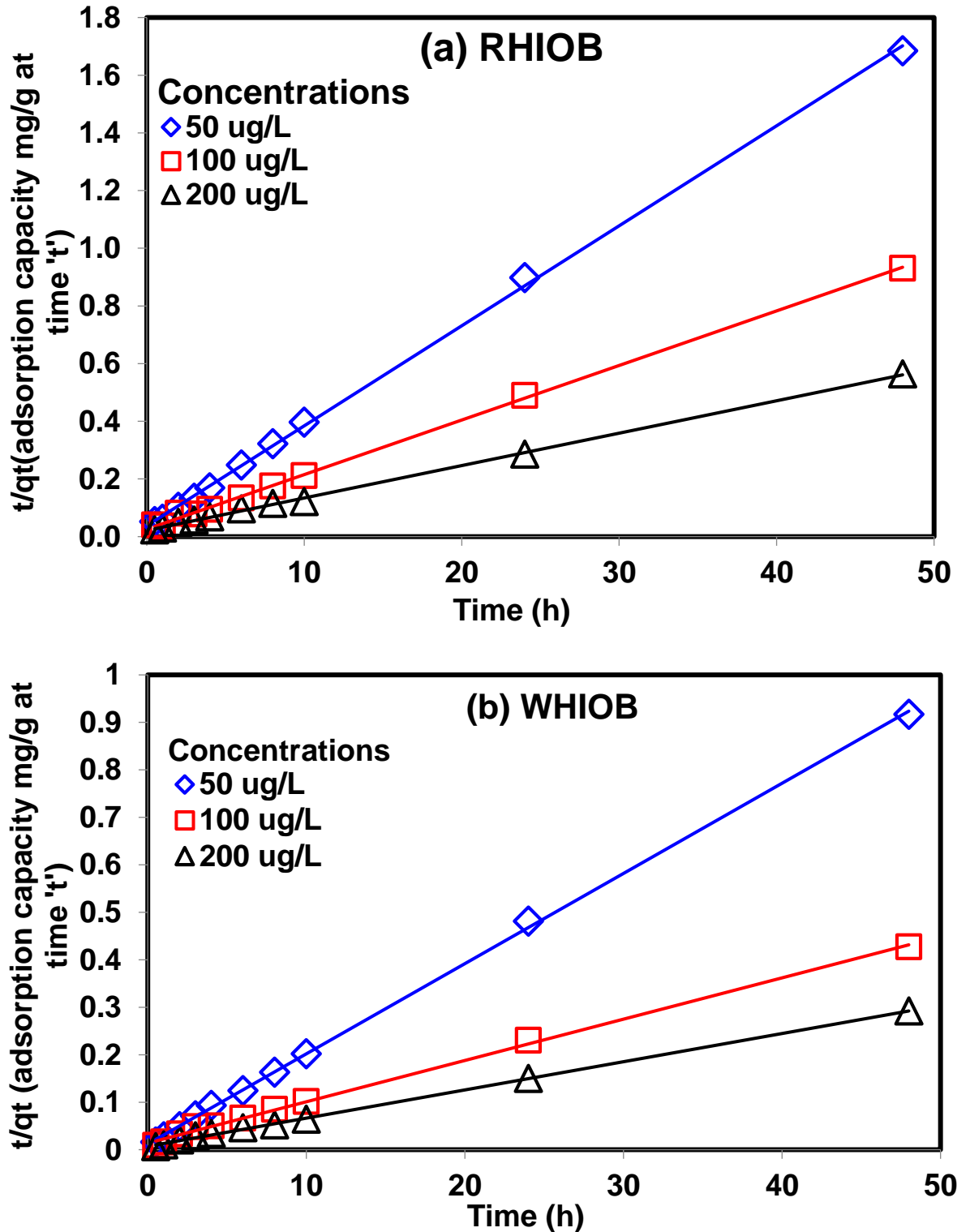


Figure 5.8. Pseudo-second-order linear kinetic plots for As(V) adsorption at different concentrations for (a) RHIOB and (b) WHIOB (pH= 5.0; dose= 2.0 g/L and 1.0 g/L respectively; temp= 25 °C; agitation= 100 rpm; particle size= 30- 50 B.S.S. mesh).

Arsenate adsorption over rice husk and wheat husk iron oxide biochar composites

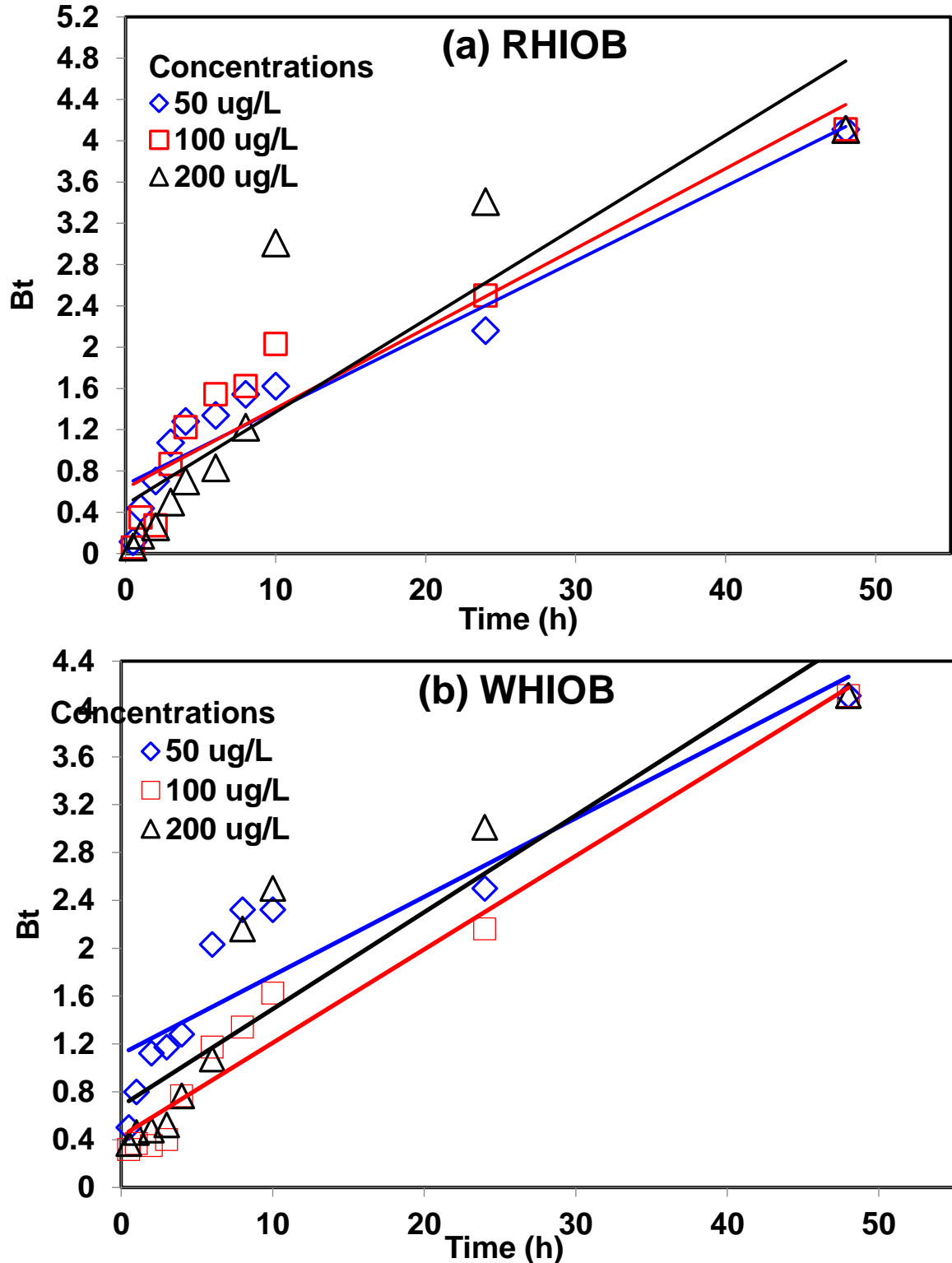


Figure 5.9. Boyd's model plots for As(V) adsorption at different concentrations for (a) RHIOB and (b) WHIOB (pH=5.0 ; dose= 2.0 g/L and 1.0 g/L respectively; temp= 25 °C ; agitation= 100 rpm; particle size= 30- 50 B.S.S. mesh).

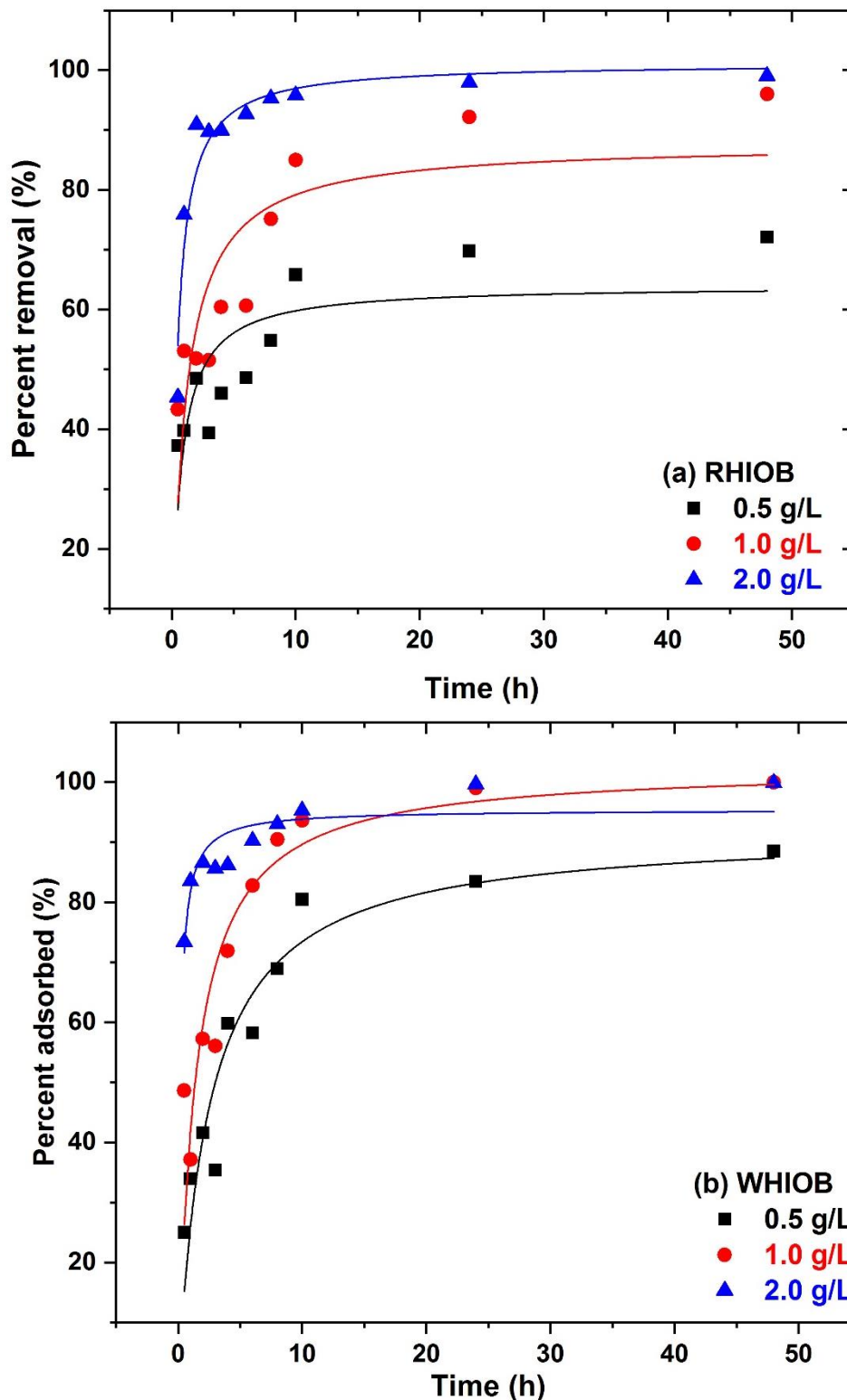


Figure 5.10. Pseudo-second-order non-linear kinetic plots of As(V) adsorption at different doses (a) RHIOB and (b) WHIOB (pH= 5.0; As(V) concentration=100 μ g/L; temp= 25 $^{\circ}$ C; agitation= 100 rpm; particle size= 30-50 B.S.S. mesh).

Arsenate adsorption over rice husk and wheat husk iron oxide biochar composites

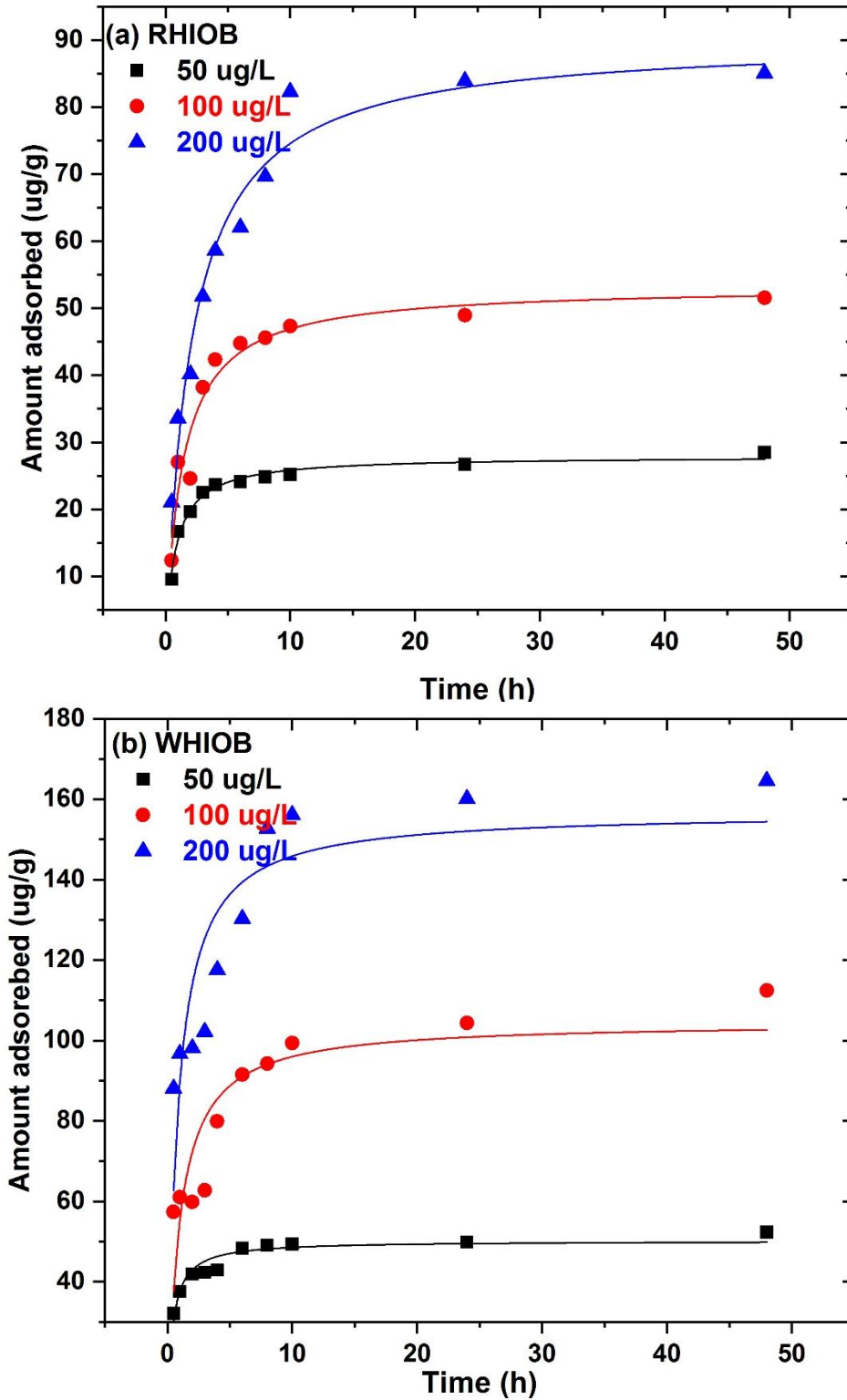


Figure 5.11. Pseudo-second-order non-linear kinetic plots of As(V) adsorption at different concentrations (a) RHIOB and (b) WHIOB (pH= 5.0; As(V) dose= 1.0 g/L, 2.0 g/L; temp= 25⁰C; agitation= 100 rpm; particle size= 30-50 B.S.S. mesh)

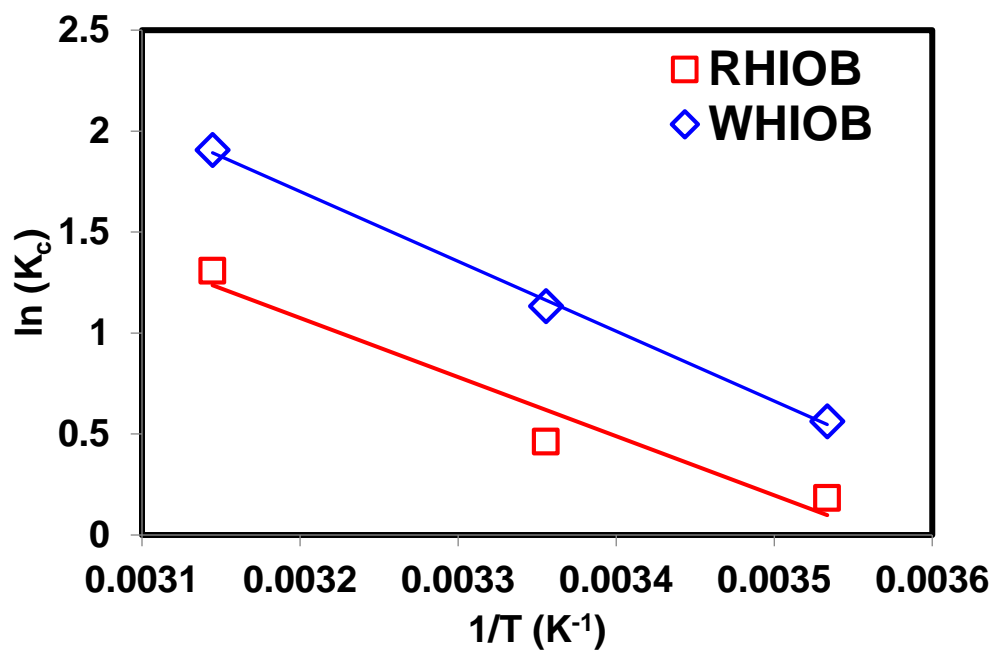


Figure 5.12. Linear plot of $\ln K_c$ versus $1/T$ for the calculation of thermodynamic parameters to evaluate As(V) adsorption onto RHIOB and WHIOB.

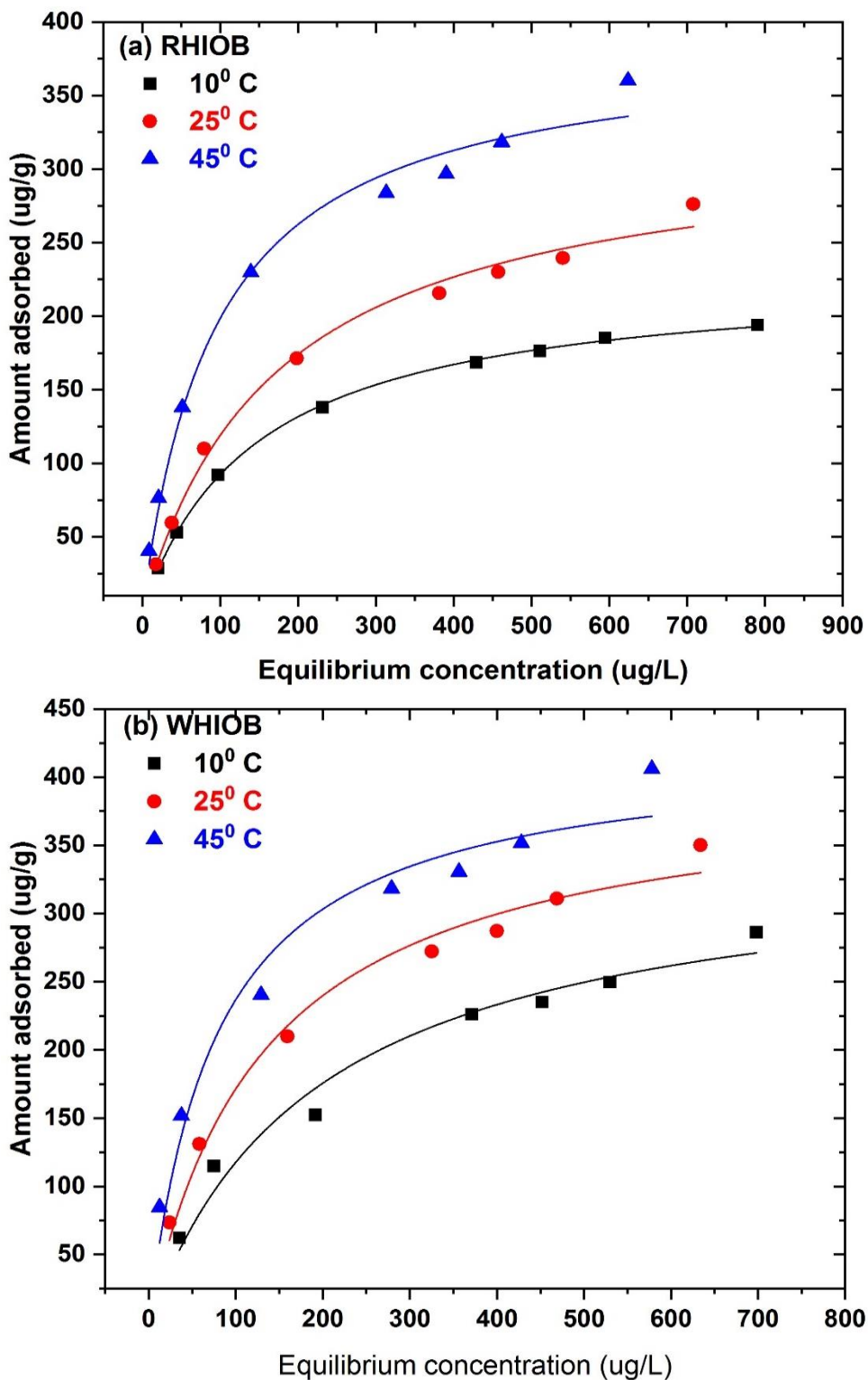


Figure 5.13. Langmuir non-linear adsorption isotherms of As(V) adsorption by (a) RHIOB and (b) WHIOB at different temperatures (pH= 5.0 ; concentration= 100 ug/L; temp= 10 °C, 25 °C, 45 °C; agitation= 100 rpm; particle size= 30- 50 B.S.S. mesh).

Arsenate adsorption over rice husk and wheat husk iron oxide biochar composites

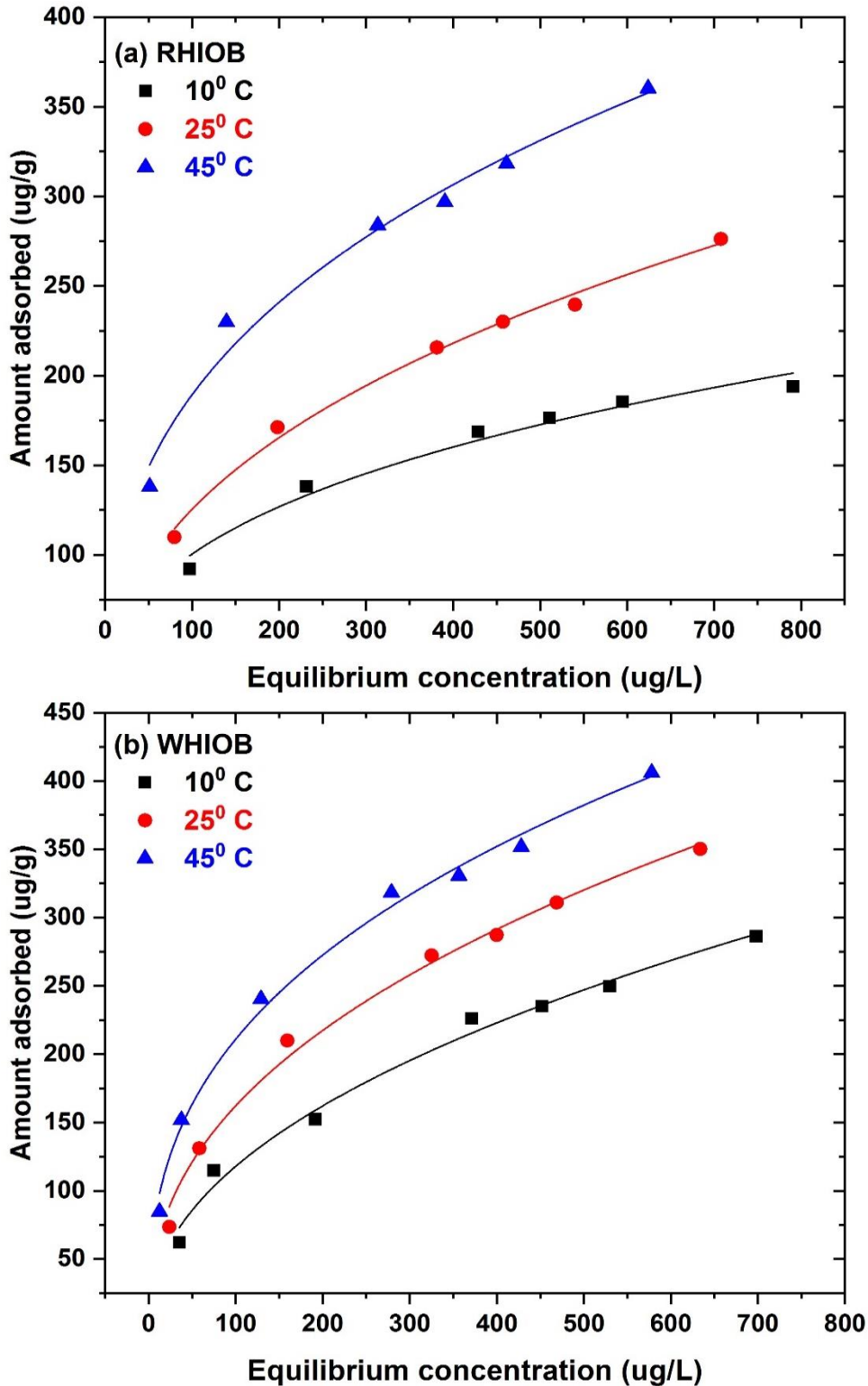


Figure 5.14. Freundlich non-linear adsorption isotherms of As(V) adsorption by (a) RHIOB and (b) WHIOB at different temperatures (pH= 5.0 ; concentration= 100 ug/L; temp= 10 °C, 25 °C, 45 °C; agitation= 100 rpm; particle size= 30- 50 B.S.S. mesh).

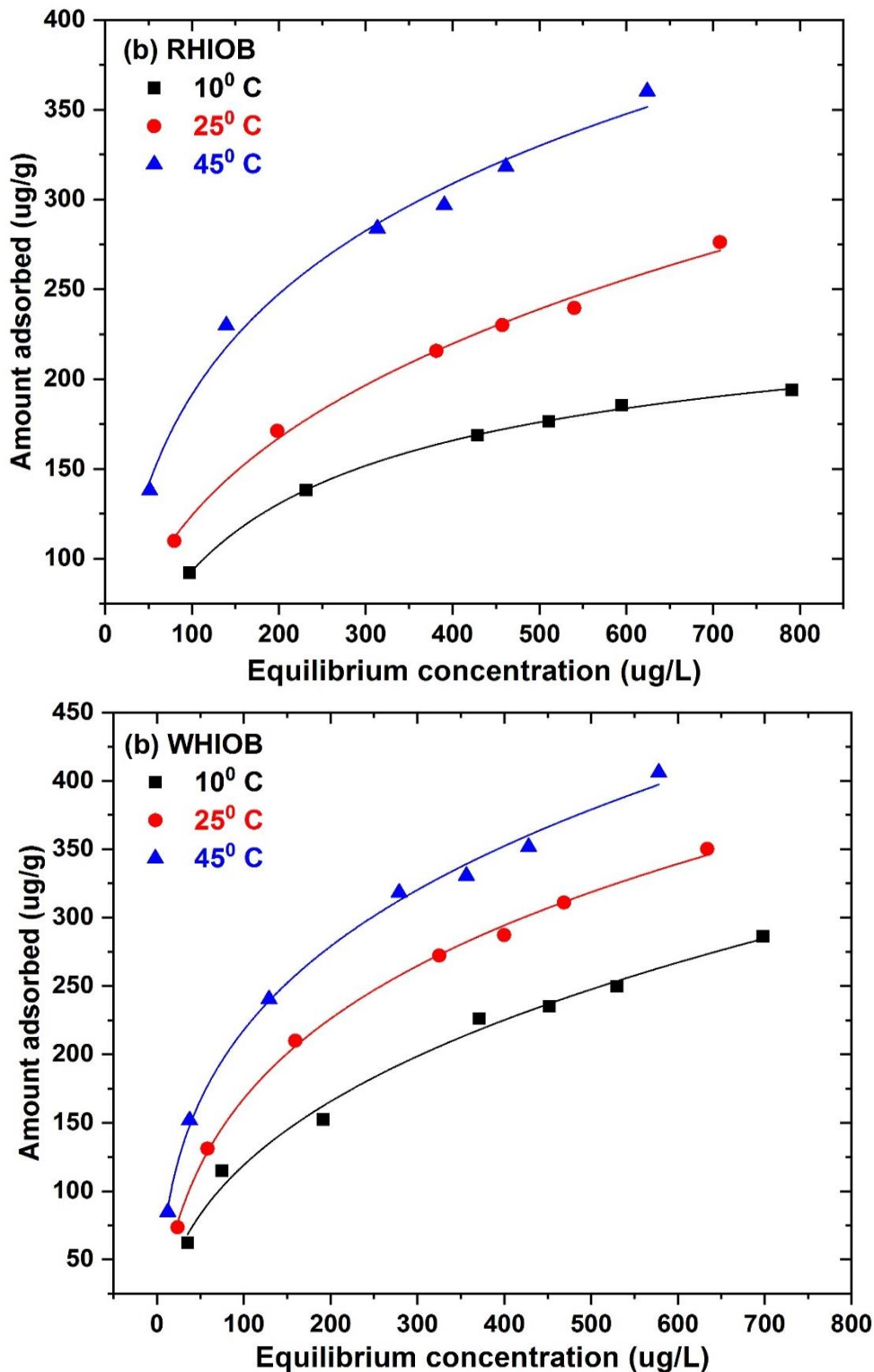


Figure 5.15. Redlich-Peterson non-linear adsorption isotherms of As(V) adsorption by (a) RHIOB and (b) WHIOB at different temperatures (pH= 5.0 ; concentration= 100 ug/L; temp= 10 °C, 25 °C, 45 °C; agitation= 100 rpm; particle size= 30- 50 B.S.S. mesh)

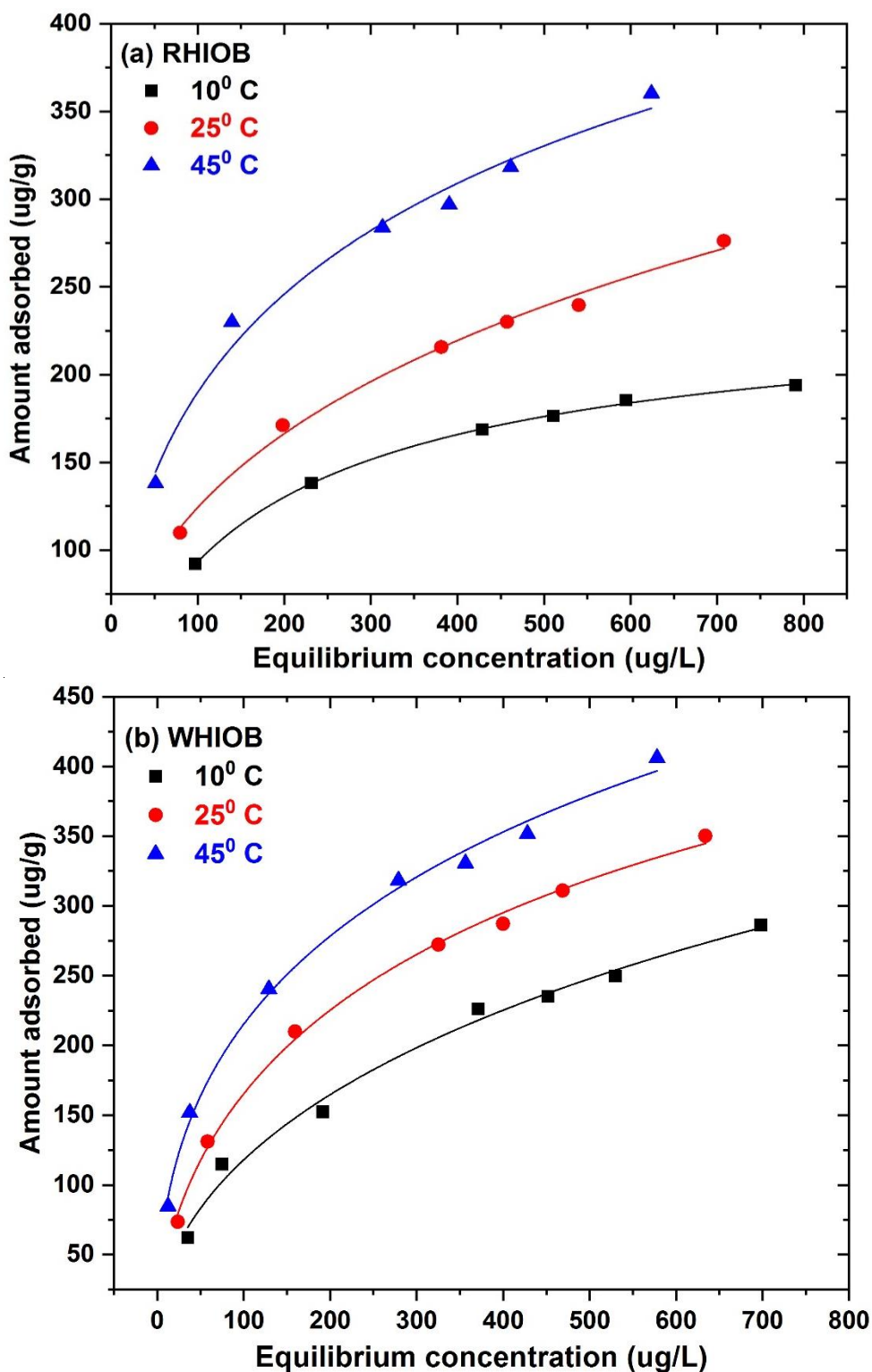


Figure 5.16. Sips non-linear adsorption isotherms of As(V) adsorption by (a) RHIOB and (b) WHIOB at different temperatures (pH= 5.0 ; concentration= 100 ug/L; temp= 10 °C, 25 °C, 45 °C; agitation= 100 rpm; particle size= 30- 50 B.S.S. mesh)

Arsenate adsorption over rice husk and wheat husk iron oxide biochar composites

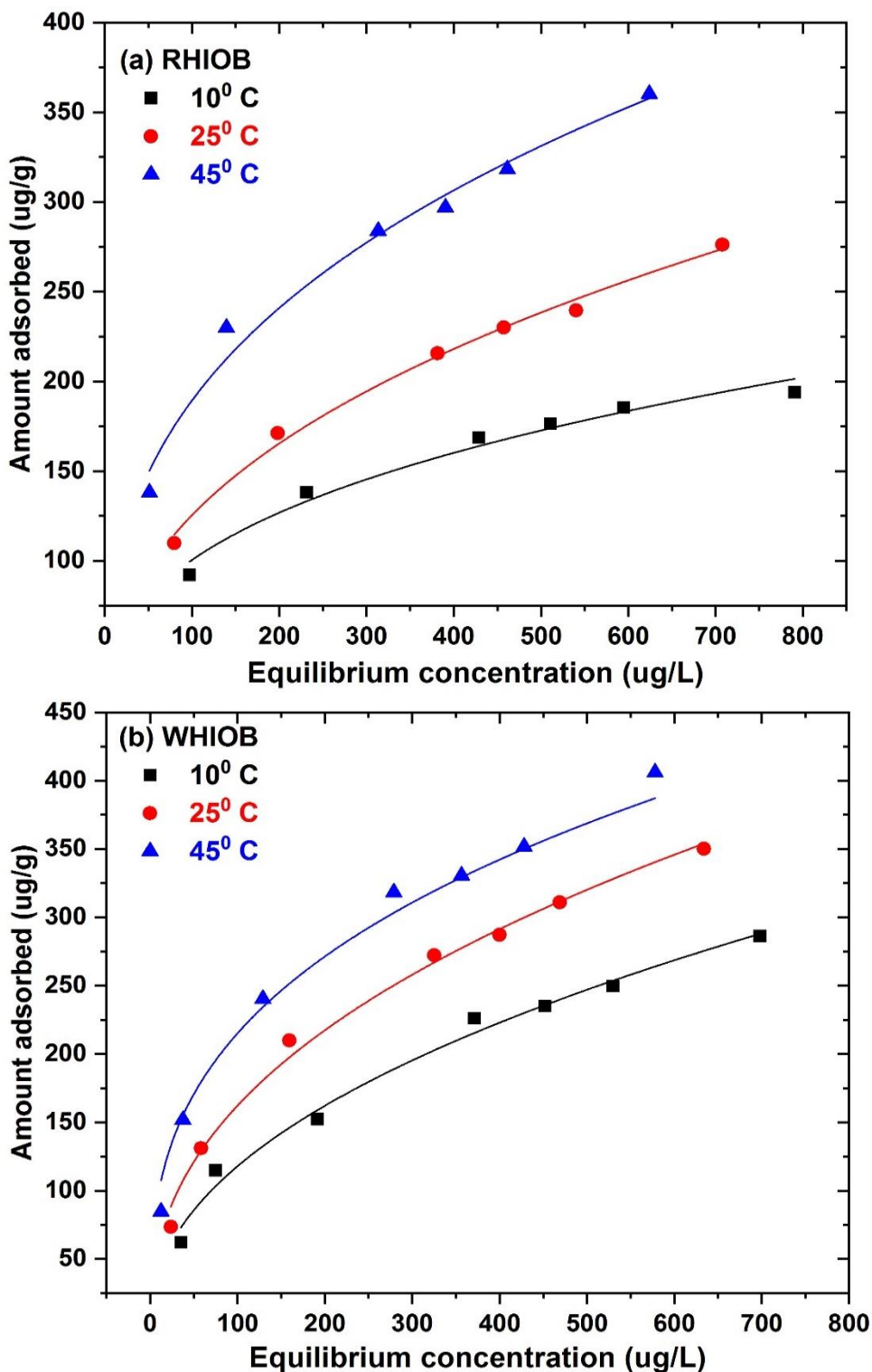


Figure 5.17. Koble-Corrigen non-linear adsorption isotherms of As(V) adsorption by (a) RHIOB and (b) WHIOB at different temperatures (pH= 5.0 ; concentration= 100 ug/L; temp= 10 °C, 25 °C, 45 °C; agitation= 100 rpm; particle size= 30- 50 B.S.S. mesh)

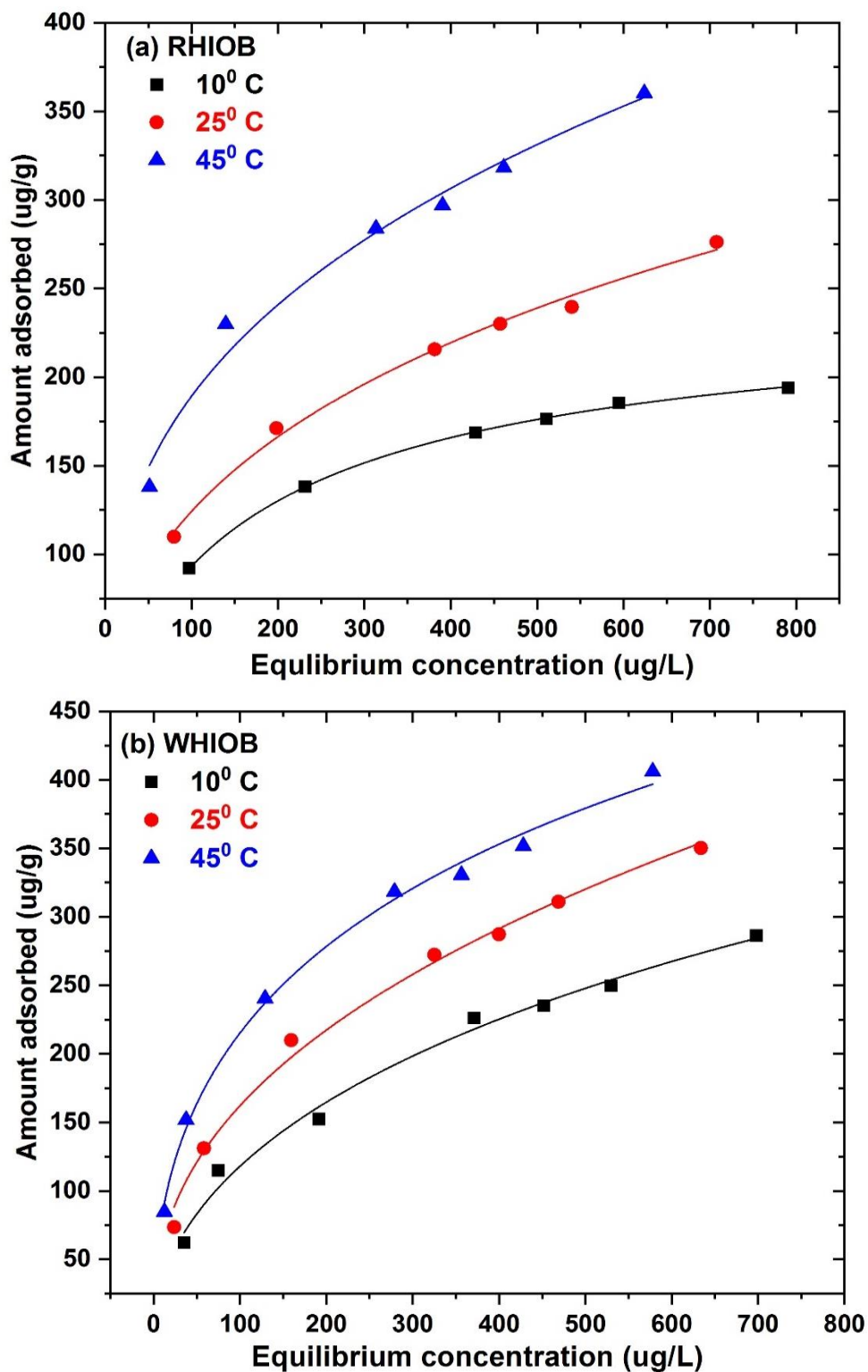


Figure 5.18. Radke-Prausnitz non-linear adsorption isotherms of As(V) adsorption by (a) RHIOB and (b) WHIOB at different temperatures (pH= 5.0 ; concentration= 100 ug/L; temp= 10 °C, 25 °C, 45 °C; agitation= 100 rpm; particle size= 30- 50 B.S.S. mesh)

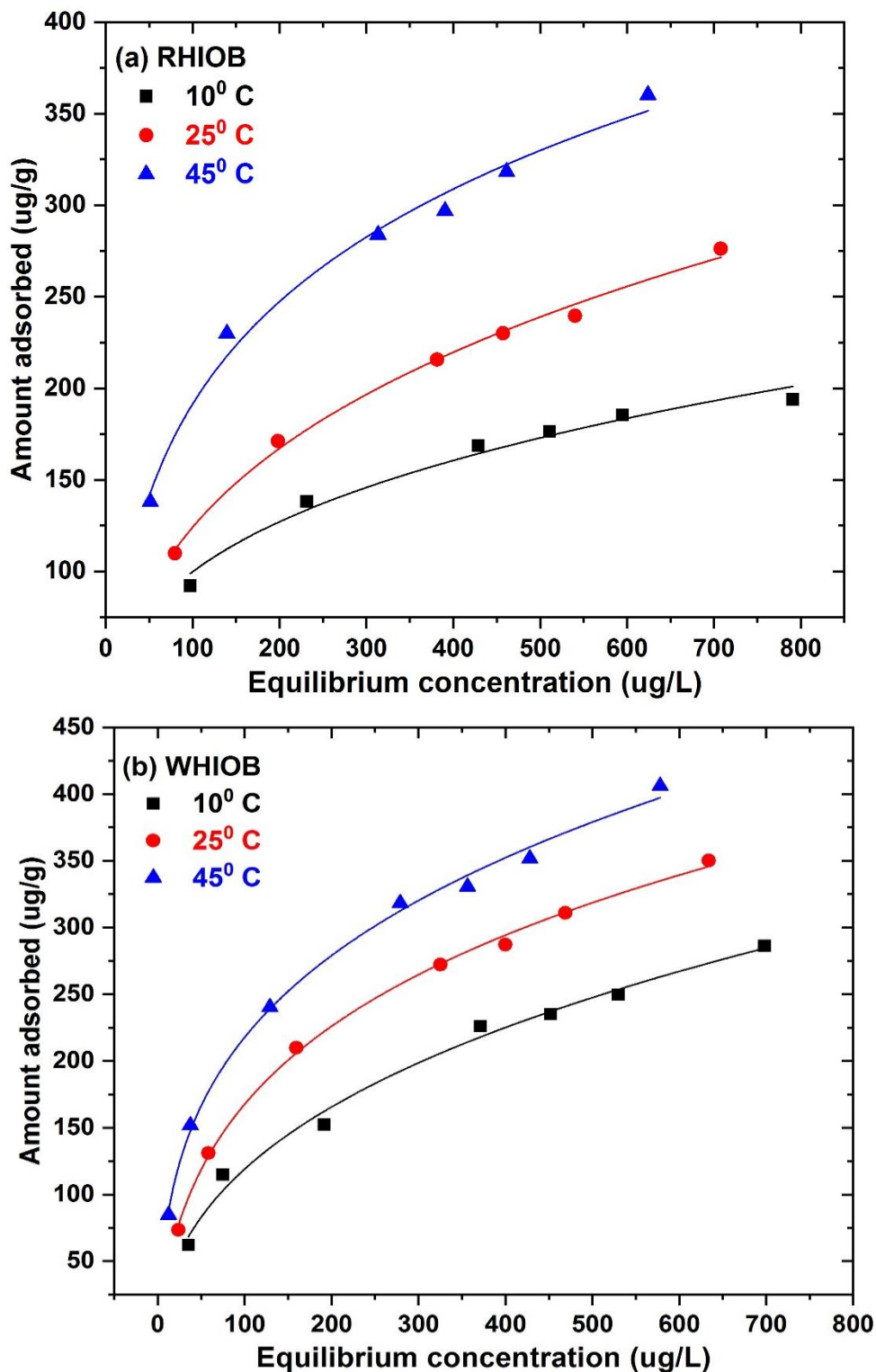


Figure 5.19. Both non-linear adsorption isotherms of As(V) adsorption by (a) RHIOB and (b) WHIOB at different temperatures (pH= 5.0 ; concentration= 100 ug/L; temp= 10 °C, 25 °C, 45 °C; agitation= 100 rpm; particle size= 30-50 B.S.S. mesh)

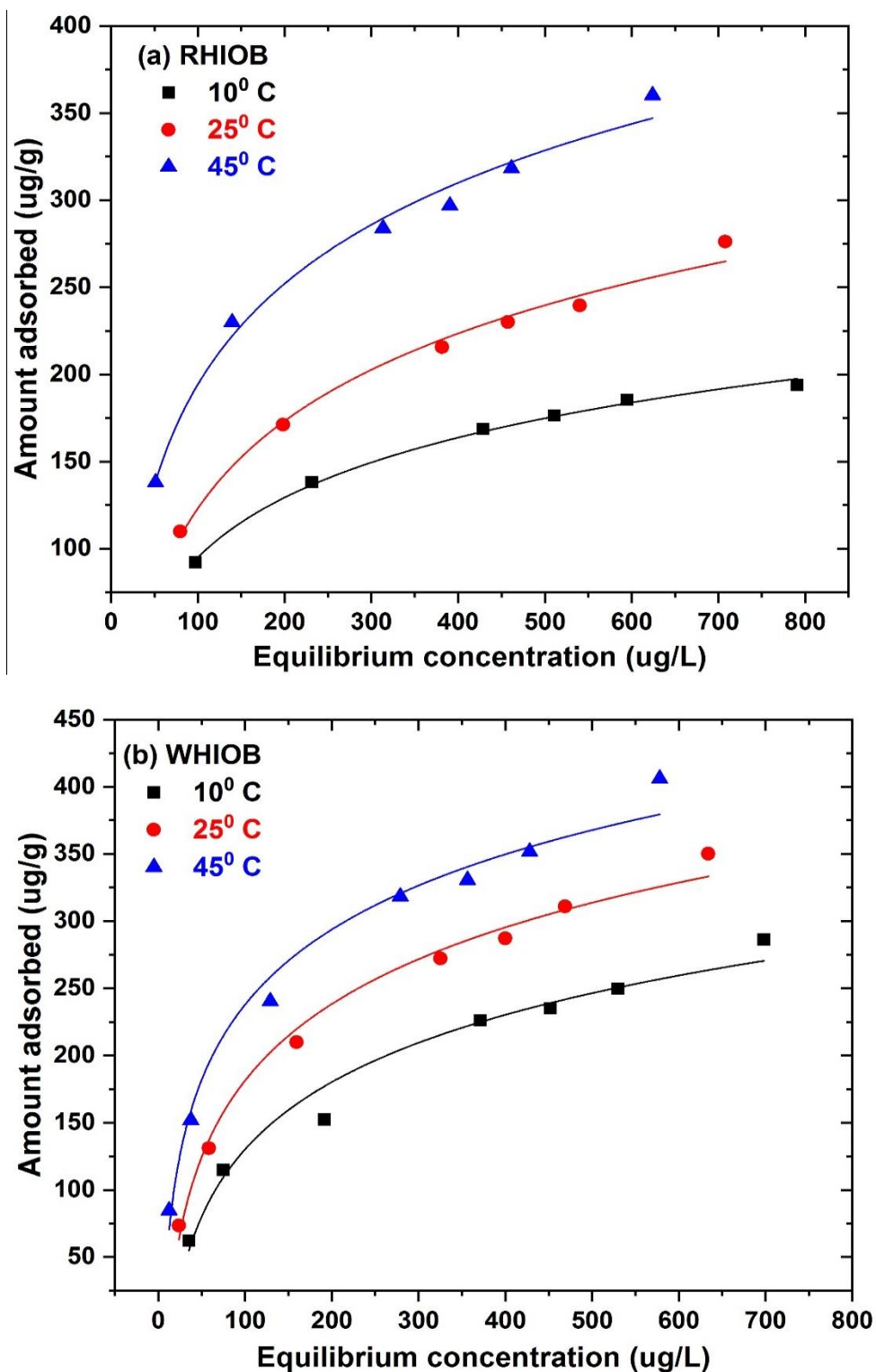


Figure 5.20. Temkin non-linear adsorption isotherms of As(V) adsorption by (a) RHIOB and (b) WHIOB at different temperatures (pH= 5.0 ; concentration= 100 $\mu\text{g/L}$; temp= 10 $^\circ\text{C}$, 25 $^\circ\text{C}$, 45 $^\circ\text{C}$; agitation= 100 rpm; particle size= 30- 50 B.S.S. mesh).

Table 5.1. Pseudo-first-order rate constant obtained from linear equations and comparison of experimental q_e values with their corresponding q_e calculated values at different adsorbent dose and As(V) concentrations.

Parameters	Linear Plot		q_e , Adsorption capacity at equilibrium <i>(amount of adsorbate adsorbed in μg)</i> <i>(amount of adsorbent used for adsorption in g)</i>	
	Second-order rate constant k_1 (h^{-1})	R^2	q_e , ($\mu g/g$) as obtained experimentally	q_e , ($\mu g/g$) as calculated using pseudo-first-order linear equation
(a) At different adsorbent dose (g/L) at [As(V)] = 100 $\mu g/L$				
RHIOB				
0.5	0.154	0.883	184.7	117.06
1.0	0.183	0.873	122.9	64.52
2.0	0.142	0.819	63.4	15.12
WHIOB				
0.5	0.163	0.796	207.1	131.67
1.0	0.143	0.742	124	67.27
2.0	0.083	0.781	61.9	20.02
(b) At different As(V) concentrations ($\mu g/L$) at an adsorbent dose of 1g/L (RHIOB) and 2g/L (WHIOB)				
RHIOB				
50	0.186	0.718	28.7	9.81
100	0.247	0.728	51.6	20.83
200	0.411	0.885	85.1	55.34
WHIOB				
50	0.196	0.645	52.4	11.65
100	0.203	0.832	112.5	49.15
200	0.306	0.832	164.6	69.51

Table 5.2: Pseudo-second-order rate constants obtained from the linear equation and comparison of experimental q_e values with their corresponding q_e calculated second order values obtained at different adsorbent dose and As(V) concentrations.

Parameters Values	Linear Plot		Non Linear Plot		q_e , Adsorption capacity at equilibrium <small>$\frac{\text{(amount of adsorbate adsorbed in } \mu\text{g)}}{\text{(amount of adsorbent used for adsorption in g)}}$</small>			Half-life time t_{50} (h)
	Second order rate constant k_2 (g/ $\mu\text{g h}$)	R^2	Second order rate constant k_2 (g/ $\mu\text{g h}$)	R^2	q_e , ($\mu\text{g/g}$) as obtained experimentally	q_e , ($\mu\text{g/g}$) as calculated using second order linear equation	q_e , ($\mu\text{g/g}$) as calculated using second order non-linear equation	
RHI OB								
At different adsorbent doses (g/L)								
0.5	0.003	0.996	0.022	0.792	93.3	92.7	84.1	7.5
1.0	0.004	0.996	0.011	0.776	117.4	120.1	87.8	6
2.0	0.040	0.999	0.023	0.924	130.1	128.4	101.2	1.5
WHIOB								
0.5	0.002	0.993	0.004	0.884	94.2	94.5	91.9	5
1.0	0.003	0.998	0.007	0.819	124	128.2	102.6	2
2.0	0.011	0.998	0.063	0.777	124.4	127.4	110.8	0.2
At different As(III) concentrations ($\mu\text{g/L}$)								
RHI OB								
50	0.035	0.996	0.044	0.981	28.7	28.9	27.9	0.2
100	0.014	0.992	0.014	0.94	51.6	52.9	53.3	0.5
200	0.006	0.994	0.005	0.968	85.1	89.3	90.2	2.5
WHIOB								
50	0.035	0.993	0.059	0.908	52.4	52.6	50.2	0.2
100	0.010	0.999	0.011	0.929	112.5	114.9	104.6	0.3
200	0.009	0.998	0.008	0.932	164.6	169.5	156.8	0.5

Table 5.3. Effective diffusion coefficients for As(V) adsorption on RHIOB and WHIOB at (a) different dose and (b) different As(V) concentrations.

Parameters	Adsorbents					
	RHIOB			WHIOB		
(a) Dose	0.5 g/L	1.0 g/L	2.0 g/L	0.5 g/L	1.0 g/L	2.0 g/L
R ²	0.6526	0.8929	0.9337	0.9318	0.9232	0.8582
Radius of the particle r_o (nm)	7.67	7.67	7.67	6.95	6.95	6.95
Effective diffusion coefficient, D_i ($\times 10^{-14}$) ($m^2 s^{-1}$)	0.51	0.51	0.37	0.37	0.35	0.2
Boyd number, B (s^{-1})	0.085	0.085	0.061	0.062	0.055	0.034
(b) Concentration	50 μ g/L	100 μ g/L	200 μ g/L	50 μ g/L	100 μ g/L	200 μ g/L
R ²	0.924	0.8788	0.7837	0.9585	0.8333	0.8303
Radius of the particle r_o (nm)	7.67	7.67	7.67	6.95	6.95	6.95
Effective diffusion coefficient, D_i ($\times 10^{-14}$) ($m^2 s^{-1}$)	0.54	0.71	0.53	0.89	0.94	0.83
Boyd number, B (s^{-1})	0.669	0.633	0.669	0.428	1.115	0.682

Table 5.4: Different thermodynamic parameters for removal of As(V) onto RHIOB and WHIOB.

Adsorbent(s)	ΔH^0 ($KJ mol^{-1}$)	ΔS^0 ($KJmol^{-1}K^{-1}$)	ΔG^0 ($KJ mol^{-1}$)		
			283 (K)	298 (K)	318 (K)
RHIOB	28.76	0.11	-0.43	-1.15	-3.46
WHIOB	24.34	0.09	-1.33	-2.81	-5.04

Table 5.5. Table 4.5. Freundlich, Langmuir, Redlich-Peterson, Toth, Sips, Radke and Prausnitz and Koble-Corrigan isotherm parameters for As(V) removal on RHIOB and WHIOB at different temperatures.

Isotherm parameters	RHIOB			WHIOB		
	10°C	25°C	45°C	10°C	25°C	45°C
Q⁰ (µg/g) experimental	220.85	276.3	380.2	286.3	365.2	410.3
Freundlich						
K _F (µg/g)	0.021	0.021	0.0004	0.014	0.023	0.004
1/n	0.34	0.39	0.98	0.46	0.42	0.37
R ²	0.976	0.994	0.983	0.989	0.993	0.994
Langmuir						
Q ⁰ (µg/g)	228.96	285.71	386.88	346.84	399.12	421.45
b	0.007	0.006	0.011	0.005	0.007	0.013
R ²	0.999	0.992	0.987	0.973	0.983	0.962
Redlich-Peterson						
K _{RP} (l/g)	1.75	6.59	8.72	5.92	6.64	21.66
a _{RP} (l/mg) ^{β_{RP}}	0.01	0.19	0.10	0.22	0.11	0.36
β _{RP}	0.94	0.68	0.77	0.63	0.72	0.69
R ²	0.999	0.995	0.987	0.986	0.998	0.996
Sips						
K _{LF} (l/g)	2.67	15.03	22.42	10.19	12.69	29.99
a _{LF} (l/mg) ^{α_{LF}}	0.006x10 ⁻⁴	1.51x10 ⁻⁴	0.001	2.68 x10 ⁻⁴	0.0014	4.62 x10 ⁻⁴
n _{LF}	0.87	0.49	0.53	0.56	0.02	0.47
R ²	0.999	0.994	0.986	0.991	0.997	0.995
Koble-Corrigan						
a	21.37	20.02	38.28	14.21	23.19	46.05

b	6.31×10^{-17}	8.88×10^{-19}	4.23×10^{-17}	1.66×10^{-18}	4.72×10^{-17}	7.68×10^{-16}
β	0.34	0.39	0.35	0.46	0.42	0.33
R^2	0.976	0.994	0.983	0.989	0.993	0.986
Radke and Prausnitz						
a	247.07	1076.56	1.91	1010.11	5616.27	1138.57
r	0.87	0.49	0.35	0.56	0.42	0.47
b	2.65	14.80	38.20	10.09	23.16	29.23
R^2	0.999	0.994	0.983	0.99	0.993	0.995
Toth						
K_T	24.72	9.76	11.38	9.38	9.25	30.97
B_T	0.68	0.19	0.10	0.22	0.11	0.36
β_T	0.68	0.67	0.79	0.63	0.72	0.69
R^2	1.000	0.995	0.988	0.991	0.998	0.998
Temkin						
B	49.59	72.42	83.44	72.21	82.23	80.71
a	0.07	0.05	0.10	0.06	0.09	0.19
R^2	0.996	0.988	0.987	0.987	0.989	0.983

CHAPTER 6

ARSENITE [As(III)] AND ARSENATE [As(V)] ADSORPTION MECHANISM ON RICE HUSK IRON-OXIDE (RHIOB) AND WHEAT HUSK IRON OXIDE BIOCHAR (WHIOB) COMPOSITES

6.1. Introduction:

Arsenic occurs in various forms in environment. It shows great diversity and variability in oxidation and chemical properties. Because of substantial variability in toxicology, mobility and absorptivity, it becomes important to determine and study the species of arsenic in aqueous systems (Quici, Meichtry, & Montesinos, 2018). Moreover, understanding the chemistry and behaviour of arsenic in the solution will facilitate researchers in increasing its removal from water. Because of low permissible limits and variation in oxidation states, combination of techniques have been applied to remove arsenic (Ammann, 2011). Arsenic exists both as organic and inorganic species in both water and soil (Plant, Kinniburgh, Smedley, Fordyce, & Klinck, 2003). It occurs as trivalent arsenites [As(III)] and pentavalent arsenates [As(V)] as prime inorganic species in natural water systems and as very less common As(0), As(-III), thio, carbonates, and cyanide complexes inorganic species (Kanematsu, Young, Fukushi, Green, & Darby, 2013; Plant et al., 2003; Smedley & Kinniburgh, 2002). Organic species of arsenic occurs as pentavalent methylated species monomethylarsonic acid (MA) or dimethylarsinic acid (DMA) (Kanematsu et al., 2013; Plant et al., 2003; Smedley & Kinniburgh, 2002).

6.2 Effect of pH and Redox (E) potential on inorganic arsenic: Eh-pH diagram

Arsenic exists as pentavalent species under oxidizing conditions that exists in surface water, and as trivalent species under reducing conditions such as groundwater (Brookins, 1988; Mohan & Pittman, 2007a; S. Song & Gallegos-Garcia, 2014). Under positive redox potential (E) values, arsenic exists as H_3AsO_4 at very low pH (< 2.0), as H_2AsO_4^- and HAsO_4^{2-} in the pH range 4-8 and as AsO_4^{3-} at very high pH (> 11.0). However at negative redox potential (E) it exists predominantly as neutral species H_3AsO_3 for low to near neutral pH and as oxyanionic species H_2AsO_3^- and HAsO_3^{2-} only at very high pH (Brookins, 1988; Bundschuh et al., 2012; Marinho, Cristovao, Boaventura, & Vilar, 2018; Mohan & Pittman, 2007b; Plant, Bone, et al., 2014; Smedley & Kinniburgh, 2002). Toxicity of As(III) is 10 times more than As(V) and 70 times more than methylated species

(Issa et al., 2011). Figure 6.1 shows Eh-pH relationship of arsenic assuming activity as 10^{-6} (Brookins, 1988). The green highlighted zone shows the region in which arsenic is either immobilized or remove through ionic adsorption under oxidising Eh/pH conditions in the pH range ~ 2.5 -8.0 (Plant, Kinniburgh, Smedley, Fordyce, & Klinck, 2014). Figure 6.2 a and b shows distribution of As(III) and As(V), respectively redox pH function (Issa et al., 2011). Arsenic adsorption unlike other anions follows complex mechanism. Several mechanisms explain its adsorption under different pH and redox conditions.

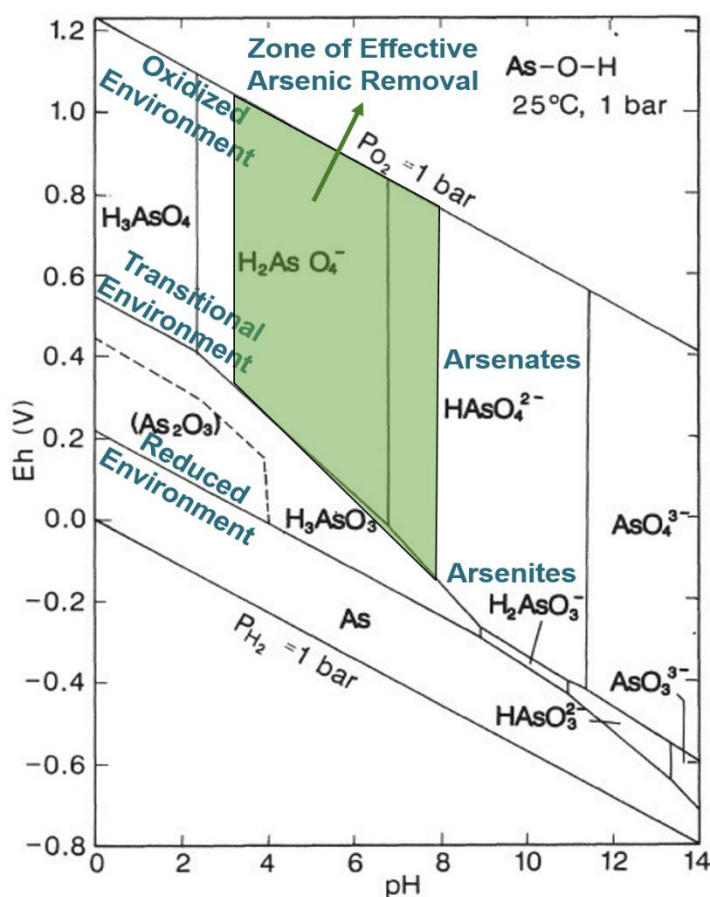


Figure 6.1. Eh-pH diagram, As-O-H part of system showing different ionization products (activity of arsenic assumed = 10^{-6}). Highlighted area shows zone of effective removal for arsenic through ionic adsorption under oxidizing conditions in pH range ~ 2.5 to ~ 8.0 . (Brookins, 1988)

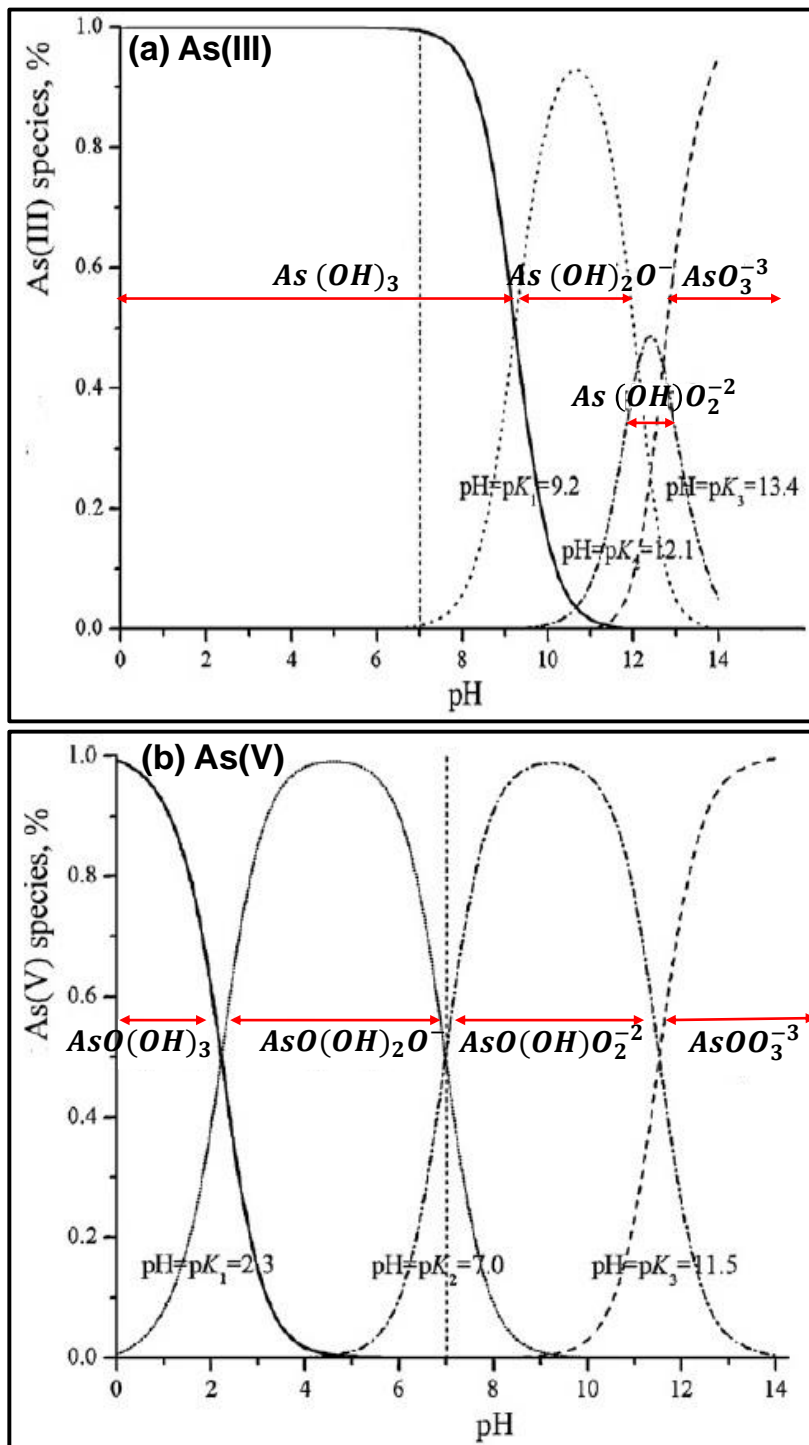
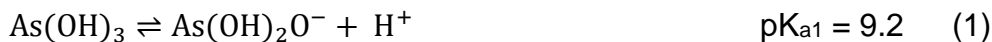


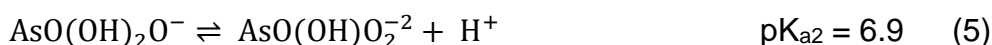
Figure 6.2. Distribution of (a) As(III) species and (b) As(V) species as function of pH values in water (Issa et al., 2011).

Arsenic speciation:

(i) As(III) speciation:



(ii) As(V) speciation:



6.3. Mechanism Description:

6.3.1. Different modes of bonding: As oxyanions and mineral surfaces

It is important to understand how of the complex formation between arsenic oxyanions and the adsorbent/mineral surface (metal oxide e.g. iron oxide, aluminium oxide) occurs. The bonding of the arsenic oxyanions on mineral surfaces and the adsorption behaviour of arsenic in natural systems has been discussed (Goldberg & Johnston, 2001).

6.3.1.1 Electrostatic Interactions:

As(V) exists as $\text{AsO(OH)}_2\text{O}^-$ species at $\text{pH} \sim 4$. At this pH, the adsorbent surfaces rich or impregnated with iron/aluminium oxides, gets protonated to give rise to positively charged surface. Hence, electrostatic attraction takes place between negatively charged arsenates and positively charged iron-oxide surfaces which facilitates the adsorption of As(V). However at the same pH (> 4), As(III) tends to exist as neutral species and remains uncharged up to pH 9.0. Hence, adsorption of arsenites cannot explain the removal by electrostatic interaction with adsorbents.

6.3.1.2. Ligand Exchange: Inner and Outer-sphere Complexation

Bonding during complex formation takes place by either inner-sphere complexation or outer-sphere complexation (Duarte et al., 2012; Kanematsu et al., 2013). Ligand exchange is based on an assumption that in homogeneous solution inner-sphere complexation occurs between adsorbent and adsorbate particles by

charge transfer through hydroxyl groups present on the mineral surface (Sherman & Randall, 2003). Outer-sphere complex formation proceeds with the transfer of electrons involving primary coordination spheres that remains intact (Torres, Gil, Galicia, & González, 1996). Whereas, the inner-sphere complex formation proceeds by the transfer of the electrons via common ligand that is shared between e.g. iron-oxide species and arsenic oxyanion species. There is absence of water molecule between the adsorbing ions e.g. arsenic oxyanions and the surface functional group e.g. iron-oxide particles (Goldberg & Johnston, 2001). Moreover, in outer-sphere complexes charge transfer occurs between e.g. arsenic oxyanions that lie outside the shear plane of adsorbent and the coordination sphere of the same (arsenic oxyanion) that is intact with the surface of adsorbent (Torres et al., 1996). There is involvement of the water molecule(s) between the surface functional group and adsorbing ions (Goldberg & Johnston, 2001).

In depth studies were conducted for arsenic adsorption on metal (Fe, Al) oxide by Goldberg & Johnston, Kanematsu et al. Shifts in the point of zero charge (PZC), reversal in electrophoretic mobility (EM) and the changes in the ionic strength during adsorption gave an idea about the adsorption mechanism (Goldberg & Johnston, 2001; Kanematsu et al., 2013; Partey, Norman, Ndur, & Nartey, 2009). EM is the measurement of the charged particles movement in presence of electric field (Goldberg & Johnston, 2001). PZC and EM are interconnected as zero EM implies there is no charged particles movement in electric field that is indicative of zero charge on surface i.e. point of zero charge, PZC. Ionic strength is the measurement of the concentration of the ions in the solution, which determines the strength of the electrical field due to ionic activity (Belessiotis, Kalogirou, & Delyannis, 2016).

1. Point of Zero Charge (PZC) and Electrophoretic Mobility (EM) :

PZC shifts of mineral/mineral oxides towards lower pH and reversal of EM with increasing arsenic concentration indicated that adsorption is taking place by inner-sphere complex formation. However, absence of shift in PZC does not necessarily concludes that complex formation will take place only through outer-sphere complex formation. This is because absence of shift in charge indicates

inner-sphere complexation as well. In this case, complex formation can be either by outer-sphere or by inner-sphere or by both outer- and inner-sphere complex formation (Fendorf, Eick, Grossl, & Sparks, 1997; Goldberg, 2002).

Adsorption studies conducted over amorphous Fe-oxides and amorphous Al-oxides by Goldberg and Johnston (Goldberg & Johnston, 2001) showed mechanism of arsenic adsorption. In case of amorphous Fe-oxide PZC shift was observed towards lower pH followed by reversal in EM with rise in As(III) and As(V) adsorption. This indicated that adsorption took place by the inner-sphere complex formation (Goldberg & Johnston, 2001). However in case of amorphous Al-oxide no PZC shift was recorded for As(III) at any concentrations. This indicated that As(III) adsorption in such case took place preferably by outer-sphere complex formation. However, possibility for the formation of both inner and outer-sphere surface complexation for As(III) adsorption cannot be ruled out (Goldberg & Johnston, 2001; Manning, Fendorf, & Goldberg, 1998).

2. Ionic Strength:

Decreasing arsenic adsorption due to increase in ionic strength of solution indicates that adsorption is taking place by the formation of the outer-sphere complexes. However, increase in the adsorption of the arsenic oxyanions on functional groups indicates the formation of inner-sphere complexes (Goldberg & Johnston, 2001; Manning et al., 1998). Increase in ionic strength in outer-sphere complexes decreases the adsorption of adsorbate ions. This is due to the competition of adsorbate ions in the solution with those of the adsorbate ions present on the adsorbent surface (Manning et al., 1998). In inner-sphere complexes adsorption of adsorbate ions increases with increase in ionic strength. This is because of the increase in the activity of the counter ions, that reduces competition of adsorbate ions present in the solution with those present on adsorbent surface (Goldberg & Johnston, 2001; Manning et al., 1998).

In studies reported by Goldberg and Johnston (Goldberg & Johnston, 2001) Adsorption of As(III) and As(V) onto Fe-oxide and Al-oxide showed absence or little effect with increase in ionic strength. This indicates that arsenite and arsenate adsorption has taken place by inner-sphere complexation. However, outer sphere

complex formation was proposed for arsenite adsorption over natural gibbsite based on ionic strength as a preferred mechanism (Duarte et al., 2012). Arsenite formed both inner and outer-sphere complexation, where outer-sphere complexation is a preferred mechanism for the adsorption (Duarte et al., 2012).

6.3.1.3 Different geometries of complex formation:

Several macroscopic and spectroscopic studies have been conducted to find the nature of complexation and different types of geometries associated with the complexation for arsenic adsorption. Based on the distances between As-Fe, As-O bonds obtained from Extended X-ray fine structure spectroscopy (EXAFS), Fourier transform infra-red spectroscopy (FT-IR), Resonant anomalous X-ray reflectivity (RAXR) in various studies possible geometries to explain arsenic adsorption are propounded (Catalano, Park, Fenter, & Zhang, 2008; Duarte et al., 2012; Farquhar, Charnock, R Livens, & J Vaughan, 2002; Foster, Brown, Parks, N. Tingle, & Voigt, 1997; Fuller, Davis, & Waychunas, 1993; Ladeira, Ciminelli, Duarte, Alves, & Ramos, 2001; Manceau, 1995; Manning et al., 1998; Pandya, 1995; G. Waychunas, Rea, Fuller, & Davis, 1993).

EXAFS and FT-IR studies showed three distances for As-Fe at 3.65 Å, 3.28 Å and 3.12 Å (G. Waychunas et al., 1993). As-Fe distance was corrected for the edge sharing complexes from 3.12 Å to 2.8 Å (Manceau, 1995). Based on these distances it was concluded that arsenates forms inner-sphere complex by (1) monodentate-mononuclear/binuclear complexes (¹V), (2) bidentate-edge sharing complexes (²E) and (3) bidentate-binuclear (two-corner) sharing complexes (²C). It was concluded that bidentate edge sharing complex (²E) is energetically unfavourable and does not explain arsenate adsorption. Moreover, bidentate-binuclear (two-corner) sharing complex (²C) formation is thermodynamically most stable and energetically favourable for explaining the complexation of arsenates over mineral oxides. Similarly, for arsenites adsorption on ferrite ions was explained by inner sphere complex formation via bidentate-binuclear (two-corner) sharing complex (²C) (Farquhar et al., 2002; Manning et al., 1998).

During adsorption of arsenic changes in As-O also occurs. In arsenates adsorption over goethite, bond distances As-OH decreases from 1.86 Å to 1.70 Å

and As(V)-O bond distances increases slightly from to 1.67 Å and 1.68 Å (Ladeira et al., 2001; Sherman & Randall, 2003). Moreover, in adsorption of arsenites over goethite As-OH bond decreases to 1.79 Å and As(III)-O bond distance increases slightly to 1.69 Å over goethite mineral (Farquhar et al., 2002; Manning et al., 1998).

Table 6.2 shows the possible mechanisms for inner-sphere complexation for arsenate and arsenite on various iron-oxides. Scheme 1-8 shows all the possible geometries for inner-sphere complexation for arsenites and arsenates over iron-oxide (magnetite).

6.3.2. As(III) and As(V) adsorption mechanism on RHIOB and WHIOB:

pH and pH_{pzc} are important factors in determining the adsorption process on adsorbent by changing the surface charges (J. Yang et al., 2015). At $pH < pH_{pzc}$ surface of adsorbent is positively charged, leading to the increase in electrostatic attraction of anionic As(III) and As(V) species. However, because of the difference in response of arsenite and arsenate species towards pH and redox potential, their adsorption mechanism also differs (X. Yang et al., 2017a). In case of As(III) species, there is competition for the adsorbent sites between neutral species (H_3AsO_3) and H_3O^+ ions in the solution at lower pH as As(III) tends to exist as $As(OH)_2O^-$ species at $pH > 9.2$ (eq 1) (Figure 6.5). Whereas, As(V) tends to exist as negatively charged species at $pH > 2.4$ (eq 4) (Figure 6.5). As pH increases degree of protonation gradually decreases over iron-oxide surface and approaches to zero at pH near pH_{pzc} . Hence, in the present study of arsenic adsorption on RHIOB and WHIOB, the maximum removal of As(III) was achieved in pH range 6.5-7.5 and for As(V) maximum removal was achieved in pH range 4.5 -5.5. The optimum pH values for the As(III) and As(V) removal is close to the pH_{pzc} values of RHIOB (~5.5) and WHIOB (~6.3) (Figure 6.5). In case of As(III) adsorption at this pH range (6.5-7.5) there was decrease in the competition between As(III) species and H_3O^+ as protonation of the adsorbent sites also get reduced and so the adsorption is high (Agrafioti, Kalderis, & Diamadopoulos, 2014; Baig et al., 2014a; Calo, Madhavan, Kirchner, & Bain, 2012; X. Yang et al., 2017a). While, in the case

of As(V) there is electrostatic attraction between arsenate anionic species and positively charged adsorbent surface sites in pH range 4.5-5.5. This causes higher removal of As(V). However, as pH further increases removal efficiency of both As(III) and As(V) decreased or remained unaffected. This can be explained due to the repulsion between negatively charged adsorbent surface in alkaline medium ($\text{pH} > \text{pH}_{\text{pzc}}$) and arsenite (HAsO_3^{2-} and AsO_3^{3-}) and arsenate (H_2AsO_4^- and HAsO_4^{2-}) (Figure 6.5). In case of arsenate, because maximum removal is taking place in pH range 4.5-5.5, H_2AsO_4^- is the dominant species that is being adsorbed over magnetite surface.

Magnetite contains iron in both divalent and trivalent states. Fe^{III} ions occupy octahedral sites whereas Fe^{II} occupies both octahedral and tetrahedral sites. It is represented as $\text{Y}[\text{XY}]_4$ ($\text{X} = \text{Fe}^{\text{II}}$, $\text{Y} = \text{Fe}^{\text{III}}$ bracket denoting octahedral sites). Sweeton and Baes (1970) considered only Fe^{2+} hydrolysis products (FeOH^+ , $\text{Fe}(\text{OH})_2^0$ and $\text{Fe}(\text{OH})_3^-$) while measuring solubility of magnetite in acidic and alkaline mediums (Rajput, Singh, Pittman, & Mohan, 2017; Sweeton & Baes, 1970). Magnetite acts as weak acid at lower pH(s) of the solution and gets protonated to generate positively charged FeOH_2^+ sites (eq 7-8) (Baig et al., 2014a). As pH increases sites gets converted to Fe-O^- species (Rajput, Singh, Pittman, & Mohan, 2017). pH_{ZPC} of magnetite is close to neutral (7.4) (Rajput, Singh, Pittman, & Mohan, 2017). The maximum removal of As(III) and As(V) was achieved at pH close to pH_{pzc} of magnetite developed over RHIOB and WHIOB which suggests adsorption happened due to the protonation of magnetite sites.

As(III) removal mechanism is slightly complicated as compared to As(V) as it tends to exist as neutral species H_3AsO_3 $\text{pH} < 7$, while arsenates exists as negatively charged species H_2AsO_4^- $\text{pH} > 2.4$ (Mohan & Pittman, 2007b; Mohan et al., 2007; Smedley & Kinniburgh, 2002; X. Yang et al., 2017a).

At $\text{pH} > 7.5$ As(III) tends to exist as negatively charged species H_2AsO_3^- , HAsO_3^{2-} and AsO_3^{3-} depicted in Scheme 1. At $\text{pH} < \text{pH}_{\text{pzc}}$ Fe-O sites over magnetite gets protonated to generate FeOH_2^+ sites (eq 7-8). Electrostatic attraction gets developed

between positively charged FeOH_2^+ over adsorbent surface and negatively charged arsenite species $[\text{HAsO}_3]^{2-}$ and arsenate species $[\text{H}_2\text{AsO}_4]^-$. For convenience and keeping pH range 7-9, HAsO_3^{2-} (Scheme 1) of As(III) and has been picked up to explain the mechanism. Similarly, H_2AsO_4^- (Scheme 5) has been picked up for As(V) in pH range 4.5-5.5. The adsorption of arsenite species $[\text{HAsO}_3]^{2-}$ and arsenate species $[\text{H}_2\text{AsO}_4]^-$ can take place either by dissociative or by associative pathway. In dissociative pathway protonation resulted in generation of positive FeOH_2^+ sites in first step followed by the adsorption of negatively charged arsenite species $[\text{HAsO}_3]^{2-}$ and arsenate species $[\text{H}_2\text{AsO}_4]^-$. However in associative pathway simultaneous protonation of magnetite Fe-O and adsorption of arsenite $[\text{HAsO}_3]^{2-}$ and arsenate $[\text{H}_2\text{AsO}_4]^-$ species followed by the removal of H_3O^+ occurred in single step. This depends upon the stability and the energy by which the pathway will be followed. However here all possible pathways have been taken into account to explain the mechanism.

Scheme 2 and scheme 6 shows dissociative and associative pathway for monodentate-mononuclear sharing complex (^1V) for As(III) and As(V) respectively. Scheme 3 and scheme 7 shows dissociative and associative pathway for bidentate-binuclear edge sharing complex (^2E) for As(III) and As(V) respectively. In addition, scheme 4 and scheme 8 shows bidentate-binuclear (two corner) sharing complex (^2C) for As(III) and As(V) adsorption. Based on the studies conducted by different researchers bidentate-binuclear (two corner) sharing complexation (^2C) is thermodynamically most stable form and hence explains the adsorption mechanism for As(III) and As(V) over magnetite particles.

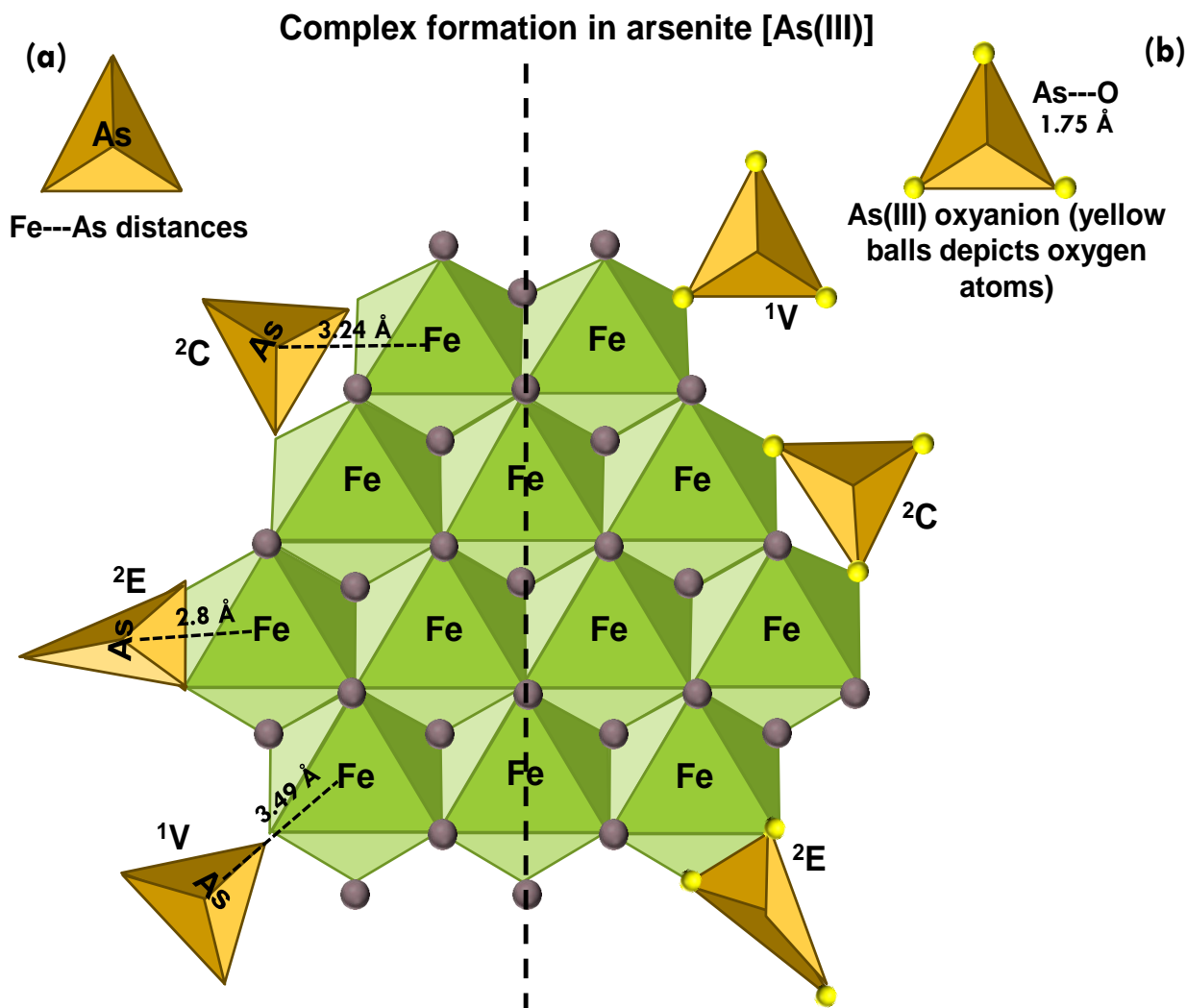


Figure 6.3. 3-D depiction of different geometries of complex formation between iron-oxide octahedron particles and arsenite tetrahedron oxyanion(s) species. Three possible geometries are shown in the figure: Bidentate-binuclear (two corner) sharing complex (2C), bidentate-edge sharing complex (2E) and monodentate-mono-nuclear corner sharing complex (1V). (a) As(III)-Fe distances and (b) Arsenite tetrahedron units (3-oxygen atoms depicted by yellow balls). The As-Fe and As-O distances are based on the distances mentioned in different studies reported in the table 6.2.

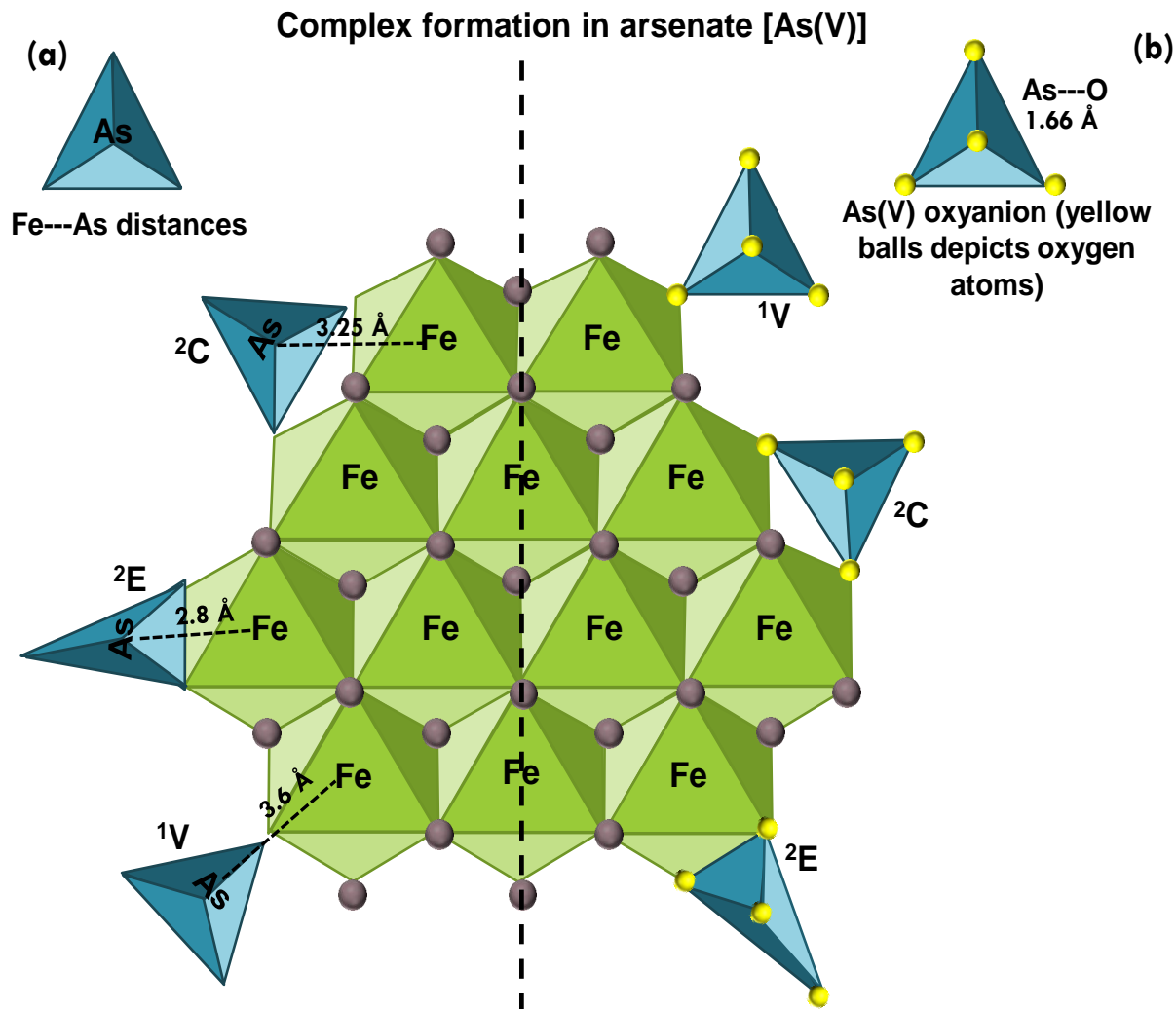


Figure 6.4. 3-D depiction of different geometries of complex formation between iron-oxide octahedron particles and arsenite tetrahedron oxyanion(s) species. Three possible geometries are shown in the figure: Bidentate-binuclear (two corner) sharing complex (^2C), bidentate-edge sharing complex (^2E) and monodentate-mononuclear corner sharing complex (^1V). (a) As(V) - Fe distances and (b) Arsenate tetrahedron units (4-oxygen atoms depicted by yellow balls). The As-Fe and As-O distances are based on the distances mentioned in different studies reported in the table 6.2.

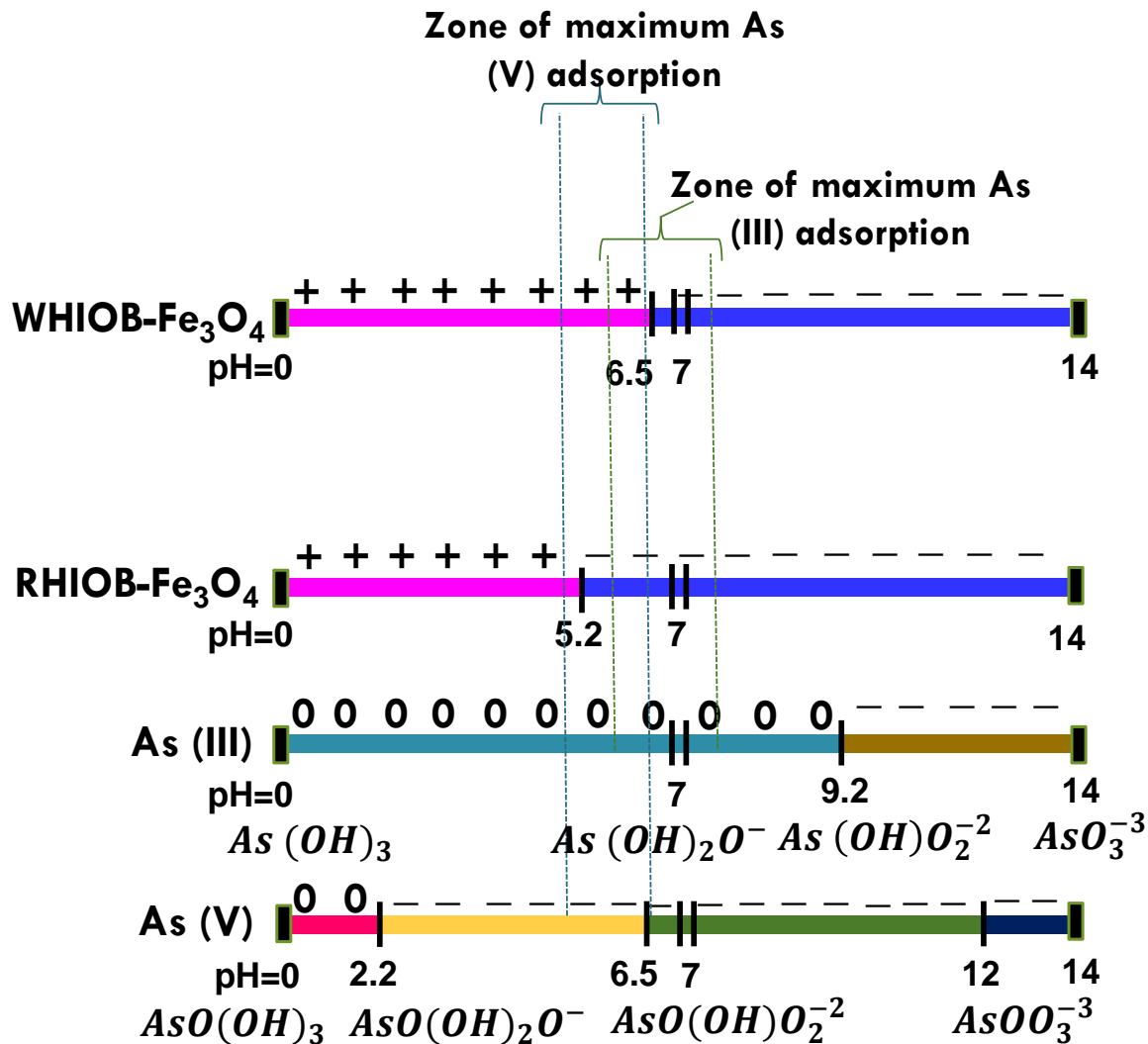
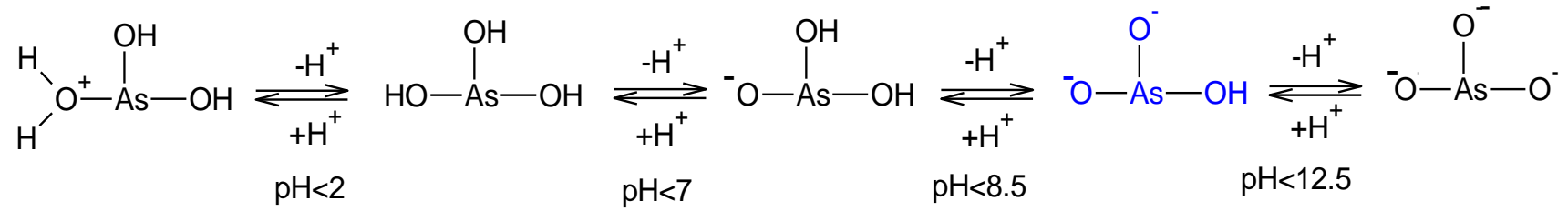
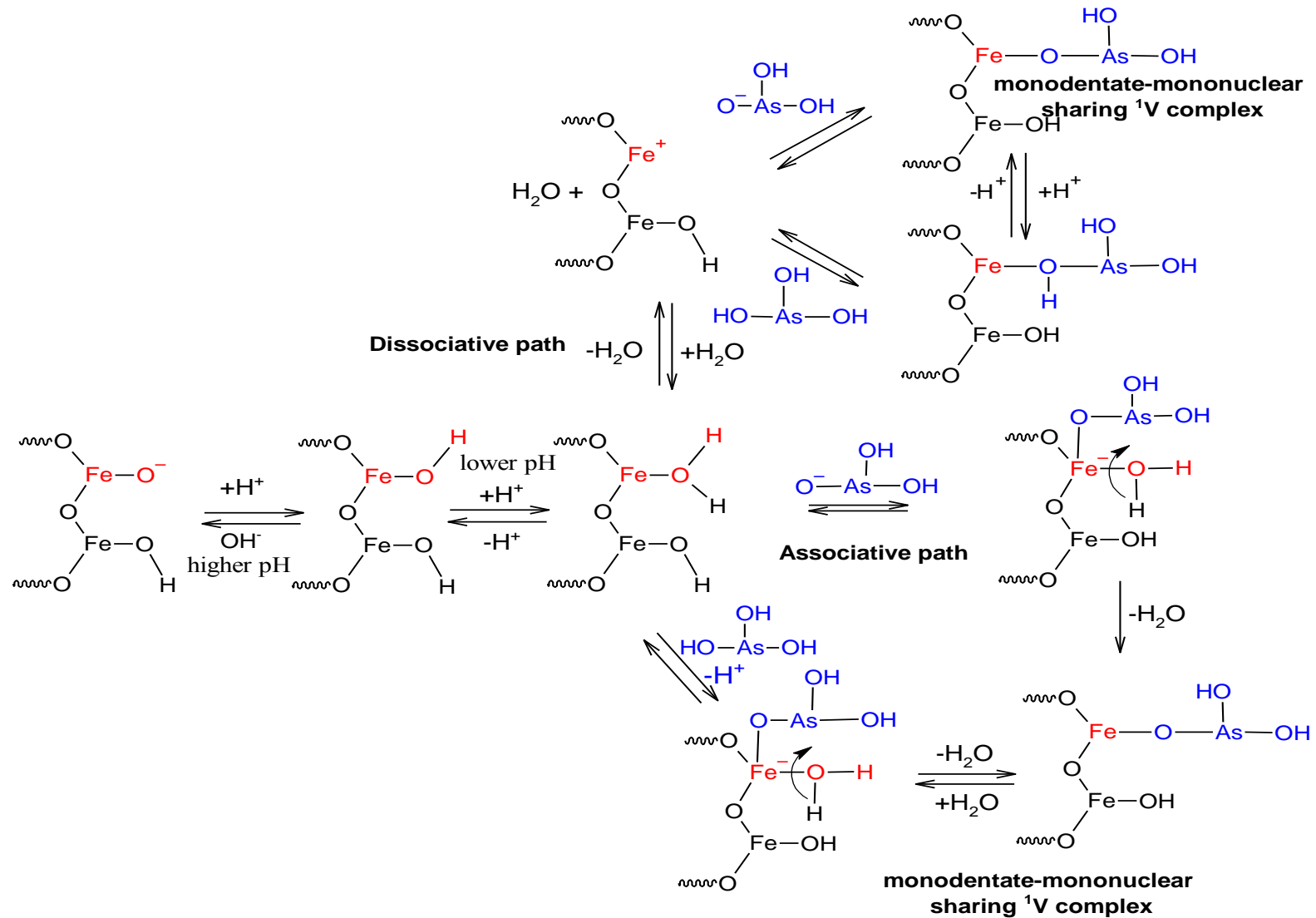


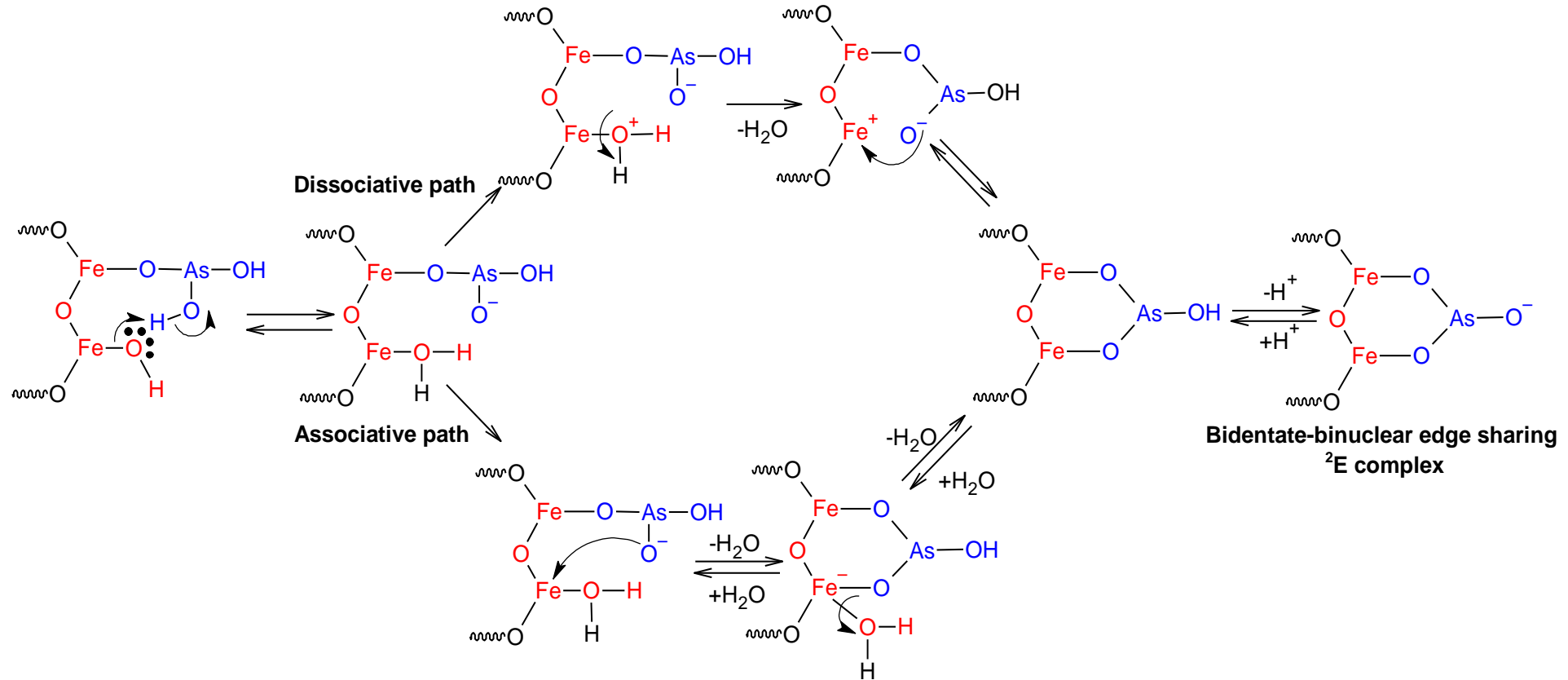
Figure 6.5. Zone of maximum adsorption for As(III) and As(V) over RHIOB and WHIOB is shown over both pH and pH_{zpc} scales. $As(OH)_3 / As(OH)_2O^-$ (pH~6.5-7.5) are the primary As(III) species adsorbed over magnetite surfaces ($FeOH_2^+$) over RHIOB and WHIOB. Similarly, for As(V) $AsO(OH)_2O^-$ (pH~5.5) is primary species involved in adsorption with magnetite surfaces over RHIOB and WHIOB.



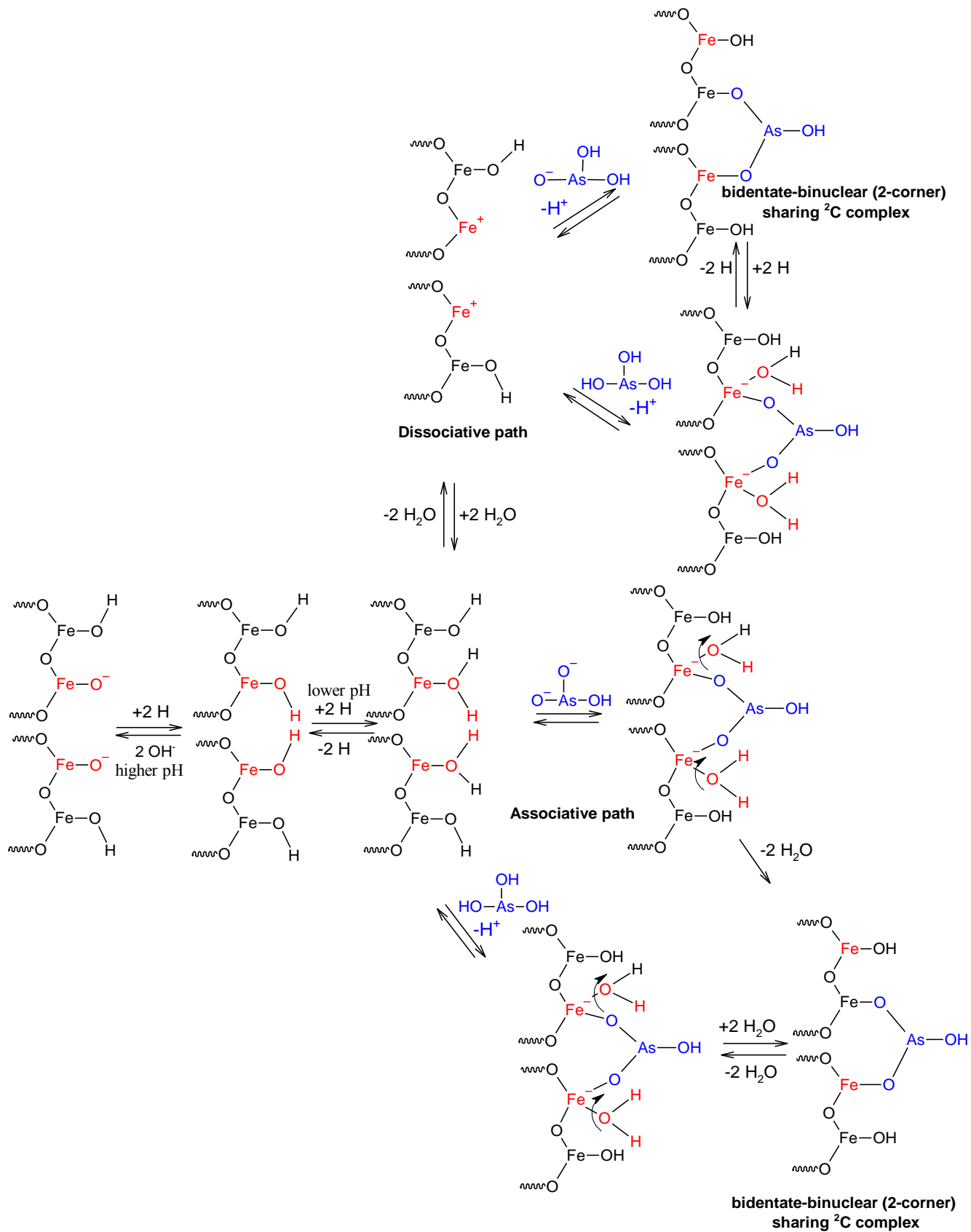
Scheme 1: General speciation of As(III) vs pH



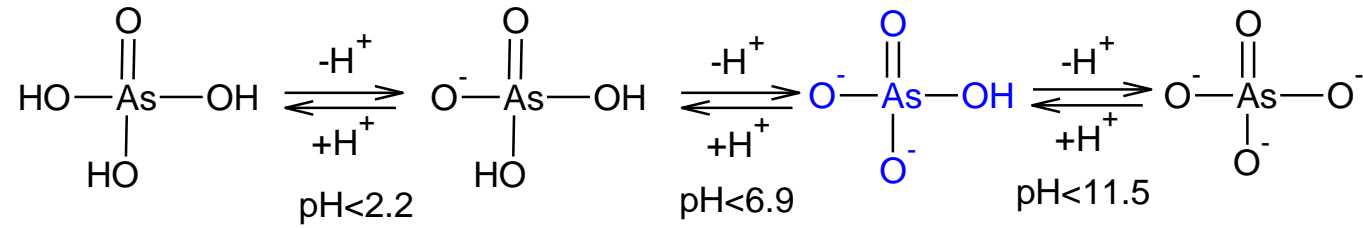
Scheme 2: Dissociative and associative paths for As(III) to form a monodentate-mononuclear sharing $1V$ complex.



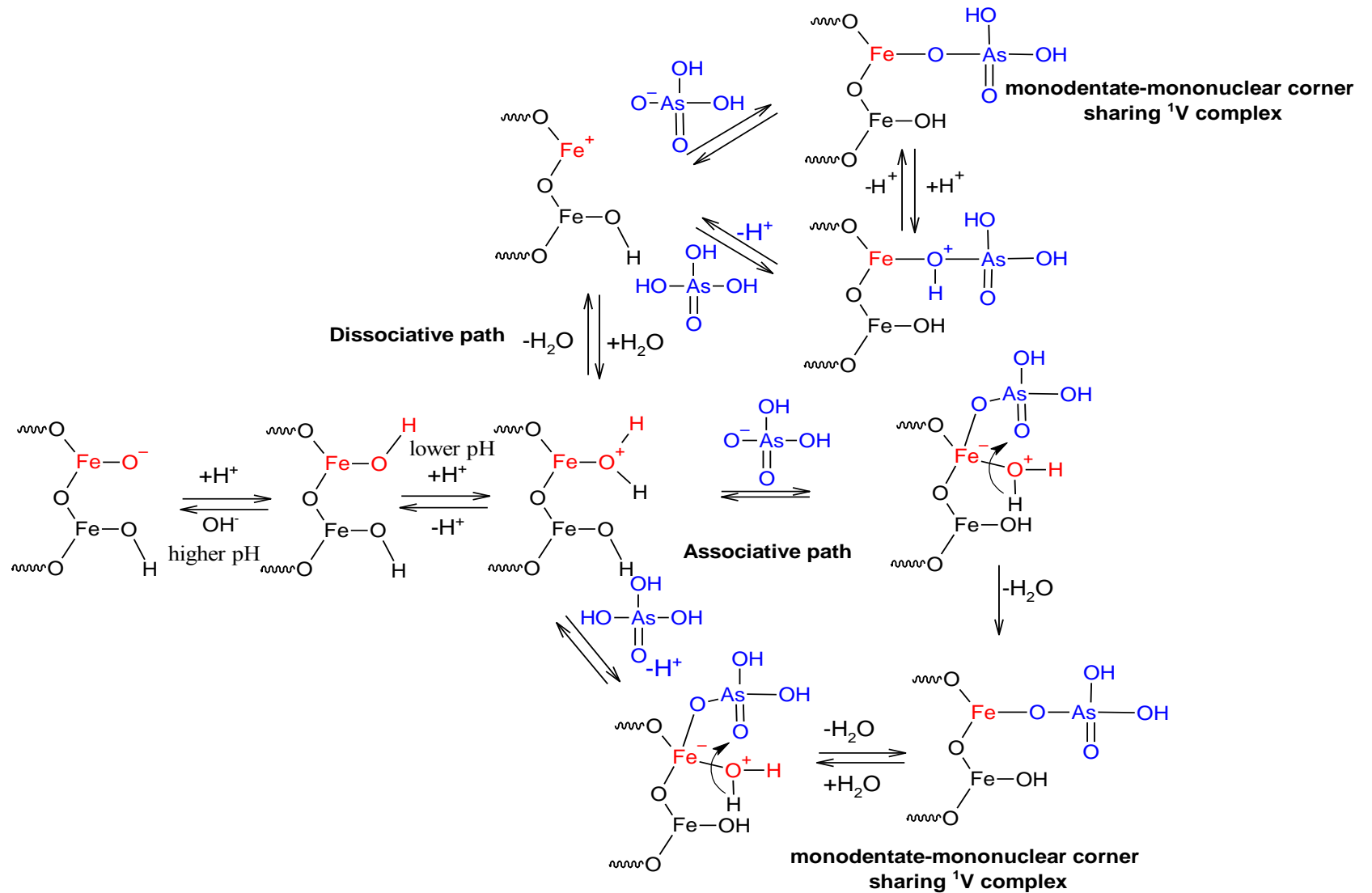
Scheme 3: Dissociative and associative paths for As(III) complex to form a bidentate-binuclear edge sharing ²E complex.



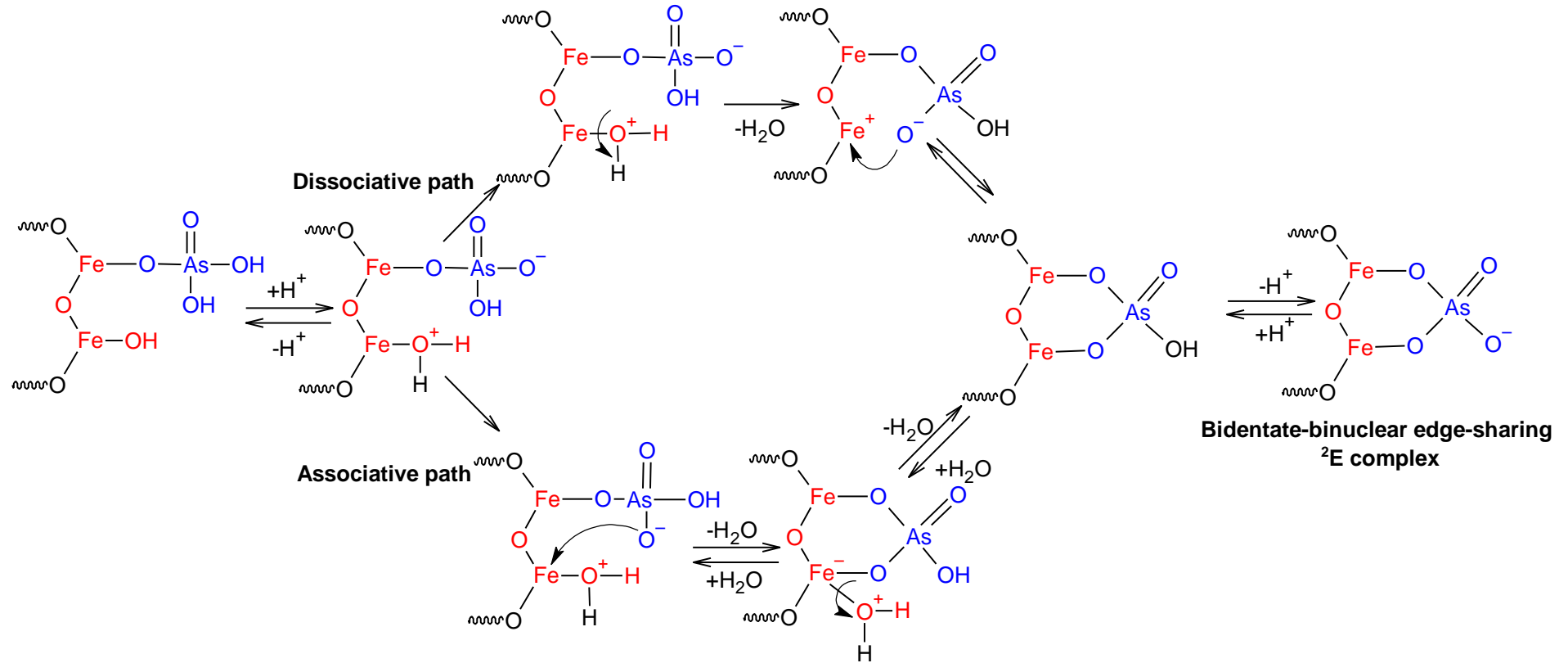
Scheme 4: Dissociative and associative paths to form monodentate As(III) complex to a bidentate-binuclear (two corner) sharing 2C complex.



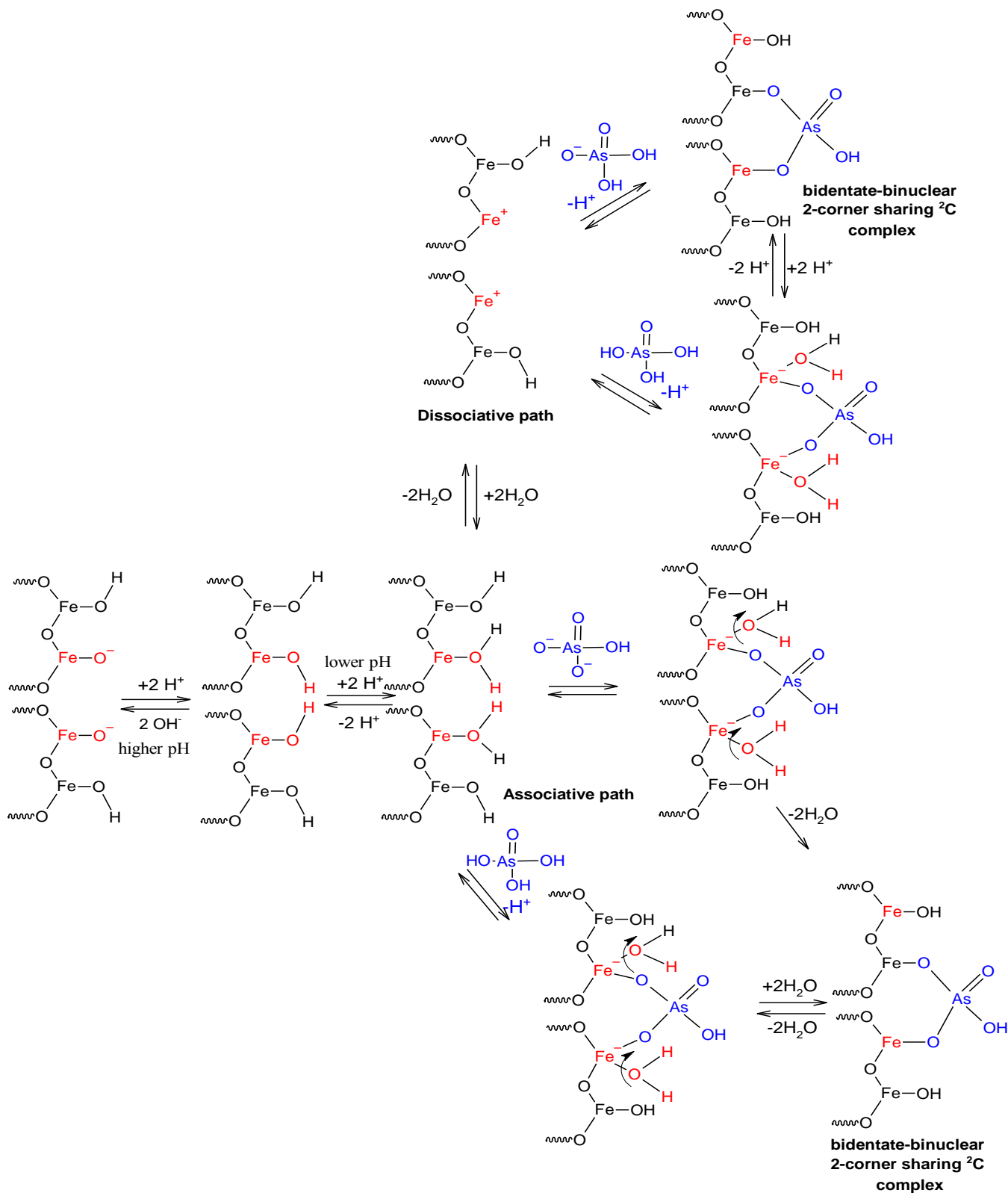
Scheme 5: General speciation of As(V) vs pH



Scheme 6: Dissociative and associative paths for As(V) to form monodentate-mononuclear corner sharing $1V$ complex.



Scheme 7: Dissociative and associative paths for As(V) complex to form bidentate-binuclear edge sharing ²E complex.



Scheme 8: Dissociative and associative paths for As(V) complex to form a bidentate-binuclear (two corner) sharing ²C complex.

Table 6.1 Thermodynamic values for different arsenic species in aqueous systems. Reproduced from Eh-pH diagrams for geochemistry by D. Brookins (Brookins, 1988).

S. No	Arsenic species (aq)	ΔG_r^0 (kcal/g)
1	H_3AsO_3	-152.92
2	$H_2AsO_3^-$	-140.33
3	$HAsO_3^{2-}$	-125.31
4	AsO_3^{3-}	-107.00
5	H_3AsO_4	-183.08
6	$H_2AsO_4^-$	-180.01
7	$HAsO_4^{2-}$	-170.69
8	AsO_4^{3-}	-154.97

Table 6.2 Possible geometries of complexes between iron-oxide octahedra found in magnetite, goethite, lepidocrocite, hematite and ferrihydrite) and arsenic oxyanions (As-O-Fe) obtained from EXAFS and XAFS studies in chronological order:

S. No.	Possible Geometries	Bidentate corner sharing complex on adjacent FeO ₆ octahedra molecule (² C) (Fe-As distance (Å))	Bidentate edge shared complex on FeO ₆ octahedra (² E)	Monodentate corner sharing complex on FeO ₆ octahedra (¹ V)	Isolated bidentate complex on FeO ₆ octahedra between sheets	Tridentate arsenate complex (³ C)	Fe-Fe edge sharing neighbouring units complex in dioctahedral FeO ₆ units	References
	Iron-oxide particles							
Iron-oxide octahedron and Arsenate (As(V)) tetrahedron : Fe-As distance								
1	Ferrihydrite	3.28 Å	3.12 Å	3.65 Å	3.36-3.65 Å	3.28-3.22 Å	3.25 Å	Waychunas et al, 1993, corrected*(G. Waychunas et al., 1993)
2	Iron-oxyhydroxides (αFeOOH, βFeOOH)	3.25 Å	2.8 Å	3.6 Å	-	-	-	Manceau, 1995 (Manceau, 1995)
3	Goethite	3.25 Å	2.83-2.85 Å	3.6 Å	-	-	-	Fendorf et al., 1997 (Fendorf et al., 1997)
4	Iron(III) oxyhydroxides	3.26 Å	2.8 Å	-	-	-	-	Foster et al., 1997 (Foster et al., 1997)

5	Goethite and lepidocrocite	3.3-3.31 Å	2.93 Å	3.62 Å	-	-	-	Farquhar et al., 2002 (Farquhar et al., 2002)
6.	Scorodite	3.31 Å	-	3.65 Å	-	-	-	Sherman and Randall, 2003 (Sherman & Randall, 2003)
7.	Goethite	3.3 Å	-	-	-	-	-	
8.	Lepidocrocite	3.32 Å	-	-	-	-	-	
9.	Hematite	3.24 Å	-	-	-	-	-	
10.	Ferrihydrite	3.38 Å	-	-	-	-	-	
Iron-oxide octahedron and Arsenite (As(III)) tetrahedron : Fe-As distance								
1.	Goethite	3.38 Å	-	3.57 Å	-	-	-	Manning et al., 1998 (Manning et al., 1998)
2.	Lepidocrocite	3.41 Å	-	-	-	-	-	Farquhar et al., 2002 (Farquhar et al., 2002)
3.	Goethite	3.31 Å	-	-	-	-	-	
4.	Gibbsite	3.24 Å	-	3.49 Å	-	-	-	Duarte et al., 2012 (Duarte et al., 2012)

*The As-Fe distance for the edge-sharing complex (2E), reported by Waychunas et al. (1993) was later corrected as 2.8 Å by Manceau et al. (1995). However, in further studies by Pandya (1994), Manning (1998), Ladeira et al. (2001) and Sherman and Randall (2003), it was concluded that As-Fe bidentate edge-sharing complex (2E) peak at 2.8 Å is energetically unfavourable and is because of the multiple scattering within arsenate/arsenite tetrahedron.

CHAPTER 7

**MULTICOMPONENT, ADSORBENT
REGENERATION, FIXED-BED, AND REAL
WATER TREATMENT STUDIES**

7.1. Introduction

Batch studies are required to optimize the basic parameters including pH, temperature, adsorbent/adsorbate concentrations. Furthermore, the data obtained by batch studies are generally not applicable in the systems as the contact time to attain equilibrium is sufficiently long as compared to the column operations. The adsorption capacity obtained from batch studies is not sufficient enough to provide information for scaling-up during column operations (Calo et al., 2012; Yanhong Li et al., 2018; López-Cervantes, Sánchez-Machado, Sánchez-Duarte, & Correa-Murrieta, 2017). In actual practice, fixed-bed reactors are being used for water treatment (Calo et al., 2012). Keeping this in mind, fixed-bed design parameters for As(III) and As(V) removal using RHIOB and WHIOB were determined (W. J. Thomas & Crittenden, 1998a). Fixed-bed studies are also essential for adsorbent regeneration as well as adsorbate recovery without dismantling the system. Continuous studies may be performed in using (a) down flow fixed bed reactors (2) upflow fixed-bed reactors and (3) fluidized bed reactors (W. J. Thomas & Crittenden, 1998b). In order to study the effectiveness of the developed material in continuous mode over As(III) and As(V) adsorption, equilibrium experiments were conducted in fixed-beds (down flow mode) of RHIOB and WHIOB (Yanhong Li et al., 2018).

In Fixed-bed adsorber, the adsorbent remains fixed during the operation. (Baskan & Pala, 2013; Calo et al., 2012). Figure 7.1 shows the ideal breakthrough curve. When the feed water (concentration C_0) passes through the layers of adsorbent and effluent is coming out contains no solute i.e. $C_f = 0$. Initial adsorption takes place in the top layer of the adsorbent bed. This zone is known as primary adsorption zone (PAZ) (Calo et al., 2012). As the feed water continues to flow down through the column, the upper layers of the adsorbent bed become saturated and adsorption starts in the lower layers. The zone that reaches equilibrium is known as saturation zone (ZS). The lower layers continue to adsorb the solute and is known as zone of no work (ZNW). The PAZ advances downwards in the column and encounters the fresh batch of the solution having more solute concentration for

the coming layers. The movement of PAZ can be explained by a S-shaped curve known as breakthrough curve (López-Cervantes et al., 2017; W. J. Thomas & Crittenden, 1998c; Yunnan et al., 2017). Figure 7.1 shows the increase in the influent solution concentration (C_i/C_0) versus treated volume with time. A point when little or no removal of solute from feed water takes place is known as breakpoint ($C_b/C_0 = 0.01-0.05$) (Dutta & Basu, 2014; Patel, 2019). After breakpoint, adsorbent fails to adsorb any more solute from feed. This is known as exhaustion point ($C_x/C_0 = 0.8-1.0$) (Dutta & Basu, 2014). V_b and V_x are the total volume of the feed water passed at break and exhaustion points (figure 7.1). Column capacity for a given feed is given by the area A_c under the breakthrough plot (figure 7.1) (Patel, 2019).

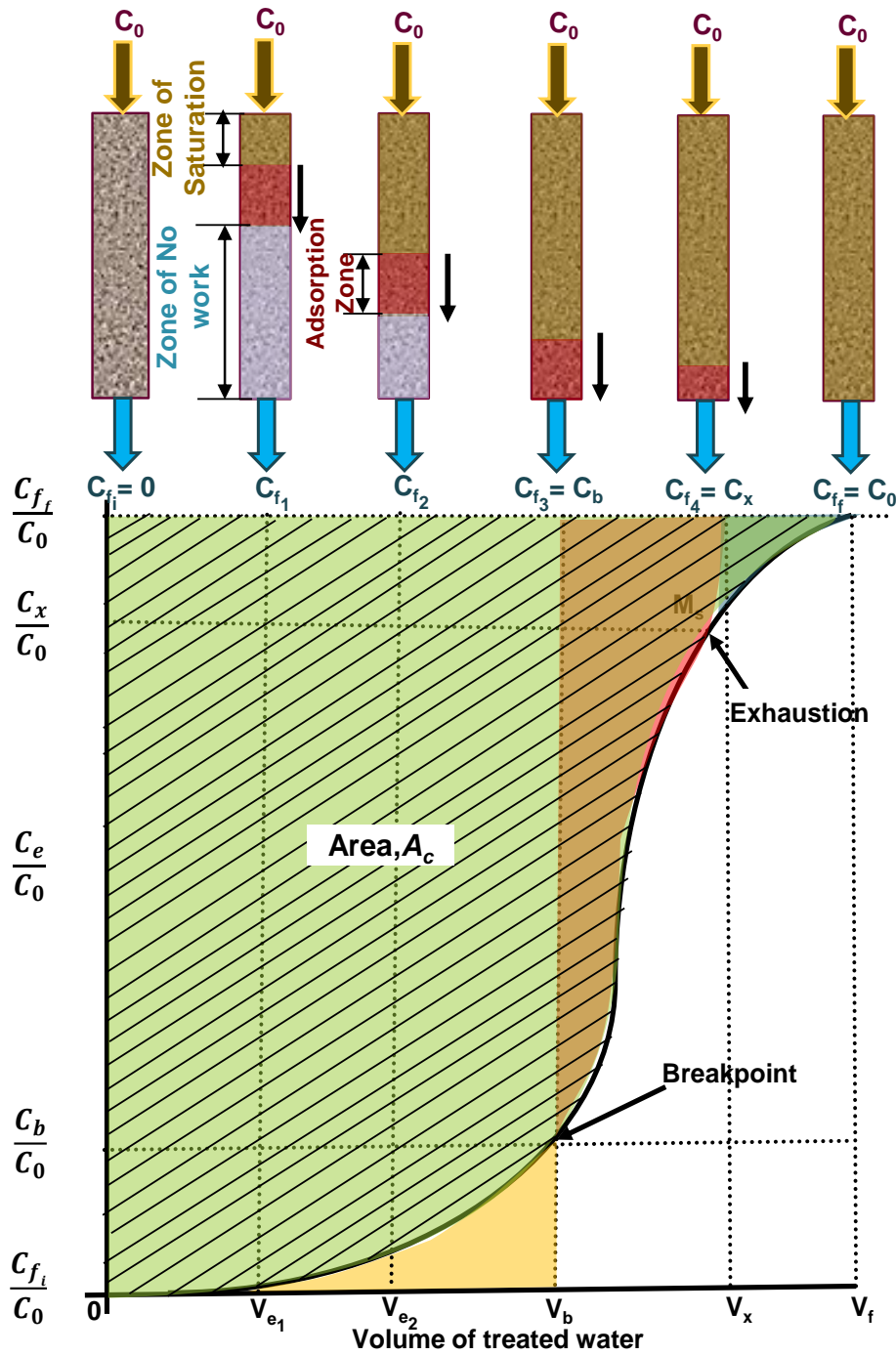


Figure 7.1. Ideal breakthrough curve.

7.2. Column adsorption experiments

Fixed-bed experiments were conducted using a glass column of length 40 cm, inner and outer diameters 2 cm and 2.5 cm, respectively. Figure 7.2 (a,b) shows

the schematic and experimental set-up for the fixed-bed studies. Column studies were carried out for (1) As(III) removal at (pH = 7.5 and $C_0 = 100 \mu\text{g/L}$) and (2) As(V) removal (pH = 5.0 and $C_0 = 100 \mu\text{g/L}$) of Columns were packed using 5.0 g of RHIOB/WHIOB (30-50 B.S.S. mesh). The bed height (D) was 5.0 cm for the fixed-bed of RHIOB/WHIOB. Constant flow rate (Q) of 5.0 ml/min was maintained using control knob. The empty-bed-contact-times of 1.6 min and 1.8 min were used for RHIOB and WHIOB, respectively.

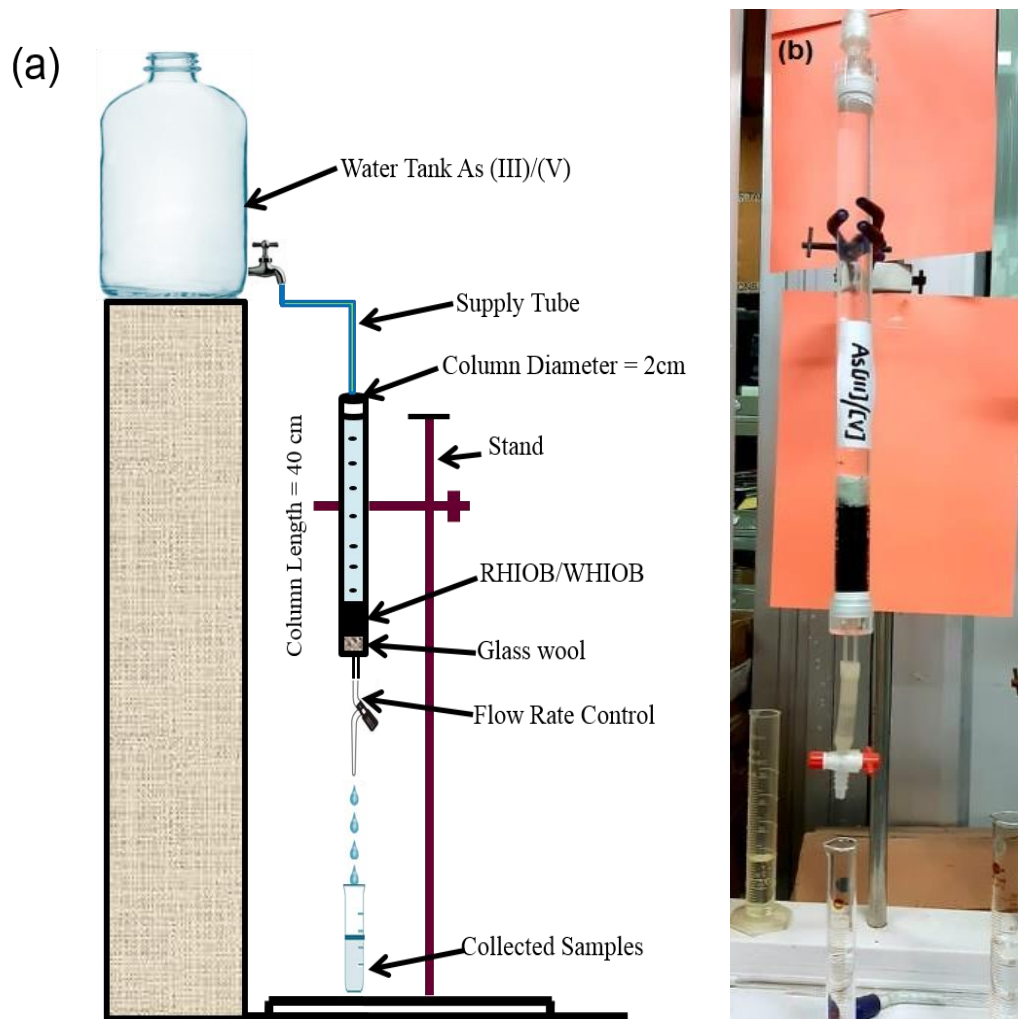


Figure 7.2. (a) Schematic of fixed-bed setup

7.3.1 Fixed bed adsorber design parameters:

Mass transfer theory given by Weber (W. J. Weber & Liu, 1980) was adopted to find the required parameters for the design of fixed-bed adsorber. C_0 and C_e are

the initial and the final concentrations of the arsenic [As(III)/As(V)] contaminated feed water. The parameters were obtained from the breakthrough curves between C_e/C_0 versus time using equations (1-10) (Patel, 2019; W. J. Thomas & Crittenden, 1998c; W. J. Weber & Liu, 1980). C_b and C_x are the concentrations at volume V_b and V_x at breakpoint and exhaustion point, respectively. \bar{V}_b and \bar{V}_x are the total effluent mass quantity per unit adsorbent cross sectional area at breakpoint and exhaustion point, respectively and were calculated using eqn. 1 and 2.

$$\bar{V}_b(\mu g/cm^2) = (C_b * V_b)/\pi r^2 \quad (1)$$

$$\bar{V}_x(\mu g/cm^2) = (C_x * V_x)/\pi r^2 \quad (2)$$

Where, C_b and C_x are concentrations in $\mu g/L$ at volumes V_b and V_x in mL. r (cm) is the radii of the cross-section of the adsorbent in the column.

The mass flow rate F_m , is expressed as mass per unit cross-sectional area of the bed. It can be calculated using eqn. 3.

$$F_m = \bar{V}_x/t_x \quad (3)$$

where, \bar{V}_x ($\mu \frac{g}{cm^2}$) is the total effluent mass quantity per unit cross sectional area of adsorbent at exhaustion, t_x is the total time (min) in reaching exhaustion/saturation point.

The time, t_δ , is defined as the time required for the movement of zone of adsorption down the length of adsorbent bed and can be calculated using eqn. 4.

$$t_\delta = \bar{V}_x - \bar{V}_b/F_m \quad (4)$$

Ratio of the carbon bed depth (D) to the time can be calculated using eqn. 5.

$$\frac{\delta}{D} = \frac{t_\delta}{t_x - t_b} \quad (5)$$

Where, t_b is the time needed for the formation of primary zone of saturation.

Fractional capacity f , i.e. fraction of adsorbate present in the adsorbent zone of the column is given in eqn. 6.

$$f = \left(1 - \frac{t_b}{t_\delta}\right) \quad (6)$$

Eqn. 7 shows the equation for the measurement of percent saturation

$$\text{Percent saturation} = \frac{D + \delta(f-1)}{D} * 100 \quad (7)$$

Area under the integrated plot between adsorbed arsenic concentrations against the flow time, total carbon capacity is determined.

Bed volume, empty-bed-contact-time (EBCT) and carbon usage rate can be calculated using given eqns. 8, 9 and 10.

$$\text{Bed volume} = (\text{Bed height} * \pi r^2) / 1000 \quad (8)$$

$$\text{EBCT} = \frac{\text{Bed volume}}{\text{Flow rate}} \quad (9)$$

$$\text{Carbon usage rate} \left(\frac{g}{L} \right) = \frac{\text{Weight of carbon in column}}{\text{Volume of breakthrough}} * 1000 \quad (10)$$

7.2.1. Column adsorption capacity (q_e):

It is important to determine the maximum adsorption capacity of the arsenic on the adsorbent. Integration of the area A_c under the breakthrough plots between C_{ads} ($C_0 - C_t$) versus time “t” (figure 7.4 and 7.5) gives the amount of As(III) adsorbed (figure 7.4 a,b) and As(V) (figure 7.5 a, b). It is expressed from eqn. 11,

$$A_c = \int_{t=0}^{t=t_{total}} C_{ads} dt \quad (11)$$

Substituting A_c in eqn. 12 calculates the total adsorbed As(III)/ (V), q_{total} ,

$$Q_{total}(\mu g) = \frac{QA_c}{1000} = \frac{Q}{1000} \int_{t=0}^{t=t_{total}} (C_0 - C_t) * dt \quad (12)$$

The total amount of As(III)/ (V) can be calculated using eqn. 13

$$M_{total}(\mu g) = \frac{C_0 Q t_{total}}{1000} \quad (13)$$

t_{total} is the total flow time (min) and Q (mL/min) is the total rate of inflow.

In order to evaluate the performance of column, the total percent removal efficiency Y for the adsorbent can be expressed as the ratio of Q_{total} and M_{total} and is given by eqn. 14.

$$Y(\%) = \frac{q_{total}}{m_{total}} * 100 \quad (14)$$

Maximum As(III)/(V) adsorption capacity $Q_{0,exp}$ ($\mu\text{g/g}$) of the column can be calculated by eqn. 15.

$$Q_{0,exp}(\mu\text{g/g}) = \frac{q_{total}}{m} \quad (15)$$

Where m is the amount of adsorbent taken in the column.

7.2.3. Fixed-bed adsorption modeling:

In order to determine adsorption capacity, life cycle, and time span of the process, Thomas and Yoon-nelson models were applied (Yanhong Li et al., 2018; López-Cervantes et al., 2017; Patel, 2019; W. J. Thomas & Crittenden, 1998b; Z. Xu, Cai, & Pan, 2013).

7.2.3.1 Thomas Model (TM)

It is one of the most commonly used models to predict the maximum adsorptive capacity of an adsorbent. Thomas model is based on the assumptions of Langmuir adsorption isotherm model and follows second-order reversible kinetics reaction (H. C. Thomas, 1944). It assumes that the axial dispersion of the adsorbent doesn't occurs. Also, the resistance due to internal and external diffusion is negligible (Dutta & Basu, 2014; Ghribi & Chlendi, 2011; Patel, 2019; W. J. Thomas & Crittenden, 1998c; Z. Xu et al., 2013). Thomas model can be represented by eqn. (16) (H. C. Thomas, 1944).

$$\ln\left(\frac{C_0}{C_t} - 1\right) = \frac{K_{TH}Q_0m}{Q} - K_{TH}C_0t \quad (16)$$

Where, C_0 ($\mu\text{g/L}$) and C_t ($\mu\text{g/L}$) are the initial concentration and concentration of the adsorbate in the solution at given time 't' (min), respectively. ' K_{TH} ' is the Thomas model constant (ml/min μg). ' Q_0 ' ($\mu\text{g/g}$) is the maximum adsorption capacity, ' m ' (g) is the mass of adsorbent packed in the column and ' Q ' (ml/min) is the flow rate. Parameters were determined for the plot of $\ln\left(\frac{C_0}{C_t} - 1\right)$ versus t . And are given in Table 7.3 (H. C. Thomas, 1944).

7.2.3.2 Yoon-Nelson Model (YNM)

Yoon-Nelson model is a simple model. The model assumes that the probability of the adsorbate to get adsorbed is directly proportional to its adsorption and adsorbent's breakthrough (Z. Xu et al., 2013; Yoon, 1984). It is calculated using eqn. 17

$$\ln \left[\frac{C_t}{C_0 - C_t} \right] = K_{YN}t - t_{0.5}K_{YN} \quad (17)$$

Where, C_0 ($\mu\text{g/L}$) and C_t ($\mu\text{g/L}$) are the initial concentration and concentration of the adsorbate in the solution at a given time 't' (min), respectively. ' K_{YN} ' is the Yoon-Nelson model constant (ml/min). $t_{0.5}$ is the time at which 50% of adsorbate (As(III)/(V)) is adsorbed over adsorbents (RHIOB and WHIOB). Parameters were obtained from the graph plot $\ln \left[\frac{C_t}{C_0 - C_t} \right]$ versus time t and are given in Table 7.4 (Yoon, 1984).

7.3. Results and discussion

7.3.1. As(III) and As(V) adsorption by RHIOB and WHIOB in Fixed-bed columns:

Fixed bed design parameters t_b , t_x , t_δ , D, Fm, f, δ , EBCT and % saturation for adsorption of As(III)/(V) over RHIOB and WHIOB are summarized in Table 7.1. These were obtained from the breakthrough curves given in figure 7.3 (a-b) for As(III) and figure 7.5 (a-b) for As(V). The breakthrough curve is 'S' shaped. In the beginning, As(III)/As(V) adsorption on RHIOB and WHIOB was fast and decreased with time .

The time to achieve breakpoint (t_b) was higher for WHIOB (198 min, As(III); 386 min, As(V)) than RHIOB (175 min, As(III); 229 min, As(V)), respectively. Also, the breakpoint time (t_b) was higher for As(V) versus As(III) on RHIOB and WHIOB. The time for the movement of the adsorption zone (t_δ) was also higher for WHIOB (1785 min, As(III); 2087 min, As(V)) than RHIOB (999 min, As(III); 1065 min, As(V)). Comparatively, t_δ was higher for As(V) than As(III) on both the adsorbent. The fractional capacity, f, As(III)/As(V) at breakpoint was higher for WHIOB (0.82, As(III); 0.9, As(V)) than RHIOB (0.78, As(III); 0.83, As(V)) (Table

7.1). The length of primary adsorption zone (δ), was higher for WHIOB (1.98 cm, As(III); 2.13 cm, As(V)) than RHIOB (1.97 cm, As(III); 2.06 cm, As(V)) over both As(III) and As(V). The percent saturation for WHIOB (84.9%, As(III); 90.14%, As(V)) is also higher than RHIOB (83.1%, As(III); 85.5% As(V)) [Table 7.1]. These parameters can be used for scaling up of the pilot-scale and full-scale operations.

Maximum adsorption capacities, Q_0 of As(III) and As(V) over RHIOB and WHIOB are summarized in Table 7.2. The parameters were obtained from the breakthrough curves of C_{ads} ($C_0 - C_t$) ($\mu\text{g/L}$) versus time t (min) (figure 7.4 (a-b), As(III); and figure 7.6 (a-b), As(V)) over RHIOB and WHIOB, respectively and fitted using equations 11-15. Moreover, amount of total As(III) and As(V) that passed through the column (M_{total} , μg) and the total amount of As(III) and As(V) adsorbed (Q_{total} , μg) over RHIOB and WHIOB were calculated (Table 7.2). Total percent removal efficiency (%Y) for As(III) and As(V) were also calculated and given in Table 7.2. It is evident from the results that WHIOB (92.11%, As(III); 96.44%, As(V)) performed better than RHIOB (88.98%, As(III); 94.31%, As(V)). Maximum As(III) and As(V) ($Q_{0,exp}$) adsorbed by RHIOB and WHIOB at equilibrium was calculated (Table 7.2.). Performance of WHIOB (105.12 $\mu\text{g/g}$, As(III); 415.11 $\mu\text{g/g}$) was better versus RHIOB (87.35 $\mu\text{g/g}$, As(III); 370.01 $\mu\text{g/g}$, As(V)). This concludes that WHIOB perform better than RHIOB. Moreover, As(V) removal was higher versus As(III) on RHIOB and WHIOB.

Experimental data were fitted to Thomas and Yoon-nelson models for As(III)/As(V). The Thomas rate constants (K_{TH}) were obtained using Thomas model (Yanhong Li et al., 2018; H. C. Thomas, 1944). The parameters for As(III) and As(V) removal were calculated from the plots given in Figures 7.7. (a, b) for As(III) and figure 7.8 (a, b) for As(V) (H. C. Thomas, 1944). Thomas constants and adsorption capacities are given in Table 7.3. The regression coefficients, R^2 for As(III) adsorption on RHIOB (0.768) and WHIOB (0.803) are shown in Table 7.3. Similarly, R^2 for As(V) adsorption on RHIOB (0.754) and WHIOB (0.839) are in good correlation (Table 7.3). The calculated values ($Q_{0,cal}$) for the adsorption

capacity of As(III) (85.21 $\mu\text{g/L}$, RHIOB; 99.82 $\mu\text{g/L}$, WHIOB) and As(V) (365.88 $\mu\text{g/L}$, RHIOB; 409.21 $\mu\text{g/L}$, WHIOB) were found closer to the experimental values ($Q_{0,\text{exp}}$) of As(III) (87.35 $\mu\text{g/L}$, RHIOB; 105.12 $\mu\text{g/L}$, WHIOB) and As(V) (370.01 $\mu\text{g/L}$, RHIOB; 415.11 $\mu\text{g/L}$, WHIOB) (Table 7.3). The Thomas rate constants (K_{TH}) for WHIOB (0.003 $\text{mL}/\mu\text{g min}$, As(III); 0.055 $\text{mL}/\mu\text{g min}$, As(V)) and RHIOB (0.002 $\text{mL}/\mu\text{g min}$, As(III); 0.031 $\text{mL}/\mu\text{g min}$, As(V)) are described in Table 7.3. WHIOB showed better column performance as compared to RHIOB for both As(III) and As(V) adsorption. In addition, As(V) showed better column performance on RHIOB and WHIOB as compared to As(III). Fitting to Thomas model concludes that external and internal diffusions are not the rate limiting steps for As(III) and As(V) adsorption process (Yanhong Li et al., 2018; López-Cervantes et al., 2017).

Yoon- Nelson model was applied to calculate the half time ($t_{0.5,\text{cal}}$) i.e. the time where 50% As(III) and As(V) concentration was adsorbed over RHIOB and WHIOB through the column and the Yoon-Nelson constant coefficient (K_{YN}). K_{YN} for WHIOB (0.0027 mL/min , As(III); 0.0094 mL/min , As(V)) and RHIOB (0.0015 mL/min , As(III); 0.0033 mL/min , As(V)) are mentioned in Table 7.4. In addition, the values of $t_{0.5,\text{cal}}$ WHIOB (935.8 min, As(III); 2532.9 min, As(V)) were higher as compared to $t_{0.5,\text{cal}}$ for RHIOB (433.5 min, As(III); 1151.8 min, As(V)) (Table 7.4). The calculated half life ($t_{0.5,\text{cal}}$) were closer to the experimental values ($t_{0.5,\text{exp}}$) for RHIOB (435.6 min, As(III); 2543.1 min, As(V)) and WHIOB (953.2 min, As(III); 1158.2 min, As(V))(Table 7.4). R^2 for As(III) on RHIOB (0.768) and WHIOB (0.803) showed good correlation between C_e/C_0 and time t (Table 7.3). R^2 for As(V) also showed better fitting on RHIOB (0.754) and WHIOB (0.839) (Table 7.4). WHIOB has better column performance as compared to RHIOB, throughout the column studies.

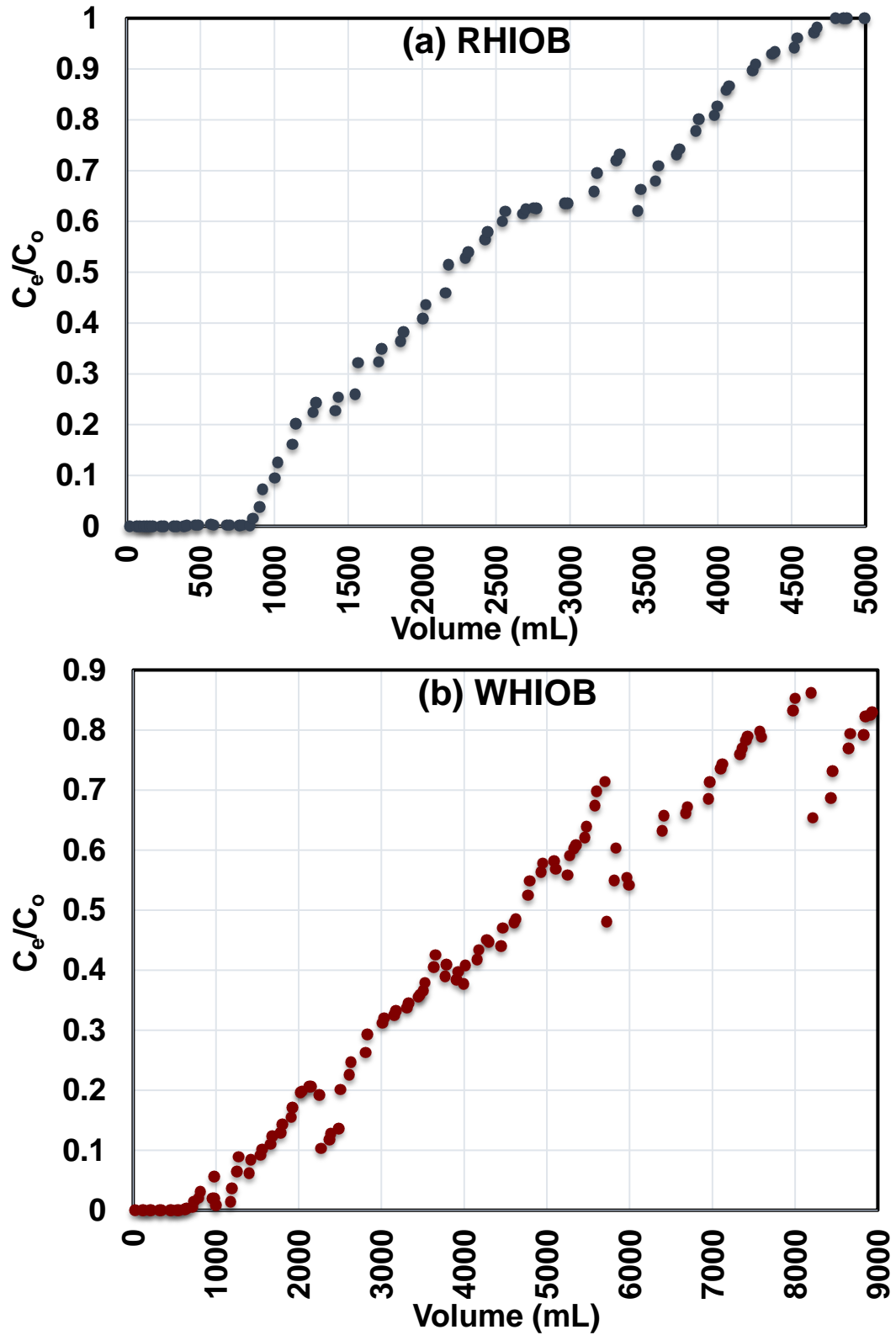


Figure 7.3. Breakthrough curves C_e/C_0 versus Volume (mL) for As(III) adsorption (a) RHIOB and (b) WHIOB (pH = 7.5, particle size = 50 – 100 mesh, initial As(III) concentration = 100 $\mu\text{g/L}$ bed height = 5 cm, Flow rate = 5.0 mL/min).

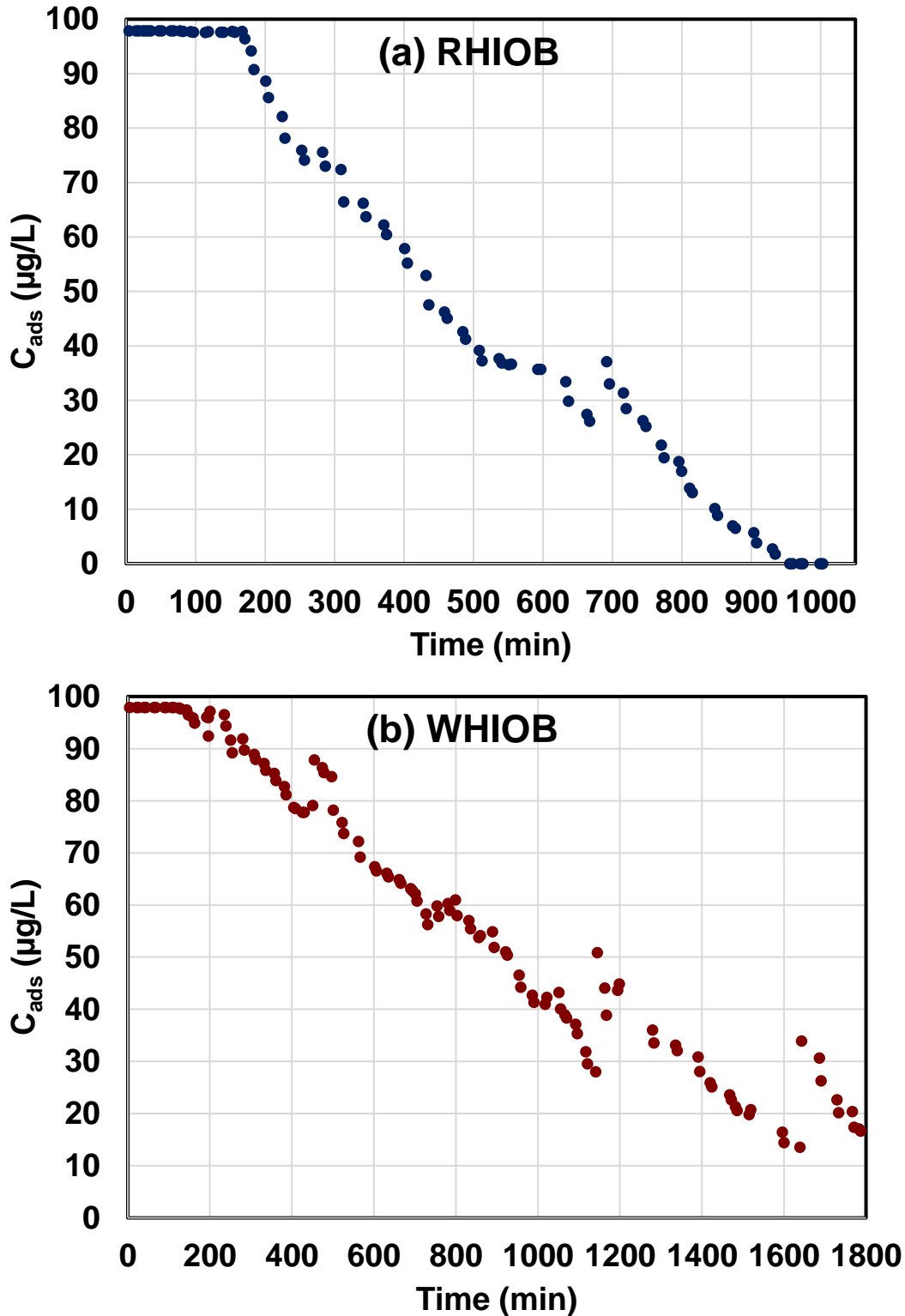


Figure 7.4. C_{ads} (C_0-C_e) versus time of effluent flow for As(III) adsorption (a) RHIOB and (b) WHIOB (pH = 7.5, particle size = 50 – 100 mesh, initial As(III) concentration = 100 $\mu\text{g/L}$ bed height = 5 cm, Flow rate = 5.0 mL/min).

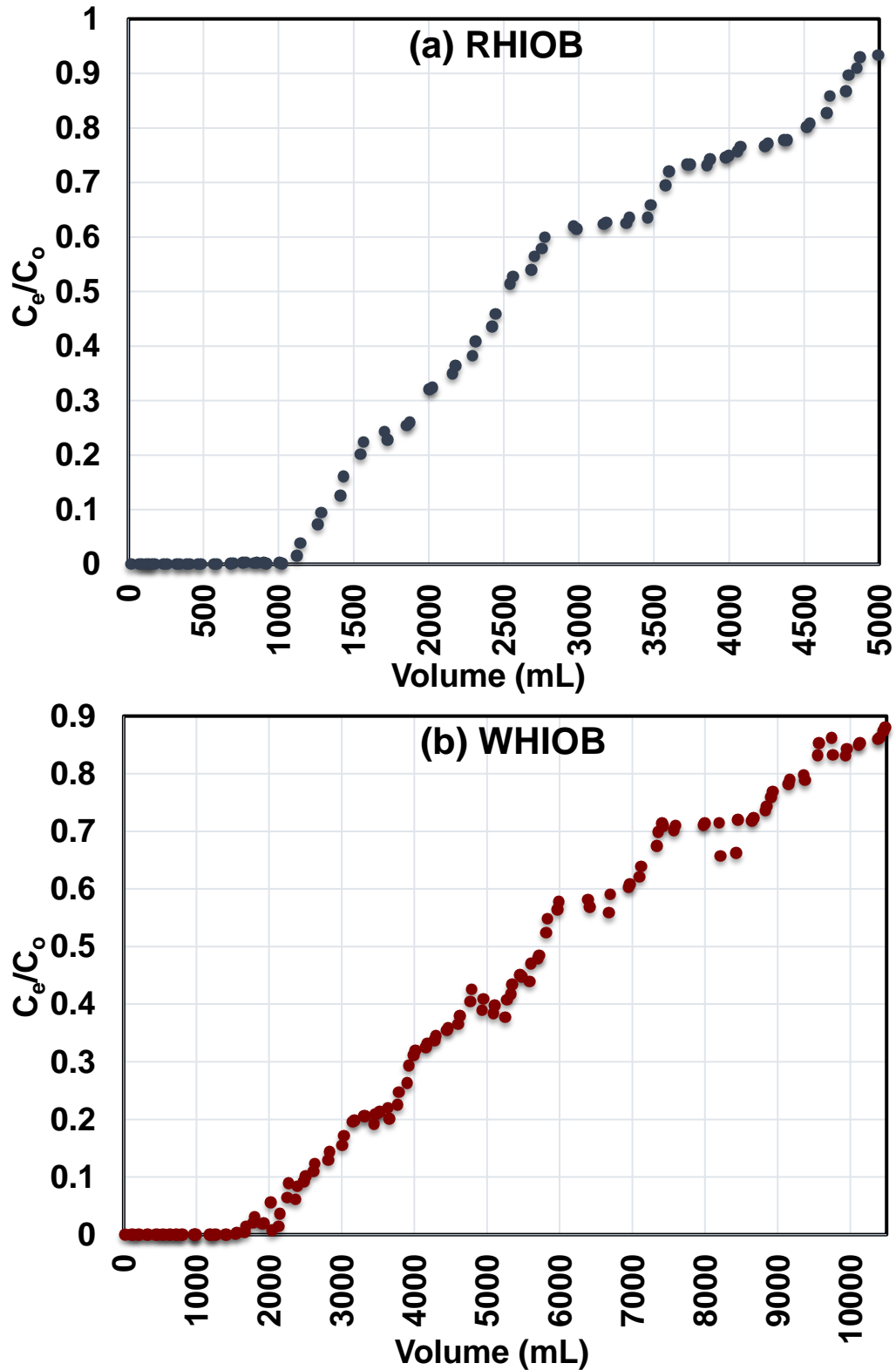


Figure 7.5. Breakthrough curves C_e/C_0 versus Volume (mL) for As(V) adsorption (a) RHIOB and (b) WHIOB (pH = 7.5/5.0, particle size = 50 – 100 mesh, initial As(V) concentration = 100 $\mu\text{g/L}$, bed height = 5 cm, Flow rate = 5.0 mL/min).

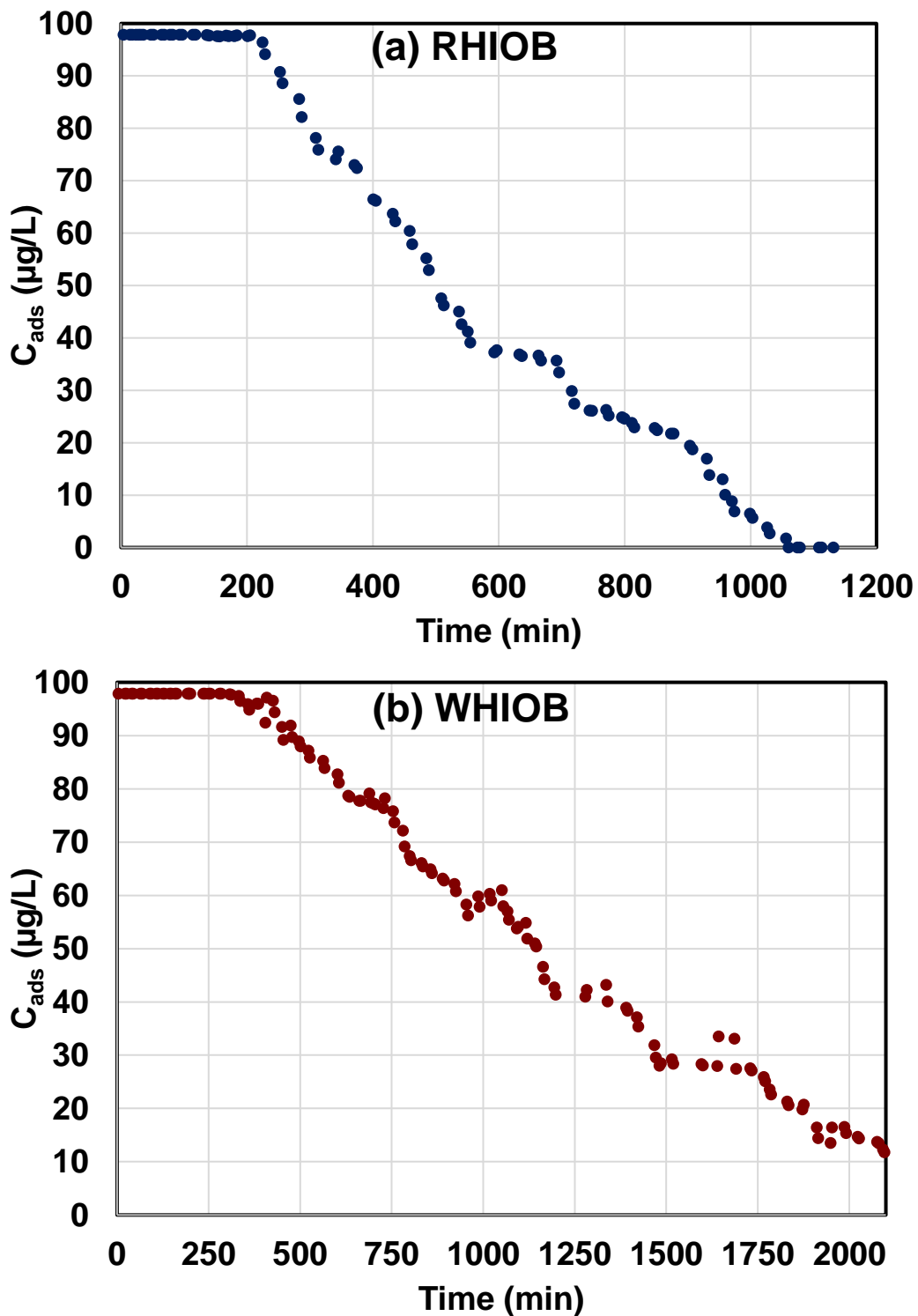


Figure 7.6. C_{ads} (C_0-C_e) versus time of effluent flow for As(V) adsorption (a) RHIOB and (b) WHIOB (pH = 7.5/5.0, particle size = 50 – 100 mesh, initial As(V) concentration= 100 $\mu\text{g/L}$, bed height = 5 cm, Flow rate = 5.0 mL/min).

Table 7.1. Fixed-bed column parameters for As(III) and As(V) adsorption by RHIOB and WHIOB.

Parameters	RHIOB As(III)	WHIOB As(III)	RHIOB As(V)	WHIOB As(V)
C_0 ($\mu\text{g/mL}$)	97.9	97.9	97.9	97.9
C_x ($\mu\text{g/mL}$)	97.0	81.3	97.1	86.14
C_b ($\mu\text{g/mL}$)	3.72	1.92	3.72	1.93
Q (min/L)	5.0	5.0	5.0	5.0
V_b ($\mu\text{g/cm}^2$)	1.02	0.6	1.36	1.18
V_x ($\mu\text{g/cm}^2$)	154.89	231.15	166.09	287.5
$(V_x - V_b)$ ($\mu\text{g/cm}^2$)	153.87	230.54	164.73	286.32
F_m ($\mu\text{g/cm}^2/\text{min}$)	0.15	0.13	0.15	0.14
D (cm)	5.0	5.0	5.0	5.0
t_x (min)	1005	1790	~1074	~2096
t_b (min)	~175	~198	~229	~386
t_δ (min)	~999	~1785	~1065	~2087
f	0.78	0.82	0.83	0.9
δ (cm)	1.97	1.98	2.06	2.13
EBCT (min)	1.5	1.6	1.5	1.6
% saturation	83.1	84.92	85.52	90.14
Carbon usage rate (g/L)	4.37	2.59	5.65	5.09
Bed Volume (L)	0.00785	0.00754	0.00785	0.00754

Table 7.2. Mathematical analysis and experimental maximum adsorption efficiency (q_{exp}) obtained by integration of the plot $C_{\text{ads}} (= C_0 - C_t)$ versus t (time).

S. No.	Synthesized material	Q_{total} (μg) (total amount of arsenic adsorbed by the column)	M_{total} (μg) (total amount of arsenic flowing through the column)	Total removal efficiency $q_{\text{total}}/m_{\text{total}}$ (%Y)	$Q_{0,\text{exp}}$ ($\mu\text{g/g}$)
As(III)					
1.	RHIOB	436.75	490.82	88.98	87.35
2.	WHIOB	525.6	570.65	92.11	105.12
As(V)					
1.	RHIOB	1850.05	1961.62	94.31	370.01
2.	WHIOB	2075.55	2152.27	96.44	415.11

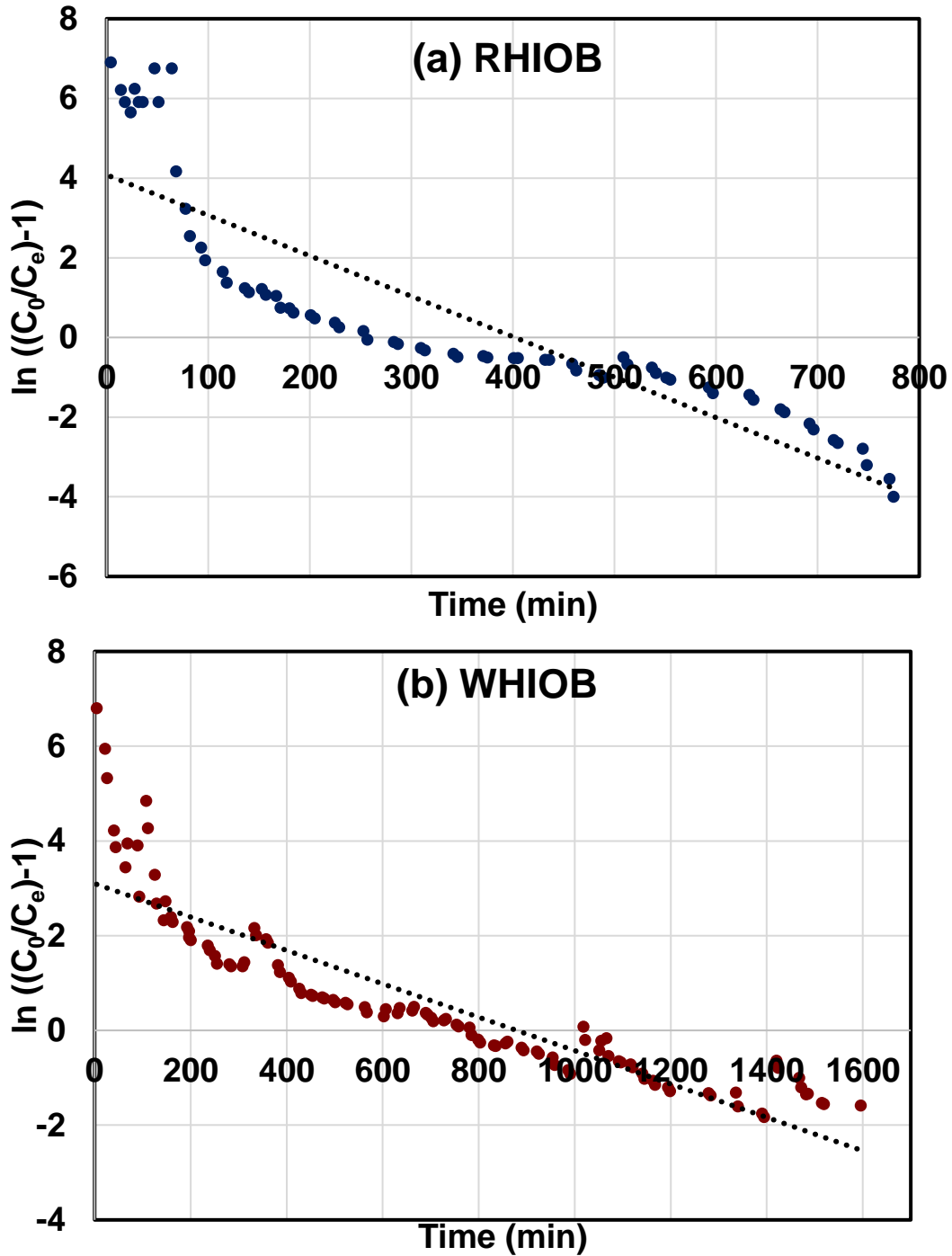


Figure 7.7. Thomas kinetic plots for adsorption of As(III) over (a) RHIOB and (b) WHIOB (pH = 7.5/5.0, particle size = 50 – 100 mesh, initial As(III) concentration = 100 $\mu\text{g/L}$, bed height = 5 cm, Flow rate = 5.0 mL/min).

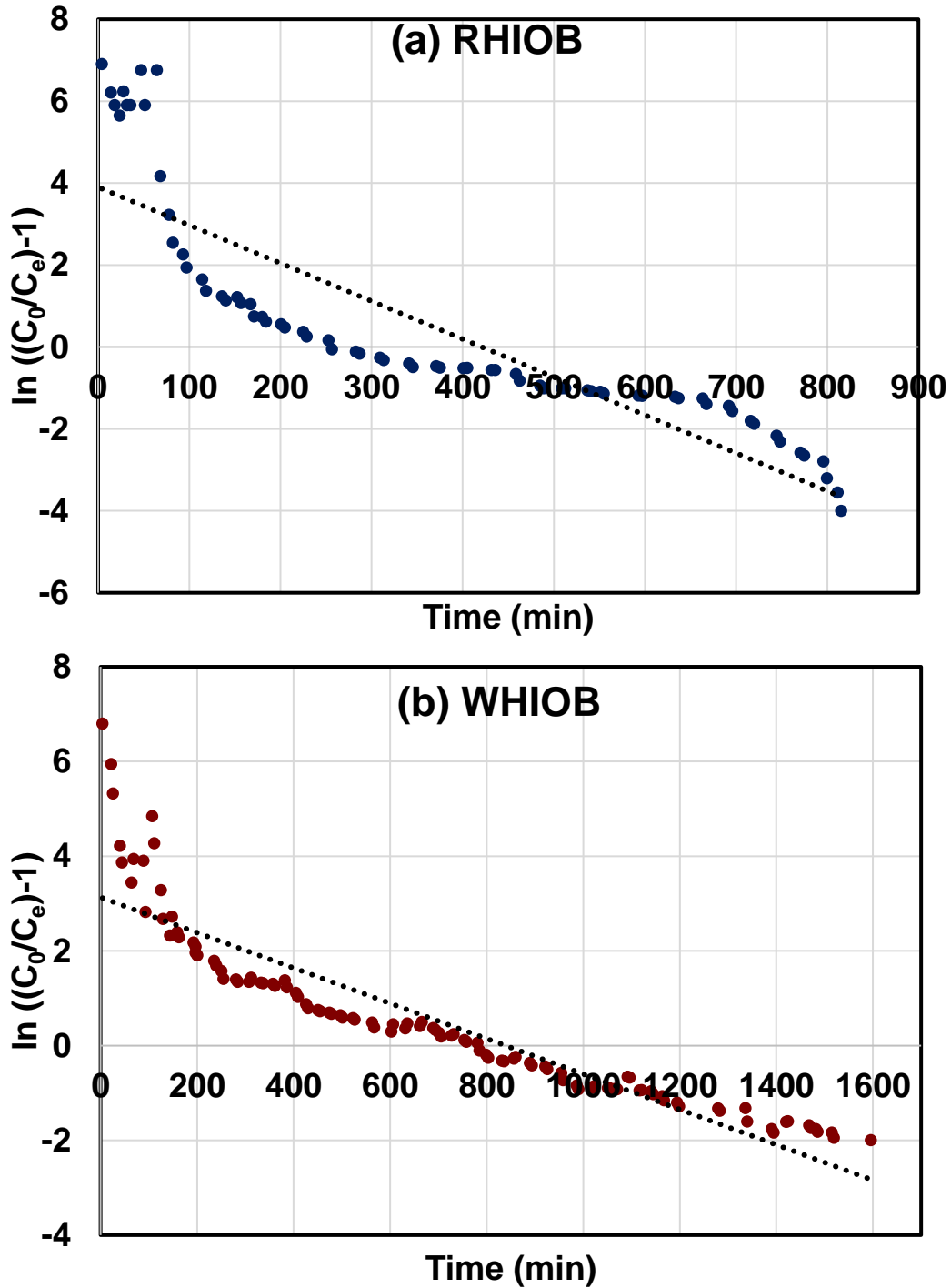


Figure 7.8. Thomas kinetic plots for adsorption of As(V) over (a) RHIOB and (b) WHIOB (pH = 7.5/5.0, particle size = 50 – 100 mesh, initial As(V) concentration = 100 $\mu\text{g/L}$, bed height = 5 cm, Flow rate = 5.0 mL/min).

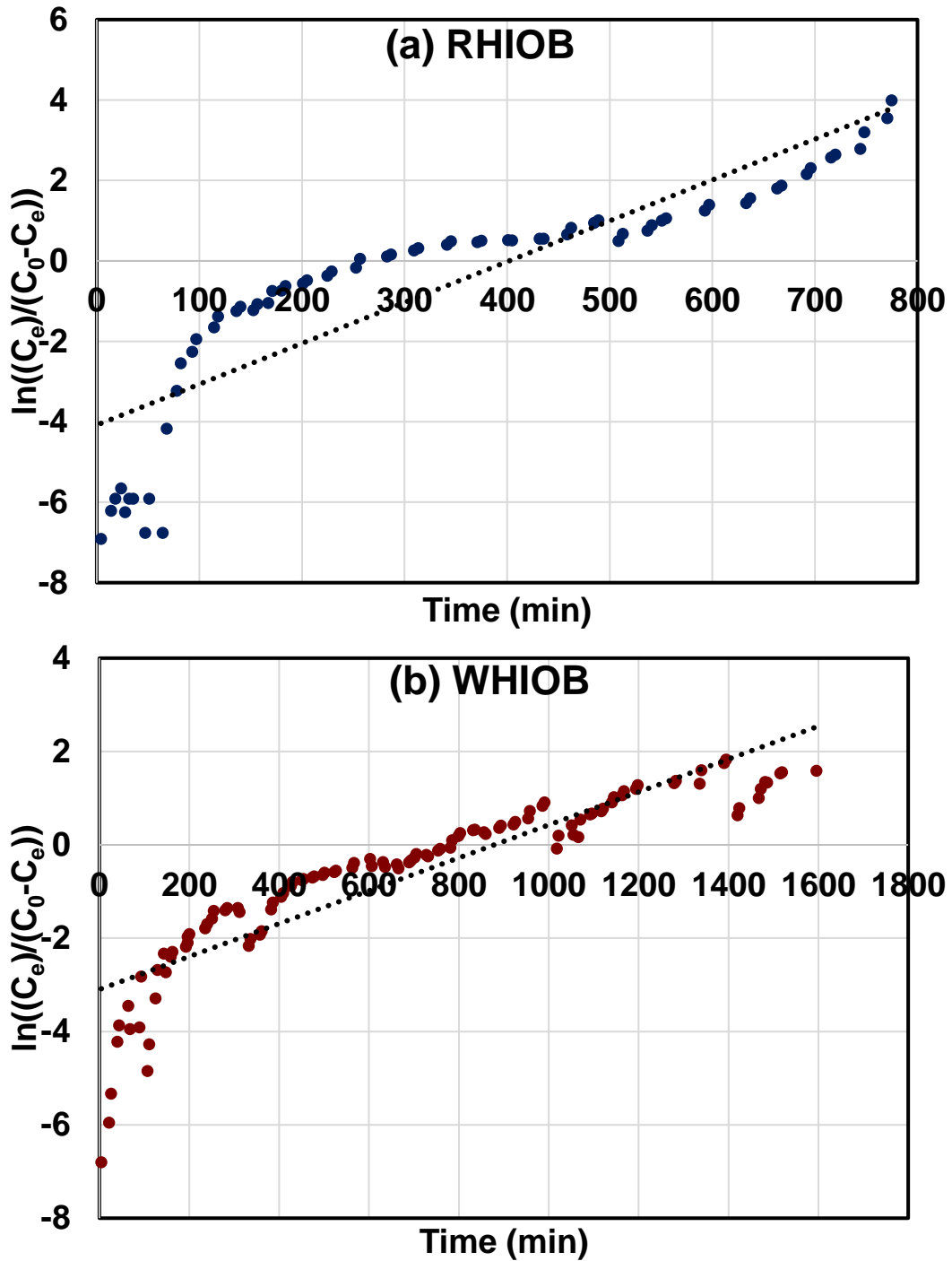


Figure 7.9. Yoon-Nelson kinetic plots for adsorption of As(III) over (a) RHIOB and (b) WHIOB (pH = 7.5/5.0, particle size = 50 – 100 mesh, initial As(III) concentration = 100 µg/L, bed height = 5 cm, Flow rate = 5.0 mL/min).

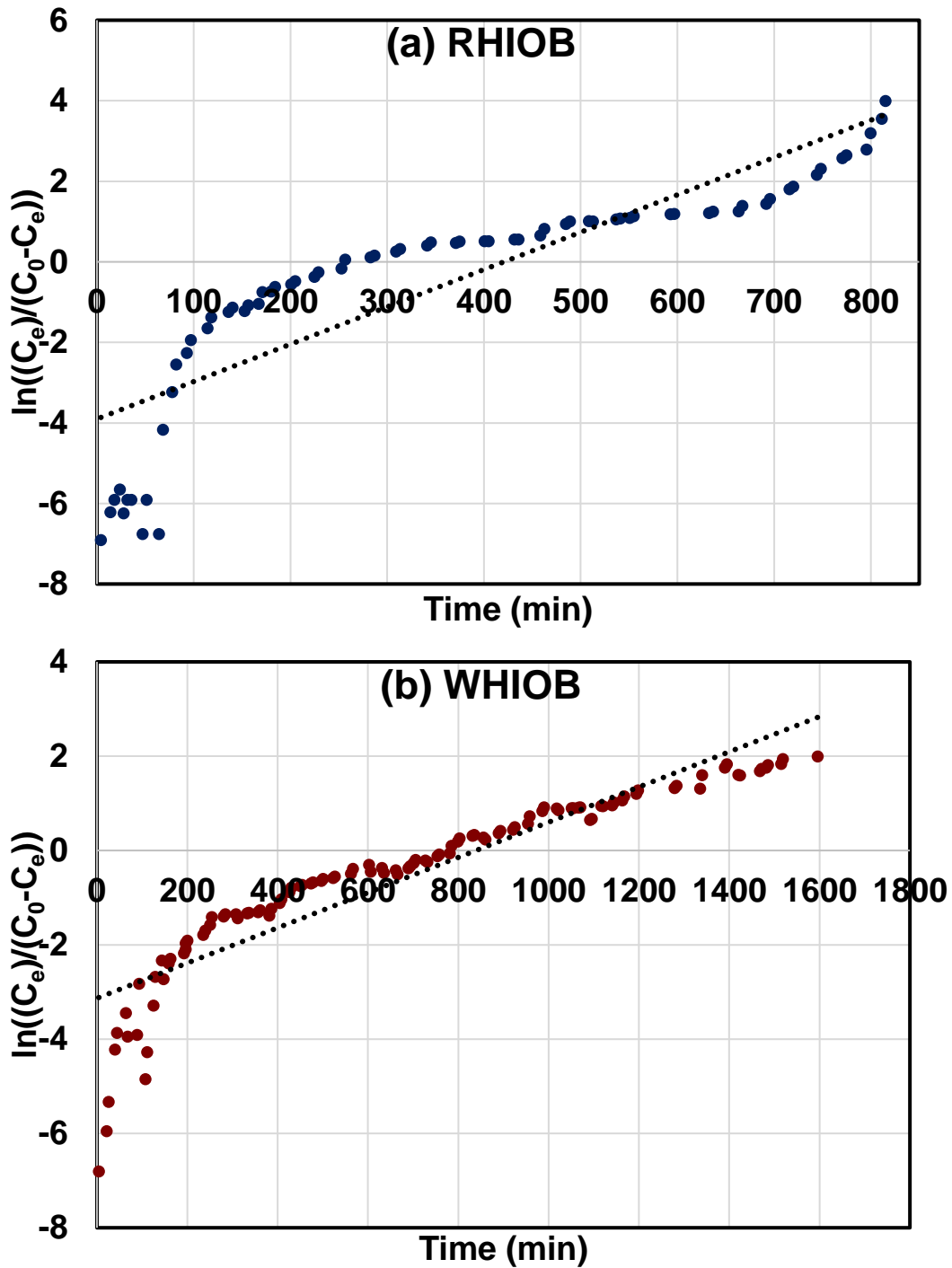


Figure 7.10. Yoon-Nelson kinetic plots for adsorption of As(V) over (a) RHIOB and (b) WHIOB (pH = 7.5/5.0, particle size = 50 – 100 mesh, initial As(V) concentration = 100 µg/L, bed height = 5 cm, Flow rate = 5.0 mL/min).

Table 7.3. Parameters obtained from linear Thomas model plot for As(III) and As(V) adsorption over RHIOB and WHIOB.

S. No.	Synthesized material	Bed height, h (cm)	C ₀ (µg/L)	Flow rate, Q (mL/min)	K _{TH} (mL/µg min)	Q _{0,cal} Calculated column capacity (µg/g)	Q _{0,exp} Experimental column capacity (µg/g)	Q _{0,cal} Calculated batch capacity (µg/g)	R ²
As(III)									
1.	RHIOB	5.0	97.89	5.0	0.002	85.21	87.35	96.14	0.7682
2.	WHIOB	5.0	97.89	5.0	0.003	99.82	105.12	110.73	0.8033
As(V)									
1.	RHIOB	5.0	97.89	5.0	0.031	365.88	370.01	386.88	0.7543
2.	WHIOB	5.0	97.89	5.0	0.055	409.21	415.11	421.45	0.8394

Table 7.4. Parameters obtained from linear Yoon-Nelson model plot for As(III) and As(V) adsorption over RHIOB and WHIOB.

S. No.	Synthesized material	Bed height, h (cm)	C ₀ (µg/L)	Flow rate, Q (mL/min)	K _{YN} (mL/min)	T _{0.5, cal} (min)	T _{0.5, exp} (min)	R ²
As(III)								
1.	RHIOB	5.0	97.89	5.0	0.0015	433.5	435.6	0.7685
2.	WHIOB	5.0	97.89	5.0	0.0027	935.8	953.2	0.8034
As(V)								
1.	RHIOB	5.0	97.89	5.0	0.0033	2532.9	2543.1	0.7541
2.	WHIOB	5.0	97.89	5.0	0.0094	1151.8	1158.2	0.8392

7.3. Desorption and Regeneration of adsorbents

Simultaneous As(III) and As(V) desorption and regeneration of exhausted adsorbent was performed using 50 mL of a wash solution prepared by mixing 0.1 N NaOH and 0.1 N NaCl.

First, batch adsorption studies were carried out separately at a pH of 7.5 for initial As(III) concentration of 100 µg/L at 25°C, and pH 5.0 for initial As(V) concentration of 100 µg/L at 25°C. The suspension was filtered and the exhausted adsorbent was collected. The adsorbent was washed using double distilled water and oven dried. The dried adsorbent was dispersed in 50 mL of the wash solution (0.1 N NaOH + 0.1 N NaCl) and kept for 24 h. The suspension was filtered. The filtrate was analyzed for As(III) and As(V) concentration desorbed from the adsorbent. This process was repeated for next three consecutive cycles to find the decrease in the efficiency of recycled adsorbents. The percent As(III) and As(V) adsorption and desorption in four consecutive cycle is shown in Figure 7.11. As(III) adsorption on RHIOB was decreased, from 90% (in the first cycle) to 86% (in the fourth cycle). Similarly, As(III) removal on WHIOB was reduced from 92% (in the first cycle) to 90% (in the fourth cycle) (Figure 7.11, A). As(V) adsorption on RHIOB was decreased from 92 % (in the first cycle) to 88 % (in the fourth cycle). Similarly, As(V) removal on WHIOB was reduced from 97 % (in the first cycle) to 93 % (in the fourth cycle) (Figure 7.11, B). A very nominal decrease in As(III) and As(V) removal clearly shows the reusability of RHIOB and WHIOB for more many cycles.

7.4. Multicomponent sorption studies

Single and multicomponent arsenite and arsenate sorption on RHIOB and WHIOB was examined in presence and absence of chloride, nitrate, sulphate, bicarbonate, phosphate, sodium, potassium, and calcium. Three sets of batch experiments were carried out to determine the arsenite (100 µg/L) and arsenate (100 µg/L) adsorption in single and multicomponent systems. These include (1) effect of individual interfering ion (100 mg/L) on As(III)/As(V) (100 µg/L) adsorption (2) effect of individual interfering ion (200 mg/L) on As(III)/As(V) (100 µg/L) adsorption (3) effect of combined interfering ions ($\text{Cl}^- : \text{NO}_3^- : \text{SO}_4^{2-} : \text{HCO}_3^- : \text{PO}_4^{3-}$

: Na⁺ : K⁺ : Ca²⁺ :: 100 : 100: 100: 100 : 100 : 100: 100 : 100 mg/L) on As(III)/As(V) (100 µg/L) adsorption (4) effect of total interfering ions in absence of phosphate ions (Cl⁻ : NO₃⁻ : SO₄²⁻ : HCO₃⁻ : Na⁺ : K⁺ : Ca²⁺ :: 100 : 100: 100: 100 : 100 : 100: 100 : 100 mg/L). Studies were conducted separately for As(III) and As(V). All the sorption studies were carried out at an adsorbent dose of 2.0 g/L for RHIOB and 1.0 g/L in case WHIOB at 25 °C and an initial pH of 7.5 for As(III) [Figure 7.12, 7.14] and 5.0 for As(V) [Figure 7.13, 7.15]. Chloride, nitrate, sodium, potassium and calcium when present individually (at 100 mg/L and 200 mg/L) do not affect the As(III) and As(V) adsorption while sulfate, bicarbonate and phosphate significantly inhibited As(III) [Figure 7.12] and As(V) adsorption [Figure 7.13]. Furthermore, As(III) and As(V) adsorption decreased more when sulfate, bicarbonate and phosphate concentrations increased from 100 mg/L to 200 mg/L. Negligible chloride and nitrate influence on As(III) and As(V) adsorption may be due to their tendency to form outer-sphere complexes with iron (oxy)hydroxides nano particles present in RHIOB and WHIOB (T. Sun et al., 2017b; L. Zhang et al., 2016; J. Zhu et al., 2015). Similarly, sulphate and bicarbonates have been reported to form more stable complexes with iron (oxy)hydroxides thereby competing with arsenic oxyanions for adsorption (Jin Zhu et al., 2015). Phosphates showed drastic inhibition in As(III) [Figure 7.12] and As(V) adsorption [Figure 7.13] on RHIOB and WHIOB. This is due to the fact that phosphate belongs to the same family as that of arsenic, therefore, showed close structural similarities (T. Sun et al., 2017b). It forms stronger inner-sphere complexes with iron (oxy)hydroxides, offering strong competition, electrostatic repulsion and hindrance for arsenic oxyanions adsorption on RHIOB and WHIOB (T. Sun et al., 2017b).

Arsenite (100 µg/L) and arsenate (100 µg/L) adsorption in presence of combined interfering ions [Cl⁻ : NO₃⁻ : SO₄²⁻ : HCO₃⁻ : PO₄³⁻ : Na⁺ : K⁺ : Ca²⁺ :: 100 : 100: 100: 100 : 100 : 100: 100 : 100 mg/L and Cl⁻ : NO₃⁻ : SO₄²⁻ : HCO₃⁻ : PO₄³⁻ : Na⁺ : K⁺ : Ca²⁺ :: 200 : 200: 200: 200 : 200 : 200: 200 : 200 mg/L) was significantly decreased on RHIOB and WHIOB [Figure 7.14-7.15]. The decrease in As(III) and As(V) adsorption was increased with rise in individual ion concentration from 100 to 200 mg/L in the multicomponent solution. Furthermore, As(III) and As(V)

adsorption in multicomponent system was also studied by taking all the above mentioned interfering ions except phosphate. Phosphate was excluded due to the fact [Figure 7.14-7.15] that it significantly decreased As(III) and As(V) adsorption when As(III) and phosphate, and As(V) and phosphate were taken together in a binary system [(As(III))/(V): 100 ug/L + PO_4^{3-} :100 mg/L) and (As(III))/(V): 100 ug/L + PO_4^{3-} : 200 mg/L). It is clear from the Figure 7.14 that As(III) adsorption on RHIOB and WHIOB does not significantly decreased when all the interfering ions except phosphate are present in solution. Similar observations were showed on As(V) adsorption [Figure 7.15]. The slight decrease in As(III) and As(V) adsorption in multicomponent system (except phosphate) is due to the interference caused by bicarbonate and sulphate ions. Phosphates do not occur in natural water. It can only present when water is contaminated with some anthropogenic source (such as fertilizers). Thus, RHIOB and WHIOB can successfully be used for As(III) and As(V) removal in single and multicomponent systems with no significant decrease in the presence of many interfering ions.

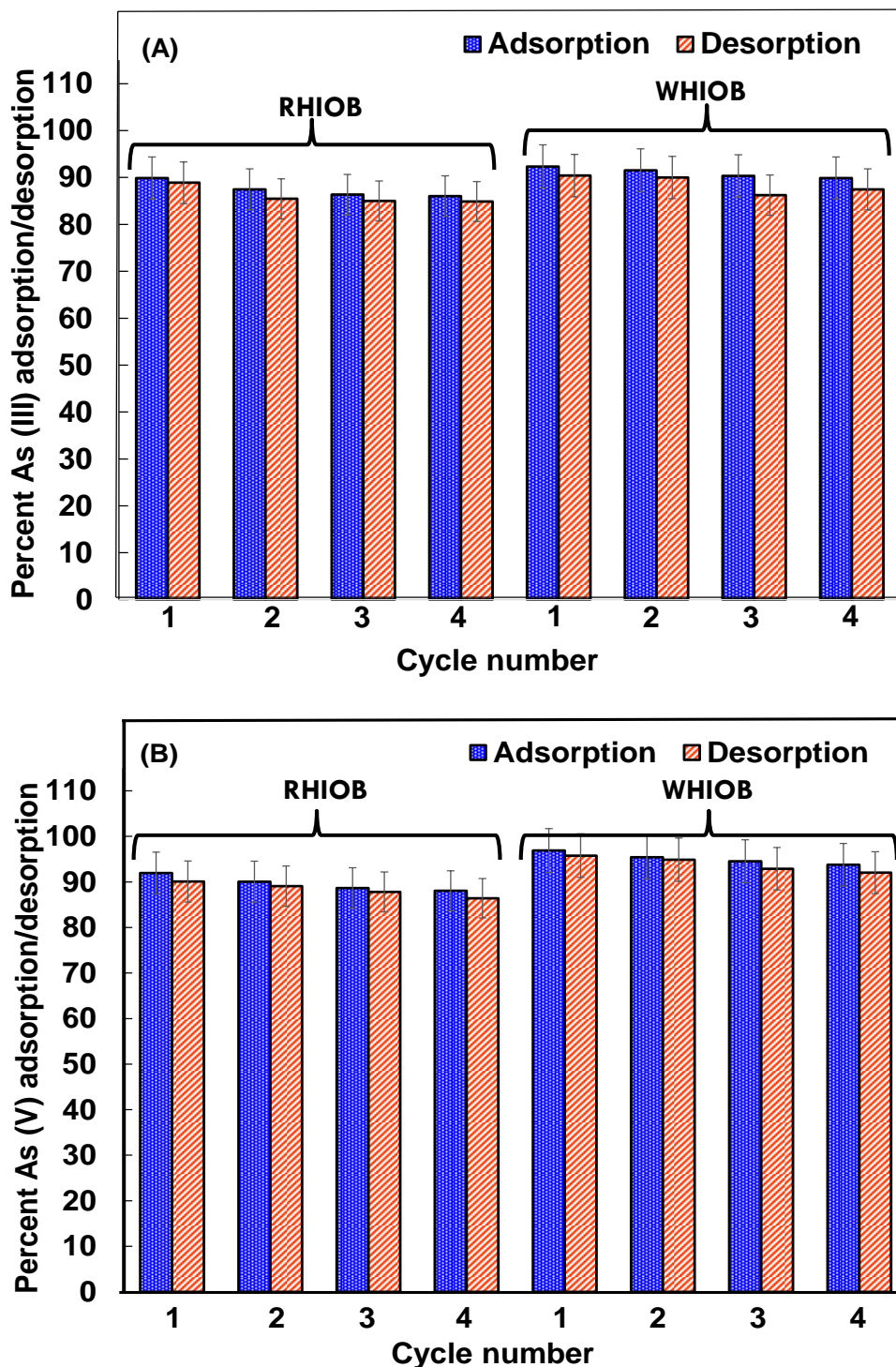


Fig.7.11. Regeneration of As by adsorption and desorption for four consecutive cycles for (A) As(III) RHIOB and WHIOB. (B) As(V) RHIOB and WHIOB. (Adsorption conditions: adsorbent dose = 2.0 g/L; initial As(III)/(V) concentration = 100 µg/L; initial pH = 7.5/5.0, agitation speed = 100 rpm, temperature = 25°C, contact time = 24 h). Desorption conditions: regenerant = 0.1 N NaOH + 0.1 N NaCl, regenerant dose = 50 mL, contact time = 6 h).

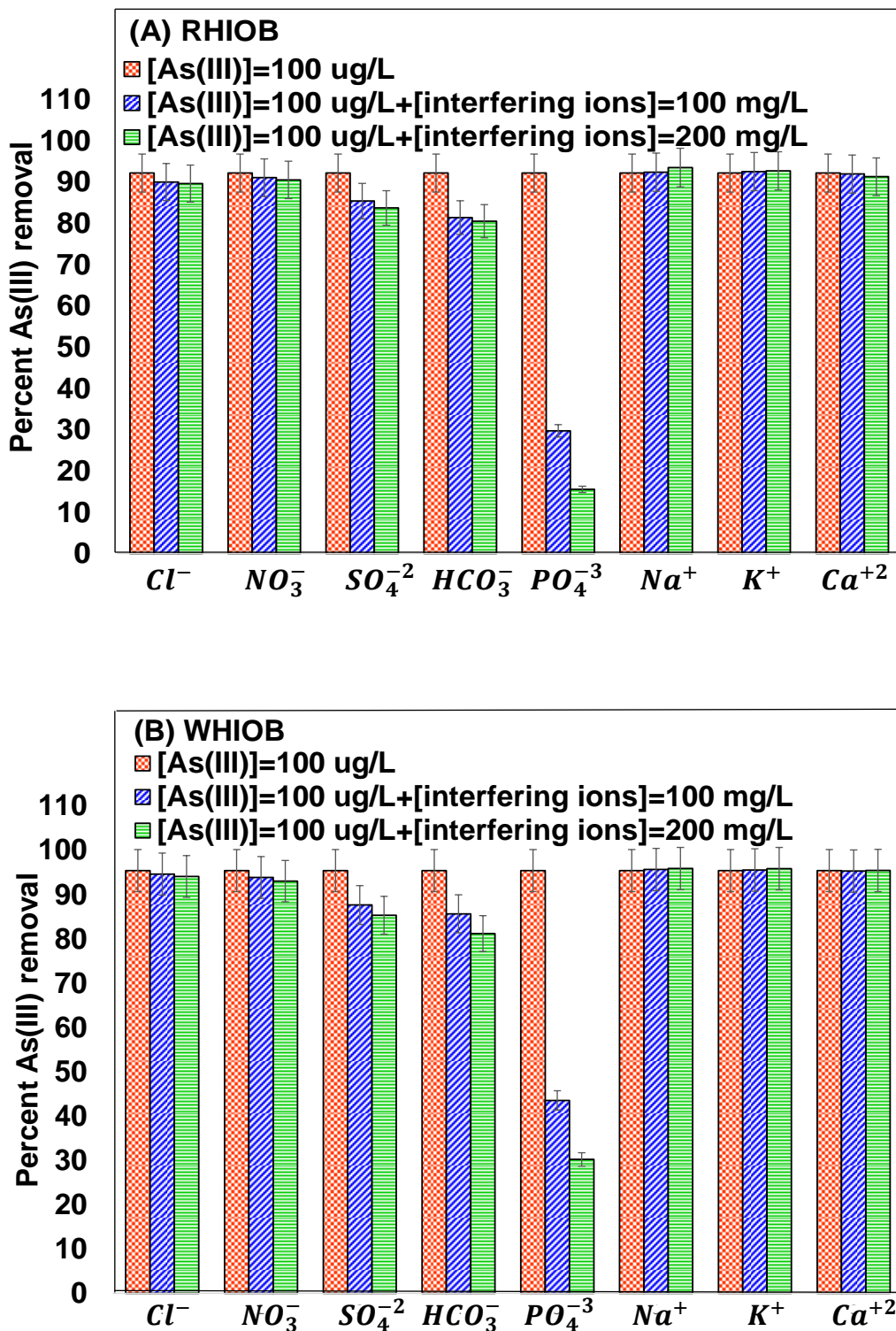


Fig.7.12. Effects of various coexisting ions on adsorption of As(III) removal by (A) RHIOB and (B) WHIOB (adsorbent dose, RHIOB = 2.0 g/L and WHIOB = 1.0 g/L, initial As(III) concentration = 100 µg/L; initial pH = 7.5, agitation speed = 100 rpm, temperature = 25°C, contact time = 24 h).

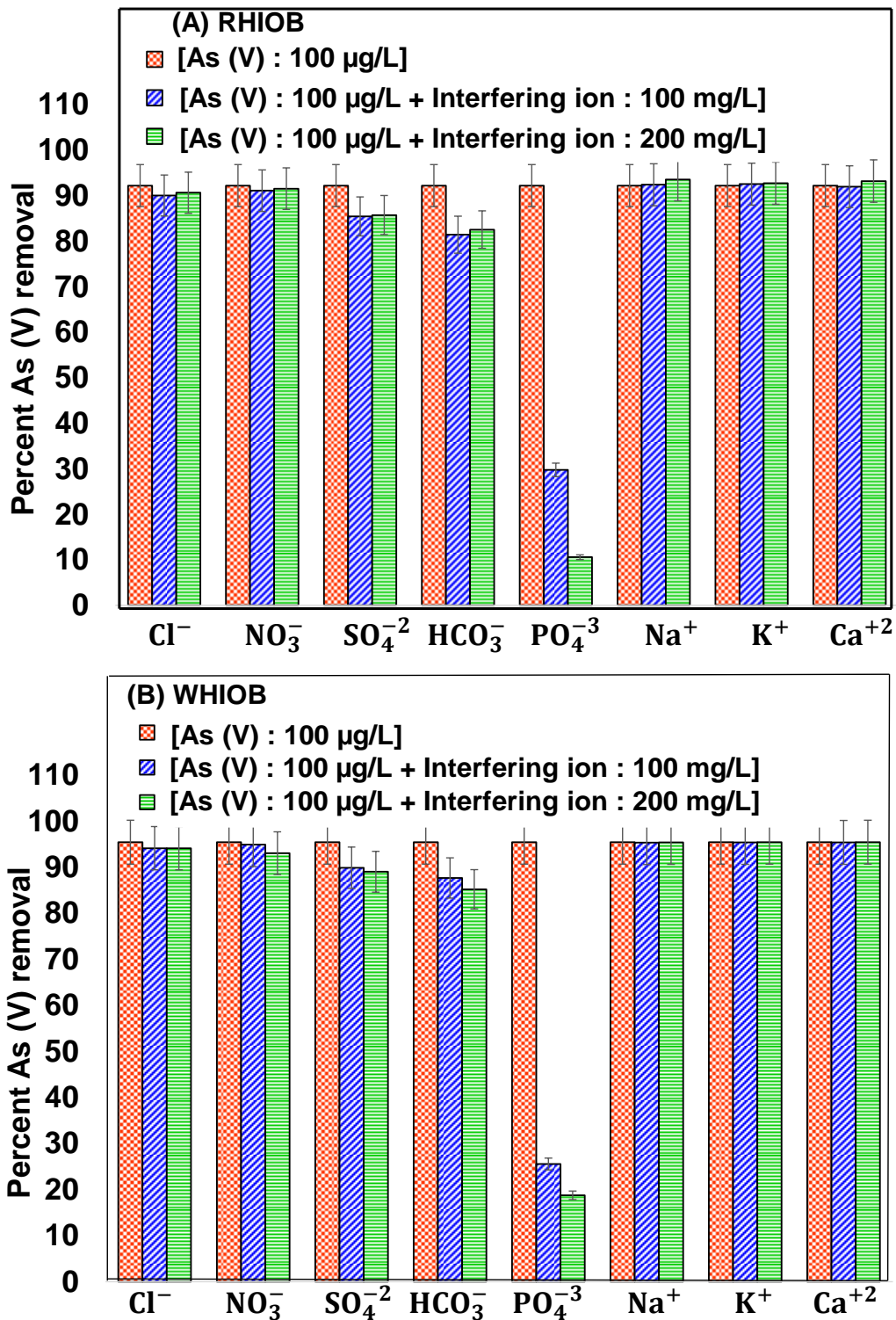


Fig.7.13. Effects of various coexisting ions on adsorption of As(V) removal by (A) RHIOB and (B) WHIOB (adsorbent dose, RHIOB = 2.0 g/L and WHIOB = 1.0 g/L, initial As(V) concentration = 100 µg/L; initial pH = 5.0, agitation speed = 100 rpm, temperature = 25⁰C, contact time = 24 h).

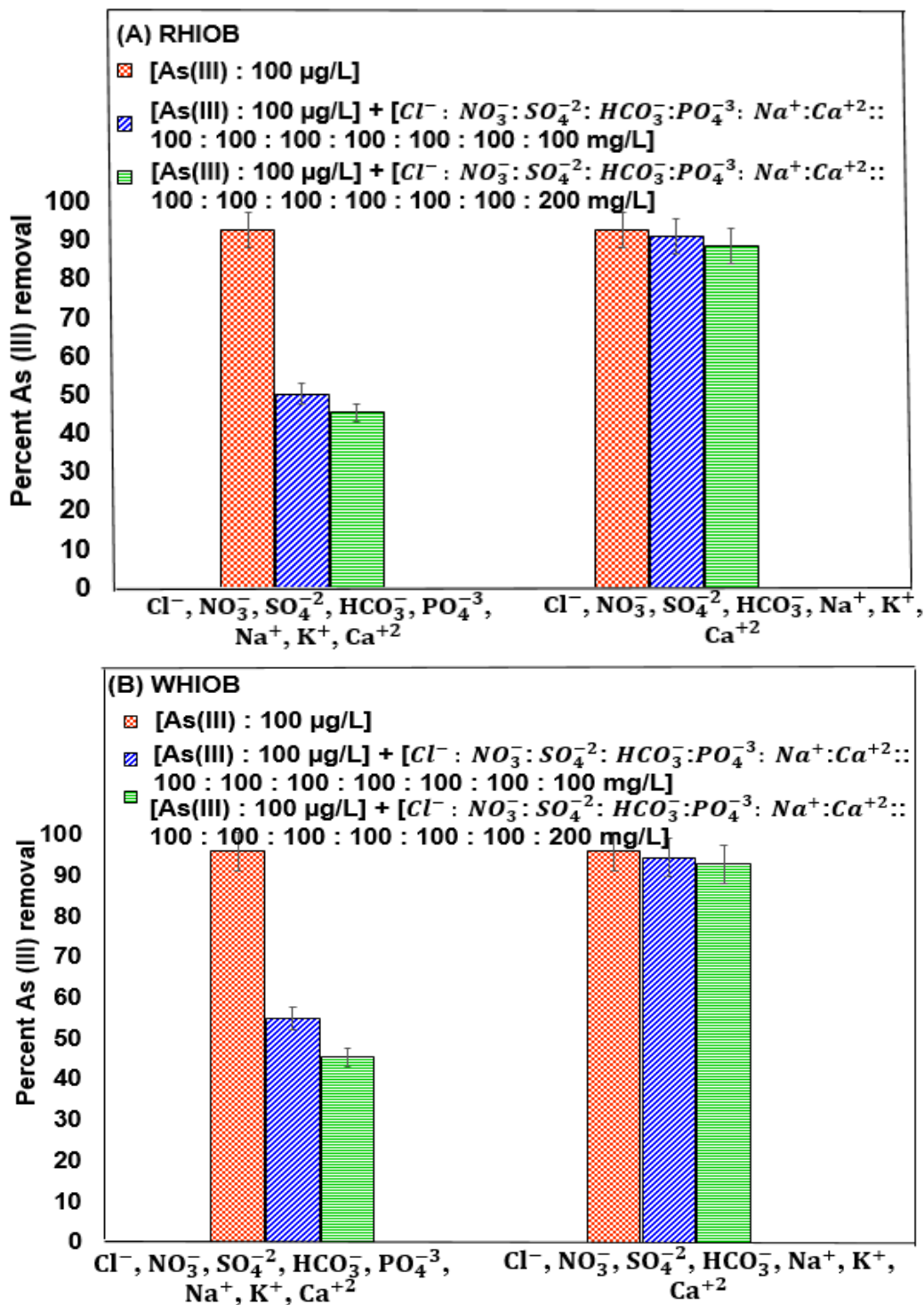


Fig.7.14. Combined effect of coexisting ions and coexisting ions minus phosphates on adsorption of As(III) removal by (A) RHIOB and (B) WHIOB (adsorbent dose, RHIOB = 2.0 g/L and WHIOB = 1.0 g/L, initial As(III) concentration = 100 µg/L; initial pH = 7.5, agitation speed = 100 rpm, temperature = 25°C, contact time = 24 h).

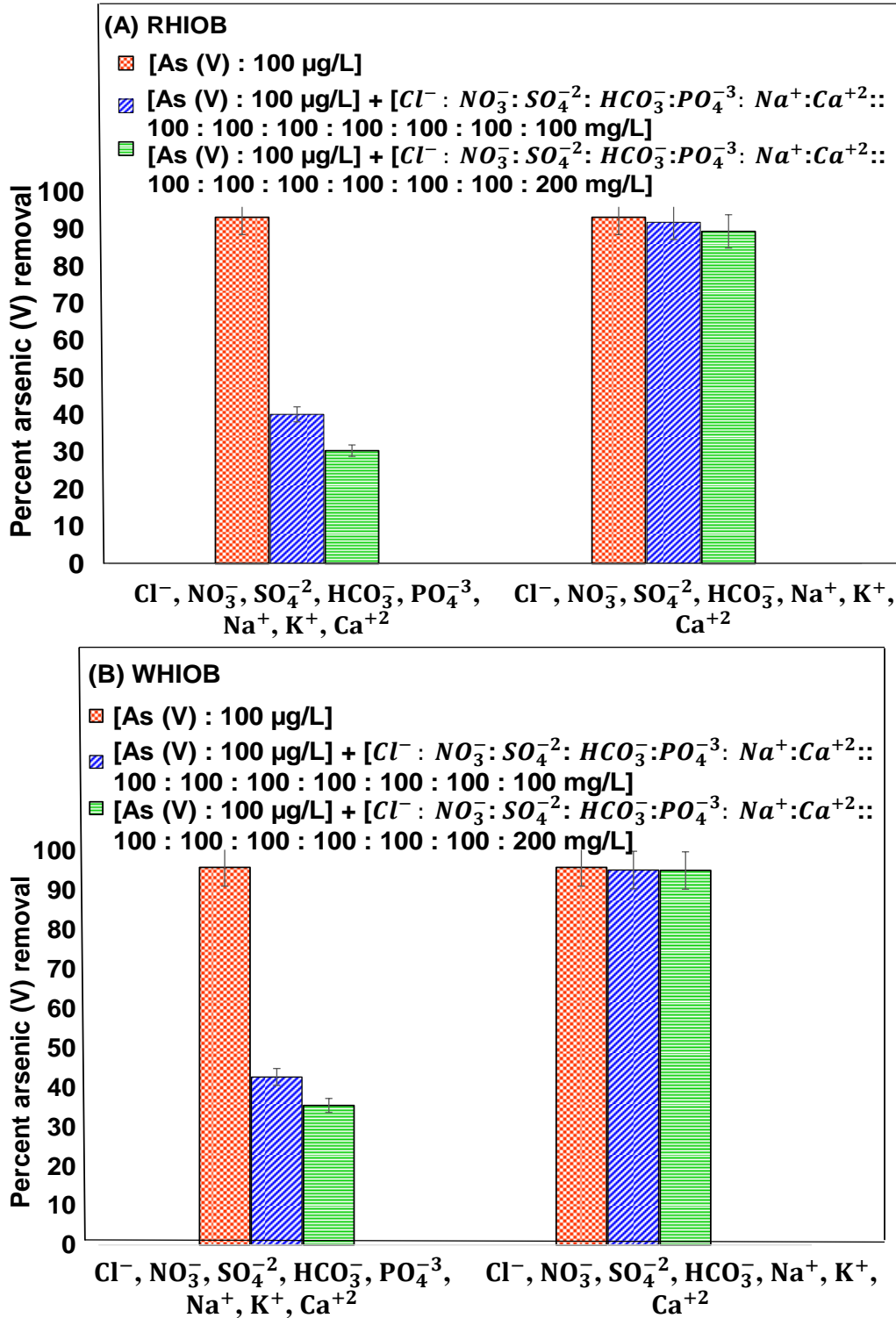


Fig.7.15. Combined effect of coexisting ions and coexisting ions minus phosphates on adsorption of As(V) removal by (A) RHIOB and (B) WHIOB (adsorbent dose, RHIOB = 2.0 g/L and WHIOB = 1.0 g/L, initial As(V) concentration = 100 µg/L; initial pH = 5.0, agitation speed = 100 rpm, temperature = 25°C, contact time = 24 h).

7.4. Application of RHIOB and WHIOB for As(III) and As(V) removal from groundwater samples:

Actual groundwater contains complex mixture of ions. Thus, it becomes important to check the applicability of developed material in real water samples. Six groundwater samples were collected from Ballia and Kushinagar districts of Uttar Pradesh, India. Table 7.5. The geographical location of the sampling area was between 26°12'-25°91' N (latitude) and 83°94'-84°30' E (longitude) for Ballia and 26°64'-26°69' N (latitude) and 83°97'-84°03' E (longitude) for Kushinagar districts. Water quality parameters including pH, conductivity, total dissolved solid (TDS), concentrations of fluoride, Na, K, Mg, Ca were measured. pH of the water is slightly alkaline due to the presence of alkaline earth metals. It is clear that trace metals are at lower concentrations. However, iron content is high that could be attributed to the samples collected from hand pumps with rust. Adsorption studies were conducted using 2.0 g/L and 1.0 g/L of RHIOB and WHIOB, respectively in 50 mL of samples. Arsenic concentrations were measured and percent removal is recorded in Table 7.6

Arsenic content in groundwater samples was high ($>10 \mu\text{g/L}$) (Table 7.6). About ~99 % of the arsenic was taken up by RHIOB and WHIOB without getting much affected with the complex ions system present in the samples (Table 7.6). WHIOB showed higher efficiency for arsenic removal as compared to RHIOB.

Table 7.5. Samples and their locations.

Sample ID	Location	Latitude	Longitude
K-2	Kasya, Kushinagar	26.64°N	83.971°E
K-42	Hata, Kushinagar	26.91°N	83.806°E
K-62	Kasya, Kushinagar	26.695°N	84.032°E
B-7	Belthara Road, Ballia	26.119°N	83.942°E
B-36	Rasra, Ballia	25.802°N	83.914°E
B-90	Bausdih, Ballia	25.910°N	84.302°E

*Map for the location is given in chapter 2 of material and methods.

Sample ID	Initial As Conc	Final As Conc	Dose	% removal	Adsorption Capacity
Units	mg/L	mg/L	g/L		mg/g
K1 R	61.5	0.06	2.0	99.90	30.72
K2 R	38.1	0.03	2.0	99.92	19.04
K3 R	35.4	0.01	2.0	99.97	17.69
B1 R	90.5	0.08	2.0	99.91	45.21
B2 R	30.9	0.03	2.0	99.90	15.44
B3 R	37.25	0.04	2.0	99.89	18.61
K1 W	61.5	0.05	1.0	99.92	61.45
K2 W	38.1	0.03	1.0	99.92	38.07
K3 W	35.4	0.01	1.0	99.97	35.39
B1 W	90.5	0.06	1.0	99.93	90.44
B2 W	30.9	0.02	1.0	99.94	30.88
B3 W	37.25	0.01	1.0	99.97	37.24

*K(1-3)/B(1-3)R denotes samples with RHIOB as adsorbent.

*K(1-3)/B(1-3)W denotes samples with WHIOB as adsorbent

Table 7.7. Different water quality parameters and elemental composition of the collected groundwater samples.

Samples	pH	Conductivity	TDS	Salinity	Na	Ca	K	Mg	Fe	Al
Units		mS/cm	mg/L	ppt	mg/L	mg/L	mg/L	mg/L	mg/L	mg/L
K1	6.95	8.05	3933	5.3	4.5	3.6	3.6	4.2	28.73	0.54
K2	6.89	19.57	9551	11.6	11.6	4.3	4.3	10.4	141.15	1.22
K3	6.89	10.42	5173	6	6	4.9	4.9	5.6	82.25	1.14
B1	6.92	9.35	4525	5.3	5.3	3.5	3.5	4.4	30.45	0.5
B2	6.91	25.72	12542	15.8	15.8	3.9	3.9	19.3	96.55	0.75
B3	6.9	17.32	8547	10.3	10.3	4.8	4.8	9.9	116.85	1.08

Ni	Zn	Ba	Pb	Cd	Co	Cr	Mn	Mo
mg/L	mg/L	mg/L	mg/L	mg/L	mg/L	mg/L	mg/L	mg/L
0.04	0.88	1.96	0.01	0	0	0.06	0.88	0
0.45	2.72	0.7	0.01	0	0	0.55	1.55	0
0.05	0.53	0.42	0.03	0	0	0.1	1.01	0
0.02	0.23	0.2	0.03	0	0	0.02	0.5	0
0.36	3.48	0.42	0.01	0	0	0.42	1.86	0
0.08	0.74	0.38	0.04	0	0	0.12	1.05	0

CHAPTER 8
CONCLUSIONS AND
RECOMMENDATIONS

Conclusions:

Low cost iron-oxide biochar composites were developed by slow co-pyrolysis of rice and wheat husks. These were designated as rice husk iron-oxide biochar (RHIOB) and wheat husk iron-oxide biochar (WHIOB) composites. RHIOB and WHIOB were characterized using XPS, XRD, FT IR, SEM and SEM-EDX, TEM, Surface area analyzer, PPMS, ICP-AES and AAS. The ultimate and quantitative analyses were also carried out.

The developed RHIOB and WHIOB were then utilized for the removal of arsenite, As(III) and arsenate, As(V) from water. Studies were conducted in batch and continuous mode using columns. Various parameters affecting removal were determined. Equilibrium and dynamic studies were conducted to optimize the pH, adsorbent dose, initial adsorbate concentration, and temperature. Kinetic data were modelled to pseudo-first order, pseudo-second order rate equations and boyd's model. Equilibrium sorption data was modelled to Freundlich, Langmuir, Sips, Redlich-Peterson, Radke and Prausnitz, Toth, Koble-Corrigan, and Temkin equations. Following conclusions are established:

1. Rice husk biochar (RHB) and wheat husk biochar (WHB) were prepared by slow pyrolysis of rice and wheat husks.
2. Rice husk iron-oxide biochar (RHIOB) and wheat husk iron-oxide biochar (WHIOB) composites were prepared (Figure 3.1).
3. WHIOB was characterized by higher iron-oxide content (19.03 % wt.) versus RHIOB (16.02 % wt.). RHIOB had more silica content (64.37 % wt.) than WHIOB (60.96 % wt.).
4. XPS studies showed the occurrence of $(\text{Fe}^{3+}/\text{Fe}^{2+})$ on RHIOB and WHIOB. In addition, it showed the occurrence of oxygen, carbon and arsenic in the composites after arsenic adsorption. De-convolution of peaks indicate the occurrence and formation of iron, oxygen and carbon associated with different As(III) and As(V) species.. No oxidation of As(III) to As(V) was observed while conducting independent studies with As(III) and As(V). XRD and FT IR peaks showed the presence of various iron-oxide species similar to those found in magnetite. Thus, it

may be concluded that magnetite (Fe_3O_4) formation, along with the formation of α - Fe_2O_3 (hematite) and β - FeOOH (akaganeite) has taken place.

5. SEM micrographs provided the morphologies of RHIOB and WHIOB. Both the composites are porous in nature. Partially filled pores were seen in the micrographs obtained for As(III)/As(V) loaded RHIOB and WHIOB. Magnetite (Fe_3O_4) nanoparticles were clearly observed in the TEM micrographs of RHIOB and WHIOB.

6. Magnetic measurement results exhibited the development of magnetization due to iron-oxide deposition in RHIOB (3.0 emu/g) and WHIOB (8.5 emu/g). Small values of remanence (M_r) and coercivity (H_r) for RHIOB and WHIOB confirmed the super-paramagnetic behavior of developed materials.

7. High surface area was obtained for WHIOB ($\sim 339 \text{ m}^2/\text{g}$) versus RHIOB ($\sim 300 \text{ m}^2/\text{g}$). Reduction in surface area of RHIOB and WHIOB after As(III)/(V) adsorption was obtained. This may be due to clogging of pores. A good correlation between micropore volume and surface area was observed for RHIOB, WHIOB, RHB and WHB.

8. pH_{zpc} values of 5.5 and 7.0 were obtained for RHIOB and WHIOB, respectively

9. Maximum As(III) and As(V) removal was achieved at pH 7.5 and pH 5.0, for RHIOB and WHIOB, respectively. Furthermore, maximum arsenic was obtained at adsorbent dose of 2.0 g/L for RHIOB and 1.0 g/L for WHIOB.

10. As(III) and As(V) kinetic data were well fitted to the pseudo-second order rate equation.

11. Boyd's diffusion model suggested that As(III) adsorption on RHIOB and WHIOB was controlled by particle diffusion at low concentrations and film diffusion at high concentrations, respectively. However, As(V) adsorption on RHIOB and WHIOB was controlled by particle diffusion at all the concentrations.

12. Thermodynamic parameters were obtained for As(III) and As(V) removal on RHIOB and WHIOB. These parameters suggested that adsorption was endothermic in nature..

13. As(III) adsorption equilibrium data were best fitted to Redlich-Peterson equation for RHIOB and Sips for WHIOB. For As(V) adsorption equilibrium data were best fitted to Toth for RHIOB and Redlich-Peterson for WHIOB..

14. RHIOB and WHIOB exhibited Langmuir maximum As(III) capacities of $Q^0 = 96.14 \mu\text{g/g}$ and $110.73 \mu\text{g/g}$ at 45°C , respectively, in the pH range of 6.5-7.5 with excellent adsorption over the pH range of 3.0-10. Similarly, As(V) adsorption capacities of $386.88 \mu\text{g/g}$ and $421.45 \mu\text{g/g}$ at 45°C on RHIOB and WHIOB, respectively were obtained. Furthermore, adsorption of As(III)/(V) on RHIOB and WHIOB was increased with increase in temperature, confirming the endothermic process. This is in agreement with the results obtained from thermodynamic studies.

15. These hybrid adsorbents successfully remediated As(III)/As(V) from low concentration mostly solutions on the exposed Fe_3O_4 and Fe_2O_3 particle surfaces. Little As(III)/As(V) adsorption occurred on non-impregnated RHB or WHB. At $\text{pH} < \text{pH}_{\text{pzc}}$, Fe-O sites over magnetite were protonated to generate FeOH_2^+ sites. Electrostatic attraction was developed between positively charged FeOH_2^+ over adsorbent surface and negatively charged arsenite species $[\text{HAsO}_3]^{2-}$ and arsenate species $[\text{H}_2\text{AsO}_4]^-$.

16. $\text{H}_3\text{AsO}_3/\text{H}_2\text{AsO}_3^-$ (pH~6.5-7.5) are the primary As(III) species adsorbed over magnetite surfaces (FeOH_2^+) over RHIOB and WHIOB. Similarly, for As(V), H_2AsO_4^- (pH~5.0) is primary specie involved in adsorption with magnetite surfaces over RHIOB and WHIOB.

17. Bidentate-binuclear (two corner) sharing complexation (^2C) is thermodynamically the most stable form and explains the As(III) and As(V) adsorption mechanism on magnetite particles of RHIOB and WHIOB.

18. Column adsorption capacities were calculated using Thomson's model. As(III) adsorption capacities of $87.35 \mu\text{g/L}$ (RHIOB) and $105.12 \mu\text{g/L}$ (WHIOB) were obtained. As(V) adsorption capacities of $370.01 \mu\text{g/L}$ and $415.11 \mu\text{g/L}$ were obtained for RHIOB and WHIOB, respectively.

19. Regeneration of RHIOB and WHIOB using 0.1 N NaOH was successfully achieved. As(III) adsorption on RHIOB was decreased from 90 % (in the first cycle) to 86 % (in the fourth cycle). Similarly, As(III) removal on WHIOB was reduced

from 92 % (in the first cycle) to 90 % (in the fourth cycle). A very nominal decrease in As(III) removal clearly shows the reusability of RHIOB and WHIOB for more many cycles.

20. As(V) adsorption on RHIOB was decreased from 92 % (in the first cycle) to 88 % (in the fourth cycle). Similarly, As(V) removal on WHIOB was reduced from 97 % (in the first cycle) to 93 % (in the fourth cycle). It clearly shows the reusability of RHIOB and WHIOB for more cycles.

21. Chloride, nitrate, sodium, potassium and calcium when present individually (at 100 mg/L and 200 mg/L] do not affect the As(III) adsorption while sulfate, bicarbonate and phosphate significantly inhibited As(III) adsorption. Furthermore, As(III) adsorption decreased more when sulfate, bicarbonate and phosphate concentrations increased from 100 mg/L to 200 mg/L. Negligible chloride and nitrate influence on As(III) adsorption may be due to their tendency to form outer-sphere complexes with iron (oxy)hydroxides nano particles present in RHIOB and WHIOB.

22. RHIOB and WHIOB composites were applied to remediate arsenic form groundwater samples collected from Ballia and Kushinagar districts, Uttar Pradesh. Almost, ~99 % removal with in the concentration range of 0.08-0.01 $\mu\text{g/L}$ (below the BIS permissible limit) was successfully achieved.

23. Developed iron-oxide composite biochars can easily be manipulated by low external magnetic fields, permitting their easy recovery from aqueous streams after use. The As(III)/ (V) adsorption capacities of RHIOB and WHIOB are comparable to other adsorbents reported for arsenic remediation from water. In literature, most of the studies were conducted in high arsenic concentration range. Many a times, these adsorbents fail to remediate when arsenic is present in low concentrations. These studies clearly demonstrated that RHIOB and WHIOB composites were successful in remediated arsenic from low as well as high concentrations.

Recommendations:

1. A holistic and extensive assessment study on the pilots involving Environmental Life Cycle Assessment (LCA), Social LCA, and Social Acceptance Analysis are required.
2. Pilot-scale studies, in lab and fields using RHIOB and WHIOB composites are recommended. This will help in scaling the product.
3. RHIOB and WHIOB can be distributed in the form of capsules, tablets, bags in the arsenic affected areas. Filter candles using RHIOB and WHIOB can be designed and distributed.

Table 8.1. Comparative evaluation of As(III) adsorption capacities of RHIOB and WHIOB versus other adsorbents.

S. No	Raw material	BET Surface area (m ² /g)	Adsorption study parameters			Langmuir adsorption capacity Q ⁰ (mg/g)	Reference
			pH	Temp (°C)	Concentration range (mg/L)		
1	Pine wood biochar	2.73	3.5	25	0.075-37.46 ^a	1.2	(Mohan et al., 2007)
2	Oak wood biochar	2.04				5.85	
3	Pine bark biochar	1.88				12.15	
4	Oak bark biochar	25.4				7.4	
5	Carbon F-400	984				0.204	
6	Magnetite-maghemite mixture	12	6.0	25	1.0-7.0 ^a	2.9	(K. Song et al., 2013)
7	Magnetic wheat straw	-	7.0-9.0	-	2.0-30.0 ^a	3.89	(Tian, Wu, Lin, Huang, & Huang, 2011)
8	Sulfate-modified iron oxide-coated sand	2.9-7.9	7.2	27	0.5-3.5 ^a	0.14	(Vaishya & Gupta, 2003)
9	Iron oxide coated sand	10.6	7.6	-	100.0 ^a	0.041	(Thirunavukkarasu, Viraraghavan, & Subramanian, 2003)
10	Iron hydroxide-coated alumina	95.7	6.0-8.0	-	0.75-3.0 ^a	7.64	(Hlavay & Polyák, 2005)
11	Iron oxide coated sand	-	7.5	27	0.1-0.8	0.029	(V. Gupta, Saini, & Jain, 2005)
12	Un-coated sand	-	7.5	27	0.1-0.8	0.006	(V. Gupta et al., 2005)
13	Iron oxide coated cement	-	6.7	27	5.0-40.0 ^a	0.69	(Kundu & Gupta, 2007)
14	Iron chitosan granules	-	7.0	-	0.05	2.32	(Anjali Gupta, Chauhan, & Sankararama

							krishnan, 2009)
15	Iron oxide coated cement	-	3.2-12.0	15	0.7-13.5 ^a	0.73	(Kundu & Gupta, 2006)
16	Ferrihydride		4.2	-	-	0.58	(Raven, Jain, & Loepfert, 1998)
17	Agricultural residue rice polish	452.0	7.0	20	0.1-10.0 ^a	0.14	(Hasan, Ranjan, & Talat, 2009)
18	Iron coated sea weeds	-	7.0	20	0.01-0.05	4.2	(Vieira, Pintor, Boaventura, Botelho, & Santos, 2017)
19	Iron impregnated charred GAP	52.2	5.0-9.0	25	0.05-2.0	3.25	(H. Yin, Kong, Gu, & Chen, 2017)
20	Unmodified alumina	189.12	6.5-7.2	-	0.84-2.02 ^a	0.92-2.16	(Pillewan et al., 2011)
21	Iron modified zeolite	-	6.0-9.0	-	0.5	0.1	(Z. Li et al., 2011)
22	Rice husk iron oxide biochar (RHIOB) composite	300.0	7.5	45	0.05-0.2^b	0.096^c	This study
23	Wheat husk iron oxide biochar (WHIOB) composite	339.0	7.5	45	0.05-0.2^b	0.113^c	This study

^a studies carried out at very high arsenic concentrations (ppm levels)

^b studies carried out at low arsenic concentrations that is usually present in water (ppb levels)

^c Since almost all the As(III) is adsorbed on the iron oxide particle surfaces, the adsorption capacity based on the weight of iron oxides deposited on the biochar was calculated for samples 22 and 23 as 0.83 and 0.82 mg As(III)/g of Fe₃O₄

Table 8.2. Comparative evaluation of As(V) adsorption capacities of RHIOB and WHIOB versus other adsorbents.

S. No	Raw material	BET Surface area (m ² /g)	Adsorption study parameters			Langmuir adsorption capacity Q ⁰ (mg/g)	Reference
			pH	Temp (°C)	Concentration range (mg/L)		
1	Chestnut shell biochar	-	4.0	25	0.2-50 ^a	17.5	(Zhou et al., 2017)
2	Magnetic gelatin modified chestnut shell biochar					45.8	
3	Magnetic mesoporous iron manganese bimetallic oxides	143.88	3.0	25	1.0-50.0 ^a	35.35	(Wen, Dai, Zhu, & Zhang, 2015)
4	Magnetite enriched particles from mill scale	-	6.5	25	1.0-50.0 ^a	13.88	(Shahid, Phearom, & Choi, 2019)
5	Bare maghemite	57.0	6.5	25	50.-350.0 ^a	90.2	(Ramos Guivar et al., 2018)
6	Binary magnetic nanocomposite	69.0				96.5	
7	Ternary magnetic nanocomposite	82.0				127.2	
8	<i>Saccharum ravanae</i> activated biochar	1248.2	6.5	26	6.0-100.0 ^a	72.1	(Saikia et al., 2017)
9	<i>Cassia fistula</i> activated biochar	-	7.0	27	0.5-5.0 ^a	0.42	(Alam et al., 2018)
10	Iron impregnated granules	1316.0	7.0	25	40.0 ^a	4.7	(Chang, Lin, & Ying, 2010)
11	Iron amended rice husk biochar	77.3	7.5	25	100-2500	606.0	(Cope, Webster, & Sabatini, 2014)
12	Iron impregnated corn straw	4.81	4.0	30	0-150.0 ^a	14.77	(Fan et al., 2018)
13	Pineapple peel composed of FeTiO _x nanoparticles	2.5	5.5		10.0-200.0 ^a	40.0	(García-Rosales et al., 2018)
14	Iron chitosan composites flakes	-	7.0	25	1.0-10.0 ^a	22.47	(Anjali Gupta et al., 2009)

15	Modified sugarcane bagasse	-	7.0	45	0.1-20.0 ^a	34.48	(Avinash Gupta, Vidyarthi, & Sankararamkrishnan, 2015)
16	Iron nanoparticles modified biochar from pineapple crown leaves	26.0	7.0	25	0.02	1.8	(Gutierrez-Muniz, Garcia-Rosales, Ordonez-Regil, Olguin, & Cabral-Prieto, 2013)
17	Synthetic pyrite	-	10.0	25	0.5-53.4 ^a	172.0	(Han, Song, Batchelor, & Abdel-Wahab, 2013)
18	Iron-impregnated corn straw biochar	297.13	6.0	25	0.25-100.0 ^a	6.8	(R. He et al., 2018)
19	Rice husk iron oxide biochar (RHIOB), composite	300.0	5.0	45	0.05-0.2^b	0.386^c	This study
20	Wheat husk iron oxide biochar (WHIOB) composite	339.0	5.0	45	0.05-0.2^b	0.431^c	This study

^a studies carried out at very high arsenic concentrations (ppm levels)

^b studies carried out at low arsenic concentrations that is usually present in water (ppb levels)

^c Since almost all the As(V) is adsorbed on the iron oxide particle surfaces, the adsorption capacity based on the weight of iron oxides deposited on the biochar was calculated for samples 19 and 20 as 2.81 and 3.15 mg As(V)/g of Fe₃O₄

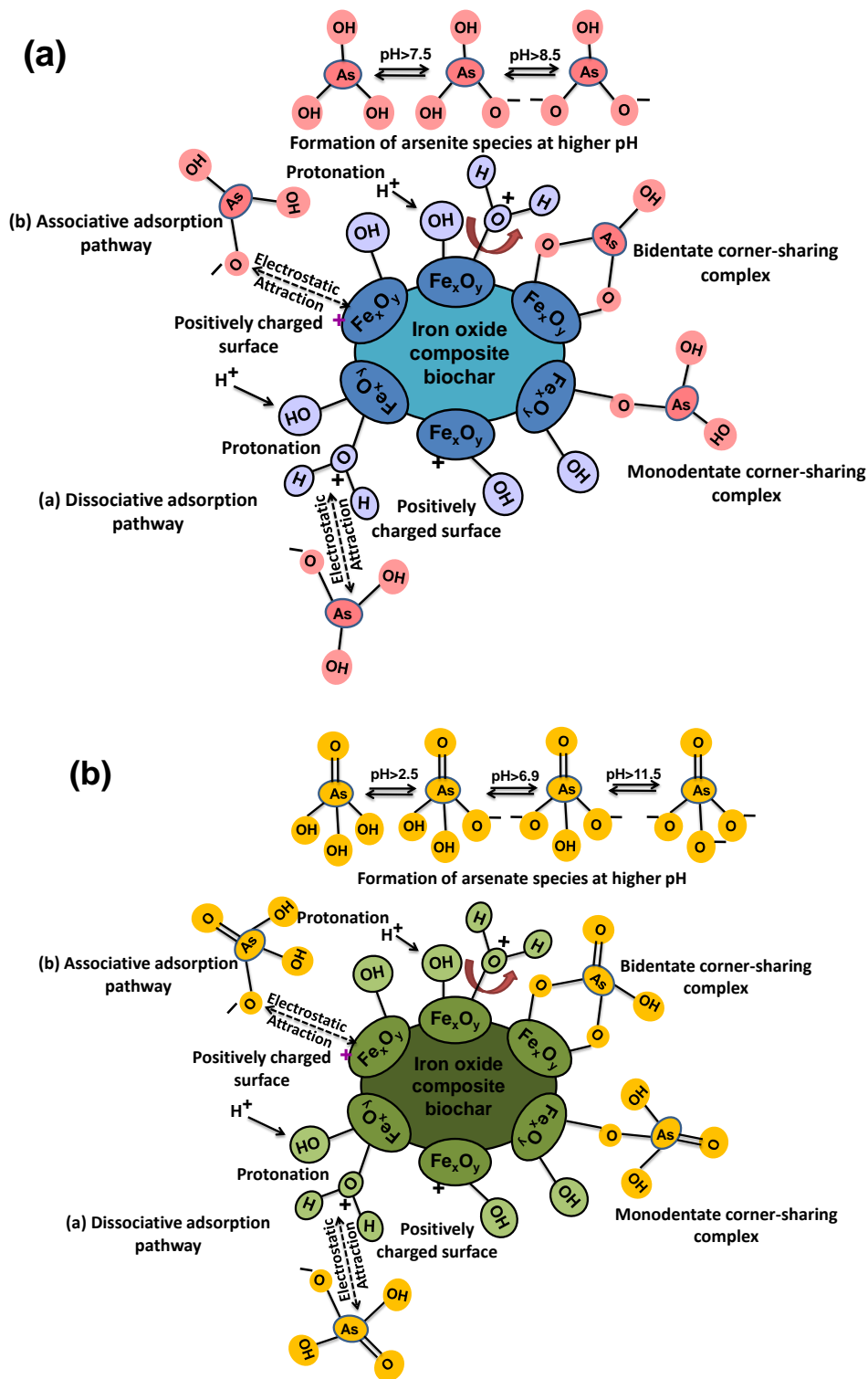


Figure 8.1. Graphical representation of different mechanisms involved in the adsorption of (a) As(III) and (b) As(V) on iron-oxide (magnetite) nanoparticles on RHIOB and WHIOB surfaces.

References

- Agrafioti, E., Kalderis, D., & Diamadopoulou, E. (2014). Arsenic and chromium removal from water using biochars derived from rice husk, organic solid wastes and sewage sludge. *J Environ Manage*, 133, 309-314. doi: <https://doi.org/10.1016/j.jenvman.2013.12.007>
- Ahiduzzaman, M., & Islam, A. K. M. S. (2016). *Preparation of porous bio-char and activated carbon from rice husk by leaching ash and chemical activation* (Vol. 5).
- Ahmed, M. B., Zhou, J. L., Ngo, H. H., & Guo, W. (2016). Insight into biochar properties and its cost analysis. *Biomass and Bioenergy*, 84, 76-86.
- Al-Wabel, M. I., Al-Omran, A., El-Naggar, A. H., Nadeem, M., & Usman, A. R. A. (2013). Pyrolysis temperature induced changes in characteristics and chemical composition of biochar produced from conocarpus wastes *Bioresource technology*, 131, 374-379.
- Alam, M. A., Shaikh, W. A., Alam, M. O., Bhattacharya, T., Chakraborty, S., Show, B., & Saha, I. (2018). Adsorption of As (III) and As (V) from aqueous solution by modified Cassia fistula (golden shower) biochar. *Applied Water Science*, 8(7), 198. doi: 10.1007/s13201-018-0839-y
- Allen, R. L. (1860). *The American farm book : or, Compend of American agriculture ; being a practical treatise on soils, manures, draining irrigation, grasses, grain, roots, fruits, cotton, tobacco, sugar cane, rice, and every staple product of the United States, with the best methods of planting, cultivating, and preparation for market ;illustrated by more than 100 engravings*. New York :: C.M. Saxton, Barker & Co. ;.
- Amidon, G. E., Meyer, P. J., & Mudie, D. M. (2017). Chapter 10 - Particle, Powder, and Compact Characterization. In Y. Qiu, Y. Chen, G. G. Z. Zhang, L. Yu & R. V. Mantri (Eds.), *Developing Solid Oral Dosage Forms (Second Edition)* (pp. 271-293). Boston: Academic Press.
- Ammann, A. (2011). *Arsenic Speciation Analysis by Ion Chromatography-A Critical Review of Principles and Applications* (Vol. 2).
- Asere, T. G., Stevens, C. V., & Du Laing, G. (2019). Use of (modified) natural adsorbents for arsenic remediation: A review. *Science of The Total Environment*, 676, 706-720. doi: <https://doi.org/10.1016/j.scitotenv.2019.04.237>
- Azmi, N., Yusup, S., & Sabil, K. M. (2017). Effect of water onto porous CaO for CO₂ adsorption: Experimental and extended isotherm model. *Journal of Cleaner Production*. *Journal of Cleaner Production*, 1-29.
- Baig, S. A., Sheng, T., Sun, C., Xue, X., Tan, L., & Xu, X. (2014a). Arsenic Removal from Aqueous Solutions Using Fe₃O₄-HBC Composite: Effect of Calcination on Adsorbents Performance. *PLOS ONE*, 9(6), e100704. doi: 10.1371/journal.pone.0100704
- Baig, S. A., Sheng, T., Sun, C., Xue, X., Tan, L., & Xu, X. (2014b). Arsenic Removal from Aqueous Solutions Using Fe₃O₄-HBC Composite: Effect of Calcination on Adsorbents Performance. *PLoS ONE*, 9(6), 1-11. doi: <https://doi.org/10.1371/journal.pone.0100704>
- Baskan, M. B., & Pala, A. (2013). Batch and Fixed-Bed Column Studies of Arsenic Adsorption on the Natural and Modified Clinoptilolite. *Water, Air, & Soil Pollution*, 225(1), 1798. doi: 10.1007/s11270-013-1798-4
- Belessiotis, V., Kalogirou, S., & Delyannis, E. (2016). Chapter One - Desalination Methods and Technologies—Water and Energy. In V. Belessiotis, S. Kalogirou & E. Delyannis (Eds.), *Thermal Solar Desalination* (pp. 1-19): Academic Press.
- Bhattacharya, S. (2016). Chapter 8 - Electrical Transport Properties of Ion-Conducting Glass Nanocomposites. In B. Karmakar, K. Rademann & A. L. Stepanov (Eds.), *Glass Nanocomposites* (pp. 181-214). Boston: William Andrew Publishing.

- Bhowmick, S., Pramanik, S., Singh, P., Mondal, P., Chatterjee, D., & Nriagu, J. (2018). Arsenic in groundwater of West Bengal, India: A review of human health risks and assessment of possible intervention options. *Science of The Total Environment*, *612*, 148-169.
- Bird, M., Keitel, C., & Meredith, W. (2017). Analysis of biochars for C,H,N,O and S by elemental analyser.
- Bonnamy, S., & Oberlin, A. (2016). Chapter 4 - Transmission Electron Microscopy. In M. Inagaki & F. Kang (Eds.), *Materials Science and Engineering of Carbon* (pp. 45-70): Butterworth-Heinemann.
- Boruah, P. K., Sharma, B., Karbhal, I., Shelke, M. V., & Das, M. R. (2017). Ammonia-modified graphene sheets decorated with magnetic Fe₃O₄ nanoparticles for the photocatalytic and photo-Fenton degradation of phenolic compounds under sunlight irradiation. *Journal of hazardous Materials*, *325*, 90-100.
- Boukhvalov, D. W., Zhidkov, I. S., Kukharenko, A. I., Slesarev, A. I., Zatsepin, A. F., Cholakh, S. O., & Kurmaev, E. Z. (2018). Stability of boron-doped graphene/copper interface: DFT, XPS and OSEE studies. *Applied Surface Science*, *441*, 978-983. doi: 10.1016/j.apsusc.2018.02.074
- Bourke, J., Manley-Harris, M., Fushimi, C., Dowaki, K., Nunoura, T., & Antal, M. J. (2007). Do All Carbonized Charcoals Have the Same Chemical Structure? 2. A Model of the Chemical Structure of Carbonized Charcoal. *Industrial & Engineering Chemistry Research*, *46*(18), 5954-5967. doi: 10.1021/ie070415u
- Boyd, G. E., Adamson, A. W., & Myers, L. S. (1947). The Exchange Adsorption of Ions from Aqueous Solutions by Organic Zeolites. II. Kinetics1. *Journal of the American Chemical Society*, *69*(11), 2836-2848. doi: 10.1021/ja01203a066
- Boyd, G. E., Adamson, A. W., Myers, L. S., & Jr. (1947). The Exchange Adsorption of Ions from Aqueous Solutions by Organic Zeolites. II. Kinetics1. *Journal of American Chemical Society*, *69* (11), 2836-2848.
- Brookins, D. G. (1988). *Eh-pH diagrams for geochemistry*. Germany: Springer.
- Brunauer, Macko, S., H. E. Emmett, P., Teller, & Edward. (1938). *Brunauer, S., Emmett, P. H. & Teller, E. Adsorption of gases in multimolecular layers. J. Am. Chem. Soc. 60, 309-319* (Vol. 60).
- Bundschuh, J., Litter, M. I., Parvez, F., Roman-Ross, G., Nicolli, H. B., Jean, J. S., . . . Toujaguez, R. (2012). One century of arsenic exposure in Latin America: a review of history and occurrence from 14 countries. *Sci Total Environ*, *429*, 2-35. doi: 10.1016/j.scitotenv.2011.06.024
- Cai, W., & Wan, J. (2007). Facile synthesis of superparamagnetic magnetite nanoparticles in liquid polyols. *Journal of colloid and interface science*, *305*, 366-370.
- Calo, J. M., Madhavan, L., Kirchner, J., & Bain, E. J. (2012). Arsenic removal via ZVI in a hybrid spouted vessel/fixed bed filter system. *Chemical Engineering Journal*, *189-190*, 237-243. doi: <https://doi.org/10.1016/j.cej.2012.02.063>
- Cao, X., & Harris, W. (2010). Properties of dairy-manure-derived biochar pertinent to its potential use in remediation. *Bioresour Technol*, *101*(14), 5222-5228. doi: <https://doi.org/10.1016/j.biortech.2010.02.052>
- Catalano, J., Park, C., Fenter, P., & Zhang, Z. (2008). *Simultaneous Inner and Outer Sphere Arsenate Adsorption on Corundum and Hematite* (Vol. 72).
- Chakraborti, D., Das, B., & Murrill, M. T. (2011). Examining India's groundwater quality management. *Environmental Science & Technology*, *45*(1), 27-33. doi: 10.1021/es101695d
- Chang, Q., Lin, W., & Ying, W.-c. (2010). Preparation of iron-impregnated granular activated carbon for arsenic removal from drinking water. *J Hazard Mater*, *184*(1), 515-522. doi: <https://doi.org/10.1016/j.jhazmat.2010.08.066>

- Chen, B., & Huang, W. (2011). Effects of compositional heterogeneity and nanoporosity of raw and treated biomass-generated soot on adsorption and absorption of organic contaminants. *Environmental pollution (Barking, Essex : 1987)*, 159(2), 550-556. doi: 10.1016/j.envpol.2010.10.010
- Chen, T., Liu, R., & Scott, N. (2016a). *Characterization of energy carriers obtained from the pyrolysis of white ash, switchgrass and corn stover - Biochar, syngas and bio-oil* (Vol. 142).
- Chen, T., Liu, R., & Scott, N. R. (2016b). Characterization of energy carriers obtained from the pyrolysis of white ash, switchgrass and corn stover - Biochar, syngas and bio-oil. *Fuel Processing Technology*, 142, 124-134.
- Cheng, G., Xu, F., Xiong, J., & Yi Wei, R. C. (2017). A novel protocol to design TiO₂-Fe₂O₃ hybrids with effective charge separation efficiency for improved photocatalysis. *Advanced Powder Technology*, 28(2), 665-670.
- Cheng, W., Tang, K., Qi, Y., Sheng, J., & Liu, Z. (2010). One-step synthesis of superparamagnetic monodisperse porous Fe₃O₄ hollow and core-shell spheres. *Journal of Materials Chemistry*, 20(9), 1799-1805. doi: 10.1039/B919164J
- Cope, C. O., Webster, D. S., & Sabatini, D. A. (2014). Arsenate adsorption onto iron oxide amended rice husk char. *Sci Total Environ*, 488-489, 554-561. doi: 10.1016/j.scitotenv.2013.12.120
- Cornell, R. M. S. U., & Schwertmann, U. (2003). *The Iron Oxides: Structure, Properties, Reactions, Occurrences, And Uses* (Vol. 34).
- de Ven, A. L. v., Mack, A., Dunner, K., Ferrari, M., & Serda, R. E. (2012). Chapter one - Preparation, Characterization, and Cellular Associations of Silicon Logic-Embedded Vectors. In N. Düzgüneş (Ed.), *Methods in Enzymology* (Vol. 508, pp. 1-16): Academic Press.
- Desta, M. B. (2013). Batch Sorption Experiments: Langmuir and Freundlich Isotherm Studies for the Adsorption of Textile Metal Ions onto Teff Straw (*Eragrostis tef*) Agricultural Waste. *Journal of Thermodynamics*, 2013, 6. doi: 10.1155/2013/375830
- Dieguez-Alonso, A., Anca-Couce, A., Frišták, V., Moreno-Jiménez, E., Bacher, M., Bucheli, T. D., . . . Schmidt, H.-P. (2019). Designing biochar properties through the blending of biomass feedstock with metals: Impact on oxyanions adsorption behavior. *Chemosphere*, 214, 743-753. doi: <https://doi.org/10.1016/j.chemosphere.2018.09.091>
- Duarte, G., Ciminelli, V., Dantas, M., Duarte, H., Vasconcelos, I., Oliveira, A., & Osseo-Asare, K. (2012). *As(III) immobilization on gibbsite: Investigation of the complexation mechanism by combining EXAFS analyses and DFT calculations* (Vol. 83).
- Dutta, M., & Basu, J. K. (2014). Fixed-bed column study for the adsorptive removal of acid fuchsin using carbon–alumina composite pellet. *International Journal of Environmental Science and Technology*, 11(1), 87-96. doi: 10.1007/s13762-013-0386-x
- Ebnesajjad, S. (2014). Chapter 4 - Surface and Material Characterization Techniques. In S. Ebnesajjad (Ed.), *Surface Treatment of Materials for Adhesive Bonding (Second Edition)* (pp. 39-75). Oxford: William Andrew Publishing.
- Ermolieff, A., Chabli, A., Pierre, F., Rolland, G., Rouchon, D., Vannuffel, C., . . . Séméria, M. N. (2001). XPS, Raman spectroscopy, X-ray diffraction, specular X-ray reflectivity, transmission electron microscopy and elastic recoil detection analysis of emissive carbon film characterization. *Surface and Interface Analysis*, 31(3), 185-190. doi: 10.1002/sia.955
- Fan, J., Xu, X., Ni, Q., Lin, Q., Fang, J., Chen, Q., . . . Lou, L. (2018). Enhanced As (V) Removal from Aqueous Solution by Biochar Prepared from Iron-Impregnated Corn Straw. *Journal of Chemistry*, 2018, 1-8. doi: 10.1155/2018/5137694
- Farquhar, M., Charnock, J., R Livens, F., & J Vaughan, D. (2002). *Mechanisms of Arsenic Uptake from Aqueous Solution by Interaction with Goethite, Lepidocrocite, Mackinawite, and Pyrite: An X-Ray Absorption Spectroscopy Study* (Vol. 36).

- Fendorf, S., Eick, M., Grossl, P., & Sparks, D. (1997). *Arsenate and Chromate Retention Mechanisms on Goethite. 1. Surface Structure* (Vol. 31).
- Fiol, N., & Villaescusa, I. (2009). *Determination of Sorbent Point Zero Charge: Usefulness in Sorption Studies* (Vol. 7).
- Foster, A., Brown, G., Parks, G. A., N. Tingle, T., & Voigt, D. (1997). *XAFS Determination of As(V) Associated with Fe(III) Oxyhydroxides in Weathered Mine Tailings and Contaminated Soil from California, U.S.A* (Vol. 7).
- Freundlich, H. (1906). Adsorption in solids. *Z. Phys. Chem*, 57, 385-470.
- Freundlich, H. (1907). Über die adsorption in lösungen. *Zeitschrift für physikalische Chemie*, 57(1), 385-470.
- Fujimoto, H. (2003). *Theoretical X-ray scattering intensity of carbons with turbostratic stacking and AB staking structures* (Vol. 41).
- Fuller, C. C., Davis, J. A., & Waychunas, G. A. (1993). Surface chemistry of ferrihydrite: Part 2. Kinetics of arsenate adsorption and coprecipitation. *Geochimica et Cosmochimica Acta*, 57(10), 2271-2282. doi: [https://doi.org/10.1016/0016-7037\(93\)90568-H](https://doi.org/10.1016/0016-7037(93)90568-H)
- García-Rosales, G., Longoria-Gándara, L. C., Cruz-Cruz, G. J., Olayo-González, M. G., Mejía-Cuero, R., & Pérez, P. Á. (2018). Fe-TiO_x nanoparticles on pineapple peel: Synthesis, characterization and As(V) sorption. *Environmental Nanotechnology, Monitoring & Management*, 9, 112-121. doi: <https://doi.org/10.1016/j.enmm.2018.01.002>
- Gaskin, J., Steiner, C., Harris, K., Das, K. C., & Bibens, B. (2008). *Effect of Low-Temperature Pyrolysis Conditions on Biochar for Agricultural Use* (Vol. 51).
- Gehrke, I., Geiser, A., & Somborn-Schulz, A. (2015). Innovations in nanotechnology for water treatment. *Nanotechnology, science and applications*, 8, 1.
- Ghribi, A., & Chlendi, M. (2011). *Modeling of Fixed Bed Adsorption: Application to the Adsorption of an Organic Dye* (Vol. 1).
- Gimelli, F. M., Bos, J. J., & Rogers, B. C. (2018). Fostering equity and wellbeing through water: A reinterpretation of the goal of securing access. *World Development*, 104, 1-9.
- Goldberg, S. (2002). Competitive Adsorption of Arsenate and Arsenite on Oxides and Clay Minerals Contribution from the George E. Brown Jr., Salinity Laboratory. *Soil Science Society of America Journal*, 66(2), 413-421. doi: 10.2136/sssaj2002.4130
- Goldberg, S., & Johnston, C. T. (2001). Mechanisms of Arsenic Adsorption on Amorphous Oxides Evaluated Using Macroscopic Measurements, Vibrational Spectroscopy, and Surface Complexation Modeling. *J Colloid Interface Sci*, 234(1), 204-216. doi: <https://doi.org/10.1006/jcis.2000.7295>
- Graber, E., & Elad, Y. (2013). Biochar Impact on Plant Resistance to Disease (pp. 41-68).
- Guo, J., Yan, C., Luo, Z., Fang, H., Hu, S., & Cao, Y. (2019). Synthesis of a novel ternary HA/Fe-Mn oxides-loaded biochar composite and its application in cadmium(II) and arsenic(V) adsorption. *J Environ Sci (China)*, 85, 168-176. doi: <https://doi.org/10.1016/j.jes.2019.06.004>
- Gupta, A., Chauhan, V. S., & Sankararamkrishnan, N. (2009). Preparation and evaluation of iron-chitosan composites for removal of As (III) and As (V) from arsenic contaminated real life groundwater. *Water Res*, 43(15), 3862-3870.
- Gupta, A., Vidyarthi, S. R., & Sankararamkrishnan, N. (2015). Concurrent removal of As(III) and As(V) using green low cost functionalized biosorbent – Saccharum officinarum bagasse. *Journal of Environmental Chemical Engineering*, 3(1), 113-121. doi: <https://doi.org/10.1016/j.jece.2014.11.023>
- Gupta, V., Saini, V., & Jain, N. (2005). Adsorption of As (III) from aqueous solutions by iron oxide-coated sand. *J Colloid Interface Sci*, 288(1), 55-60.

- Gutierrez-Muniz, O. E., Garcia-Rosales, G., Ordonez-Regil, E., Olguin, M. T., & Cabral-Prieto, A. (2013). Synthesis, characterization and adsorptive properties of carbon with iron nanoparticles and iron carbide for the removal of As(V) from water. *J Environ Manage*, *114*, 1-7. doi: 10.1016/j.jenvman.2012.09.027
- Han, D. S., Song, J. K., Batchelor, B., & Abdel-Wahab, A. (2013). Removal of arsenite(As(III)) and arsenate(As(V)) by synthetic pyrite (FeS₂): synthesis, effect of contact time, and sorption/desorption envelopes. *J Colloid Interface Sci*, *392*, 311-318. doi: 10.1016/j.jcis.2012.09.084
- Hao, L., Ouyang, T., Lai, L., Liu, Y.-X., Chen, S., Hu, H., . . . Wang, J.-J. (2014). Temperature effects on arsenate adsorption onto goethite and its preliminary application to arsenate removal from simulative geothermal water. *RSC Advances*, *4*(94), 51984-51990. doi: 10.1039/C4RA08318K
- Harikishore Kumar Reddy, D. (2017). Water Pollution Control Technologies. In M. A. Abraham (Ed.), *Encyclopedia of Sustainable Technologies* (pp. 3-22). Oxford: Elsevier.
- Harvey, O. R., Herbert, B. E., Rhue, R. D., & Kuo, L.-J. (2011). Metal Interactions at the Biochar-Water Interface: Energetics and Structure-Sorption Relationships Elucidated by Flow Adsorption Microcalorimetry. *Environmental Science & Technology*, *45*(13), 5550-5556. doi: 10.1021/es104401h
- Hasan, S., Ranjan, D., & Talat, M. (2009). "Rice Polish" for the removal of arsenic from aqueous solution: optimization of process variables. *Industrial & Engineering Chemistry Research*, *48*(9), 4194-4201.
- Hawkes, S. J. (1997). What is a "heavy metal"? *Journal of Chemical Education*, *74*(11), 1374.
- He, R., Peng, Z., Lyu, H., Huang, H., Nan, Q., & Tang, J. (2018). Synthesis and characterization of an iron-impregnated biochar for aqueous arsenic removal. *Sci Total Environ*, *612*, 1177-1186. doi: 10.1016/j.scitotenv.2017.09.016
- He, X., Deng, F., Shen, T., Yang, L., Chen, D., Luo, J., . . . Wang, F. (2019). Exceptional adsorption of arsenic by zirconium metal-organic frameworks: Engineering exploration and mechanism insight. *J Colloid Interface Sci*, *539*, 223-234. doi: <https://doi.org/10.1016/j.jcis.2018.12.065>
- Hlavay, J., & Polyák, K. (2005). Determination of surface properties of iron hydroxide-coated alumina adsorbent prepared for removal of arsenic from drinking water. *J Colloid Interface Sci*, *284*(1), 71-77.
- Ho, Y. S., & McKay, G. (1999a). Pseudo-second order model for sorption processes. *Process Biochemistry*, *34*, 451.
- Ho, Y. S., & McKay, G. (1999b). Pseudo-second order model for sorption processes. *Process Biochemistry*, *34*(5), 451-465. doi: [https://doi.org/10.1016/S0032-9592\(98\)00112-5](https://doi.org/10.1016/S0032-9592(98)00112-5)
- Hu, X., Ding, Z., Zimmerman, A. R., Wang, S., & Gao, B. (2015). Batch and column sorption of arsenic onto iron-impregnated biochar synthesized through hydrolysis. *Water Res*, *68*, 206-216. doi: <https://doi.org/10.1016/j.watres.2014.10.009>
- Huang, Y., Yin, X., Wu, C., Wang, C., Xie, J., Zhou, Z., . . . Li, H. (2009). Effects of metal catalysts on CO₂ gasification reactivity of biomass char. *Biotechnology Advances*, *27*(5), 568-572.
- Hwang, S., Choi, H., Park, M., Kim, J. U., & Jeon, M. (2015). Evolution of iron nanoparticles by controlling oxidation states for carbon nanotubes growth. *Materials Chemistry and Physics*, *162*, 509-517. doi: <https://doi.org/10.1016/j.matchemphys.2015.06.021>
- Issa, N. B., Rajaković-Ognjanović, V. N., Marinković, A. D., & Rajaković, L. V. (2011). Separation and determination of arsenic species in water by selective exchange and hybrid resins. *Anal Chim Acta*, *706*(1), 191-198. doi: <https://doi.org/10.1016/j.aca.2011.08.015>

- Jia, Y., Xu, L., Wang, X., & Demopoulos, G. P. (2007). Infrared spectroscopic and X-ray diffraction characterization of the nature of adsorbed arsenate on ferrihydrite. *Geochimica et Cosmochimica Acta*, 71(7), 1643-1654. doi: <https://doi.org/10.1016/j.gca.2006.12.021>
- Jin, C., Ge, C., Xu, G., Peterson, G., Jian, Z., Wei, Y., & Zhu, K. (2017). Influence of nanoparticle size on ethanol gas sensing performance of mesoporous α -Fe₂O₃ hollow spheres. *Materials Science and Engineering: B*, 224, 158-162. doi: <https://doi.org/10.1016/j.mseb.2017.07.015>
- Jin, C., Ge, C., Xu, G., Peterson, G., & Zhu, K. (2017). Influence of nanoparticle size on ethanol gas sensing performance of mesoporous α -Fe₂O₃ hollow spheres. *Materials Science and Engineering: B*, 224, 158-162.
- Joseph, S. D., Camps-Arbestain, M., Lin, Y., Munroe, P., Chia, C. H., Hook, J., . . . Amonette, J. E. (2010). An investigation into the reactions of biochar in soil. *Soil Research*, 48(7), 501-515.
- K. Sharma, R., Wooten, J., L. Baliga, V., Lin, X., Geoffrey Chan, W., & R. Hajaligol, M. (2004). *Characterization of chars from pyrolysis of lignin* (Vol. 83).
- Kanematsu, M., Young, T. M., Fukushi, K., Green, P. G., & Darby, J. L. (2013). Arsenic(III, V) adsorption on a goethite-based adsorbent in the presence of major co-existing ions: Modeling competitive adsorption consistent with spectroscopic and molecular evidence. *Geochimica et Cosmochimica Acta*, 106, 404-428. doi: <https://doi.org/10.1016/j.gca.2012.09.055>
- Keiluweit, M., Nico, P. S., Johnson, M. G., & Kleber, M. (2010). Dynamic Molecular Structure of Plant Biomass-Derived Black Carbon (Biochar). *Environmental Science & Technology*, 44(4), 1247-1253. doi: 10.1021/es9031419
- Kloss, S., Zehetner, F., Dellantonio, A., Hamid, R., Ottner, F., Liedtke, V., . . . Soja, G. (2012). *Characterization of Slow Pyrolysis Biochars: Effects of Feedstocks and Pyrolysis Temperature on Biochar Properties* (Vol. 41).
- Knicker, H., Hilscher, A., González-Vila, F. J., & Almendros, G. (2008). *A New Conceptual Model for the Structural Properties of Char Produced during Vegetation Fires* (Vol. 39).
- Koble, R. A., & Corrigan, T. E. (1952). Adsorption isotherms for pure hydrocarbons. *Industrial & Engineering Chemistry*, 44(2), 383-387.
- Koble, R. A., & Corrigan, T. E. (1952). Adsorption isotherms for pure hydrocarbons. *Ind. Eng. Chem.*, 44(2), 383-387.
- Köferstein, R., Walther, T., Hesse, D., & Ebbinghaus, S. G. (2013). Preparation and characterization of nanosized magnesium ferrite powders by a starch-gel process and corresponding ceramics. *Journal of Materials Science*, 48(19), 6509-6518. doi: 10.1007/s10853-013-7447-x
- Kumar, K. V., Castro, M. M. d., Martinez-Escandell, M., M. Molina-Sabio, Silvestre-Albero, J., & Rodriguez-Reinoso, F. (2010). A continuous site energy distribution function from Redlich-Peterson isotherm for adsorption on heterogeneous surfaces. *Chemical Physics Letters*, 492, 187-192.
- Kundu, S., & Gupta, A. (2006). Arsenic adsorption onto iron oxide-coated cement (IOCC): regression analysis of equilibrium data with several isotherm models and their optimization. *Chemical Engineering Journal*, 122(1-2), 93-106.
- Kundu, S., & Gupta, A. (2007). Adsorption characteristics of As (III) from aqueous solution on iron oxide coated cement (IOCC). *J Hazard Mater*, 142(1-2), 97-104.
- Ladeira, A., Ciminelli, V., Duarte, H., Alves, M., & Ramos, A. Y. (2001). *Mechanism of anion retention from EXAFS and density functional calculations: Arsenic (V) adsorbed on gibbsite* (Vol. 65).

- Langmuir, I. (1916). The constitution and fundamental properties of solids and liquids. Part I. Solids. *Journal of the American chemical society*, 38(11), 2221-2295.
- Langmuir, I. (1918). THE ADSORPTION OF GASES ON PLANE SURFACES OF GLASS, MICA AND PLATINUM. *Journal of the American Chemical Society*, 40(9), 1361-1403. doi: 10.1021/ja02242a004
- Lata, S., & Samadder, S. (2016). Removal of arsenic from water using nano adsorbents and challenges: a review. *J Environ Manage*, 166, 387-406.
- Lee, J., Sarmah, A., & Kwon, E. (2019a). Production and Formation of Biochar (pp. 3-18).
- Lee, J., Sarmah, A. K., & Kwon, E. E. (2019b). Chapter 1 - Production and Formation of Biochar. In Y. S. Ok, D. C. W. Tsang, N. Bolan & J. M. Novak (Eds.), *Biochar from Biomass and Waste* (pp. 3-18): Elsevier.
- Lehmann, J., Rillig, M. C., Thies, J., Masiello, C. A., Hockaday, W. C., & Crowley, D. (2011). Biochar effects on soil biota – A review. *Soil Biology and Biochemistry*, 43(9), 1812-1836. doi: <https://doi.org/10.1016/j.soilbio.2011.04.022>
- Lei, R., Ni, H., Chen, R., Zhang, B., & Li, Y. (2017). Growth of Fe₂O₃/SnO₂ nanobelt arrays on iron foil for efficient photocatalytic degradation of methylene blue. *Chemical Physics Letters*, 673(1-6).
- Lei, W., Liu, Y., Si, X., Xu, J., Du, W., Yang, J., . . . Lin, J. (2017). Synthesis and magnetic properties of octahedral Fe₃O₄ via a one-pot hydrothermal route. *Physics Letters A*, 381(4), 314-318. doi: <https://doi.org/10.1016/j.physleta.2016.09.018>
- Li, X., Zhang, Q., Hou, B., Ye, J., & Li, X. (2017). Flotation separation of quartz from collophane using an amine collector and its adsorption mechanisms. *Powder Technology*, 318, 224-229.
- Li, Y., Zhang, H., Wu, B., & Guo, Z. (2017). Improving the oxidation resistance and stability of Ag nanoparticles by coating with multilayered reduced graphene oxide. *Applied Surface Science*, 425, 194-200. doi: <https://doi.org/10.1016/j.apsusc.2017.07.054>
- Li, Y., Zhu, Y., Zhu, Z., Zhang, X., Wang, D., & Xie, L. (2018). *Fixed-bed column adsorption of arsenic(V) by porous composite of magnetite/hematite/carbon with eucalyptus wood microstructure* (Vol. 26).
- Li, Z.-Q., Yang, J.-C., Sui, K.-W., & Yin, N. (2015). Facile synthesis of metal-organic framework MOF-808 for arsenic removal. *Materials Letters*, 160, 412-414. doi: <https://doi.org/10.1016/j.matlet.2015.08.004>
- Li, Z., Jean, J.-S., Jiang, W.-T., Chang, P.-H., Chen, C.-J., & Liao, L. (2011). Removal of arsenic from water using Fe-exchanged natural zeolite. *J Hazard Mater*, 187(1-3), 318-323.
- Liang, J.-l., Sun, W.-d., Li, Y.-l., Zhu, S.-y., Li, H., Liu, Y.-l., & Zhai, W. (2013). An XPS study on the valence states of arsenic in arsenian pyrite: implications for Au deposition mechanism of the Yang-shan Carlin-type gold deposit, western Qinling belt. *Journal of Asian Earth Sciences*, 62, 363-372.
- Lin, C.-H., Johnston, C., Grant, R., & Heber, A. (2018). *Application of Open Path Fourier Transform Infrared Spectroscopy (OP-FTIR) to Measure Greenhouse Gas Concentrations from Agricultural Soils*.
- Lindblad, E. B., & Duroux, L. (2017). Chapter 18 - Mineral Adjuvants**The present chapter is an updated version of the chapter “Mineral Adjuvants,” published in Immunopotentiators in Modern Vaccines, p. 217–233. Ed. Virgil Schijns & Derek O'Hagan, Elsevier Science Publishers (2005). In V. E. J. C. Schijns & D. T. O'Hagan (Eds.), *Immunopotentiators in Modern Vaccines (Second Edition)* (pp. 347-375): Academic Press.
- Liu, S., Huang, B., Chai, L., Liu, Y., Zeng, G., Wang, X., . . . Zhou, Z. (2017). Enhancement of As(v) adsorption from aqueous solution by a magnetic chitosan/biochar composite. *RSC Advances*, 7(18), 10891-10900. doi: 10.1039/C6RA27341F

- Liu, T., Yang, Y., Wang, Z.-L., & Sun, Y. (2016). Remediation of arsenic(III) from aqueous solutions using improved nanoscale zero-valent iron on pumice. *Chemical Engineering Journal*, 288, 739-744. doi: <https://doi.org/10.1016/j.cej.2015.12.070>
- López-Cervantes, J., Sánchez-Machado, D. I., Sánchez-Duarte, R. G., & Correa-Murrieta, M. A. (2017). Study of a fixed-bed column in the adsorption of an azo dye from an aqueous medium using a chitosan–glutaraldehyde biosorbent. *Adsorption Science & Technology*, 36(1-2), 215-232. doi: 10.1177/0263617416688021
- M. Deem, L., & Crow, S. (2017). Biochar.
- Ma, X., Yuan, S., Yang, L., Li, L., Zhang, X., Su, C., & Wang, K. (2013). Fabrication and potential applications of CaCO₃-lentinan hybrid materials with hierarchical composite pore structure obtained by self-assembly of nanoparticles. *Cryst Eng Comm*, 15(41), 8288-8299.
- Ma, X., Zhou, B., Budai, A., Jeng, A., Hao, X., Wei, D., . . . Rasse, D. (2016). *Study of Biochar Properties by Scanning Electron Microscope – Energy Dispersive X-Ray Spectroscopy (SEM-EDX)*.
- Madrid, J. A., & Lanzón, M. (2017a). Synthesis and morphological examination of high-purity Ca(OH)₂ nanoparticles suitable to consolidate porous surfaces. *Applied Surface Science*, 424, 2-8. doi: <https://doi.org/10.1016/j.apsusc.2017.03.210>
- Madrid, J. A., & Lanzón, M. (2017b). Synthesis and morphological examination of high-purity Ca(OH)₂ nanoparticles suitable to consolidate porous surfaces. *Applied Surface Science*, 424(1), 2-8.
- Manceau, A. (1995). The mechanism of anion adsorption on iron oxides: Evidence for the bonding of arsenate tetrahedra on free Fe(O, OH)₆ edges. *Geochimica et Cosmochimica Acta*, 59(17), 3647-3653. doi: [https://doi.org/10.1016/0016-7037\(95\)00275-5](https://doi.org/10.1016/0016-7037(95)00275-5)
- Manning, B., Fendorf, S., & Goldberg, S. (1998). *Surface Structures and Stability of Arsenic(III) on Goethite: Spectroscopic Evidence for Inner-Sphere Complexes* (Vol. 32).
- Marinho, B. A., Cristovao, R. O., Boaventura, R. A. R., & Vilar, V. J. P. (2018). As(III) and Cr(VI) oxyanion removal from water by advanced oxidation/reduction processes-a review. *Environ Sci Pollut Res Int*. doi: 10.1007/s11356-018-3595-5
- Masek, O., Buss, W., Roy-poirier, A., Lowe, W., Peters, C., Brownsort, P., . . . Sohi, S. (2018). Consistency of biochar properties over time and production scales: A characterisation of standard materials. *Journal of Analytical and Applied Pyrolysis*. doi: 10.1016/j.jaap.2018.02.020
- Mazumder, D. G., & Dasgupta, U. (2011). Chronic arsenic toxicity: studies in West Bengal, India. *The Kaohsiung journal of medical sciences*, 27(9), 360-370.
- Mikutta, C., & Kretzschmar, R. (2011). Spectroscopic Evidence for Ternary Complex Formation between Arsenate and Ferric Iron Complexes of Humic Substances. *Environmental Science & Technology*, 45(22), 9550-9557. doi: 10.1021/es202300w
- Milonjic, S., M. Kopečni, M., & E. Ilić, Z. (1983). *The point of zero charge and adsorption properties of natural magnetite* (Vol. 78).
- Moeck, P., & Bjørge, R. (2007). *Lattice-Fringe Fingerprinting: Structural identification of nanocrystals by HRTEM* (Vol. 1026).
- Mohan, D., & Pittman, C. U. (2007a). Arsenic removal from water/wastewater using adsorbents-- A critical review. *J Hazard Mater*, 142(1-2), 1-53. doi: 10.1016/j.jhazmat.2007.01.006
- Mohan, D., & Pittman, C. U. (2007b). Arsenic removal from water/wastewater using adsorbents— A critical review. *J Hazard Mater*, 142(1), 1-53. doi: <https://doi.org/10.1016/j.jhazmat.2007.01.006>
- Mohan, D., Pittman, C. U., Bricka, M., Smith, F., Yancey, B., Mohammad, J., . . . Gong, H. (2007). Sorption of arsenic, cadmium, and lead by chars produced from fast pyrolysis of wood and

- bark during bio-oil production. *J Colloid Interface Sci*, 310(1), 57-73. doi: <https://doi.org/10.1016/j.jcis.2007.01.020>
- Mohan, D., Rajput, S., Singh, V. K., Steele, P. H., Pittman, C. U., & Jr. (2011). Modeling and evaluation of chromium remediation from water using low cost bio-char, a green adsorbent. *Journal of hazardous Materials*, 188(1-3), 319-333.
- Mohan, D., Sarswat, A., Singh, V. K., Alexandre-Franco, M., Pittman, C. U., & Jr. (2011). Development of magnetic activated carbon from almond shells for trinitrophenol removal from water. *Chemical Engineering Journal*, 172(2-3), 1111-1125.
- Mohan, D., Sharma, R., Singh, V. K., Steele, P., & Pittman, C. U. (2012). Fluoride Removal from Water using Bio-Char, a Green Waste, Low-Cost Adsorbent: Equilibrium Uptake and Sorption Dynamics Modeling. *Industrial & Engineering Chemistry Research*, 51(2), 900-914. doi: 10.1021/ie202189v
- Mohan, D., & Singh, K. P. (2002). Single- and multi-component adsorption of cadmium and zinc using activated carbon derived from bagasse--an agricultural waste. *Water Research*, 36(9), 2304-2318.
- Mohan, D., Singh, K. P., Sinha, S., & Gosh, D. (2004). Removal of pyridine from aqueous solution using low cost activated carbons derived from agricultural waste materials. *Carbon*, 42, 2409-2421.
- Mohan, D., Singh, P., Sarswat, A., Steele, P. H., Pitmann, C. U., & Jr. (2015). Lead sorptive removal using magnetic and nonmagnetic fast pyrolysis energy cane biochars. *Journal of colloid and interface science*, 448, 238-250.
- Mohan, D., Singh, P., Sarswat, A., Steele, P. H., & Pittman, C. U. (2015). Lead sorptive removal using magnetic and nonmagnetic fast pyrolysis energy cane biochars. *J Colloid Interface Sci*, 448, 238-250. doi: <https://doi.org/10.1016/j.jcis.2014.12.030>
- Mostafa, M., & Hoinkis, J. (2012). Nanoparticle adsorbents for arsenic removal from drinking water: a review. *Int J Environ Sci Manag Eng Res*, 1(1), 20-31.
- Murty, M., & Kumar, S. (2011). Water pollution in India: an economic appraisal. India infrastructure report. *Water: policy and performance for sustainable development*.
- Murty, M. N., & Kumar, S. (2011). Water pollution in India: an economic appraisal. *India infrastructure report*, 19, 285-298.
- Mussa, Z. H., Al-Qaim, F. F., Othman, M. R., Abdullah, M. P., Latip, J., & Zakria, Z. (2017). Pseudo first order kinetics and proposed transformation products pathway for the degradation of diclofenac using graphite-PVC composite as anode. *Journal of the Taiwan Institute of Chemical Engineers*, 72, 37-44. doi: <https://doi.org/10.1016/j.jtice.2016.12.031>
- Nagajyoti, P. C., Lee, K. D., & Sreekanth, T. (2010). Heavy metals, occurrence and toxicity for plants: a review. *Environmental chemistry letters*, 8(3), 199-216.
- Nath, B. K., Chaliha, C., & Kalita, E. (2019). Iron oxide Permeated Mesoporous rice-husk nanobiochar (IPMN) mediated removal of dissolved arsenic (As): Chemometric modelling and adsorption dynamics. *J Environ Manage*, 246, 397-409. doi: <https://doi.org/10.1016/j.jenvman.2019.06.008>
- Nethaji, S., Sivasamy, A., & Mandal, A. B. (2013). Adsorption isotherms, kinetics and mechanism for the adsorption of cationic and anionic dyes onto carbonaceous particles prepared from Juglans regia shell biomass. *International Journal of Environmental Science and Technology*, 10(2), 231-242. doi: 10.1007/s13762-012-0112-0
- Nguyen, B. T., Lehmann, J., Hockaday, W. C., Joseph, S., & Masiello, C. A. (2010). Temperature Sensitivity of Black Carbon Decomposition and Oxidation. *Environmental Science & Technology*, 44(9), 3324-3331. doi: 10.1021/es903016y

- P. Gallios, G., Tolkou, A., Katsoyiannis, I., Stefusova, K., Vaclavikova, M., & Deliyanni, E. (2017). *Adsorption of Arsenate by Nano Scaled Activated Carbon Modified by Iron and Manganese Oxides* (Vol. 9).
- Padmavathy, K. S., Madhu, G., & Haseena, P. V. (2016). A study on Effects of pH, Adsorbent Dosage, Time, Initial Concentration and Adsorption Isotherm Study for the Removal of Hexavalent Chromium (Cr (VI)) from Wastewater by Magnetite Nanoparticles. *Procedia Technology*, 24, 585-594. doi: <https://doi.org/10.1016/j.protcy.2016.05.127>
- Pandya, K. (1995). *Multiple-scattering effects in x-ray-absorption fine structure: Chromium in a tetrahedral configuration* (Vol. 50).
- Partey, F., Norman, D. I., Ndur, S., & Nartey, R. (2009). Mechanism of arsenic sorption onto laterite iron concretions. *Colloids and Surfaces A: Physicochemical and Engineering Aspects*, 337(1), 164-172. doi: <https://doi.org/10.1016/j.colsurfa.2008.12.018>
- Patel, H. (2019). Fixed-bed column adsorption study: a comprehensive review. *Applied Water Science*, 9(3), 45. doi: 10.1007/s13201-019-0927-7
- Pillewan, P., Mukherjee, S., Roychowdhury, T., Das, S., Bansiwaj, A., & Rayalu, S. (2011). Removal of As (III) and As (V) from water by copper oxide incorporated mesoporous alumina. *J Hazard Mater*, 186(1), 367-375.
- Plant, J. A., Bone, J., Voulvoulis, N., Kinniburgh, D. G., Smedley, P. L., Fordyce, F. M., & Klinck, B. (2014). 11.2 - Arsenic and Selenium. In H. D. Holland & K. K. Turekian (Eds.), *Treatise on Geochemistry (Second Edition)* (pp. 13-57). Oxford: Elsevier.
- Plant, J. A., Kinniburgh, D. G., Smedley, P. L., Fordyce, F. M., & Klinck, B. A. (2003). Arsenic and Selenium. 9, 17-66. doi: 10.1016/B0-08-043751-6/09047-2
- Plant, J. A., Kinniburgh, D. G., Smedley, P. L., Fordyce, F. M., & Klinck, B. A. (2014). Arsenic and Selenium. *Treatise on Geochemistry 2nd Edition*, 45. doi: 10.1016/B978-0-08-095975-7.00902-5
- Prakongkep, N., Gilkes, R., Wiriyakitnateekul, W., Duangchan, A., & Darunsontaya, T. (2013). *The Effects of Pyrolysis Conditions on the Chemical and Physical Properties of Rice Husk Biochar* (Vol. 3).
- Proctor, A., & Toro-Vazquez, J. F. (2009). Chapter 10 - The Freundlich Isotherm in Studying Adsorption in Oil Processing. In G. R. List (Ed.), *Bleaching and Purifying Fats and Oils (Second Edition)* (pp. 209-219): AOCS Press.
- Qiu, G., Gao, T., Hong, J., Tan, W., Liu, F., & Zheng, L. (2017). Mechanisms of arsenic-containing pyrite oxidation by aqueous arsenate under anoxic conditions. *Geochimica et Cosmochimica Acta*, 217, 306-319. doi: <https://doi.org/10.1016/j.gca.2017.08.030>
- Qiu, G., Gao, T., Hong, J., & Zheng, L. (2017). Mechanisms of arsenic-containing pyrite oxidation by aqueous arsenate under anoxic conditions. *Geochimica et Cosmochimica Acta*, In Press.
- Qiu, X., Lv, L., Li, G., Han, W., Wang, X., & Li, L. (2008). Vibration spectral properties, thermal stability, and their potential application in removing cadmium ions. *Journal of Thermal Analysis and Calorimetry*, 91(3), 873-878.
- Quici, N., Meichtry, J., & Montesinos, N. (2018). Use of Nanoparticulated Iron Materials for Chromium, Arsenic and Uranium Removal from Water.
- Radke, C. J., & Prausnitz, J. M. (1972a). Adsorption of Organic Solutes from Dilute Aqueous Solution of Activated Carbon. *Industrial & Engineering Chemistry Fundamentals*, 11(4), 445-451. doi: 10.1021/i160044a003
- Radke, C. J., & Prausnitz, J. M. (1972b). Adsorption of organic solutes from dilute aqueous solution on activated carbon. *Industrial and Engineering Chemistry Fundamental*, 11, 445-451.
- Rahmi, R., & Lelifajri, L. (2017). *Influence of heat treatment on eggshell particles as low cost adsorbent for methylene blue removal from aqueous solution* (Vol. 10).

- Rajput, S., Pittman, C. U., Jr., & Mohan, D. (2016). Magnetic magnetite (Fe_3O_4) nanoparticle synthesis and applications for lead (Pb^{2+}) and chromium (Cr^{6+}) removal from water. *Journal of colloid and interface science*, 468, 334-346.
- Rajput, S., Singh, L. P., Pittman, C. U., Jr., & Mohan, D. (2017). Lead (Pb^{2+}) and copper (Cu^{2+}) remediation from water using superparamagnetic maghemite ($\gamma\text{-Fe}_2\text{O}_3$) nanoparticles synthesized by Flame Spray Pyrolysis (FSP). *Journal of colloid and interface science*, 492, 176-190.
- Rajput, S., Singh, L. P., Pittman, C. U., & Mohan, D. (2017). Lead (Pb^{2+}) and copper (Cu^{2+}) remediation from water using superparamagnetic maghemite ($\gamma\text{-Fe}_2\text{O}_3$) nanoparticles synthesized by Flame Spray Pyrolysis (FSP). *J Colloid Interface Sci*, 492, 176-190. doi: <https://doi.org/10.1016/j.jcis.2016.11.095>
- Rakhecha, P. (2018a). Water Environment Management in India *Reference Module in Earth Systems and Environmental Sciences*: Elsevier.
- Rakhecha, P. (2018b). Water Environment Management in India.
- Ramos Guivar, J. A., Bustamante D, A., Gonzalez, J. C., Sanches, E. A., Morales, M. A., Raez, J. M., . . . Arencibia, A. (2018). Adsorption of arsenite and arsenate on binary and ternary magnetic nanocomposites with high iron oxide content. *Applied Surface Science*, 454, 87-100. doi: <https://doi.org/10.1016/j.apsusc.2018.04.248>
- Ramos Guivar, J. A., Sanches, E. A., Bruns, F., Sadrollahi, E., Morales, M. A., López, E. O., & Litterst, F. J. (2016). Vacancy ordered $\gamma\text{-Fe}_2\text{O}_3$ nanoparticles functionalized with nanohydroxyapatite: XRD, FTIR, TEM, XPS and Mössbauer studies. *Applied Surface Science*, 389, 721-734. doi: <https://doi.org/10.1016/j.apsusc.2016.07.157>
- Ratner, B. D. (2013). Chapter I.1.5 - Surface Properties and Surface Characterization of Biomaterials. In B. D. Ratner, A. S. Hoffman, F. J. Schoen & J. E. Lemons (Eds.), *Biomaterials Science (Third Edition)* (pp. 34-55): Academic Press.
- Raven, K. P., Jain, A., & Loeppert, R. H. (1998). Arsenite and arsenate adsorption on ferrihydrite: kinetics, equilibrium, and adsorption envelopes. *Environmental Science & Technology*, 32(3), 344-349.
- Redlich, O., & Peterson, D. L. (1959). A Useful Adsorption Isotherm. *The Journal of Physical Chemistry*, 63(6), 1024-1024. doi: 10.1021/j150576a611
- Redlich, O., & Peterson, D. L. (1959). A useful adsorption isotherm. *Journal of Physical Chemistry*, 63(6), 1024-1024.
- Reichenberg, D. (1953a). Properties of Ion-Exchange Resins in Relation to their Structure. III. Kinetics of Exchange. *Journal of the American Chemical Society*, 75(3), 589-597. doi: 10.1021/ja01099a022
- Reichenberg, D. (1953b). Properties of Ion-Exchange Resins in Relation to their Structure. III. Kinetics of Exchange. *Journal of American Chemical Society*, 75(3), 589-597.
- Rotzsche, H. (1991). The Solid Support *Journal of Chromatography Library* (Vol. 48, pp. 160-185): Elsevier.
- Rouquerol, J., Llewellyn, P., & Rouquerol, F. (2007). Is the bet equation applicable to microporous adsorbents? In P. L. Llewellyn, F. Rodriguez-Reinoso, J. Rouquerol & N. Seaton (Eds.), *Studies in Surface Science and Catalysis* (Vol. 160, pp. 49-56): Elsevier.
- Saikia, R., Goswami, R., Bordoloi, N., Senapati, K. K., Pant, K. K., Kumar, M., & Kataki, R. (2017). Removal of arsenic and fluoride from aqueous solution by biomass based activated biochar: Optimization through response surface methodology. *Journal of Environmental Chemical Engineering*, 5(6), 5528-5539. doi: 10.1016/j.jece.2017.10.027

- Salem Attia, T. M., Hu, X. L., & Yin, D. Q. (2014). Synthesised magnetic nanoparticles coated zeolite (MNCZ) for the removal of arsenic (As) from aqueous solution. *Journal of Experimental Nanoscience*, 9(6), 551-560.
- Santra, D., & Sarkar, M. (2016). Optimization of process variables and mechanism of arsenic (V) adsorption onto cellulose nanocomposite. *Journal of Molecular Liquids*, 224, 290-302. doi: <https://doi.org/10.1016/j.molliq.2016.09.104>
- Sarswat, A., & Mohan, D. (2016). Sustainable development of coconut shell activated carbon (CSAC) & a magnetic coconut shell activated carbon (MCSAC) for phenol (2-nitrophenol) removal. *RSC Advances*, 6(88), 85390-85410.
- Sasaki, K., Nakano, H., Wilopo, W., Miura, Y., & Hirajima, T. (2009). Sorption and speciation of arsenic by zero-valent iron. *Colloids and Surfaces A: Physicochemical and Engineering Aspects*, 347(1), 8-17. doi: <https://doi.org/10.1016/j.colsurfa.2008.10.033>
- Shaarani, F. W., & Hameed, B. H. (2010). Batch adsorption of 2,4-dichlorophenol onto activated carbon derived from agricultural waste. *Desalination*, 255(1), 159-164. doi: <https://doi.org/10.1016/j.desal.2009.12.029>
- Shahid, M. K., Phearom, S., & Choi, Y.-G. (2019). Adsorption of arsenic (V) on magnetite-enriched particles separated from the mill scale. *Environmental earth sciences*, 78(3), 65.
- Shao, B., Guan, Y., Tian, Z., Guan, X., & Wu, D. (2016). Advantages of aeration in arsenic removal and arsenite oxidation by structural Fe (II) hydroxides in aqueous solution. *Colloids and Surfaces A: Physicochemical and Engineering Aspects*, 506, 703-710.
- Sharma, R. K., Yadav, M., & Gupta, R. (2017). Chapter Five - Water Quality and Sustainability in India: Challenges and Opportunities. In S. Ahuja (Ed.), *Chemistry and Water* (pp. 183-205): Elsevier.
- Shen, X. (2016). 10 - Molecularly Imprinted Photocatalysts. In S. Li, S. Cao, S. A. Piletsky & A. P. F. Turner (Eds.), *Molecularly Imprinted Catalysts* (pp. 211-228). Amsterdam: Elsevier.
- Sherlala, A. I. A., Raman, A. A. A., Bello, M. M., & Buthiyappan, A. (2019). Adsorption of arsenic using chitosan magnetic graphene oxide nanocomposite. *J Environ Manage*, 246, 547-556. doi: <https://doi.org/10.1016/j.jenvman.2019.05.117>
- Sherman, D., & Randall, S. R. (2003). *Surface complexation of arsenic(V) to iron(III) (hydr)oxides: structural mechanism from ab initio molecular geometries and EXAFS spectroscopy*, *Geochim* (Vol. 67).
- Siddiqui, S. I., & Chaudhry, S. A. (2017). Arsenic removal from water using nanocomposites: a review. *Current Environmental Engineering*, 4(2), 81-102.
- Singh, B., Camps-Arbestain, M., & Lehmann, J. (2017). *Biochar : a guide to analytical methods / editors: Balwant Singh, Marta Camps-Arbestain and Johannes Lehmann*. Clayton South, VIC: CSIRO Publishing.
- Singh, B., Fang, Y., & Johnston, C. (2016). *A Fourier-Transform Infrared Study of Biochar Aging in Soils* (Vol. 80).
- Sips, R. (1948). Combined form of Langmuir and Freundlich equations. *J. Chem. Phys*, 16(429), 490-495.
- Smedley, P. L., & Kinniburgh, D. G. (2002). A review of the source, behaviour and distribution of arsenic in natural waters. *Applied Geochemistry*, 17(5), 517-568. doi: [https://doi.org/10.1016/S0883-2927\(02\)00018-5](https://doi.org/10.1016/S0883-2927(02)00018-5)
- Smith, G. C. (1994). *Surface analysis by electron spectroscopy : measurement and interpretation*. New York: Plenum Press.
- Smith, N. J. H. (1980). ANTHROSOLS AND HUMAN CARRYING CAPACITY IN AMAZONIA*. *Annals of the Association of American Geographers*, 70(4), 553-566. doi: 10.1111/j.1467-8306.1980.tb01332.x

- Sombroek, W. G. (1966). *Amazon soils : a reconnaissance of the soils of the Brazilian Amazon region*. Wageningen: Centre for Agricultural Publications and Documentation.
- Song, K., Kim, W., Suh, C.-Y., Shin, D., Ko, K.-S., & Ha, K. (2013). *Magnetic iron oxide nanoparticles prepared by electrical wire explosion for arsenic removal* (Vol. 246).
- Song, S., & Gallegos-Garcia, M. (2014). Chapter 11 - Arsenic Removal from Water by the Coagulation Process. In M. Fanun (Ed.), *The Role of Colloidal Systems in Environmental Protection* (pp. 261-277). Amsterdam: Elsevier.
- Song, X., Li, L., Geng, Z., Zhou, L., & Ji, L. (2017). Effective and selective adsorption of As (III) via imprinted magnetic Fe₃O₄/HTCC composite nanoparticles. *Journal of Environmental Chemical Engineering*, 5(1), 16-25.
- Sparks, D. L. (2003). 5 - Sorption Phenomena on Soils. In D. L. Sparks (Ed.), *Environmental Soil Chemistry (Second Edition)* (pp. 133-186). Burlington: Academic Press.
- Steiner, C. (2018). Biochar: A Guide to Analytical Methods. By B. Singh, M. Camps-Arbestain & J. Lehmann (eds). Published by CRC Press, Boca Raton, FL, USA, 2017. ix + 320 pp, Paperback, £44.99 (ISBN 9781498765534). *Soil Use and Management*, 34(1), 163-164. doi: 10.1111/sum.12389
- Su, H., Ye, Z., & Hmidi, N. (2017). High-performance iron oxide–graphene oxide nanocomposite adsorbents for arsenic removal. *Colloids and Surfaces A: Physicochemical and Engineering Aspects*, 522, 161-172. doi: <https://doi.org/10.1016/j.colsurfa.2017.02.065>
- Sun, J., Zhang, X., Zhang, A., & Liao, C. (2019). Preparation of Fe–Co based MOF-74 and its effective adsorption of arsenic from aqueous solution. *J Environ Sci (China)*, 80, 197-207. doi: <https://doi.org/10.1016/j.jes.2018.12.013>
- Sun, T., Zhao, Z., Liang, Z., Liu, J., Shi, W., & Cui, F. (2017a). Efficient removal of arsenite through photocatalytic oxidation and adsorption by ZrO₂-Fe₃O₄ magnetic nanoparticles. *Applied Surface Science*, 416, 656-665. doi: <https://doi.org/10.1016/j.apsusc.2017.04.137>
- Sun, T., Zhao, Z., Liang, Z., Liu, J., Shi, W., & Cui, F. (2017b). Efficient removal of arsenite through photocatalytic oxidation and adsorption by ZrO₂-Fe₃O₄ magnetic nanoparticles. *Applied Surface Science*, 416, 656-665. doi: 10.1016/j.apsusc.2017.04.137
- Sverjensky, D. A. (1994). Zero-point-of-charge prediction from crystal chemistry and solvation theory. *Geochimica et Cosmochimica Acta*, 58(14), 3123-3129. doi: [https://doi.org/10.1016/0016-7037\(94\)90184-8](https://doi.org/10.1016/0016-7037(94)90184-8)
- Sweeton, F. H., & Baes, C. F. (1970). *The solubility of magnetite and hydrolysis of ferrous ion in aqueous solutions at elevated temperatures* (Vol. 2).
- Tan, K. L., & Hameed, B. H. (2017). Insight into the adsorption kinetics models for the removal of contaminants from aqueous solutions. *Journal of the Taiwan Institute of Chemical Engineers*, 74, 25-48. doi: <https://doi.org/10.1016/j.jtice.2017.01.024>
- Tan, Z., Lin, C. S. K., Ji, X., & Rainey, T. J. (2017). Returning biochar to fields. *Applied Soil Ecology*, 116, 1-11. doi: 10.1016/j.apsoil.2017.03.017
- Tang, C. Y., & Yang, Z. (2017). Chapter 8 - Transmission Electron Microscopy (TEM). In N. Hilal, A. F. Ismail, T. Matsuura & D. Oatley-Radcliffe (Eds.), *Membrane Characterization* (pp. 145-159): Elsevier.
- Te, B., Wichitsathian, B., & Yossapol, C. (2017). Adsorptive behavior of low-cost modified natural clay adsorbents for arsenate removal from water. *Int. J. Geomate*, 12, 1-7.
- Temkin, M., & Pyzhev, V. (1940). Recent modifications to Langmuir isotherms.
- Temkin, M. I., & Pyzhev, V. (1940). Kinetics of ammonia synthesis on promoted iron catalysts. *Acta physiochim. URSS*, 12(3), 217-222.
- Thirunavukkarasu, O., Viraraghavan, T., & Subramanian, K. (2003). Arsenic removal from drinking water using iron oxide-coated sand. *Water, air, and soil pollution*, 142(1-4), 95-111.

- Thomas, H. C. (1944). Heterogeneous Ion Exchange in a Flowing System. *Journal of the American Chemical Society*, 66(10), 1664-1666. doi: 10.1021/ja01238a017
- Thomas, W. J., & Crittenden, B. (1998a). 1 - The development of adsorption technology. In W. J. Thomas & B. Crittenden (Eds.), *Adsorption Technology & Design* (pp. 1-7). Oxford: Butterworth-Heinemann.
- Thomas, W. J., & Crittenden, B. (1998b). 5 - Processes and cycles. In W. J. Thomas & B. Crittenden (Eds.), *Adsorption Technology & Design* (pp. 96-134). Oxford: Butterworth-Heinemann.
- Thomas, W. J., & Crittenden, B. (1998c). 6 - Design procedures. In W. J. Thomas & B. Crittenden (Eds.), *Adsorption Technology & Design* (pp. 135-186). Oxford: Butterworth-Heinemann.
- Thommes, M., Cychosz, K. A., & Neimark, A. V. (2012). Chapter 4 - Advanced Physical Adsorption Characterization of Nanoporous Carbons. In J. M. D. Tascón (Ed.), *Novel Carbon Adsorbents* (pp. 107-145). Oxford: Elsevier.
- Tian, Y., Wu, M., Lin, X., Huang, P., & Huang, Y. (2011). Synthesis of magnetic wheat straw for arsenic adsorption. *J Hazard Mater*, 193, 10-16.
- Torres, L. M., Gil, A. F., Galicia, L., & González, I. (1996). Understanding the Difference between Inner- and Outer-Sphere Mechanisms: An Electrochemical Experiment. *Journal of Chemical Education*, 73(8), 808. doi: 10.1021/ed073p808
- Toth, J. (1971). State equation of the solid-gas interface layers. *Acta Chim. Hung.*, 69, 311-328.
- Turk, T. (2017). Removal of dissolved arsenic by pyrite Ash waste. *Mine Water and the Environment*, 36(2), 255-263.
- Uchimiya, M., Wartelle, L. H., Klasson, K. T., Fortier, C. A., & Lima, I. M. (2011). Influence of Pyrolysis Temperature on Biochar Property and Function as a Heavy Metal Sorbent in Soil. *Journal of Agricultural and Food Chemistry*, 59(6), 2501-2510. doi: 10.1021/jf104206c
- Vaishya, R. C., & Gupta, S. K. (2003). Modelling arsenic (III) adsorption from water by sulfate-modified iron oxide-coated sand (SMIOCS). *Journal of Chemical Technology & Biotechnology: International Research in Process, Environmental & Clean Technology*, 78(1), 73-80.
- Viegas, R., Campinas, M., Costa, H., & Rosa, M. (2014). *How do the HSDM and Boyd's model compare for estimating intraparticle diffusion coefficients in adsorption processes* (Vol. 20).
- Viegas, R. M. C., Campinas, M., Costa, H., & Rosa, M. J. (2014). How do the HSDM and Boyd's model compare for estimating intraparticle diffusion coefficients in adsorption processes. *Adsorption*, 20, 737-746.
- Vieira, B. R., Pintor, A. M., Boaventura, R. A., Botelho, C. M., & Santos, S. C. (2017). Arsenic removal from water using iron-coated seaweeds. *J Environ Manage*, 192, 224-233.
- Vogtmann, E., Xiang, Y.-B., Li, H.-L., Levitan, E. B., Yang, G., Waterbor, J. W., . . . Wu, Q.-J. (2013). Fruit and vegetable intake and the risk of colorectal cancer: results from the Shanghai Men's Health Study. *Cancer Causes & Control*, 24(11), 1935-1945.
- Wang, M., Yu, X., Yang, C., Yang, X., Lin, M., Guan, L., & Ge, M. (2017). Removal of fluoride from aqueous solution by Mg-Al-Zr triple-metal composite. *Chemical Engineering Journal*, 322, 246-253. doi: 10.1016/j.cej.2017.03.155
- Wang, S.-y., Tang, Y.-k., Li, K., Mo, Y.-y., Li, H.-f., & Gu, Z.-q. (2014). Combined performance of biochar sorption and magnetic separation processes for treatment of chromium-contained electroplating wastewater. *Bioresour Technol*, 174, 67-73.
- Wang, S., Gao, B., Li, Y., Mosa, A., Zimmerman, A. R., Ma, L. Q., . . . Migliaccio, K. W. (2015). Manganese oxide-modified biochars: Preparation, characterization, and sorption of arsenate and lead. *Bioresour Technol*, 181, 13-17. doi: <https://doi.org/10.1016/j.biortech.2015.01.044>

- Waychunas, G., Rea, B. A., Fuller, C., & Davis, J. (1993). *Surface chemistry of ferrihydrite: Part 1. EXAFS studies of the geometry of coprecipitated and adsorbed arsenate* (Vol. 57).
- Waychunas, G. A., Kim, C. S., & Banfield, J. F. (2005). Nanoparticulate Iron Oxide Minerals in Soils and Sediments: Unique Properties and Contaminant Scavenging Mechanisms. *Journal of Nanoparticle Research*, 7(4), 409-433. doi: 10.1007/s11051-005-6931-x
- Weber, K., & Quicker, P. (2018). Properties of biochar. *Fuel*, 217, 240-261. doi: <https://doi.org/10.1016/j.fuel.2017.12.054>
- Weber, W. J., & Liu, K. T. (1980). DETERMINATION OF MASS TRANSPORT PARAMETERS FOR FIXED-BED ADSORBERS. *Chemical Engineering Communications*, 6(1-3), 49-60. doi: 10.1080/00986448008912520
- Wen, Z., Dai, C., Zhu, Y., & Zhang, Y. (2015). Arsenate removal from aqueous solutions using magnetic mesoporous iron manganese bimetal oxides. *RSC Advances*, 5(6), 4058-4068.
- Westerhoff, P., De Haan, M., Martindale, A., & Badruzzaman, M. (2006). *Arsenic Adsorptive Media Technology Selection Strategies* (Vol. 41).
- Wu, C., Huang, L., Xue, S.-G., Huang, Y.-Y., Hartley, W., Cui, M.-q., & Wong, M.-H. (2017). Arsenic sorption by red mud-modified biochar produced from rice straw. *Environmental Science and Pollution Research*, 24(22), 18168-18178.
- Xing-zhu, M., Xiao-yu, H., Xue-li, C., Zhong-chao, G., Dan, W., & Bao-ku, Z. (2016). *Study on Biochar Properties Analysis with Scanning Electron Microscope-Energy Dispersive X-Ray Spectroscopy (SEM-EDX)* (Vol. 36).
- Xu, F., Chen, H., Dai, Y., Wu, S., & Tang, X. (2019). Arsenic adsorption and removal by a new starch stabilized ferromanganese binary oxide in water. *J Environ Manage*, 245, 160-167. doi: <https://doi.org/10.1016/j.jenvman.2019.05.071>
- Xu, P., Zeng, G. M., Huang, D. L., Feng, C. L., Hu, S., Zhao, M. H., . . . Liu, Z. F. (2012). Use of iron oxide nanomaterials in wastewater treatment: a review. *Sci Total Environ*, 424, 1-10. doi: 10.1016/j.scitotenv.2012.02.023
- Xu, Z., Cai, J.-g., & Pan, B.-c. (2013). Mathematically modeling fixed-bed adsorption in aqueous systems. *Journal of Zhejiang University SCIENCE A*, 14(3), 155-176. doi: 10.1631/jzus.A1300029
- Yang, J.-S., Kim, Y.-S., Park, S.-M., & Baek, K. (2014). Removal of As (III) and As (V) using iron-rich sludge produced from coal mine drainage treatment plant. *Environmental Science and Pollution Research*, 21(18), 10878-10889.
- Yang, J., Chai, L., Yue, M., & Li, Q. (2015). Complexation of arsenate with ferric ion in aqueous solutions. *RSC Advances*, 5(126), 103936-103942. doi: 10.1039/C5RA21836E
- Yang, X., Xia, L., Li, J., Dai, M., Yang, G., & Song, S. (2017a). *Adsorption of As(III) on porous hematite synthesized from goethite concentrate* (Vol. 169).
- Yang, X., Xia, L., Li, J., Dai, M., Yang, G., & Song, S. (2017b). Adsorption of As(III) on porous hematite synthesized from goethite concentrate. *Chemosphere*, 169, 188-193.
- Yang, Y. X., Liu, M. L., Zhu, H., Chen, Y. R., & Jia, Y. Q. (2008). Preparation, characterization, magnetic property, and Mössbauer spectra of the β -FeOOH nanoparticles modified by nonionic surfactant. *Journal of Magnetism and Magnetic Materials*, 320(21), 132-136.
- Yang, Z., Lv, J., Pang, H., Yan, W., Qian, K., Guo, T., & Guo, Z. (2015). Facile Synthesis of Coaxial CNTs/MnOx-Carbon Hybrid Nanofibers and Their Greatly Enhanced Lithium Storage Performance. *Sci Rep*, 5, 17473. doi: 10.1038/srep17473

<https://www.nature.com/articles/srep17473#supplementary-information>

- Yin, H., Kong, M., Gu, X., & Chen, H. (2017). Removal of arsenic from water by porous charred granulated attapulgite-supported hydrated iron oxide in batch and column modes. *Journal of Cleaner Production*, 166, 88-97.
- Yin, Y., Zhou, T., Luo, H., Geng, J., Yu, W., & Jiang, Z. (2019). Adsorption of arsenic by activated charcoal coated zirconium-manganese nanocomposite: Performance and mechanism. *Colloids and Surfaces A: Physicochemical and Engineering Aspects*, 575, 318-328. doi: <https://doi.org/10.1016/j.colsurfa.2019.04.093>
- Yoon, Y. H. N., J.H. (1984). Application of gas adsorption kinetics. I. A theoretical model for respirator cartridge service life. *American Industrial Hygiene Association Journal*, 45(8), 509-516.
- Yu, W., Luo, M., Yang, Y., Wu, H., Huang, W., Zeng, K., & Luo, F. (2019). Metal-organic framework (MOF) showing both ultrahigh As(V) and As(III) removal from aqueous solution. *Journal of Solid State Chemistry*, 269, 264-270. doi: <https://doi.org/10.1016/j.jssc.2018.09.042>
- Yu, X., Tong, S., Ge, M., Zuo, J., Cao, C., & Song, W. (2013). One-step synthesis of magnetic composites of cellulose@iron oxide nanoparticles for arsenic removal. *Journal of Materials Chemistry A*, 1(3), 959-965. doi: 10.1039/C2TA00315E
- Yunnen, C., Ye, W., Chen, L., Lin, G., Jinxia, N., & Rushan, R. (2017). Continuous Fixed-Bed Column Study and Adsorption Modeling: Removal of Arsenate and Arsenite in Aqueous Solution by Organic Modified Spent Grains. *Polish Journal of Environmental Studies*, 26(4), 1847-1854. doi: 10.15244/pjoes/68869
- Zhang, L., Zhu, T., Liu, X., & Zhang, W. (2016). Simultaneous oxidation and adsorption of As(III) from water by cerium modified chitosan ultrafine nanobiosorbent. *J Hazard Mater*, 308, 1-10. doi: <https://doi.org/10.1016/j.jhazmat.2016.01.015>
- Zhang, L., Zhu, T., Liu, X., & Zhang, W. (2016). Simultaneous oxidation and adsorption of As(III) from water by cerium modified chitosan ultrafine nanobiosorbent. *J Hazard Mater*, 308, 1-10. doi: 10.1016/j.jhazmat.2016.01.015
- Zhang, M., & Gao, B. (2013). Removal of arsenic, methylene blue, and phosphate by biochar/AlOOH nanocomposite. *Chemical Engineering Journal*, 226, 286-292. doi: <https://doi.org/10.1016/j.cej.2013.04.077>
- Zhong, B., Wang, C., Yu, Y., Xia, L., & Wen, G. (2017). Facile fabrication of carbon microspheres decorated with B(OH)₃ and α-Fe₂O₃ nanoparticles: Superior microwave absorption. *J Colloid Interface Sci*, 505, 402-409. doi: <https://doi.org/10.1016/j.jcis.2017.05.116>
- Zhou, Z., Liu, Y.-g., Liu, S.-b., Liu, H.-y., Zeng, G.-m., Tan, X.-f., . . . Cai, X.-x. (2017). Sorption performance and mechanisms of arsenic (V) removal by magnetic gelatin-modified biochar. *Chemical Engineering Journal*, 314, 223-231.
- Zhu, J., Baig, S. A., Sheng, T., Lou, Z., Wang, Z., & Xu, X. (2015). Fe₃O₄ and MnO₂ assembled on honeycomb briquette cinders (HBC) for arsenic removal from aqueous solutions. *J Hazard Mater*, 286, 220-228. doi: <https://doi.org/10.1016/j.jhazmat.2015.01.004>
- Zhu, J., Baig, S. A., Sheng, T., Lou, Z., Wang, Z., & Xu, X. (2015). Fe₃O₄ and MnO₂ assembled on honeycomb briquette cinders (HBC) for arsenic removal from aqueous solutions. *J Hazard Mater*, 286, 220-228. doi: 10.1016/j.jhazmat.2015.01.004
- Zhuang, Z., Huang, L., Wang, F., & Chen, Z. (2015). Effects of cyclodextrin on the morphology and reactivity of iron-based nanoparticles using Eucalyptus leaf extract. *Industrial Crops and Products*, 69, 308-313. doi: <https://doi.org/10.1016/j.indcrop.2015.02.027>
- Zimmerman, A., & Gao, B. (2013). The Stability of Biochar in the Environment (pp. 1-40).

PUBLICATIONS

- “Development and application of Fe-biochar composite for arsenic removal from water”. P. Singh and D. Mohan, (2006). In P. Bhattacharya et al. (Ed.) Proceedings on Arsenic Research and Global Sustainability, As 2016. CRC Press. (pp. 539). **ISSN No.2154-6568.**
- “Mechanistic studies of As(III) remediation over developed iron-oxide biochar nanocomposites: Sorption studies and characterization”, **P. Singh**, D. Mohan, American Chemical Society (2018), 256. **ISSN No.: 0270-3009.**
- “Biochar production and applications in soil fertility and carbon sequestration – a sustainable solution to crop residue burning in India”, D. Mohan, K. Abhishek, A. Sarswat, M. Patel, **P. Singh** and C. U. Pittman, RSC Advances (Royal Society of Chemistry, 2018), Vol. 8, pp. 508-520. **ISSN No.: 2046-2069.**
- “Lead sorptive removal using magnetic and nonmagnetic fast pyrolysis energy cane biochars”, D. Mohan, **P. Singh**, A. Sarswat, P. H. Steele, C. U. Pittman Jr, Journal of Colloid and Interface Science (Elsevier, 2015), Vol. 448, Pg. 238-250. **ISSN No.: 1095-7103**

COMMUNICATED

- “Sustainable Low Concentration Arsenite [As(III)] Removal in Single and multicomponent systems using Hybrid Iron Oxide-Biochar Nanocomposite Adsorbents-A mechanistic study”, **P. Singh**, A. Sarswat, D. Mohan. Communicated for publication (Journal of Molecular Liquids, Ref. No. MOLLIQ_2019_3006, Elsevier).
- “Emerging techniques for removal of arsenic from drinking water in rural and peri-urban areas: Review on methods, experience from, and options for Latin America.” R. Kumar, M. Patel, **P. Singh**, J. Bundschuh, D. Mohan. (Science of the Total Environment, Ref. No. STOTEN-D-19-03070, Elsevier).
https://www.researchgate.net/profile/Prachi_Singh40
<https://scholar.google.co.in/citations?user=3AU85oAAAAAJ&hl=en>

PATENTS

- “Method, Design and Development of Pyrolysis Reactor for Biochar Production from Agricultural Residue”, M. Patel, R. Kumar, **P. Singh** and D. Mohan. Indian Patent. Patent No. TEMP/E-1/10073/2018-DEL
- “Rice Husk Iron-Oxide Biochar Composite (RHIOB) and Wheat Husk Iron-Oxide Biochar Composite (WHIOB) for As(III) removal from water”, **P. Singh**, A. Sarswat, D. Mohan. Indian Patent. Patent No. 201811010032